

# *SiO<sub>2</sub>-2012*

9<sup>th</sup> Symposium SiO<sub>2</sub> Advanced Dielectrics and Related Devices

*Presqu'île de Giens – Hyères (France)*

17-20 June 2012



# **INDEX**

<b>Committees .....</b>	3
<b>Technical Program .....</b>	4
<b>Oral Contributions .....</b>	4
Session 1: Defect generation and transformation .....	11
Session 2 : Electronic and atomic structure Si-SiO <sub>x</sub> -SiO <sub>2</sub>	27
Session 3 : Laser irradiation .....	37
Session 4 : Radiation effects .....	45
Session 5 : SiO <sub>2</sub> atomic structure .....	55
Session 6 : Radiation effects - Rare earth .....	63
Session 7 : Modeling .....	73
<b>Poster Session .....</b>	79

# **COMMITTEES**

## **Conference chairs**

Bertrand POUMELLEC and Matthieu LANCRY

Institut de Chimie Moléculaire et des Matériaux d'Orsay, University of Paris-Sud 11

## **Symposium Committee**

Jean-Luc AUTRAN, University of Provence, France

Aziz BOUKENTER, University Saint-Etienne, France

Marco CANNAS, University of Palermo, Italy

Sylvain GIRARD, CEA DAM, Ile de France

Michel HOUSSA, IMEC, Leuven, Belgium

Matthieu LANCRY, University of Paris Sud 11, France

Maurizio MONTAGNA, University of Trento, Italy

Youcef OUERDANE, University Saint-Etienne, France

Philippe PAILLET, CEA-DIF, SEIM, France

Bertrand POUMELLEC, University Paris Sud 11, France

Nicolas RICHARD, CEA DAM Ile de France; DCRE, France

Sandro SANTUCCI, University of L'Aquila, Italy

Angela SEDDON, University of Nottingham, UK

Alexander SHLUGER, University College London, UK

## **Local Organizing Committee**

Matthieu Lancry, Bertrand Poumellec, Antoine Weickman, Rudy Desmarchelier,  
Adelhouhad Erraji-Chahid, Sylvain Girard, Manon Heili, Nicolas Richard, Annie Millet  
ICMMO, University of Paris-Sud 11

## TECHNICAL PROGRAM

### **Sunday, June 17th**

18h00-19h30	• Conference Registration and welcome cocktail
19h30-21h00	<i>Dinner</i>

### **Monday, June 18th**

9h00-9h10	• Conference opening
9h10-12h50	• Session 1 : Defect generation and transformations
10h50-11h10	<i>Coffee break</i>
13h00-14h30	<i>Lunch</i>
14h30-16h00	• Session 2 : Electronic and atomic structure Si/SiO <sub>x</sub> /SiO <sub>2</sub>
16h00-16h30	<i>Coffee Break</i>
16h30-17h50	• Session 3 : Laser irradiation
19h30-21h00	<i>Dinner</i>

### **Tuesday, June 19th**

9h00-10h30	• Session 4 : Radiation effects
10h30-11h00	<i>Coffee break</i>
11h00-12h30	• Session 5 : SiO <sub>2</sub> atomic structure
12h30-14h00	<i>Lunch</i>
14h00-18h00	<i>Free Time</i>
18h00-19h30	<i>Cocktail</i>
19h30-21h30	<i>Conference Dinner</i>
21h30-00h30	“Party”

### **Wednesday, June 20th**

9h00-10h30	• Session 6 : Radiation effects / Rare earth
10h30-11h00	<i>Coffee Break</i>
11h00-12h00	• Session 7 : Modeling Session
12h00-12h10	• Concluding remarks
12h30-14h00	<i>Lunch</i>

# Monday, June 18th

## Session 1: Defect generation and transformations

- 9h10 **D. Griscom**  
“On the natures of radiation-induced point defects in GeO<sub>2</sub>-SiO<sub>2</sub> glasses : reevaluation of a 27-year-old ESR and optical data set”
- 10h **L. Skuja**, K. Kajihara, H. Hosono  
“Thermostimulated luminescence of interstitial O<sub>2</sub> in F<sub>2</sub> laser-irradiated glassy SiO<sub>2</sub>”
- 10h30 **C.M. Carbonaro**, R. Corpino, P.C. Ricci, M. Salis, A. Anedda  
“Filling the pores of mesoporous silica to investigate the origin of visible photoluminescence of surface centers”
- 11h20 **A.N. Trukhin**, K.M. Golant, J. Teteris  
“Luminescence of unfused F-doped 95%SiO<sub>2</sub>-5%GeO<sub>2</sub> amorphous films fabricated by SPCVD. Absence of GeODC(I) defects”
- 11h50 **Pukhkaya V.**, Ollier N.  
“EPR study of defects in Yb-doped Na-aluminosilicate glasses”
- 12h10 **G. Iovino**, S. Agnello, F. M. Gelardi  
“Dependence of O<sub>2</sub> diffusion dynamics on pressure and temperature in silica nanoparticles”
- 12h30 A.F. Zatsepин, **E.A. Buntov**, V.S. Kortov, V.A. Pustovarov, H.-J. Fitting  
“On the Origin of the Green-Violet PL Bands in the Selenium-Implanted Silica Films”

## Session 2 : Electronic and atomic structure Si-SiO<sub>x</sub>-SiO<sub>2</sub>

- 14h30 **A. Stesmans**, P. Somers, V. V. Afanas'ev  
“Multi-frequency ESR analysis of interfacial Ge dangling bond defects in (100)Si/SiO<sub>2</sub>/Si<sub>1-x</sub>Ge<sub>x</sub>/SiO<sub>2</sub> heterostructures”
- 15h **M. Cannas**, L. Vaccaro, L. Spallino, A.F. Zatsepин, E.A. Buntov, A.V. Ershov, I.A. Chugrov  
“Impact of Poly-Reoxidation Process Step on Tunnel Oxide Reliability: Charge Trapping and Data Retention”
- 15h20 **G. Just**, J.-L. Ogier, A. Regnier, J. Postel-Pellerin, F.Lalande, P.Masson  
“Impact of Poly-Reoxidation Process Step on Tunnel Oxide Reliability: Charge Trapping and Data Retention”
- 15h40 **M. Jivanescu**, A. Stesmans, R. Kurstjens, and F. Dross  
“Interface nature of ordered thermally oxidized Si nanowires”

## Session 3 : Laser Irradiation

- 16h30 **C. P. Gonschior**, K.-F. Klein, T. Sun, K. T. V. Grattan  
“Generation of periodic surface structures on silica fibre surfaces with 405 nm CW diode lasers”
- 16h50 **X. He**, C. Fan, B. Poumellec, M. Lancry, F. Brisset, Q. Liu, G. Chen, X. Zhao  
“Controllable local photo-induced crystallization in SiO<sub>2</sub>-based glasses by femtosecond laser”
- 17h10 **L. Spallino**, L. Vaccaro, S. Agnello, M. Cannas  
“Effects induced by UV laser radiation on the blue luminescence of silica nanoparticles”
- 17h30 **S. Chouli**, E. Freysz  
“Time resolved measurements of gratings photo- induced by femtosecond pulses in a lead doped glass”

**Thursday, June 19th**

## Session 4 : Radiation effects

- 9h Michael McLain, **Fred Hartman**, Tom Zarick, Tim Sheridan  
“Prompt Radiation-induced Conductivity in SiO<sub>2</sub> Dielectrics at High Dose Rates”
- 9h30 **L. Vaccaro**, M. Cannas, S. Girard, A. Alessi, A. Boukenter, Y. Ouerdane, R. Boscaino  
“Influence of fluorine on the fiber performance studied through the NBOHC-related 1.9 eV microluminescence”
- 9h50 A. Morana, A. Boukenter, Y. Ouerdane, S. Girard, M. Cannas, J. Périsse, J.-R. Macé  
“Thermal bleaching of gamma-induced-defects in optical fibers”

## Session 5 : SiO<sub>2</sub> Atomic Structure

- 11h **V. Martinez**, C. Martinet, D. de Ligny, B. Champagnon, S. Ses  
“Impact of the fictive temperature on the silica glass anomaly compressibility: in-situ Raman spectroscopy at high pressure”
- 11h30 **M. Heili**, M. Lancry, E. Burov, C. Le Losq, D. Neuville, and B. Poumellec  
“Impact of fictive temperature on glass density and structure of Ge-doped silica glasses”
- 11h50 **A.Alessi**, S. Agnello, G. Buscarino, F.M. Gelardi  
Raman investigation of silica nanoparticles structure
- 12h10 **T. Crémoux**, M. Dussauze, V. Rodriguez, E. Fargin, T. Cardinal

## Wednesday, June 20th

### Session 6 : Radiation effects - Rare earth

- 9h      Thierry Deschamps, **Nadège Ollier**  
“Gamma rays radiation effects on  $\text{SiO}_2\text{-Al}_2\text{O}_3\text{-P}_2\text{O}_5$  doped  $\text{Yb}^{3+}$  optical fiber preforms: effect of the Al/P dopants”
- 9h30     **L. Mescia**, S. Girard, G. Fornarelli, A. Giaquinto, F. Prudenzano, M. De Sario, A. Boukenter, Y. Ouerdane  
“Optimum design of radiation-hardened and high power  $\text{Er}^{3+}\text{-Yb}^{3+}$ -codoped fiber amplifiers by means of particle swarm approach”
- 9h50     **M. Vivona**, S. Girard, C. Marcandella, E. Pinsard, A. Laurent, T. Robin, B. Cadier, M. Cannas, A. Boukenter, Y. Ouerdane  
“Radiation responses of Yb/Er-doped phosphosilicate optical fibers: hardening mechanisms related to Ce-codoping”
- 10h10    Valérie Mauroy, **Wilfried Blanc**, Michèle Ude, Stanislaw Trzesien, Bernard Dussardier  
“Growth of rare-earth doped oxydenanoparticles in silica fibers”

### Session 7 : Modeling

- 11h     **Layla MARTIN-SAMOS**, Nicolas RICHARD, Sylvain GIRARD, Aziz BOUKENTER, Youcef OUERDANE, Jean-Pierre MEUNIER  
“First-principles study of electronic and optical properties of intrinsic defects in a-SiO<sub>2</sub>”
- 11h30    **AI-Moatasem EI-Sayed**, Alexander Shluger, Matthew Watkins  
“Electron trapping defects in bulk silica “

# Poster Session

- P1. Hydrogen reaction kinetics of the GeP<sub>b1</sub> defect at the (100)Si<sub>1-x</sub>Ge<sub>x</sub>/SiO<sub>2</sub> interface  
*N. H. Thoan, A. Stesmans, K. Keunen, and V. V. Afanas'ev*
- P2. Active area definition for embedded devices with phase change memory and logic  
*Mario Francesco Pistoni, Patrizia Bernardinello, Stefano Colombo*
- P3. Geant4 Physics Processes for Microdosimetry Simulation: Very Low Energy Electromagnetic Models for Electrons in Silicon Dioxide  
*Mélanie Raine, Marc Gaillardin, Philippe Paillet*
- P4. Optical characterization of Polysilazane based SOD thin films as a function of the growth parameters.  
*Pier Carlo Ricci, Gianluca Gulleri, Francesco Fumagalli, Carlo Maria Carbonaro, Riccardo Corpino*
- P5. Contact module definition for 110 nm Technology node on BCD platforms  
*M. Pistoni, S. Paolillo, I. Venegoni*
- P.6. Establishing the Link between Densification Mechanisms and Interface Nanostructure in High-k Deposition on Silicon Oxide: A Multi-Scale Modeling Study  
*C. Mastail, A. Estève, N. Richard, M. Djafari Rouhani, G. Landa and A. Hemeryck*
- P.7 Development of an Empirical Model for Fast prediction of Non Volatile Memory Reliability  
*H. Aziza, J.M. Portal, J. Plantier, C. Reliaud, A. Regnier, J.L. Ogier*
- P.8 Investigation of charge losses through dielectrics in a NVM array using data retention gate stress  
*J. Postel-Pellerin, G. Micolau, P. Chiquet, J. Melkonian, R. Laffont, F. Lalande, J.L. Ogier*
- P.9 Comparison of electronic and optical properties of mixed SiO<sub>2</sub>-GeO<sub>2</sub> amorphous system by first-principles  
*Nicolas Richard, Layla Martin-Samos, Sylvain Girard, Aziz Boukenter, Youcef Ouerdane, Jean-Pierre Meunier*
- P.10 Vibrations of Oxygen Interstitials α-Quartz  
*A.N. Kislov, A.F. Zatsepin, I.A. Aleksashina*
- P11. Early Silicon interstitial generation Silicon Oxide Amorphisation via Ring Pattern Nuclei  
*C. Mastail, A. Hemeryck, A. Estève, N. Richard, M. Djafari Rouhani and G. Landa*
- P12. A new fast gate current measurement protocol for the study of transient regimes in metal-oxide-semiconductor structures  
*Philippe Chiquet, Pascal Masson, Gilles Micolau, Romain Laffont, J. Postel-Pellerin, Frédéric Lalande, Bernard Bouteille, Arnaud Regnier*
- P13. Porous Silica as host for PEG-supported coumarin molecules  
*C.M. Carbonaro, M.F. Casula, P.C. Ricci, M. Cubeddu, G. Tocco*
- P14. Temperature dependence of O<sub>2</sub> singlet photoluminescence in silica nanoparticles  
*S. Agnello, L. Vaccaro, G. Iovino, M. Cannas, K. Kajihara*

- P15. Properties of methyl radical induced by irradiation in high-purity amorphous SiO<sub>2</sub> and in natural SiO<sub>2</sub>-clathrate Melanophlogite  
*G. Buscarino, S. Agnello, F.M. Gelardi and R. Boscaino*
- P16. Comparative study of fused silica materials for ArF laser applications  
*Christian Mühlig, Simon Bublitz, Helmut Bernitzki*
- P17. Influence of the Substrate tube Quality on TSL Features of Yb-doped Silica Preforms of Optical Fibres  
*M. Benabdesselam, F. Mady*
- P18. Design of mid-infrared Er<sup>3+</sup>-doped microsphere laser  
*F. Prudenzano, L. Mescia, P. Bia, M. De Sario*
- P19. Luminescence of fused and unfused Bi-doped amorphous silica fabricated by SPCVD  
*Anatoly Trukhin, Janis Teteris, Aleksey Bazakutsa and Konstantin Golant*
- P20. Investigation on the generation process of HO<sub>2</sub>• radicals induced by γ-ray irradiation in O<sub>2</sub>-loaded fumed silica  
*G. Buscarino, S. Agnello, A. Parlato, F. M. Gelardi*
- P21. Tracking of defects induced by IR-femtosecond laser irradiation in silica  
*R. Desmarchelier, M. Lancry, B. Poumellec and B. Bourguignon*
- P22. A physico-chemical approach for the modification energy threshold by femtosecond laser irradiation in glasses  
*B. Poumellec and M. Lancry*
- P23. Spectral UV-losses in 355 nm pulsed laser delivery system at low temperatures  
*J. C. Heimann, C. P. Gonschior, K.-F. Klein, G. Hillrichs, E. Takala*

# Session 1

## Defect generation and transformations



# On the natures of radiation-induced point defects in $\text{GeO}_2\text{-SiO}_2$ glasses: reevaluation of a 27-year-old ESR and optical data set

David L. Griscom

impactGlass research international, San Carlos, Sonora, México  
mail to: 3938 E Grant Rd #131, Tucson, AZ 85712, USA.

## ABSTRACT

27-year-old electron spin resonance (ESR) and optical data pertaining to isochronal annealing studies of x-ray induced defect centers in a  $\text{GeO}_2\text{-SiO}_2$  glass are revisited here with the object of extracting new insights regarding the fundamental natures of these defects. It is concluded [1] that (i) the paramagnetic Ge(1) and Ge(2) centers are two energetically inequivalent configurations of a single trapped-electron defect, in analogy to what is known to be the case for the Ge(II) and Ge(I) centers respectively in  $\alpha$  quartz [Isoya et al., J. Chem. Phys. **69**, 4876 (1978)] and (ii) the germanium lone pair center (GLPC) stably traps holes only in pairs and hence remains ESR silent.

**PACS Keywords:** fiber optics, electron spin resonance, Ge-doped silica, radiation-induced defect centers, optical spectroscopy

## 1 INTRODUCTION

Twenty seven years ago, my colleague at the Naval Research Laboratory Joe Friebele and I respectively performed optical absorption and electron-spin-resonance (ESR) isochronal annealing experiments from  $\sim 100$  K to  $\sim 900$  K following x-irradiation at 77 K of separate subsamples of a  $\text{GeO}_2\text{-SiO}_2$  glass cut from the core of an experimental fiber-optic preform. To my knowledge, such a concurrent pair of ESR and optical experiments carried out over such an extended temperature range has never again been repeated. Therefore, the data that we obtained back then remain relevant to a still-highly-active field of research. Unfortunately, however, Joe and I failed to completely describe our experimental details – or our methods of data analysis – in our sole publication on the subject, a short review article for conference proceedings [2]. Worse still, it turns out that we each lost our respective spectra, calculations, and other records pertaining to these experiments. Thus, my presentation will necessarily begin by describing our original experiments and methods of analysis as best as we have been able to recall them.

I will next present Joe's and my original isochronal-anneal figure with certain changes reflecting my deduced reconstruction of some important but heretofore unrevealed details of our experiments. I will then explain why this new graph appears to be the key to resolving decades-old disagreements regarding the natures of the paramagnetic Ge(1) and Ge(2) centers, as well as the hole-trapping properties of twofold-coordinated germaniums (commonly termed “germanium lone pair centers” or GLPCs). Crucial

to this objective was the previously noted [3] high degree of correspondence between the ESR spin Hamiltonian parameters of the Ge(1) and Ge(2) centers in irradiated  $\text{GeO}_2\text{-SiO}_2$  glasses and those of their far better characterized doppelgangers in Ge-doped crystalline  $\alpha$  quartz [4], i.e., the Ge(II) and Ge(I) centers, respectively. Elucidated for the first time in [1] was the similarity of the temperature dependencies of the relative number densities of the Ge(1) and Ge(2) centers radiation-induced in the glasses at cryogenic temperatures to those rigorously determined [4] for the Ge(II) and Ge(I) centers, respectively, in  $\alpha$  quartz. Because of this similarity I argued in [1] that the former pair of defects, like the latter, represents two energetically inequivalent configurations of an electron trapped on a  $\text{GeO}_4$  tetrahedron, the short-range details of which are typical of *both* of these polymorphs of silicon dioxide. Thus, the  $\text{GeO}_4$  tetrahedra that trap electrons in Ge-doped silica glasses must possess a degree of quartz-like local structure – a revelation certain to lead to a very different understanding of silica glass structure.

## 2 THE DETAILS OF THIS WORK HAVE BEEN PUBLISHED ELSEWHERE

The above Abstract and Introduction are taken nearly verbatim from a recently published article by the author [1]. A detailed PowerPoint presentation of the process and results of this tortuous piece of science archeology will be created explicitly for presentation at the Hyères meeting.

- [1] On the natures of radiation-induced point defects in  $\text{GeO}_2\text{-SiO}_2$  glasses: reevaluation of a 26-year-old ESR and optical data set, D.L. Griscom, Optical Materials Express Vol. 1, 400-412 (2011).
- [2] E.J. Friebele and D.L. Griscom, "Color centers in glass optical fiber waveguides," in *Defects in Glasses - MRS Vol. 61*, F.J. Galeener, D.L. Griscom, M.J. Weber, Eds. (Materials Research Society, 1986), pp. 319-331
- [3] D.L. Griscom, "Trapped-electron centers in pure and doped glassy silica: A review and synthesis," J. Non-Cryst. Solids **357**, 1945-1962 (2011).
- [4] J. Isoya, J.A. Weil and R.F.C. Claridge, "The dynamic interchange and relationship between germanium centers in  $\alpha$  quartz," J. Chem. Phys. **69**, 4876-4884 (1978).

# Thermostimulated luminescence of interstitial O<sub>2</sub> in F<sub>2</sub> laser-irradiated glassy SiO<sub>2</sub>

L. Skuja\*, K. Kajihara\*\*, H. Hosono\*\*\*

\* Institute of Solid State Physics, University of Latvia  
8 Kengaraga str., Riga, LV1063 Latvia

\*\* Department of Applied Chemistry, Graduate School of Urban Environmental Sciences,  
Tokyo Metropolitan University  
1-1 Minami-Osawa, Hachioji 192-0397, Japan

\*\*\* Materials and Structures Laboratory, Tokyo Institute of Technology,  
4259 Nagatsuta, Midori-ku, Yokohama 226-8503, Japan

## ABSTRACT

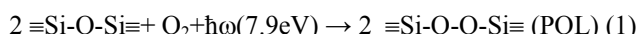
Low-temperature thermostimulated infrared luminescence band at 1272 nm due to interstitial O<sub>2</sub> molecules in F<sub>2</sub> laser-irradiated oxygen-rich SiO<sub>2</sub> glass was observed in the 120-210 K region with peak intensity at 180 K. The luminescence is accompanied by a slight increase in concentration of interstitial O<sub>2</sub> molecules, which have been previously destroyed by laser irradiation. This low-temperature O<sub>2</sub> recovery process precedes the main O<sub>2</sub> recovery stage at 500..600 K, attributed in the previous studies to the diffusion of interstitial O atoms in the form of peroxy linkages, which are immobile at lower T's. The probable mechanisms of the low-temperature O<sub>2</sub> recovery stage, including trapping/detrapping of charge carriers or recombination of close pairs of O interstitials are discussed.

**PACS Keywords:** silica, point defects, interstitial oxygen, thermostimulated luminescence

## 1 INTRODUCTION

Intrinsic point defects in pure SiO<sub>2</sub> glass are formed predominantly by Frenkel (vacancy-interstitial) mechanism, as contrasted to formation of pairs of dangling bonds [1]. Oxygen vacancies are generally associated with the characteristic optical absorption (OA) band at 7.6 eV. In contrast, O interstitials, which are thought to exist in SiO<sub>2</sub> as peroxy linkages ("POL", Si-O-O-Si bonds) [2], do not have a distinct and easy-to-use spectroscopic signature. However, their presence can be confirmed indirectly by creation of their dimerized form - an interstitial O<sub>2</sub> molecule, which possesses a distinct infrared luminescence band at 1272 nm (0.97 eV).

It has been previously reported that interstitial O can be generated in oxygen-surplus a-SiO<sub>2</sub> by F<sub>2</sub>-laser photolysis of interstitial O<sub>2</sub> molecules:



and that the interstitial O<sub>2</sub> molecules can be subsequently restored by annealing at temperatures above 500 K [3].

This process is assumed to be due to the onset of diffusion and bi-molecular recombination of POL's with diffusion activation energy of  $\Delta E \approx 1.1$  eV. According to this basic model, no restoration of O<sub>2</sub> should take place at temperatures lower than 300 K.

The present paper reports experimental evidence for additional processes, which restore a fraction of photolyzed O<sub>2</sub> molecules at much lower temperatures, between 120 and 210K. The possibilities that this low-temperature process is due to electron/hole trapping or due to recombination of close pairs of POLs are discussed.

## 2 EXPERIMENTAL

Synthetic "dry" SiO<sub>2</sub> glass, manufactured by oxidation in oxygen plasma, containing  $4 \times 10^{17}$  interstitial O<sub>2</sub> molecules/cm<sup>3</sup> and  $1.5 \times 10^{17}$  hydroxyl (silanol, Si-OH) groups (analog of commercial Suprasil W brand) was studied. The sample was placed in a liquid N<sub>2</sub> cryostat (Oxford Optistat DN) equipped with CaF<sub>2</sub> windows and irradiated at T=80K with 7.9 eV photons from F<sub>2</sub> excimer laser (Lambda Physik, Compex 101). Some samples were photo-bleached by UV light ( $\hbar\omega = 3.3\text{-}4.3$  eV). The Raman and O<sub>2</sub> infrared luminescence spectra were measured by Nicolet 960 Fourier transform Raman spectrometer with Nd-YAG laser (1064.1 nm) excitation and a cooled Ge photodetector. Optical absorption (OA) spectra were obtained by Hitachi U4000 (visible and ultraviolet (UV) range) and JASCO VU201 (vacuum UV range) spectrometers.

## 3 RESULTS

Fig. 1 shows the overlapping Raman scattering and O<sub>2</sub> photoluminescence (PL) spectra measured under 1064.1 nm excitation at T=80K. Spectrum 1 is measured for unirradiated sample, and shows strong O<sub>2</sub> PL band at 7868 cm<sup>-1</sup>. After F<sub>2</sub> laser irradiation (T=80 K, 28.4 J/cm<sup>2</sup>) the intensity of O<sub>2</sub> PL band diminishes to 10% from the initial value (spectrum 2). After warming up to 300K (warming rate 4 K/minute) and cooling down to 80 K the

intensity of O<sub>2</sub> PL partially recovers (to 18% from the initial value, Spectrum 3).

Figure 2 shows thermostimulated luminescence glow curve, featuring a distinct peak at 182 K. At all temperatures the luminescence spectrum consists of a single emission band due to O<sub>2</sub> molecules whose position (7852 cm<sup>-1</sup>) is, however slightly red-shifted from the O<sub>2</sub> PL band (Fig.1, 7868 cm<sup>-1</sup>). This TSL signal becomes detectable at 118K and vanishes at 210K. It reappears at 278K indicating a presence of another TSL glow peak above the upper limit of the measured temperature range (350K, Fig.2).

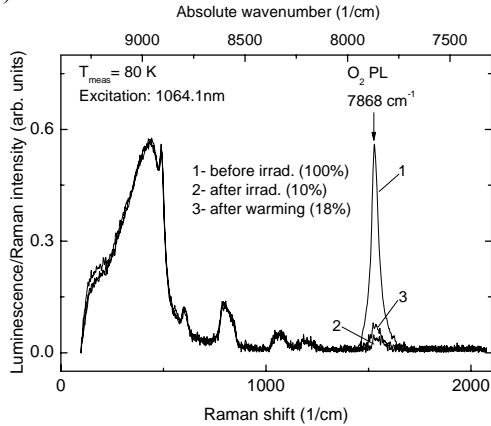


Fig.1. Superposition of silica Raman and O<sub>2</sub> photoluminescence spectra in oxygen-rich SiO<sub>2</sub> glass, before (1) and after (2) irradiation at 80 K by F<sub>2</sub> laser photons (7.9 eV). Spectrum 3 shows the partial recovery of O<sub>2</sub> concentration after warming the sample to 300K. All spectra were measured at 80K.

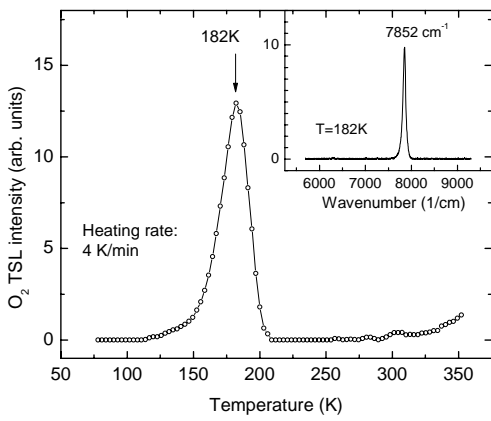


Fig.2. Thermostimulated luminescence (TSL) peak of interstitial oxygen molecules in O<sub>2</sub> in oxygen-rich SiO<sub>2</sub> glass, irradiated at 80 K by F<sub>2</sub> laser photons (7.9 eV). Inset shows the spectrum of TSL, measured at T=182 K.

Vacuum UV optical absorption spectrum of pristine sample showed a broad absorption wing in 6.8-8.0 eV

region, whose intensity correlated well with the values, calculated from the concentration of interstitial O<sub>2</sub> and the known spectrum of OA cross section values [4]. This absorption wing decreased after F<sub>2</sub> laser irradiation. Laser-induced UV OA spectra were dominated by a wide UV band with peak at 4.8 eV with shape similar to OA of non-bridging oxygen hole centers. UV-photobleaching experiments indicated that induced OA spectrum contains also a 4.8 eV peak characteristic to interstitial ozone molecules.

## 4 DISCUSSION

The presence of TSL glow peak at 182 K (Fig.2) and the 8% recovery of the initial O<sub>2</sub> concentration in the temperature range 80-300K (Fig.1) indicate that apart from the main O<sub>2</sub> recovery stage at  $\approx$ 500 K there exists another, minor O<sub>2</sub> recovery process, which has much lower activation energy. For the simplest case of the 1st order recombination process, the fitting of the initial stage of TSL glow peak ("initial rise method") yields activation energy of 0.11 eV.

This low activation energy O<sub>2</sub> recovery process in principle could be caused either by purely electronic process (e.g., by trapping of hole on O<sub>2</sub><sup>-</sup> molecular ion and resulting in O<sub>2</sub> molecule in electronically excited state) or by dimerization of two closely spaced (paired) interstitial oxygens (i.e., two peroxy linkages (POLs)). The former alternative is rendered less probable by the absence of electron paramagnetic resonance (EPR) evidence for O<sub>2</sub><sup>-</sup> ions in F<sub>2</sub> laser-irradiated silica. On the other hand, the calculated activation barrier for creation of O<sub>2</sub> molecule from two POLs is around 1 eV [5], much higher than the experimental value of 0.11 eV. Thus, additional alternatives like close pairs of POL with oxygen-excess point defects, such as peroxy radicals, non-bridging oxygen hole centers or ozone molecules, or reactions including hydrogen or chlorine impurities should be considered too. Further experimental work is needed to distinguish between these alternatives.

L.S. travel was supported by European regional development fund grant 2010/0204/2DP/2.1.1.2.0./10/APIA/VIAA/010

## REFERENCES

- [1] K. Kajihara, M. Hirano, L. Skuja, H. Hosono, Phys. Rev. B 78, 09421, 2008.
- [2] D. R. Hamann, Phys. Rev. Lett., 81, 3447 (1998).
- [3] L. Skuja, M. Hirano, K. Kajihara, H. Hosono, Phys. Chem. Glasses, 43C, 145, 2002.
- [4] K. Kajihara, T. Miura, H. Kamioka, A. Aiba, M. Uramoto, Y. Morimoto, M. Hirano, L. Skuja, H. Hosono, J. Non-Crystalline Solids, 354, 224, 2008.
- [5] A. L. Shluger, J. L. Gavartin, M. A. Szymanski, A. M. Stoneham, Nucl. Instr. Meth. Phys. Res. B166-167, 1, 2000.

# Filling the pores of mesoporous silica to investigate the origin of visible photoluminescence of surface centers.

C.M. Carbonaro<sup>\*,\*\*</sup>, R. Corpino<sup>\*,\*\*</sup>, P.C. Ricci<sup>\*</sup>, M. Salis<sup>\*</sup>, A. Anedda<sup>\*,\*\*</sup>

<sup>\*</sup>Department of Physics, University of Cagliari

Campus of Monserrato, s.p. n° 8, km 0.700, 09042 Monserrato (Italy)

<sup>\*\*</sup>C.G.S. Centro Grandi Strumenti, Department of Physics, University of Cagliari

Campus of Monserrato, s.p. n° 8, km 0.700, 09042 Monserrato (Italy)

## ABSTRACT

The emission properties of mesoporous silica are investigated by filling the pores of the transparent matrix with different solvents and gasses. The modifications induced on the surface texture of silica matrices with different pore diameters by the interaction of the emitting surface centers with the filling media are discussed aiming to assign the origin of the gathered UV and visible emissions.

**PACS Keywords:** porous silica, photoluminescence, surface centers

## 1 INTRODUCTION

Nanostructured silica, such as nanoparticles, nanorods, nanotubes and nanowires, finds a large number of surface-related applications ranging from the catalysis field (as nano and micro reactors) to chromatography, from biomedicine (as host for drug delivery systems) to photonics and integrated optoelectronics [1]. To spark off the increasing scientific and industrial interest in these materials is the possibility of fine-tuning their shape, size and morphology, depending on the synthesis strategy applied. In addition the possible applications are largely connected to the chemistry and texture of the silica surface. Since the surface of nanosized silica is typically covered by a moiety of silanol groups (Si-OH), the silane and siloxane chemistry can play a role into engineering a specific silica based device. Indeed nanostructured silica displays surface related optical, electrical and mechanical properties due to the presence of intrinsic or extrinsic defect centers [2]. Among the others, we are mainly concerned on the photoluminescence (PL) properties of nanosized silica which exhibits PL features in the UV (at about 340 nm) and visible range, at about 450 nm. The latter depends on the texture of the silica surface and is related to the degree of cross-linking between silica precursors in sol-gel synthesis [3]. The emission is characterized by VUV and UV excitation channels and a bi-exponential decay time with short lifetime of about 2-4 ns and a long lifetime of about tens of ns (typically 20 ns) [4, 5]. The PL intensity can be increased upon thermal treatment up to 400° C and is

affected by aging and annealing in different gaseous environments (increase with oxygen, decrease with nitrogen) [4, 5]. In addition also the interaction with H<sub>2</sub>O<sub>2</sub> or different solvent (polar, non polar and protic) can modify the PL features by quenching or increasing its intensity, changing the decay time or evidencing a vibrational structure [5]. The attribution of this emission to a specific surface center has been long debated in the last decade, the proposed models including surface silanol groups, carbon impurities and self-trapped excitons. Concerning the origin of the blue emission the carbon-related species were excluded and a silicon/oxygen related defect pair consisting of dioxasilirane and silylene groups was proposed [3, 4]. In a recent paper we investigated the effect of the aging process on the emission properties of mesoporous silica and the possibility to regenerate them through a strong oxidation procedure by H<sub>2</sub>O<sub>2</sub> [6]. Since the emission properties are related to texture, morphology and coverage of silica surface, being the interaction among different silanol groups related to the pore size of the matrix, in this work we focus our attention on the modification induced on the PL features of mesoporous silica with different pore diameters by the aging and regeneration procedure. The work also aims to study the interaction of the silica surface with different gasses and solvents.

## 2 METHODS

The two set of investigated samples (S1 and S2) are sol-gel synthesized commercial porous silica monoliths (diameter 5 mm, thickness 2 mm) produced by Geltech Inc. (US) with pore diameter distribution sharply peaked at 3.2 (18.2) nm (BET analysis, 5% of standard deviation), a pore volume of 0.488 (1.203) cm<sup>3</sup>g<sup>-1</sup> with a specific surface area of 594 (264) m<sup>2</sup>g<sup>-1</sup> and a density of about 1.2 (0.6) g cm<sup>-3</sup> for S1 and S2 (under brackets) respectively.

Samples were analyzed “as received”, after aging because of long exposure to ambient atmosphere or filled with different solvents and gasses. The whole set of measurements was carried out at room temperature and at atmospheric pressure.

Time resolved PL were carried out by exciting the sample with the emission at 250 nm of an optical parametric oscillator with frequency doubler device

(Spectra Physics MOPO), seeded by a pulsed Nd-YAG laser (Spectra Physics QuantaRay PRO-270). The excitation pulse energy was of about 1 mJ/pulse and pulse-width at half-maximum was 8 ns with 10 Hz repetition rate. PL measurements were performed in 90° geometry, focusing the emitted light signal onto the entrance slit of a monochromator (ARC Spectra Pro 300i) with spectral bandwidth of 0.1 eV. The signal was detected by a gatable intensified CCD (Princeton Instruments PIMAX). Depending on PL bands under examination different time delays from excitation pulse and time gates were used. PL spectra were corrected for the spectral response of the optical system.

Optical absorption measurements were carried out in transmission mode by irradiating the sample with light in the near UV and visible range and detecting the transmitted signal with a photonic multichannel analyzer (PMA11 Hamamatsu), bandwidth of 1 nm.

### 3 RESULTS AND DISCUSSION

It was previously reported that when exciting at 250 nm with synchrotron radiation the PL spectrum of mesoporous silica typically shows two large emission bands peaked at about 340 and 450 nm, the intensity of the UV band being twice the intensity of the blue band [6].

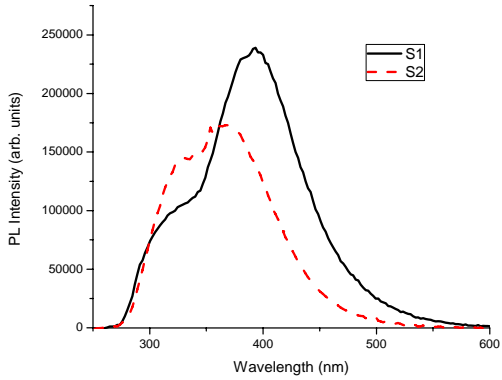


Figure 1: zero time delay PL spectra of aged S1 and S2 samples excited at 250 nm.

Fig. 1 shows the PL spectra recorded on S1 and S2 samples after long aging at ambient atmosphere. The two spectra refers to the zero time delay acquisition, that is the first recorded spectra after the laser shot. Two broad and smooth PL bands are detected, peaked at about 330 and below 400 nm. As compared to the data reported in the literature there are few important differences to be pointed out: first, the relative contribution of the two emission bands is reversed, being the blue band more intense than the UV band. Second, the peak position of the blue emission band is blue-shifted at about 390 and 360 nm in the S1 and S2 samples respectively. In addition the gathered PL profile is smooth, with no vibrational features. Concerning the aging

procedure, we can observe that the induced modifications are different in the two samples: indeed the relative contribution of the UV band with respect to the blue one is larger in S2 samples than in S1. The decay curves of the two samples are in the nanosecond regime and show a fast decay of few ns (that is as fast as the laser) and a slow decay of tens of ns. However, as the PL intensity decreases the PL profile undergoes modifications: the contribution of the UV band is strongly reduced (showing that its decay time is faster than the blue band one) and the peak position of the blue band red shift to about 415 nm in both the samples. Fig. 2 reports the zero time delay spectrum and the PL emission recorded after 45 ns in the case of the S1 samples, comparable trend being observed in the case of S2 samples.

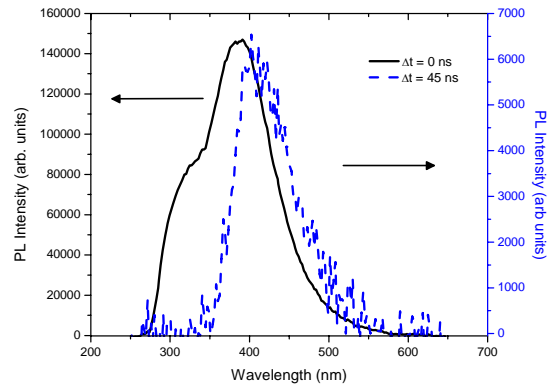


Figure 2: PL spectra of aged S1 samples excited at 250 nm at zero time delay from the laser shot and after 45 ns.

The reported data indicated that the silica surface is covered by a distribution of emitting centers whose spectral properties depends on the morphology of the surface itself and which are sensitive to the interaction with the surrounding environment. They can be regarded as the fingerprint of the texture of the samples and their structural and chemical composition can be studied through the interactions with different solvents and gasses.

### REFERENCES

- [1] L.M. Tong, R.R. Gattass, J.B. Ashcom, S.L. He, J.Y. Lou, M.Y. Shen, I. Maxell, E. Mazur, Nature 426, 816, 2003.
- [2] S. Banerjee, A. Datta, Langmuir 26, 1172, 2010.
- [4] A. Nishimura, N. Sagawa, T. Uchino, Phys. Chem. Lett. 113, 4260, 2009.
- [5] A. Nishimura, S. Harada, T. Uchino, J. Phys. Chem C 114, 8568, 2010
- [6] S. Banerjee, S. Honkote, A. Datta, J. Phys. Chem C 115, 1576, 2011.
- [7] C.M. Carbonaro, P.C. Ricci, R. Corpino, M. Marceddu, A. Anedda, J. Non-Cryst. Solids 357, 1904, 2011.

# Luminescence of unfused F-doped 95% $\text{SiO}_2$ -5% $\text{GeO}_2$ amorphous films fabricated by SPCVD. Absence of GeODC(I) defects

A.N. Trukhin<sup>1</sup>, K.M. Golant<sup>2</sup>, J. Teteris<sup>1</sup>

<sup>1</sup>University of Latvia, Solid State Physics Institute,  
LV-1063, Riga, Latvia

<sup>2</sup>Kotel'nikov Institute of Radio-engineering and Electronics of RAS,  
125009 Moscow, Russia

## ABSTRACT

Influence of fluorine additive on luminescence of germanium oxygen deficient centers (GeODCs) in amorphous germanosilicate films fabricated by the surface-plasma chemical vapor deposition (SPCVD) is studied. Deposited on silica substrates films of about 100 micron in thickness with “high” (~4.2 wt. %) and “low” (~0.5 wt. %) fluorine content are investigated. It is found that absorption and luminescence associated with GeODCs in “high” and “low” F content films differ. In particular absorption coefficient in the band at 5 eV as well as intensity of blue luminescence are significantly higher for “high” F content film. We attribute the observed effect to a significant increase of viscosity in the “high” F material, which leads to immediate structural relaxation of the film during the deposition even without subsequent material fusion by external heating. Absorption and luminescence features of unfused “high” F film are typical for GeODC(II) type of defects. No manifestation of a hypothetical GeODC(I) is found in either “high” or “low” F content film.

**PACS Keywords:** germanium and fluorine doped silica, luminescence, surface-plasma chemical vapor deposition technology

## 1 INTRODUCTION

Our experiments are performed to address the question if a hypothetical GeODC(I) defect can be identified in amorphous material composed by 95% of silica and 5% of germania. We focused on the search of any empirical evidence for the presence of GeODC(I) defect abstracting oneself from its particular structure such as Ge-Ge and Si-Ge oxygen vacancies or something along those lines.

It is well known that in pure silica with oxygen deficiency one can identify SiODC(I) defects, which are characterized by the luminescence band centered at 7.6 eV. Presence of these defects in addition to SiODCs(II) or twofold coordinated silicon centers [1], which also have the 7.6 eV band in their luminescence spectrum, is confirmed by specific spectral and kinetics parameters of the 7.6 eV luminescence band.

Starting point for our research is based on the fact that properties of SiODC(I) can be strongly affected by fluorine incorporation in silica network. Similarity between GeODC(II) or twofold coordinated germanium and SiODC(II) or twofold coordinated silicon let one expect to find out a similarity between GeODC(I) and SiODC(I) as well. For this reason the observation of an impact of fluorine on luminescence associated with GeODCs could serve as an indication of the presence of GeODC(I) in the material.

## 2 EXPERIMENTAL

Samples of germanosilicate  $\text{Si}_{0.95}\text{Ge}_{0.05}\text{O}_2$  material in the form of 100 micron thick films are synthesized by the surface plasma chemical vapor deposition (SPCVD) on high purity UV grade silica substrates. Silicon and germanium tetrachlorides vapors mixed with oxygen are used as the raw materials in deposition. To produce fluorine doped material, high purity  $\text{CF}_4$  is added to the gas mixture. Fluorine content in a glass is controlled by setting a ratio of  $\text{SiCl}_4$  and  $\text{CF}_4$  flows. Substrate temperature during the deposition is kept as high as 1100 C. Two kinds of samples with different (4.2 wt. % and 0.5 wt. %) fluorine content are synthesized.

There are two significant features, which addition of fluorine brings to SPCVD chemistry. Firstly, fluorine effectively substitutes chlorine, which is inevitable contamination for silica, if  $\text{SiCl}_4$  is used as the raw material for deposition. Secondly, even a small addition of fluorine to silica significantly reduces its softening temperature. For this reason heavily F-doped silica layer could be considered as fused material in conditions of the deposition at a substrate temperature of 1100 C [3].

248 nm, 193 nm and 157 nm wavelengths excimer lasers are used to excite luminescence in our experiments.

## 3 RESULTS

In both “low” and “high” F content samples all the three lasers excite two luminescence bands, a blue one and a UV one. Decay kinetics and intensities of these bands strongly depend on excitation laser wavelength for the “low” F film

and are independent on it for the “high” F one. In the “low” F film the 248 nm wavelength laser excites conventional blue band with decay time  $t \sim 100 \mu\text{s}$  and fast UV band with  $t \sim 4 \text{ ns}$ . Intensity of the “low” F film luminescence is about 500 times smaller than that one for the “high” F film.

Spectral and kinetics parameters of luminescence excited by 157 nm wavelength laser for both types of films are shown in Fig. 1. It is seen that in the “high” F film such excitation yields luminescence spectrum and decay time constant, which are characteristic for the excitation of twofold coordinated germanium. In the “low” F film blue luminescence is unusually fast and UV band is not observed at all.

The difference in spectral and kinetics characteristics of luminescence is observed for the 193 nm wavelength laser excitation as well. Blue band decay takes place within  $\sim 50 \mu\text{s}$  time interval and is strongly non-exponential. In both 157 nm and 193 nm wavelengths laser excitation a long time (hours) exposure leads to an increase of the blue and UV bands luminescence intensities.

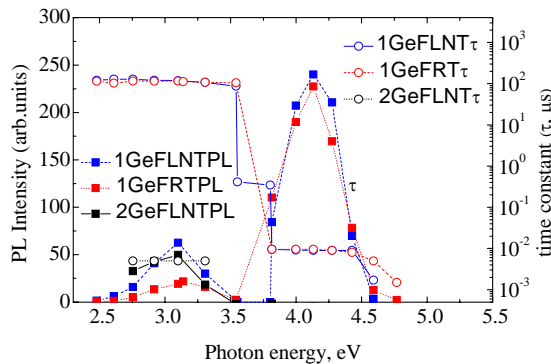


Figure 1. Intensity and  $\tau$  spectra of luminescence under  $\text{F}_2$  (157 nm wavelength) laser pulses. 1GeF - “high” F, 2GeF - “low” F. RT -293 K, LNT – 80 K.

#### 4 DISCUSSION

Depending on concentration, fluorine additive in different ways modifies luminescence properties of the unfused material obtained by the SPCVD method. This could be associated with the dependence of softening temperature on fluorine content in the material. In unfused fluorine free samples GeODCs stay in a latent state and yield shortly living luminescence under the excitation by the ArF laser [4]. Apparently similar defects in a latent state are responsible for luminescence in the “low” F sample.

As for the “high” F sample, the “ordinary” GeODC’s blue band luminescence with decay time of  $110 \pm 10 \mu\text{s}$  is observed for all three types of the excimer lasers excitation. UV band is observed with time constants of  $6 \pm 1 \text{ ns}$  for 248 nm,  $10-25 \text{ ns}$  for 193 nm and  $9 \text{ ns}$  for 157 nm wavelength excitation. So the effect of “high” F includes softening temperature decrease, which acts similarly to fusion in the case of fluorine free samples.

In the 7.6 eV spectral band, which corresponds to SiODC(I) and to hypothetical GeODC(I), no shortening of the luminescence decay time for the “high” F sample is observed in passing from 157 nm to 248 nm excitation wavelength lasers. In F containing samples SiODC(I) could be suppressed, but no suppression of GeODCs absorption by fluorine additive is observed thus indicating the absence of the GeODCs(I). Excitation by both 193 nm and 157 nm wavelength lasers yields a longer duration of luminescence decay for the UV band. Possible nature of this effect is related to fluorine interaction with other defects. Excitation by high energy photons can transfer ODCs for a short period of time to an active state. The effect is similar to that one observed in fluorine free unfused material, in which ODCs are terminated by chlorine contamination.

#### 5 CONCLUSION

Our study shows that the addition of fluorine to germanosilicate unfused material fabricated by SPCVD leads to the formation of GeODC(II) defects, provided fluorine concentration is high enough. Viscosity decrease associated with fluorine additive works like a fusion in temperature conditions of the SPCVD process.

It is found that fluorine additive suppress luminescence of SiODCs(I) centers. However, no evidence is found to confirm the availability of GeODC(I) centers in the samples under investigation. This means that in germanosilicate amorphous materials only SiODC(I) centers could contribute to luminescence in the 7.6 eV spectral band.

#### ACKNOWLEDGMENTS

This work is supported by the Latvian Council grants 09.1125 and 09.1126 as well as Material Science program (IMIS). Spectral-kinetics investigations are supported with ERAF project 2010/0275/2DP//2.1.1.0/10/APIA/VIAA/124.

#### REFERENCES

- [1] Skuja, L.N. Streletsky, A.N. Pakovich, A.B. “A new intrinsic defect in amorphous  $\text{SiO}_2$ ”, Solid State Commun. **50**, 1069-1072, 1984.
- [2] L.N.Skuja, A.N.Trukhin, A.E.Plaudis, “Luminescence in germanium-doped glassy  $\text{SiO}_2$ ”, Phys.Stat.Sol.(a) 84 K153-K157, 1984.
- [3] R. E. Youngman, S. Sen, “Structural role of fluorine in amorphous silica”, J. Non-Cryst. Solids, 349, 10-16, 2004.
- [4] A. Trukhin, K.M. Golant, J. Teteris, “Absorption and luminescence in amorphous  $\text{Si}_x\text{Ge}_{1-x}\text{O}_2$  films fabricated by SPCVD” J. Non-Cryst. Solids, submitted for publication

# EPR study of defects in Yb-doped Na-aluminosilicate glasses

V. Pukhkaya, N. Ollier

Laboratoire des Solides Irradiés  
LSI, Ecole Polytechnique, route de Saclay, 91128, Palaiseau Cedex, France

## ABSTRACT

Paramagnetic defects formation and post-irradiation relaxation was investigated in Yb-doped aluminosilicate glasses as a function of the glass composition and irradiation conditions (irradiation type and dose). The nature and content of the defect is correlated to ASI index and Yb doping. Yb<sup>3+</sup> ions stimulate [Al]<sup>0</sup> centers formation and, the presence of Yb-clusters, limit efficiently the relaxation of defects.

**PACS Keywords:** aluminosilicate glasses, Electronic Paramagnetic Resonance, irradiation, defects, Yb

## 1 INTRODUCTION

Silica-based optical fibers containing some rare-earth elements (Er<sup>3+</sup>, Nd<sup>3+</sup>, Yb<sup>3+</sup>, Tm<sup>3+</sup>) can be used either for laser application or telecommunication (amplification of the signal).

Ionizing irradiation gives rise to point defect creation in the glass that can impact the luminescence properties of Yb<sup>3+</sup> ions [1]. We are concerned here by the links between the initial Yb glass structure (Yb repartition and environment) and the defect formation and its relaxation behavior.

## 2 EXPERIMENTAL SETUP AND RESULTS

Glass samples were prepared with the appropriated amounts of SiO<sub>2</sub>, Al<sub>2</sub>O<sub>3</sub>, Na<sub>2</sub>CO<sub>3</sub> and Yb<sub>2</sub>O<sub>3</sub>. The initial chemicals were mixed and melted at 1400°C in Pt-Au crucibles and then quenched rapidly at room temperature. All glasses were afterwards annealed at 580°C to release mechanical strengths. The glass compositions are presented in table 1.

Glass samples were irradiated with 2.5 MeV electrons (LSI, SIRIUS) and with 1.25 MeV gamma-rays (INSTN, Tunisia).

Paramagnetic defects were characterized at room temperature with an X-band EMX Bruker spectrometer, (9.8 GHz). The modulation of the field was 20 mT for 1 mW microwave power.

Under electron irradiation below 6 MGy only hole centers were detected by EPR in glasses. Among them, 3 types of defects can be distinguished: HC<sub>1</sub> defects (hole center on non-bridging oxygen at close presence of alkali ion), Peroxy radicals ≡Si—O—O· and [Al]<sup>0</sup> centers which are hole centers on NBO, bonded to Al ions [2].

Sample name	SiO <sub>2</sub> , % mol.	Al <sub>2</sub> O <sub>3</sub> , % mol.	Na <sub>2</sub> O, % mol.	ASI, Al/Na mol.
AS22	74	6	20	0.3
AS23	68	12	20	0.6
AS24	62	18	20	0.9
AS26	58	22	20	1.1
AS24_0	62	18	20	0.9
AS24_05	62	18	20	0.9
AS24_8	62	18	20	0.9

Table 1: Nominal glass compositions, in all glasses except “AS24\_x” concentration of Yb is 5% mass. Yb<sub>2</sub>O<sub>3</sub>, x=0 – no Yb, x=05 - 0.5% mass. Yb<sub>2</sub>O<sub>3</sub>, x=8 - 8% mass. Yb<sub>2</sub>O<sub>3</sub>.

In Yb-doped electron-irradiated glasses the defect amount increases with Aluminum Saturation Index (ASI) decreases, (fig. 1). With further ASI increasing more [Al]<sup>0</sup> centers were created. Yb-doping of AS24 glass leads to total defects’ amount decreasing, but relative content of [Al]<sup>0</sup> centers increasing.

Concerning effect of composition and Yb-incorporating in gamma-irradiated glasses, we observed the same general tendency as in previous case. Nevertheless, the impact of irradiation type exists. In glass with the lowest Al content under gamma-irradiation defects are created less efficiently, and relatively more HC<sub>1</sub> are seen. At the other side, in glass with the highest Al content there is relatively lower amount of [Al]<sup>0</sup> centers formed.

The total amount of defects decreases in time up to 3 months. In Yb-doped electron-irradiated samples relaxation rate is slower in glasses with higher Al content – AS24 and AS26. Presence of Yb in AS24 gives rise to quicker relaxation process (fig. 2). Glass composition has the same impact on relaxation rates in gamma-irradiated samples. Despite that in gamma-irradiated glasses with lower [Al]<sup>0</sup> center content and higher relative HC<sub>1</sub> amount relaxation rate is slower than in case of electron-irradiation. The contrast effect is thus observed in samples containing more aluminum oxide.

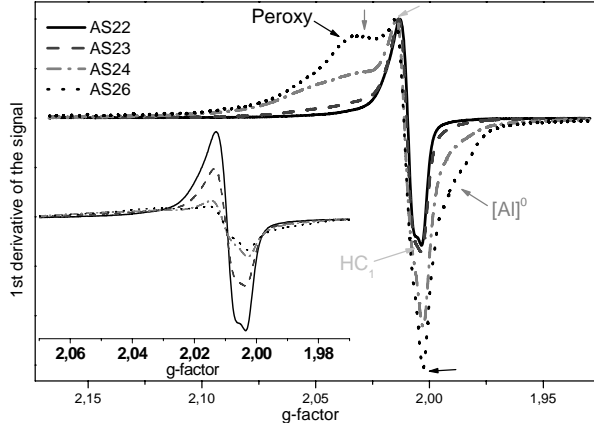


Figure 1: Normalized by  $g=2.013$  EPR spectra of Yb-doped e-irradiated AS glasses, dose  $10^5$  Gy. Spectra normalized by mass and gain is in the inset.

### 3 DISCUSSION

When Al content increases in glasses with a constant Na content, the  $\text{Na}^+$  ions are used to compensate the charge of  $\text{AlO}_4^-$  entities so the glass become less polymerized with a NBO decrease and thus we easily understand the origin of the  $\text{HC}_1$  defect decrease associated to the  $[\text{Al}]^0$  centers increase under irradiation. During irradiation process  $\text{Yb}^{3+}$  ions can be reduced by trapping some electron [4]. Adding Yb leads to a decrease of the total amount of defect because  $\text{Yb}^{3+}$  ions can consume some hole and electron and compete with defect formation in agreement with [4-5].

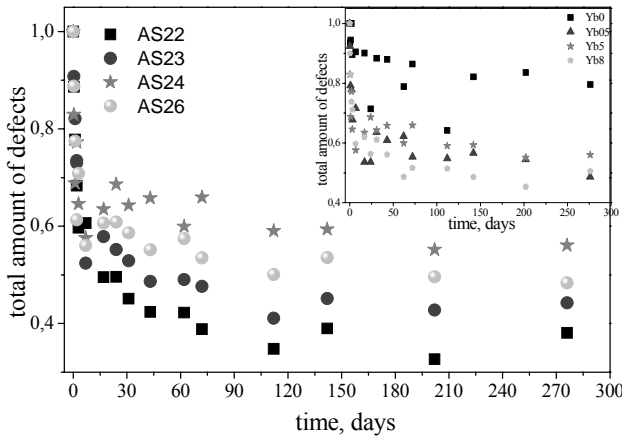


Figure 2: Relaxation of total amount of paramagnetic defects calculated from double integration of EPR spectra of Yb-doped e-irradiated AS glasses, dose  $10^5$  Gy, normalization by 1<sup>st</sup> day, AS24\_Ybx in the inset.

In [3] it was shown that in AS24 and AS26 glasses Yb ions tend to form clusters more efficiently than in AS22 and AS23. We observe less defect amount in glasses with higher Yb-clusters content. That allows us to conclude that Yb ions being under clustering may trap some charges more efficiently than well-dissolved Yb in glass network.

Moreover, the relaxation rate of defects depends on the glass composition, slower for AS24 and AS26. We thus propose than an effective and persistent charge trapping of Yb ions that are under clustering form can delay the charge recombination with defects. Higher relaxation rate with Yb-doping can be due to the proximity of Yb with some defect such as  $[\text{Al}]^0$  center explain an easier charge recombination. (fig. 1). We observe finally an increase of relative amount of  $\text{HC}_1$  defects in time; and a clear anticorrelation between  $[\text{Al}]^0$  centers amount and  $\text{HC}_1$  defects.

### 4 CONCLUSIONS

In Yb-doped aluminosilicate glasses, the amount of Yb-clusters influences on point defects formation under irradiation and their afterwards relaxation. It seems that Yb ions involved into clustering can be more efficient in trapping charge during irradiation than well-dissolved ions and induce a slower relaxation rate of defects.

### REFERENCES

- [1] N. Ollier, J.-L. Doualan, V. Pukhkaya, T. Charpentier, R. Moncorgé, S. Sen J. of Non-Cryst. Solids 357, 1037-1043, 2011.
- [2] D.L. Griscom, E.J. Friebel Phys. Rev. B 24, 4896-4898, 1981.
- [3] B. Schaudel, Thèse de Doctorat de l'Université Paris VI, 2000.
- [4] N. Ollier, R. Planchais, B. Boizot, Nucl. Instr. and Meth. in Phys. Res. B 266, 2854–2858, 2008.
- [5] E. Malchukova, B. Boizot, D. Ghaleb, G. Petite, JNCS, 352, 297-303, 2006.

# /Dependence of O<sub>2</sub> diffusion dynamics on pressure and temperature in silica nanoparticles

G. Iovino\*, S. Agnello\*, F. M. Gelardi\*

\*Physics Department, University of Palermo  
Via Archirafi 36, 90123, Palermo, Italy

## ABSTRACT

An experimental study of the diffusion properties of oxygen molecules in silica nanoparticles is reported. By thermal treatments at temperatures up to 160°C the diffusion has been investigated both in outgassing and in loading dynamics. The obtained results evidence that the diffusion process is governed by Fick's theory both for entrance and exit of oxygen. Furthermore, a dependence of the O<sub>2</sub> content on the pressure is found showing a tendency to leveling at high pressure independently on temperature. This latter finding evidences a limit of O<sub>2</sub> solubility in silica.

**PACS Keywords:** oxygen diffusion, nanosilica, near-infrared photoluminescence, Raman.

## 1 INTRODUCTION

Amorphous SiO<sub>2</sub> is a prototype material in the study of physical properties of vitreous systems and is important in technology for its applications in optics and electronics devices. Miniaturization of electronics devices shifted the scientific interest toward nanosized silica. In this context, the investigation of O<sub>2</sub> diffusion in nanosilica represents an interesting topic, on the one hand from a basic physics point of view, on the other hand because the interstitial O<sub>2</sub> affects the properties the host system. This work extends the wide investigation made on O<sub>2</sub> diffusion in bulk silica to nanosilica and investigates a range of low temperature and high pressure not studied in bulk systems.

## 2 EXPERIMENTAL

The diffusion experiments were carried out on hydrophilic silica nanoparticles (commercially known as Aereosil fumed silica) produced by the pyrogenic technique and having a purity larger than 99.8%. The starting material, which is a powder of spherical particles, was pressed at about 0.3 GPa to obtain tablets. Data reported in this work refer to tablets produced by 20 nm average radius nanoparticles powder. The investigation of diffusion was made by measuring the interstitial O<sub>2</sub> volume average concentration in nanoparticles after thermal treatments either in air or in O<sub>2</sub> atmosphere. Concentration was

determined from PL amplitude of interstitial O<sub>2</sub> at 1272 nm under laser excitation at 1064 nm [1,2]. Measurements were performed by a FT-Raman spectrometer (RAMII Bruker) equipped with a Nd:YAG laser source (1064 nm emission wavelength) at 500 mW beam power. The spectral resolution was 15 cm<sup>-1</sup>. Raman spectra so acquired present both the Raman bands of silica and the PL band of interstitial O<sub>2</sub>, enabling a direct estimation of this latter content.

### 2.1 Outgassing experiments

As grown material contains interstitial O<sub>2</sub> molecules. In outgassing experiments, the sample was thermally treated in air in a furnace to outgas these O<sub>2</sub> molecules. In order to determine the diffusion coefficient, the O<sub>2</sub> content was measured after treatments of increasing duration until the equilibrium value was reached. The furnace temperature was stabilized within ±1°C. The sample heating and cooling times between room and thermal treatment temperatures were about 2 minutes.

### 2.2 Loading experiments

Sample was first thermally treated at 300°C for 5 minutes in air to completely remove native oxygen. Then the outgassed sample was put in a stainless steel pipe placed in the same furnace used for outgassing experiments. Pipe was emptied by a vacuum pump down to pressure of about 0.1 mbar and then filled with O<sub>2</sub>. No heating time was present in these experiments because when oxygen was added the sample has already reached the treatment temperature. At the end of thermal treatment the sample and the pipe were cooled in about 1 minute. In order to find out the diffusion coefficient, treatments of different duration were made until O<sub>2</sub> equilibrium value was reached for each temperature and pressure investigated.

## 3 RESULTS AND DISCUSSION

In Figure 1, the relative variation of interstitial O<sub>2</sub> concentration (C<sub>i</sub>, C<sub>f</sub> and C(t) are the initial, final and at time t O<sub>2</sub> volume average concentrations, respectively) is reported as a function of the treatment time divided by the square of the average particles radius, r. Three different O<sub>2</sub>

external pressures at 130°C are shown. The data relative to the treatment in air refer to an outgassing experiment in which the interstitial O<sub>2</sub> concentration decreases on increasing time. The other data sets are obtained from loading experiments in which oxygen enters into the nanoparticles.

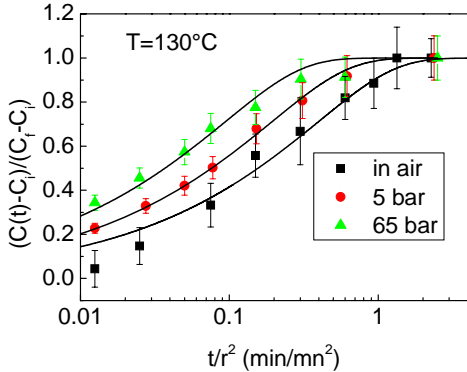


Figure 1: Relative variation at 130°C of volume average O<sub>2</sub> concentration as a function of time  $t$  divided by the square of average particle radius  $r$ .  $C_i$ ,  $C_f$  and  $C(t)$  are defined in the text. Solid lines are the best fit curves obtained by fitting experimental data with eq. (1).

According to the solution of Fick's diffusion equation, the relative variation of volume average O<sub>2</sub> concentration at time  $t$ , in the case of uniform initial distribution of O<sub>2</sub> molecules within a sphere of radius  $r$ , and supposing that the equilibrium value on the particle's inner surface is achieved instantaneously, can be put in the following form [3]:

$$\frac{C(t)-C_i}{C_f-C_i} = 1 - \frac{6}{\pi^2} \sum_{n=1}^{\infty} \frac{1}{n^2} \exp\left(-\frac{\pi^2 n^2 D t}{r^2}\right) \quad (1)$$

where  $D$  is the diffusion coefficient.

Lines reported in Fig. 1 are the best fit curves obtained by fitting the experimental data with eq.(1). The agreement between experimental data and the model is good if a dependence of diffusion coefficient on external O<sub>2</sub> pressure is introduced. In particular, the diffusion coefficient increases on increasing the pressure as can be seen from data shown in fig. 1. Diffusion coefficient values from the best fit curves are  $(0.18 \pm 0.06)$  nm<sup>2</sup>/min,  $(0.40 \pm 0.03)$  nm<sup>2</sup>/min,  $(0.6 \pm 0.01)$  nm<sup>2</sup>/min for in air (0.2 bar partial O<sub>2</sub> pressure), at 5 bar and at 65 bar treatments, respectively.

Figure 2 shows the equilibrium concentration values of interstitial O<sub>2</sub> as a function of thermal treatment O<sub>2</sub> pressure at two different temperatures. At low pressure the O<sub>2</sub> concentration is proportional to pressure in agreement with the Henry's law. At higher pressure the data deviate from linear trend and show saturation at a value of O<sub>2</sub>

concentration that does not depend on temperature. A qualitatively similar behavior was observed for hydrogen and helium dissolution in bulk silica [4]. Regarding the relationship between interstitial O<sub>2</sub> concentration and temperature, O<sub>2</sub> content increases on decreasing temperature as observed for O<sub>2</sub> dissolution in bulk silica.

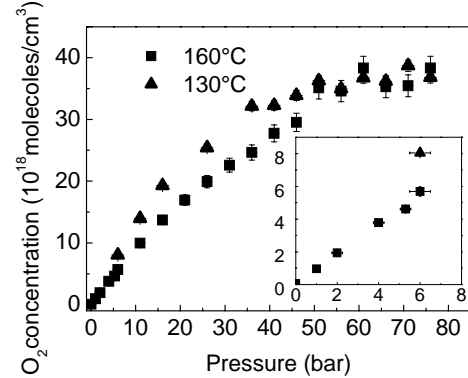


Figure 2: Dependence of interstitial O<sub>2</sub> concentration at diffusive equilibrium on the thermal treatments O<sub>2</sub> pressure for two different temperatures. The inset shows a zoom of the low pressure data.

## 4 CONCLUSION

Diffusion properties of O<sub>2</sub> molecules in nanosilica were experimentally investigated at temperatures below 160 °C and pressure from 0.2 to 75 bar. The diffusion kinetics can be described by Fick's diffusion equation in a spherical geometry approximation. The obtained diffusion coefficients depend on O<sub>2</sub> pressure during the thermal treatment. Equilibrium value of interstitial O<sub>2</sub> concentration depends on pressure and temperature. In particular, it increases on increasing pressure and on decreasing temperature. A departure from Henry's law was found at high pressure where interstitial O<sub>2</sub> content is independent on external O<sub>2</sub> pressure.

## REFERENCES

- [1] L. Skuja and B. Guttler, Phys. Rev. lett. 77, 2093, (1996).
- [2] S. Agnello et al., J. Phys. Chem. C, 115, 12831, (2011).
- [3] J. Crank, ed., The mathematics of diffusion: Second Edition (Clarendon Press, Oxford, 1979).
- [4] J.E. Shelby, J.Appl. Phys., 47, 135, (1976).

# On the Origin of the Green-Violet PL Bands in the Selenium-Implanted Silica Films

A.F. Zatsepin\*, E.A. Buntov\*, V.S. Kortov\*, V.A. Pustovarov\*, H.-J. Fitting\*\*

\*Ural Federal University,

Mira street, 19, 620002, Ekaterinburg, Russia

\*\*Institute of Physics, University of Rostock,  
Universitätsplatz 3, D-18051 Rostock, Germany

## ABSTRACT

In this paper we present the results of low-temperature photoluminescence (PL) investigation of thin  $\text{SiO}_2$  films implanted with  $\text{Se}^+$  ions. Besides selenium nanoclusters luminescence (1.8 eV),  $\text{SiO}_2:\text{Se}^+$  films demonstrate intensive PL bands in the green and violet spectral regions. Their exclusive occurrence in the nanostructured samples points out their nanocluster-matrix interface origin. The green band has three components ascribed to local surface defects and excitons. The violet elementary band is related to triplet transitions of specific oxygen-deficient centers.

**PACS Keywords:** thin films, ion implantation, defects, excitons, photoluminescence.

## 1 INTRODUCTION

Ion implantation is an efficient method for the synthesis of dielectric structures with semiconductor quantum dots, which are luminescence active in the visible region of the spectrum owing to the confinement effect. In addition to clustered ion implants, irradiation can lead to the formation of point defects and continuum deformations of the atomic lattice of the matrix, which have a considerable effect on the whole set of the electronic properties of materials. Particularly the implantation of semiconducting (Si, C, Sn, Se) elements leads to appearance of visible luminescence of unknown nature in the green-violet spectral region. The present work is aimed to study the origin and behavior of the most intensive PL peaks of the  $\text{SiO}_2:\text{Se}^+$  system.

## 2 EXPERIMENTAL

Time-resolved photoluminescence (PL) spectra in the range of 1.3-6.0 eV, time-resolved PL excitation spectra (4-12 eV), and the PL decay kinetics were measured at  $T = 7\text{-}300\text{K}$  using the selective VUV-excitation (SUPERLUMI station, Beam-line I, HASYLAB, DESY). The PL spectra was measured using 0.3-m monochromator model ARC Spectra Pro-308i and R6358P photomultiplier (Hamamatsu). The excitation spectra were normalized to the same number of SR-exciting photons using sodium salicylate. The samples under study were  $\text{SiO}_2$  films (500 nm) on a silicon substrate irradiated by  $\text{Se}^+$  ions ( $E = 330$  keV,  $F = 5 \cdot 10^{16}$  ions/cm<sup>2</sup>) and annealed in  $\text{N}_2$  protecting environment at 900°C during 1 hour. An additional 1-hour air annealing at 500°C was applied in order to investigate the oxidation processes.

## 3 RESULTS AND DISCUSSION

The ion-implanted and once annealed  $\text{SiO}_2:\text{Se}^+$  and  $\text{SiO}_2:\text{Sn}^+$  samples show similar sets of PL bands at the 1.5 – 3.8 eV region (Fig. 1). The most pronounced maxima are 2.5-2.6 eV (G-band) and 3.3-3.4 eV (V-band) ones. The parameters of four deconvoluted Gaussian peaks are presented in Table 1.

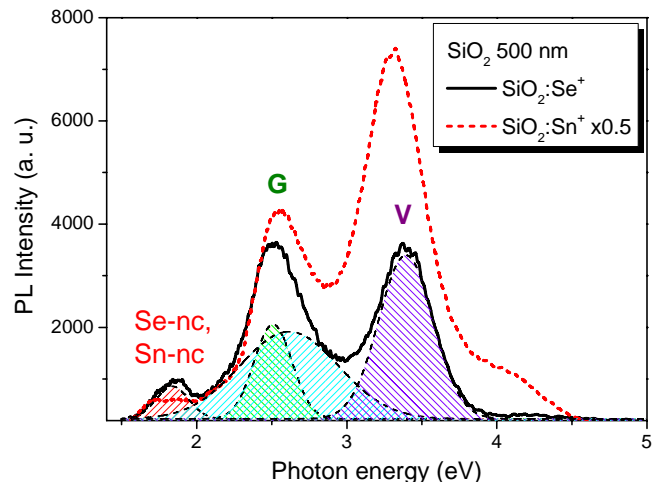


Figure 1: PL spectra of  $\text{SiO}_2:\text{Se}^+$  and  $\text{SiO}_2:\text{Sn}^+$  films annealed at  $T = 900\text{ }^\circ\text{C}$  under 13 eV excitation.

Parameter	Se-nc	STE	$\text{Si}(\text{O}_2)$	SiODC	V-band
$\text{N}_2$	$h\nu_m$	1.84	2.51	2.62	3.39
	FWHM	0.22	0.25	0.66	0.36
air	$h\nu_m$	1.85	2.53	2.64	2.72
	FWHM	0.14	0.23	0.76	0.16

Table 1: Gaussian decomposition results for the PL spectra of once ( $\text{N}_2$ ) and twice ( $\text{N}_2 + \text{air}$ ) annealed  $\text{SiO}_2:\text{Se}^+$  films.

Ion implantation together with subsequent annealing could create selenium, tin and silicon nanoclusters within the oxide structure. Known electron microscopy and optical

absorption studies of the Se-implanted silica directly prove the occurrence of 3-10 nm sized selenium nanocrystals with a band gap energy ranging from 1.9 to 2 eV [1]. Such evidence allows us to ascribe the 1.85 eV band to the Se-nc photoluminescence. Its 0.2 eV red shift during heating to 300 K is caused by band gap temperature dependence observed for Se-ncs [1]. Gaussian deconvolution of the G-band reveals two components (2.5 eV and 2.6 eV bands having different halfwidths) responsible for its nonelementary shape. Contrary, the V-band has truly Gaussian profile peaked at 3.4 eV.

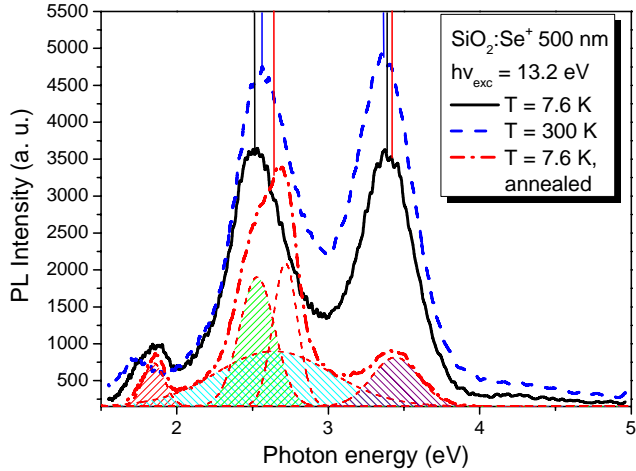


Figure 2: Temperature and annealing effects on the shape of 2.5 eV and 3.4 eV PL bands for Se-implanted samples.

It can be seen from the Fig. 2 that PL spectrum intensity for the green and violet bands increases by one third while temperature grows from 8 K to 300 K. Simultaneously the G-band shows a tiny 0.05 eV blue shift. Further annealing in the air environment introduces a noticeable blue shift of the G-band (0.13 eV) and reveals its nonelementary composition (Fig. 2). The V-peak loses 70% of its intensity, possibly due to oxidation or defect healing processes. The 1.85 eV PL band does not shift but becomes narrowed after annealing, probably due to crystallization of nanoclusters.

The excitation spectra for G and V bands (Fig. 3) have complex shape with several peaks within 4-6 eV (defect-related [2]), 8-11 eV regions and a sharp maximum near 12 eV. Air annealing leads to the smoothing of the entire PLE spectra. One can notice that the G-band is efficiently excited through 10.5 eV and 12 eV PLE maxima, which may be attributed to  $\text{SiO}_2$  excitons. Contrary, for V-band the low energy 4-6 eV excitation is more intensive and comparable to high energy exciton-related peaks.

At helium temperatures all the photoluminescence bands demonstrate microsecond-range kinetics. However the room temperature measurements reveal a complex PL decay law for the V-band under high energy excitation ( $h\nu > 10.4$  eV), comprising two exponentials with  $\tau_1 = 11.4$  ns and  $\tau_2 = 91$  ns.

The 4-7 eV excitation through point defects is more efficient for the V-band revealing its defect-related nature.

A strong effect of air annealing on the V-peak allows its preliminary interpretation as a triplet luminescence of selenium-related kind of oxygen-deficient centers.

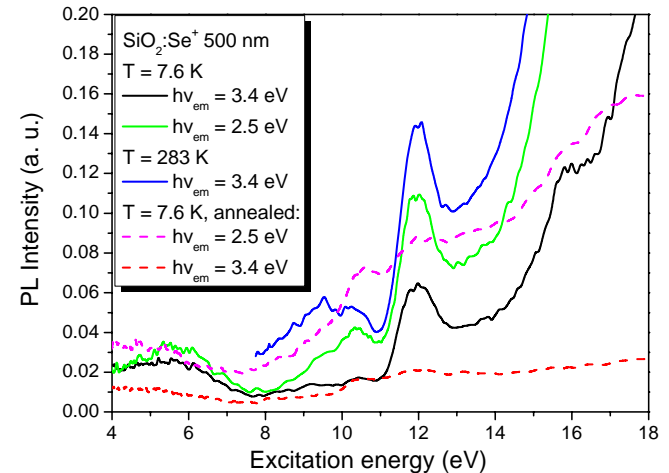


Figure 3: PL excitation spectra of the once (solid) and twice (dash) annealed  $\text{SiO}_2:\text{Se}^+$  samples.

Alternatively, the G-band shows its complex composition after air annealing (fig. 2), comprising three Gaussian components instead of two listed in table 1. The possible candidates for these maxima are triplet-singlet transitions of SiODCs, hydrogen-related species [3],  $\text{SiO}_2$  self-trapped excitons photoluminescence (STEPL) and dioxasilyrane-type surface defects [4].

The PL bands observed appear only after both implantation and thermal treatment with the nanoparticle forming implants. Taking into account the nano-sized structure of the host matrix one can suggest a crucial role of Se-nc/ $\text{SiO}_2$  interface defects, so the occurrence of strained dioxasilyrane and HRS is quite probable.

## 4 CONCLUSION

The results obtained allow to conclude that the green and violet bands are the consequence of the silica matrix structure change during nanocluster formation. Their origin is related to the nanocluster-matrix interface states. According to spectral and kinetic analysis, the green band comprises components ascribed to dioxasilyrane, SiODCs, and self-trapped excitons. The violet luminescence is presumably ascribed to triplet transitions of the specific defects of oxygen-deficient type.

## REFERENCES

- [1] Ueda, A., Wu, M., Aga R. et al. Surface & Coatings Technology 201 (2007) 8542–8546.
- [2] Zatsepin, A.F., Buntov, E.A., Kortov, V.S. et al. J. Phys.: Condens. Matter 24 (2012) 045301
- [3] Glinka, Yu.D., Lin, S.-H., Chen, Y.-T. Phys. Rev. B (2002) 66, 035404.
- [4] Vaccaro, L., Morana, A., Radzig, V., Cannas, M. J. Phys. Chem. C (2011), 115, 19476–19481.

## Session 2

Electronic and atomic structure  
Si-SiO<sub>x</sub>-SiO<sub>2</sub>



# Multi-frequency ESR analysis of interfacial Ge dangling bond defects in (100)Si/SiO<sub>2</sub>/Si<sub>1-x</sub>Ge<sub>x</sub>/SiO<sub>2</sub> heterostructures

A. Stesmans, P. Somers, and V. V. Afanas'ev

Department of Physics, University of Leuven, Celestijnenlaan 200 D, 3001 Leuven, Belgium

## ABSTRACT

Multi-frequency electron spin resonance (ESR) study of the GeP<sub>b1</sub> (Ge dangling bond (DB)) interface defect in SiO<sub>2</sub>/Ge<sub>x</sub>Si<sub>1-x</sub>/SiO<sub>2</sub>/(100)Si heterostructures shows that the ESR signal width is dominated by inhomogeneous broadening due to a strain-induced spread in g. This results in frequency (v)-dependent peak-to-peak broadening of  $\Delta B_{pp}^{SB}/v = 0.62$  G/GHz for the applied magnetic field  $\mathbf{B}/g_3$  principal axis. Compared to the familiar Si P<sub>b</sub>-type interface defects in (100)Si/SiO<sub>2</sub>, the enhanced v-dependent broadening scales with the spin-orbit coupling constant ratio  $\lambda(\text{Ge})/\lambda(\text{Si})$ . The results adduce quantitative support for the assignment of GeP<sub>b1</sub> as a Ge DB-type interface center.

**PACS Keywords:** Ge interface defect, atomic nature, point defect, ESR, SiGe/insulator structure.

## 1 INTRODUCTION

The GeP<sub>b1</sub> defect has recently been unveiled [1] by conventional electron spin resonance (ESR) as a Ge dangling bond (DB) type center at interfaces of Ge<sub>x</sub>Si<sub>1-x</sub> with SiO<sub>2</sub> in condensation grown SiGe-on-insulator (SGOI) structures. The center features monoclinic-I ( $C_{2v}$ ) symmetry with principal g values  $g_1=2.0338$ ,  $g_2=2.0386$ ,  $g_3=2.0054$ , with the lowest value ( $g_3$ ) axis  $24\pm 2^\circ$  off a <111> direction towards the [100] interface normal  $\mathbf{n}$ . The defect occurrence shows a systematic variation as function of x, reaching maximum densities of  $\sim 6.8 \times 10^{12}$  cm<sup>-2</sup> per Si/SiO<sub>2</sub> interface for x~0.7, to disappear for x outside the 0.45-0.87 range.

Through combination of ESR with current-voltage (C-V) observations, the defect was found to operate as an electron trap, with a convincing quantitative one-to-one correspondence between the GP<sub>b1</sub> and trap densities.[2] By studying the microwave frequency dependent properties of the ESR signal (shape), one may assess the influence of the interface quality through its impact on the site-to-site variability of this point defect, otherwise fully linked to a single (substrate) crystal. These interface properties may then be contrasted with those of the superb Si/SiO<sub>2</sub> interface as assessed similarly through the properties of the archetypal Si DB (P<sub>b</sub>-type) interface centers. Here, we report on the results of such multifrequency ESR study of the device-relevant interfacial Ge DB defect.

## 2 EXPERIMENTAL DETAILS

Samples studied were SiO<sub>2</sub>/(100)Ge<sub>x</sub>Si<sub>1-x</sub>/SiO<sub>2</sub>/(100)Si entities with x in the range  $0.28 \leq x \leq 0.93$ , obtained through the condensation technique starting from epitaxially growing a Si<sub>0.73</sub>Ge<sub>0.27</sub> layer (104 nm thick) on a Si(22 nm)/SiO<sub>2</sub>/(100)Si (SOI) substrate wafer, followed by epi-Si (6 nm) capping. More details are given elsewhere [3].

Conventional cw first harmonic X (~9 GHz), K (~20.3) band, and Q (~34 GHz)-band ESR measurements were performed in the adiabatic mode over the temperature range 4.2-10 K. The spectra angular dependence was studied for the applied field  $\mathbf{B}$  rotating in the [0̄11] plane, with  $\phi_B$  (angle of  $\mathbf{B}$  with the interface normal  $\mathbf{n}$ ) varying over 90°.

## 3 EXPERIMENTAL RESULTS

Figure 1 illustrates the influence of the microwave resonance frequency, v, on the GeP<sub>b1</sub> signal observed in the (100)Si/Si<sub>0.27</sub>Ge<sub>0.73</sub>/SiO<sub>2</sub> sample for  $\mathbf{B}/\mathbf{n}$ , revealing substantial v-dependent broadening. This is quantified in Fig. 2, showing the  $\Delta B_{pp}$  data as a function of v measured on an x=0.73 sample for two directions of  $\mathbf{B}$ , i.e.,  $\phi_B=0^\circ$  ( $\mathbf{B}/\mathbf{n}$ ) and  $31^\circ$  ( $\mathbf{B}/g_3$  direction, the presumed DB axis).

Two prominent effects come to the fore: (a) It reveals a dominant inhomogeneous line broadening, exhibiting a closely linear behavior, with, as suggested, a small residual ( $v \rightarrow 0$ ) linewidth; (b), the broadening depends on  $\phi_B$ , significantly decreasing for  $\mathbf{B}$  tilting away from  $\mathbf{n}$  ( $\phi_B=0^\circ$ ) to  $\phi_B=31^\circ$ . The latter can be more aptly demonstrated by replotted the  $\Delta B_{pp}$  data as a function of angle  $\theta (=|\phi_B-31^\circ|)$  of  $\mathbf{B}$  with the presumed DB axis ( $g_3$  direction) for the three observational frequencies. Such figure clearly exposes the increase in  $\Delta B_{pp}$  as  $\mathbf{B}$  tilts away from the ( $g_3$ ) DB direction.

## 4 ANALYSIS AND DISCUSSION

The analysis of the linewidth data was done using the previously obtained insight on the v and  $\phi_B$  dependence of P<sub>b</sub>-type defects at the Si/SiO<sub>2</sub> interface as back drop [4, 5].

In the case of the Si/SiO<sub>2</sub> interface, the ESR signal width ( $\Delta B_{pp}$ ) of the P<sub>b</sub>-type defects consists of two superimposed contributions: In addition to the  $\phi_B$  and frequency independent residual part, there is a considerable ( $\phi_B$  and v dependent) Gaussian broadening monotonically growing as  $\mathbf{B}$  tilts away from the DB axial direction. The Gaussian part is attributed to strain induced variations in the

g matrix, predominantly in  $g_{\perp}$  value, based on the insights provided by the molecular orbital calculations [6]. Building

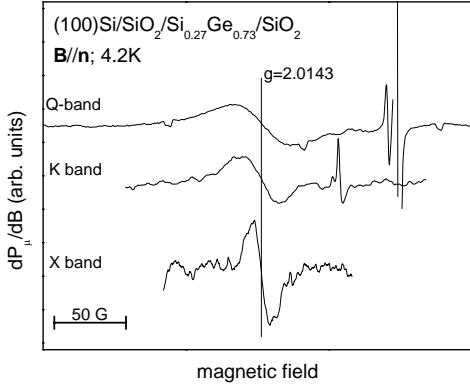


**Fig. 1** First derivative GeP<sub>b1</sub> ESR spectra observed at  $g=2.0143$  on a  $\text{SiO}_2/\text{Si}_{1.027}\text{Ge}_{0.73}/\text{SiO}_2$  sample for  $\mathbf{B}/\mathbf{n}$  using three different frequencies, clearly illustrating the  $v$ -dependent line broadening.

on this, the P<sub>b</sub>-type defect  $\Delta B_{pp}$  data is consistently

described [6] as a function of resonance frequency and/or magnet angle using the expression

$$\Delta B_{pp}(\varphi_B) = \frac{1}{2} \Delta B_{pp}^L + \left\{ [\Delta B_{pp}^{SB}(\varphi_B)]^2 + \frac{1}{4} (\Delta B_{pp}^L)^2 \right\}^{1/2} \quad (1)$$

with  $\Delta B_{pp}^L$  the residual ( $v \rightarrow 0$ ) linewidth and

$$\Delta B_{pp}^{SB} = \frac{2hv}{\beta} \left( \frac{g_{\parallel} \cos^2 \varphi_B}{g^3} \sigma g_{\parallel} + \frac{g_{\perp} \sin^2 \varphi_B}{g^3} \sigma g_{\perp} \right) \quad (2)$$

the width of the inhomogeneous Gaussian broadening due to the admittedly Gaussian spreads  $\sigma g_{\perp}$  and  $\sigma g_{\parallel}$  and in  $g_{\perp}$  and  $g_{\parallel}$ , respectively. As to GeP<sub>b1</sub>, there may additionally be present a Gaussian contribution, to first order  $\varphi_B$  independent, due to unresolved <sup>73</sup>Ge ( $I=9/2$ ) hf broadening, which contribution is assimilated in  $\Delta B_{pp}^L$ . In the context of

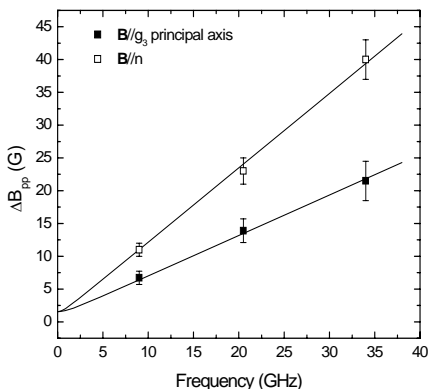


**Fig. 2**  $\Delta B_{pp}$  values measured on an  $x=0.73$  sample as a function of the angle  $\theta$   $\mathbf{B}$  makes with the principal  $g_3$  direction using three resonance frequencies. The solid curves represent optimized least square fittings using Eq. 2, yielding the values for  $\Delta B_{pp}^L$ ,  $\sigma g_{\perp}$  and  $\sigma g_{\parallel}$  (see text).

monoclinic-I type defects (like P<sub>b1</sub> and GP<sub>b1</sub>)  $g_{\parallel}$  must be interpreted here as the g value along to the DB axis, i.e.,  $g_3$ ,

and  $g_{\perp}$  as the g value perpendicular to the DB direction in the plane of rotation of  $\mathbf{B}$ , i.e.,  $g_1$ . Equation 2 is based on the assumptions  $\Delta B_{pp}^{SB} \propto 2\sigma g$  and  $\sigma g_{\parallel}/\sigma g_{\perp} = |g_{\parallel}/g_0|/|g_{\perp}/g_0| = \Delta B_{pp\parallel}^G / \Delta B_{pp\perp}^G$ .

Comparing the  $\Delta B_{pp}(v)$  results for the current GeP<sub>b1</sub> defect signal to the ones obtained for the P<sub>b</sub>-type defects at the  $\text{Si}/\text{SiO}_2$  interface [5], a similar frequency and  $\varphi_B$  dependence is observed, pointing to a comparable nature of the line broadening. Accordingly, optimized least square fitting of all  $\Delta B_{pp}$  data [Fig. 2 and  $\Delta B_{pp}(\theta)$  plot] using Eq. 2, yields self consistently the values of  $\Delta B_{pp}^L = 1.56(10)$ ,  $\sigma g_{\perp} = 0.0075(5)$  and,  $\sigma g_{\parallel} = 0.00174(5)$ . For the  $v$ -dependent dominant inhomogeneous line broadening (cf. fitted curves in Fig. 2), inferred values are  $\Delta B_{pp}^{SB}/v = 0.62 \pm 0.01 \text{ G/GHz}$  for  $\mathbf{B}/g_3$  principal axis ( $\theta \sim 31^\circ$ ), increasing to  $1.13 \pm 0.01 \text{ G/GHz}$  for  $\mathbf{B}/\mathbf{n}$ . Within experimental accuracy, this indicates that  $\Delta B_{pp}$  of the GP<sub>b1</sub> signal can be seen as a superposition of a residual ( $v$  and  $\varphi_B$  independent) part and a dominant Gaussian strain induced broadening.

From the comparison of the data of GeP<sub>b1</sub> and P<sub>b</sub>-type centers, various aspects are worth mentioning: (a) the spread  $\sigma g_{\perp}$  on  $g_{\perp}$  for the GeP<sub>b1</sub> defect is significantly larger than for P<sub>b</sub>-type defects. Recalling that  $\sigma g_{\perp}$  should scale with  $\lambda$  ( $\lambda_{\text{Ge}}/\lambda_{\text{Si}} \sim 6.6$ ), this significantly larger  $g_{\perp}$  quantitatively confirms GP<sub>b1</sub> as a Ge DB type defect. Interestingly, also  $\sigma g_{\parallel}$  is significantly higher, and even also scales with  $\lambda$ ; (b) the residual ( $\varphi_B$  independent) width,  $\Delta B_{pp}^L$ , is found to be equal within experimental accuracy, to that of P<sub>b</sub> at the (111)Si/SiO<sub>2</sub> interface, somewhat larger than the values found for P<sub>b0</sub> and P<sub>b1</sub>.

## 5 CONCLUSION

Study of the GP<sub>b1</sub> ESR signal width shows that compared to the Si P<sub>b</sub>-type defects at the (100)Si/SiO<sub>2</sub> interface, the spreads  $\sigma g_{\parallel}$ ,  $\sigma g_{\perp}$  are significantly enhanced (ca. 6-7  $\times$ ) scaling in proportion to the spin-orbit coupling constant  $\lambda$  ( $\lambda_{\text{Ge}}/\lambda_{\text{Si}} \approx 6.6$ ), herewith supporting the Ge DB nature of GP<sub>b1</sub>.

## REFERENCES

- [1] A. Stesmans, P. Somers, and V. V. Afanas'ev, Phys. Rev. B **79**, 195301 (2009)
- [2] V. Afanas'ev, M. Houssa, A. Stesmans, L. Souriau, R. Loo, and M. Meuris, Appl. Phys. Lett. **95**, 222106 (2009)
- [3] L. Souriau, V. Terzieva, F. Loosen, F. Clemente, B. Brijs, A. Moussa, M. Caymax, M. Meuris, Thin Solid Films **517**, 23 (2008)
- [4] K. L. Brower, Phys. Rev. B **33**, 4471 (1986)
- [5] D. Pierreux and A. Stesmans, Phys. Rev. B **66**, 165320 (2002)
- [6] G. Watkins and J. Corbet, Phys. Rev. **134**, 1359 (1964)

# Quantum confinement effects observed by the photoluminescence of $\text{SiO}_x/\text{SiO}_2$ multilayers.

M. Cannas\*, L. Vaccaro\*, L. Spallino\*, A.F. Zatsepin \*\*, E.A. Buntov \*\*, A.V. Ershov \*\*\*, I.A. Chugrov \*\*\*

\*Dipartimento di Fisica, Università di Palermo, Via Archirafi 36, I-90123 Palermo, Italy

\*\*Ural Federal University, Mira Street 19, Ekaterinburg, 620002 Russia

\*\*\* Lobachevsky State University, 23/3 Gagarin Ave, Nizhni Novgorod, 603950.

## ABSTRACT

Spectral and decay features related to the red emission from Si nanocrystals were investigated by time-resolved photoluminescence spectra carried out on  $\text{SiO}_x/\text{SiO}_2$  nanosized multilayers. On decreasing the  $\text{SiO}_x$  thickness from 8.4 nm to 2.2 nm this luminescence band exhibits a blue-shift from 1.65 eV to 1.75 eV and its lifetime increases from 12 $\mu$ s to 17  $\mu$ s. These results are discussed on the basis of previous models proposed in literature and agree with quantum confinement effects arising from differently sized Si nanocrystals in our samples.

**Keywords:**  $\text{SiO}_x/\text{SiO}_2$  mulilayers, Si nanocrystal, quantum confinement, time-resolved photoluminescence.

## 1 INTRODUCTION

Si nanocrystals embedded in  $\text{SiO}_2$  exhibit emission properties favorable in view of the realization of efficient and versatile optical nanodevices. The Si miniaturization down to nanoscale induces, in fact, a visible photoluminescence (PL), surprising for a not highly emissive material [1]. It has been also demonstrated that the smaller the Si nanocrystals are, the more the PL is shifted towards the blue range. A great effort has been, therefore, devoted to design systems with controlled Si nanocrystal size thus leading to tunable emission sources. One of the production methods consists of the phase separation of Si and  $\text{SiO}_2$  induced by high temperature ( $\sim 1000$  °C) annealing of  $\text{SiO}_x$ ,  $1 \leq x \leq 2$  being the stoichiometric index [2].

Though this PL has been widely investigated over the last decades, its microscopic origin is still debated [3]. The main proposed models are the quantum confinement of excitons or localized defects states at the Si/ $\text{SiO}_2$  interface [3-5], in the latter case the defect structure being not yet unambiguously identified. Therefore, it is crucial to investigate in details the excitation/emission pathway also to single out intra-center or energy transfer processes. The dependence on energy and intensity of excitation and the temperature effectiveness provide useful finding to clarify this issue. In this work we report a study of PL emitted from Si

nanocrystals generated by annealing of  $\text{SiO}_x/\text{SiO}_2$  multilayers, taking advantage of combined use of time-resolved spectroscopy and a tunable laser excitation.

## 2 EXPERIMENTAL METHODS

We studied amorphous  $\text{SiO}_x/\text{SiO}_2$  multilayers grown on a p-type crystalline Si (100) substrate in vacuum ( $1.5 \times 10^{-4}$  Pa). The  $\text{SiO}_x$  layers were produced by evaporation of SiO powder from tantalum effusion source, whereas the  $\text{SiO}_2$  ones were created by electron-beam evaporation of fused quartz. The substrate temperature was stabilized at  $200 \pm 10$  °C. The pressure of SiO and  $\text{SiO}_2$  vapors were  $7 \times 10^{-4}$  and  $2 \times 10^{-2}$  Pa, respectively. The total thickness of the structure was measured by the interference microscope MII-4. Some samples were annealed for 2 hours at 1100°C in dry nitrogen atmosphere. The characteristics of investigated samples are reported in Table 1.

Sample	Layer thickness $\text{SiO}_x/\text{SiO}_2$ (nm)	Annealing Temp. (°C)	Layers number
1	2.2/2.8	Deposited at 200 °C	64
2	2.2/2.8	1100	64
3	4.4/2.8	1100	32
4	8.4/2.8	1100	50

Table 1: List of investigated samples and their characteristics.

Time resolved PL spectra were carried out under different excitation energies provided by the II (2.48 eV), III (3.50 eV), IV (4.66 eV) and V (5.82 eV) harmonic of a Nd:YAG laser (pulse width  $\sim 5$  ns, repetition rate 10Hz). The emitted light was spectrally resolved by a grating (150 grooves  $\text{mm}^{-1}$  and 300 nm blaze), and then acquired by an intensified charge coupled device camera driven by a delay generator (PI-MAX Princeton Instruments) setting the acquisition time window,  $W_T$ , and the delay,  $T_D$ , respect to the arrival of laser pulses. This setup is equipped with a

He-flow cryostat to perform measurements as a function of temperature in the range 300-10 K.

### 3 RESULTS AND DISCUSSION

Under visible and ultraviolet (UV) excitation a luminescence centered in the red spectral region is observed in the samples annealed at 1100 °C. This emission is characteristic of Si nanocrystals formed by phase separation of the  $\text{SiO}_x$  layers [2, 4]; such a process does not occur in the not annealed Sample 1. Normalized PL spectra, excited at 4.66 eV and acquired with  $W_T = 100 \mu\text{s}$  and  $T_D = 1 \mu\text{s}$ , are reported in Figure 1. The spectral lineshape depends on the sample characteristics: the main effect concerns the peak blue-shift, from 1.65 eV to 1.75 eV on decreasing the  $\text{SiO}_x$  thickness from 8.2 nm to 2.2 nm. This finding agrees with a quantum confinement associated with Si nanocrystals with sizes that increase on increasing the  $\text{SiO}_x$  thickness [6].

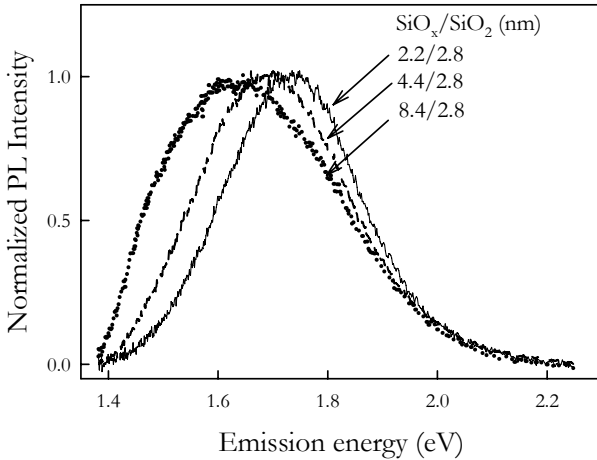


Figure 1: Normalized PL spectra acquired in  $\text{SiO}_x/\text{SiO}_2$  multilayers differing for the  $\text{SiO}_x$  thickness.

The decay features of this red-PL are shown in Figure 2; the curves are derived by collecting time-resolved spectra with  $W_T = 5 \mu\text{s}$  and  $T_D$  varying from 1 to 51  $\mu\text{s}$ . The decay occurs in the  $\mu\text{s}$  timescale; the lifetime  $\tau$ , estimated as the time necessary to reduce the PL intensity to a factor  $1/e$ , increases from  $12 \pm 1 \mu\text{s}$  to  $17 \pm 1 \mu\text{s}$  on decreasing the  $\text{SiO}_x$  thickness. In agreement with previous works [6], this trend could be related to a variation of the stoichiometric index that increases on increasing the  $\text{SiO}_x$  thickness.

In conclusion, these results evidence that, owing to the Si nanocrystals related quantum confinement effects,  $\text{SiO}_x/\text{SiO}_2$  nanosized multilayers with controlled  $\text{SiO}_x$  thickness are promising as tunable light emitters.

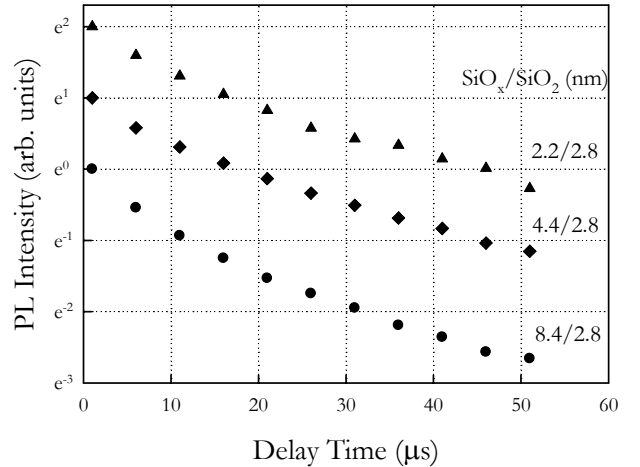


Figure 2: Decay curves monitored at the maximum intensity of the red PL in the  $\text{SiO}_x/\text{SiO}_2$  multilayers. For viewing purposes, the curves are arbitrarily shifted.

### REFERENCES

- [1] L.T. Canham, Appl. Phys. Lett, 57, 1046, 1990.
- [2] J. Heitman, R. Scholz, M. Schmidt, M. Zacharia, J. Non-Cryst. Solids, 299-302, 1075, 2002.
- [3] X.X. Wang, J.G. Zhang, L. Ding, B.W. Cheng, W.K. Ge, J.Z. Yu, Q.M. Wang, Phys. Rev. B, 72, 195313, 2005.
- [4] S. Godefroo, M. Hayne, M. Jivanescu, A. Stesmans, M. Zacharias, O. I. Lebedev, G. Van Tendeloo, V.V. Moshchalkov, Nature Nanotechnology, 3, 174, 2008.
- [5] F. Zatsepin, E. A. Buntov, V. S. Kortov, D. I. Teltebaum, A. N. Mikhaylov, A. I. Belov, J. Phys. Condens. Matter, 24, 045301, 2012.
- [6] S. Kim, D.H. Shin, D.Y. Shin, C.O. Kim, J.H. Park, S.B. Yang, S.-H Choi, S.J. Yoo, J.-G. Kim, J. Nanomaterials, 2012, 572746, 2012.

# Impact of Poly-Reoxidation Process Step on Tunnel Oxide Reliability: Charge Trapping and Data Retention

G. Just<sup>1,2\*</sup>, J.-L. Ogier<sup>1</sup>, A. Regnier<sup>1</sup>, J. Postel-Pellerin<sup>2</sup>, F. Lalande<sup>2</sup>, P. Masson<sup>3</sup>

<sup>1</sup> STMicroelectronics, 190 Avenue Célestin Coq, 13106 Rousset, France

<sup>2</sup> Im2np, Université Aix-Marseille, rue Frédéric Joliot-Curie, 13451 Marseille, France

<sup>3</sup> Université Nice-Sophia Antipolis, Polytech' Nice Sophia, 1645 route des Lucioles, 06410 Biot, France

\* Corresponding author, Tel.: +33442685771; E-mail address: [guillaume.just@st.com](mailto:guillaume.just@st.com)

## ABSTRACT

In this paper, we investigate a particular CMOS Flash process step, the poly-reoxidation, and its impact on tunnel oxide reliability. Based on electrical characterizations performed on capacitors, this work permits to evaluate charge trapping in tunnel oxide and at the Si-SiO<sub>2</sub> interface for two poly-reoxidation process recipes, ISSG (In-Situ Steam Generated) and RTP (Rapid Thermal Process). Retention measurements performed on CAST (Cell Array Structure Test) gives access to data retention behaviors of these two processes. Partly due to the lack of hydrogen atoms in RTP process, we show a better behavior in retention and a lower charge trapping for RTP process than ISSG.

**Keywords:** Poly-reoxidation, oxide reliability, charge trapping, retention, ISSG, RTP

## 1. INTRODUCTION

It is well known that tunnel oxide quality is a major concern for Non-Volatile Memories (NVM) reliability. So, each process step has to be studied with particular care. One of the key process steps is the poly-reoxidation which is realized after the gate stack etching. During this etching, the tunnel oxide may be impacted by possible degradations on its edges (source/drain side) as illustrated in Fig1. Poly-reoxidation, consisting in precisely controlling tunnel oxide growth, is done to fill these eventual degradations.

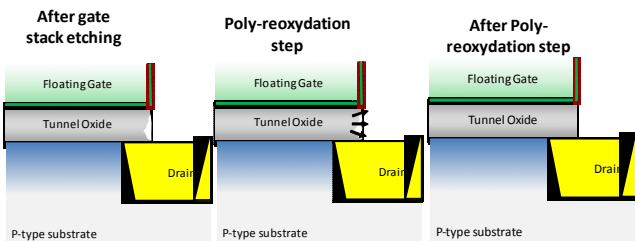


Fig1. Cross-section schematic view (along channel length) showing the interest of poly-reoxidation step

In this context, the main purpose of this paper is to evaluate the impact of poly-reoxidation process recipe on tunnel oxide reliability.

This paper is organized as follows: the second section describes the studied devices, electrical measurements and main differences between the two processes. In section 3, after an introduction on interface traps formalism, measurements results on charge trapping and data retention are shown and discussed. Some concluding remarks are given in section 4.

## 2. EXPERIMENTAL DETAILS

Studied devices are large area MOS tunnel capacitors ( $2.10^3 \text{ cm}^2$ ) with a 10.6 nm tunnel oxide thickness embedded on a 0.18 μm CMOS process technology node. Measures are performed on two capacitor structures: “plate” (poly-silicon area on active area) and “inter-digited” capacitors, these last ones taking into account geometrical effects we encountered on a cell memory layout. To evaluate charge trapping, we performed two types of test:

- Constant Current Stress (CCS) consists in stressing a device under a constant current (+/- polarity) and monitoring the V<sub>g</sub> shift versus time.
- C(V) & stress consists in following the C(V) characteristics evolution before and after a stress (negative CCS). This allows us to quantify charge trapping densities in oxide and at the Si-SiO<sub>2</sub> interface.

To compare the retention behaviors, we performed Gate Stress (GS) test on CAST (thousand cells in parallel) [1], by monitoring the V<sub>T</sub> shift at two current levels, in order to characterize intrinsic (due to oxide growth) and extrinsic (due to weakest cells) charge losses. The reoxidation process recipes are detailed in Fig2. One main difference is that ISSG contains hydrogen specie (H<sub>2</sub>) while RTP does not. As underlined in [2-3], it is generally known that hydrogen atoms are a key point in trap creation.

Poly-reoxidation recipes		
Process	ISSG	RTP
Temperature (°C)	1025	1025
Type	Wet	Dry
% O <sub>2</sub>	33	0
Pressure	Low	Atmospheric
Growth time (s)	11	28
Thickness (Å)	53	40

Fig2 : Main differences of studied poly-reoxidation process recipes

## 3. MEASUREMENTS RESULTS

In order to simplify further explanations, we first recall the formalism used to describe Si-SiO<sub>2</sub> interface traps (or states). Interface traps are divided in two categories: donor-type (positively charged if empty and neutral if filled) and acceptor-type (neutral if empty and negatively charged if filled) interface traps are located in the lower and upper half-band gap of silicon respectively. The filling of interface states is given by the position of Fermi level E<sub>F</sub> at Si-SiO<sub>2</sub> interface. Below E<sub>F</sub>, interface states are filled by electrons while they are empty above it

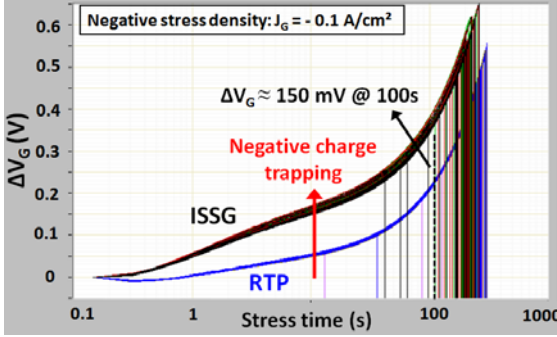


Fig3. CCS results under negative stress constraint.

Constant Current Stress (CCS) results, presented in Fig3, show  $\Delta V_g$  shift ( $\Delta V_g = V_g(t) - V_g(t_0)$ ) versus stress time, under a negative stress density applied on the gate. Positive  $\Delta V_g$  results in trapping of negative charges due to electrons trapped close to the substrate. Negative  $\Delta V_g$  means a positive charges trapping, generally attributed to either hole trapping, or electron de-trapping, caused by impact ionization [4-5]. We also observe a significant difference in oxide trapping behavior between RTP vs. ISSG. The quantity of trapped charges is more important for ISSG than RTP process, for both stress polarities (+/-). Also, same CCS results are found for the two types of structure, plate and inter-digited capacitors. Then, we cannot attribute this behavior to a localized effect at poly-silicon/oxide edges (re-oxidized regions) but most probably spread in the volume of oxide, changing tunnel oxide intrinsic properties.

$C(V)$  characteristics measured after stress (not shown) indicate a decrease of the mid-gap voltage. For this voltage, the Fermi level is located at the middle of silicon band-gap at the interface and the interface traps are neutral. This shift of the mid-gap voltage allows the determination of the fixed charges ( $N_f$ ) trapped in the volume of oxide, which are positive in this case. The shift of the threshold voltage,  $V_T$ , results from the presence of fixed charges and acceptor-type interface traps ( $N_{it_a}$ ) while the shift of the flat band voltage,  $V_{FB}$ , is due to the presence of fixed charges and donor-type interface traps ( $N_{it_d}$ ).

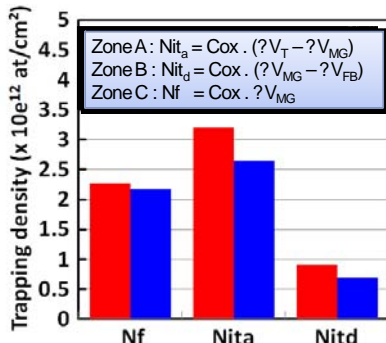


Fig4. Calculated charge trapping densities from  $C(V)$  measurements after stress

On Fig4, we reported, from  $C(V)$  characteristics evolution and equations, charge trapping densities for both fixed charges and interface states. As already shown with CCS results, more charge trapping is found for ISSG process versus RTP. The main contribution results in negative charges, due to electrons trapped in acceptor-type

interface states. Hence, we assume that the poly-reoxidation process step has an impact on intrinsic quality of tunnel oxide.

Retention results, in Fig5, show the shift of  $\Delta V_T$  ( $\Delta V_T = V_T(t) - V_T(t_0)$ ) in a cumulated Weibull plot. Generally, we evaluate at 63.2% of the population the shift of  $\Delta V_T$ . This shift is higher for the ISSG process for both intrinsic and extrinsic behaviors, thus confirming the better behavior of RTP process.

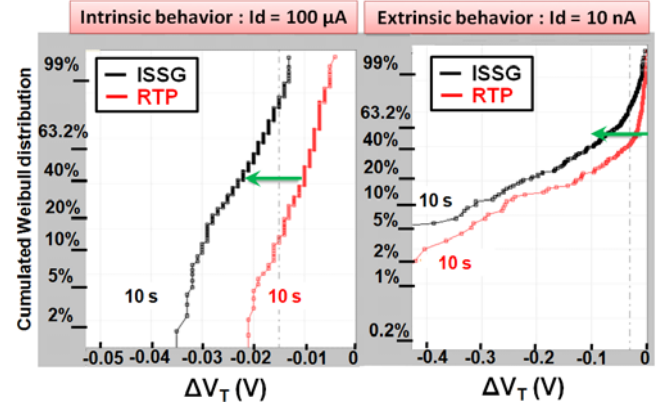


Fig5 : Retention results showing a better behavior for RTP process.

## 4. CONCLUSIONS

In this paper, we have studied the impact of poly-reoxidation on tunnel oxide reliability, through charge trapping study on capacitors and retention measures on CAST. A better retention behavior is observed for RTP process versus ISSG, as well as a lower charge trapping, partly due to the lack of hydrogen specie in RTP process. We have shown that charge trapping does not seem to be localized at poly-silicon/oxide edges (re-oxidized regions), but most probably spread in the volume of oxide, leading to a change in tunnel oxide intrinsic properties.

## REFERENCES

- [1] P. Cappelletti, R. Bez, D. Cantarelli, D. Nahmad, L. Ravazzi, "CAST: An electrical stress test to monitor single bit failures in Flash-EEPROM structures", Microelectronics Reliability, vol.37, pp 473-481, 1997
- [2] D.J. Di Maria, E. Cartier, D. Arnold, "Impact ionization, trap creation, degradation, and breakdown in  $\text{SiO}_2$  films on silicon", Journal of Applied Physics, Vol.73 (7), pp 3367-3384, 1993
- [3] Y.B. Park, D.K. Shroder, "Degradation of Thin Tunnel Gate Oxide Under Constant Fowler-Nordheim Current Stress for a Flash EEPROM", IEEE Transactions On Electron Devices, Vol.45(3), 1998
- [4] I. C. Chen, S. E. Holland, and C. Hu, "Electrical breakdown in thin gate and tunneling oxides", IEEE Trans. Electron Devices, vol. ED-32, pp 413-422, 1985
- [5] M. P. Fazan, M. Dutoit, C. Martin, and M. Illegems, "Charge generation in thin  $\text{SiO}_2$  polysilicon-gate MOS capacitors", Solid State Electron., vol. 30, pp. 829 834, 1987

# Interface nature of ordered thermally oxidized Si nanowires

M. Jivanescu\*, A. Stesmans\*, R. Kurstjens\*\*, and F. Dross\*\*

\* Department of Physics, KU Leuven, Celestijnenlaan 200D, 3001, Leuven, Belgium  
\*\*IMEC, Kapeldreef 75, B-3001 Leuven, Belgium

## ABSTRACT

The low-temperature electron spin resonance (ESR) technique was used to investigate the interface-specific point defects in ordered arrays of single crystalline Si nanowires (NWs) embedded in  $\text{SiO}_2$ , obtained by top-down etching of (100)Si. This reveals the presence of  $\text{P}_{\text{b}0}$  centers at the NW Si/ $\text{SiO}_2$  interfaces as dominant paramagnetic defect assembly. The analysis of the appearing  $\text{P}_{\text{b}}$ -type defect system leads to the conclusion that the interface of the Si NWs with the surrounding  $\text{SiO}_2$  matrix is bordered mainly by  $\{110\}$  facets. The inherent interface quality appears to be restricted by the thermal oxidation procedure.

**PACS Keywords:** nanowires, defects, electron spin resonance, silicon, solar cells.

## 1 INTRODUCTION

The demand for renewable energy supply is ever increasing, and here, solar energy harvesting is on the shortlist. “Third generation” photovoltaic (PV) technologies aim to decrease the Watt-peak price by boosting device efficiency without significant areal cost increase [1] through making maximal use of non-toxic and abundantly available materials.

Given the fact that more than 95 % of integrated circuit electronics is Si-based, the industry is already well equipped for working with this material. So the most straightforward material of choice as basis for solar cells would obviously be Si, if it weren’t for its limited bandgap ( $\approx 1.1$  eV). By stacking Si structures with wider bandgap (as affected by quantum confinement) on Si substrates, one may construct tandem cells with improved absorption efficiency compared to the now used polycrystalline Si solar cells. It is possible to reach even  $\approx 3.5$  eV band gap for 1.3-nm diameter Si wires.

Conforming to reliability demands, Si NWs are usually embedded in  $\text{SiO}_2$ . But then one has to pay attention to the formed Si/ $\text{SiO}_2$  interface generally hosting inherent electrically and optically active Si dangling bond (DB)-type defects –termed  $\text{P}_{\text{b}}$ -type centers as identified by electron spin resonance (ESR). These Si DBs drastically impede Si-based device functionality. In this work, to identify and qualify inherently occurring paramagnetic point defects, an extensive investigation is performed on crystallographic ordered Si NW arrays thus maintaining the single crystallinity [2–4] ESR resolving power. This is at variance

with previous such ESR work mainly done on powders of Si NWs [5–7].

## 2 EXPERIMENTAL DETAILS

Crystallographically ordered Si NWs were etched down into (100)Si wafers using a sequence of lithography, dry etching, and thermal oxidation (1150 °C) steps. The procedure resulted in Si NWs (90 nm pitch) with top and foot diameters in the range  $\varnothing = 2.5$  nm–8.5 nm and  $\varnothing = 15$ –25 nm, respectively, of which the broader bottom parts taper upward quite rapidly into much longer and narrower wires of smaller  $\varnothing$ . The so obtained NWs are covered by a thin thermal Si oxide layer, but are still fragile. To keep the NWs aligned and prevent breaking, the inter-wire space was (partially) filled by chemical vapor deposited a- $\text{SiO}_2$ . To maximally reveal inherent paramagnetic point defects, as fabricated slices have been exposed to vacuum UV (VUV) irradiation ( $\approx 10.02$  eV) for  $\sim 3$  h. For a final ESR test, the NWs of a similar sample were mostly removed ( $\approx 95$  % of their length) through chemical etching.

K-band ( $\approx 20.5$  GHz) ESR measurements were carried out at 4.2 K in the adiabatic mode for various directions of the applied magnetic field  $\mathbf{B}$ , at angle  $\varphi_{\mathbf{B}}$  with the [100] sample normal, in the (011) Si plane. Continuous wave first-derivative absorption spectra ( $dP_{\mu r}/dB$ , where  $dP_{\mu r}$  is the reflected microwave power) were measured using sinusoidal modulation (100 kHz; amplitude  $B_m$ ) of  $\mathbf{B}$ . Defect densities were determined by making use of calibrated co-mounted Si:P markers [ $g(4.2$  K) = 1.99869, spin  $S = 1/2$ ] through double numerical integration of the computer-simulated  $dP_{\mu r}/dB$  signals. Attained relative and absolute density accuracies are estimated at about 10 % and 20 %, respectively.

## 3 RESULTS AND ANALYSIS

Angle dependent ESR observations were made on as annealed and VUV irradiated Si NWs samples and representative spectra for the latter sample (higher density) are shown in Fig. 1 for four different  $\varphi_{\mathbf{B}}$  angles. The as-annealed samples show angle dependent signals of  $\text{P}_{\text{b}0}$  and  $\text{P}_{\text{b}1}$  defects pertaining to Si/ $\text{SiO}_2$  interfaces, with corresponding density of  $[\text{P}_{\text{b}0}] \approx 1.9 \times 10^{12} \text{ cm}^{-2}$  and  $[\text{P}_{\text{b}1}] \approx 5.4 \times 10^{11} \text{ cm}^{-2}$ . It is important to note that the density of the latter center is only a fraction of the former. For an overview on the salient properties of  $\text{P}_{\text{b}}$ -type defects see,

e.g., Refs. [2–4]. As expected, upon VUV irradiation a-SiO<sub>2</sub> specific E' centers are generated and the density of P<sub>b0</sub> centers is increased.

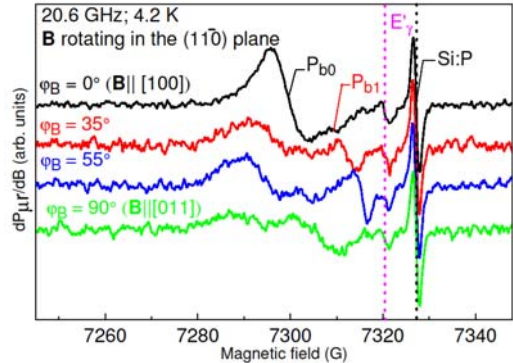


Figure 1: Representative K-band spectra ( $P_{pr} = 8 \times 10^{-7}$  mW;  $B_m = 0.7\text{--}1$  G) taken at 4.2 K on the NW system after VUV irradiation.

The P<sub>b</sub>-type defects may provide useful information on the morphology of the Si NWs. Away from  $\phi_B = 0^\circ$  both the P<sub>b0</sub> and P<sub>b1</sub> signal each split in multiple branches, as also observable in Fig. 1. The small density P<sub>b1</sub> signals are overwhelmed by those of P<sub>b0</sub> centers, so, it is almost impossible to include the former centers in this in depth investigation. Thus we focus on P<sub>b0</sub> centers as crystalline probes by constructing a g map of the zero-crossing g values g<sub>c</sub> corresponding to the P<sub>b0</sub> signals for various  $\phi_B$  angles. The thus constructed g map is shown in Fig. 2. The g map may be consistent with (100)Si/SiO<sub>2</sub> interfaces but then an equal amount of P<sub>b1</sub> centers is expected [8]. The P<sub>b0</sub> defects are accompanied by P<sub>b1</sub> centers for the (100)Si/SiO<sub>2</sub> interfaces, but not for the (110)Si/SiO<sub>2</sub> ones [4].

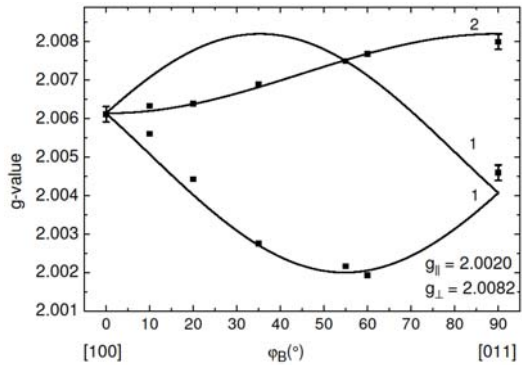


Figure 2: Inferred angular g map of P<sub>b0</sub> centers pertaining to Si/SiO<sub>2</sub> interfaces in the Si NW arrays sample. The curves represent optimized fittings for trigonal symmetry [4] corresponding to P<sub>b0</sub> centers at (110) and/or (100)Si/SiO<sub>2</sub> interfaces. The numbers marked near the various branches indicate expected relative signal intensity, in agreement with experimental observation.

To distinguish between the P<sub>b</sub>-type defects located at the NW-Si/SiO<sub>2</sub> and substrate Si/SiO<sub>2</sub> interfaces, about  $\approx 95\%$

the NWs length was etched away on one sample. ESR remeasurement gave a density of  $[P_{b0}] \approx 1.5 \times 10^{12}$  cm<sup>-2</sup> for the (mainly) bottom interface, quite comparable to that of the macroscopic standard thermal (100)Si/SiO<sub>2</sub> interface [8]. We thus conclude that the majority of the P<sub>b0</sub> centers observed on the unetched samples are located on the facets of Si NWs, at the interface with the embedding SiO<sub>2</sub>. We estimate a P<sub>b0</sub> density per effective as-annealed NW facets area of  $[P_{b0}^{\text{NW}}] \approx 3.2 \times 10^{12}$  cm<sup>-2</sup>, indicating a lower quality of the interface than the technologically favored standard (100)Si/SiO<sub>2</sub> [8].

The low P<sub>b1</sub> density indicates that the majority of P<sub>b0</sub> defects would pertain to a {110}Si/SiO<sub>2</sub> type of interface but we cannot exclude at least a minority of the facets to be {100}Si/SiO<sub>2</sub> type since one cannot discriminate on the basis of P<sub>b0</sub> spectral ESR parameters. So, given the geometry of the fabricated Si nanopillars and after evaluating the different possibilities, we conclude that the Si/NWs facets are a mix of {110} and {100} planes, with the pillar cross section approaching an (irregular) octagonal shape.

## 4 CONCLUSIONS

Thermally oxidized arrays of crystalline Si NWs etched in (100) Si substrates show substantial amounts of inherent P<sub>b</sub>-type interface defects, mainly P<sub>b0</sub>. While the bottom plane of the NWs shows a spectrum typical for a standard quality (100)Si/SiO<sub>2</sub> interface, as expected for the applied sample fabrication procedures, the defect situation changes for the NWs. The interface of the NWs with the embedding SiO<sub>2</sub> (thermally grown) exhibit an enhanced system of P<sub>b0</sub> centers, lowering the system quality below that of standard thermal (100)Si/SiO<sub>2</sub>. But, to the benefit of insight, overall analysis of the occurring P<sub>b</sub>-type defect enables to infer useful information on the faceting of NWs: predominantly {110}, and, to a lesser extent, {100} facets, their cross section approaching an irregular octagon shape (truncated {110} squares).

## REFERENCES

- [1] M. A. Green, *Third Generation Photovoltaics: Ultra-High Efficiency at Low Cost* (Springer-Verlag, 2003).
- [2] E. H. Poindexter and P. J. Caplan, *Prog. Surf. Sci.* **14**, 201 (1983).
- [3] A. Stesmans, B. Nouwen, and V. V. Afanas'ev, *Phys. Rev. B* **58**, 15801 (1998).
- [4] K. Keunen, A. Stesmans, and V. V. Afanas'ev, *Phys. Rev. B* **84**, 085329 (2011).
- [5] A. Baumer, M. Stutzmann, M. S. Brandt, F. C. K. Au, and S. T. Lee, *Appl. Phys. Lett.* **85**, 943 (2004).
- [6] R. P. Wang, *Appl. Phys. Lett.* **88**, 142104 (2006).
- [7] L.-B. Luo, X.-B. Yang, F.-X. Liang, H. Xu, Y. Zhao, X. Xie, W.-F. Zhang, and S.-T. Lee, *J. Phys. Chem. C* **115**, 18453 (2011).
- [8] A. Stesmans and V. V. Afanas'ev, *Phys. Rev. B* **57**, 10030 (1998).

# Session 3

## Laser irradiation



# Generation of periodic surface structures on silica fibre surfaces with 405 nm CW diode lasers

C. P. Gonschior<sup>\*,\*\*</sup>, K.-F. Klein<sup>\*</sup>, T. Sun<sup>\*\*</sup>, K. T. V. Grattan<sup>\*\*</sup>

<sup>\*</sup>Technische Hochschule Mittelhessen, Competence Centre “Optical Technologies and Systems”,  
Wilhelm-Leuschner-Str. 13, 61169 Friedberg, Germany,

e-mail: cornell.p.gonschior@iem.thm.de, telephone: +49-6031-604 218

<sup>\*\*</sup>City University London, Northampton Square, London EC1V 0HB, United Kingdom

## ABSTRACT

Periodic surface structures are observed on the proximal end-faces of fused silica fibres after long-term irradiation with 405 nm CW diode lasers. The surface structures are generated three magnitudes of order below the damage threshold and exhibit multiple bends, break-ups and bifurcations. They are thus not the result of an interference effect. On the other hand, they are very similar to periodic surface structures found with femto-second laser irradiation of wide band-gap insulators. Important parameters in the generation of the surface structures are power density, surface roughness, polarization direction and the generation of ultraviolet defect centres.

**PACS Keywords:** single-mode laser, single-mode fibre, surface damage, periodic surface structures, ultraviolet defect centres

## 1 INTRODUCTION

Periodic surface structures found on silica fibre end-faces operated in the near ultraviolet (NUV) negatively impact the transmission behaviour of the fibres [1]. At 405 nm wavelength the CW power densities in the laser beam waist and fibre core are in the range of 0.5 to 2.5 MW/cm<sup>2</sup>. The high values are obtained when laser and fibre are operating in the single-mode regime. Despite being below the material damage threshold by a factor of thousand, laser light with this power density is capable of deforming the fused silica surface over a duration of several days.

Comparing femto-second laser experiments with the long-term CW irradiation of fused silica fibres at 405 nm wavelength indicates common parameters for the generation of surface structures [2,3,4]. Besides the dependence on power density, we found that surface roughness affects the generation time and that the structural orientation correlates with the polarization direction of the laser light. Furthermore, ultraviolet defect centres induced in the fibre core material by two-photon absorption play a vital role in the generation of the periodic surface structures on fused silica surfaces [1,5].

After introducing the experimental setup and describing the sample preparation, the results of the damaging experiments will be discussed. The discussion will conclude with a comparison with femto-second laser experiments.

## 2 EXPERIMENTAL

For the long-term damage experiments two diode laser modules with high-power 405 nm GaN diodes are used. Details are given in Table 1 for the multi-mode (MML) and single-mode laser (SML). A consistent output power is achieved through current and temperature stabilisation. The imaging and alignment system was found to be very stable, mechanically and temperature wise. The fibre under test had a length of 1 m in all cases. Thermopile power meters were used for the power detection.

Parameter	MML double diode	SML
Number of laser diodes	2 (cross-polarized)	1
Output power $P_{\text{out}}$ / mW	300	150
Calculated spot diameter $2 \cdot w_0$ / $\mu\text{m}$	5.9	2.78
Calculated power density in spot $I_{\text{spot}}$ / kW/cm <sup>2</sup>	1100	2450

Table 1: Overview of diode laser modules.

Different kinds of fibres were used. The main differences are the light guiding scheme and the mode-field diameter. The low-mode fibre (LMF) has a core diameter of 15  $\mu\text{m}$  and the single-mode fibres (SMF) have a mode-field diameter in the range of 2.5 to 3.2  $\mu\text{m}$ . All fibres have an undoped synthetic silica core.

The total coupling efficiency from SML to SMF is in the order of 50 to 60 %. For the MML, a total coupling efficiency of about 25 % to the SMF and about 75 % to the LMF was obtained.

With the MML power densities in the order of 100 to 130 kW/cm<sup>2</sup> are achieved in the core of LMF. In the SMF

the core power density increases to 0.9 to 1.3 MW/cm<sup>2</sup>. If used with the SML the core power densities in SMF range from 1.6 to 2 MW/cm<sup>2</sup>. The actual power density on the surface is higher than the core power density.

The different end-face preparation methods were described in a prior publication [1]. The produced samples were either glued-and-polished, cleaved-and-clamped or cleaved-fused-and-clamped. Fusing in this case means flame-polishing with a fusion arc from a standard telecommunications splicer.

The surface roughness was measured with atomic force microscopy (AFM). The roughness for polished samples was in the order of 2 nm, for cleaved samples about 0.4 nm and 0.1 to 0.2 nm for flame-polished samples.

### 3 DISCUSSION

The recorded losses during the damage experiments correlated with the end-face quality. Polished samples of LMF had an average induced loss of 1 dB/day and cleaved samples of 0.27 dB/day, if damaged with the MML. Cleaved samples of all SMF types also had a reduced loss of about 0.2 to 0.5 dB/day, either damaged with MML or SML. Flame polished samples show a delay of the damaging process, but then have behave similar to cleaved samples.

In all cases a modification on the launching end-face could be seen. Either a cross shape, if damaged with the MML, or a spot, if damaged with the SML, were seen. With an AFM a ripple structure on the protruding modification was discovered. Figure 1 shows an example for the MML and Figure 2 for the SML (the polarization is denoted by the arrows).

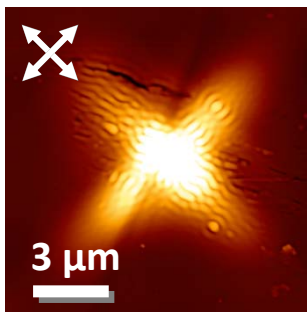


Figure 1: AFM micrograph of the proximal end of a cleaved SMF damaged with the MML (500 nm high).

A periodicity of 300 to 400 nm was determined. The ripples are oriented parallel to the polarization direction of the laser light. The duration of irradiation and the induced loss are an indication for the height of the structure and the clarity of the ripple.

This surface structure acts as a scattering centre on the fibre end-face, which partially or fully covers the fibre core. The induced loss is broadband and can only be measured spectrally in SMF. Additionally the generation of defect

centres at 214 nm (E' centre) and a reduction at 245 nm (Oxygen deficient centre) was seen. These are very strong indications for a two-photon process breaking silicon bonds.

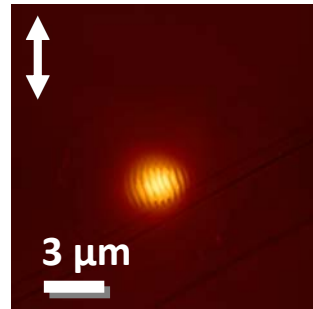


Figure 2: AFM micrograph of the proximal end of a cleaved SMF damaged with the SML (700 nm high).

Similar surface structures with ripples are seen in femtosecond laser experiments, also exhibiting bifurcations, bends and break-ups. The current model explains these structures by self-organisation of an unstable surface layer by duelling processes of desorption and self-diffusion [4]. We suggest that in our case the fibre surface is destabilised by two-photon surface ionisation leading to Coulomb repulsion. The thickness of the unstable layer is increased by surface roughness and generation of defect centres [5].

### 4 CONCLUSION

We showed that the damage occurring on silica fibre end-faces during irradiation are due to the generation of a periodic surface structure. It is suggested that this ripple structure is formed by a self-organising process of an unstable surface layer. The generation of E' centres enhances the destabilisation.

### 5 ACKNOWLEDGEMENTS

We would like to acknowledge support through AiF grant FKZ 1702X09, Jan Heimann, Omicron Laserage GmbH, Prof. Georg Hillrichs and Fraunhofer Institute for Mechanics of Materials in Halle.

### REFERENCES

- [1] Gonschior et.al., Proc. SPIE 8218-0A (2012).
- [2] Henyk et.al., Appl. Phys. A-Mater. 69, S355-S358 (1999).
- [3] Varlamova et.al., Appl. Surf. Sci. 253, 7932–7936 (2007).
- [4] Reif et.al., Recent advances in laser processing of materials, 275-290 (2006).
- [5] Reif, Opt. Eng. 28, 1122-1132 (1989).

# Controllable local photo-induced crystallization in SiO<sub>2</sub>-based glasses by femtosecond laser

X. He\*, \*\*, C. Fan\*, \*\*\*, B. Poumellec\*, M. Lancry\*, F. Brisset\*, Q. Liu\*\*, \*\*\*\*, G. Chen\*\*\*, X. Zhao\*\*

\*Institut de Chimie Moléculaire et des Matériaux d'Orsay, UMR CNRS-UPS 8182, Bâtiment 410,  
Université de Paris Sud 11, 91405 Orsay Cedex, France

\*\*State Key Laboratory of Silicate Materials for Architectures, School of Materials Science and  
Engineering, Wuhan University of Technology, Wuhan, 430070, China

\*\*\*Key Laboratory for Ultrafine Materials of Ministry of Education, School of Materials Science and  
Engineering, East China University of Science and Technology, Shanghai 200237, China

\*\*\*\*School of Physics and Technology, Wuhan University, Wuhan, 430070, China

E-mail: Bertrand.Poumellec@u-psud.fr, qmliu@whu.edu.cn

## ABSTRACT

Crystal precipitation is induced locally in the glass 32.5Li<sub>2</sub>O-27.5Nb<sub>2</sub>O<sub>5</sub>-40SiO<sub>2</sub> fabricated by traditional melt-quenching method, by irradiation in volume with femtosecond laser at different pulse energies. Scanning Electron Microscopy and Electron Backscattered Diffraction were used to characterize the size and orientation of crystals. The mechanism of controllable crystallization and orientation will be shortly presented to show that femtosecond laser could be regarded as a useful tool to modify as desired glass in bulk.

**PACS Keywords:** SiO<sub>2</sub>-based glass, femtosecond laser, controllable crystallization.

## 1 INTRODUCTION

The use of femtosecond laser (fs laser) to rationally manipulate micro-/nano-structures inside transparent materials arises from several material interactions which offer very promising opportunities to manufacture new non-linear materials, nano-devices and optical elements by manipulation of the nano-structural properties of the composite medium [1-8]. This is great interest since it allows engineering the optical properties of the material *via* controlling distribution, size and spatial orientation of particles in glass. As LiNbO<sub>3</sub> single crystal is an excellent ferroelectric material with electro-optical, pyroelectrical, piezoelectrical, photorefractive and nonlinear properties [9], it has attracted many researchers' attentions to obtain non-central symmetric crystals in glass through various ways. In present work, the direct photo-induced precipitation of crystals will be taken in silica-based glass by ultra-short laser irradiation *via* manipulation of applied pulse energy in 32.5Li<sub>2</sub>O-27.5Nb<sub>2</sub>O<sub>5</sub>-40SiO<sub>2</sub> (LNS) glass. And the size and orientation of these crystals are characterized by Scanning Electron Microscope - Electron Backscattered Diffraction (SEM - EBSD) method. We also

discuss the mechanism of controllable crystallization in glass using femtosecond laser in this paper.

## 2 EXPERIMENTAL

The silica-based glass 32.5Li<sub>2</sub>O-27.5Nb<sub>2</sub>O<sub>5</sub>-40SiO<sub>2</sub> was prepared by conventional melt-quenching technique. Glass melting and sample processing conditions were described in Ref. [10]. Laser lines writing process was taken by the femtosecond laser system (Satsuma, Amplitude Systèmes Ltd.) at 1030 nm with pulse duration 300 fs at 300 kHz. The laser beam was focused at 350 μm below the surface using a 0.6 NA microscopy objective with the scanning speed at 5 μm/s. The polarization was linear and parallel to the scanning direction. The pulse energy was varied regularly from 0.6 up to 1.6 μJ/pulse measured by microscope objective. The sample was cleaved along the direction perpendicular to the written lines after irradiation, polished to optical quality and subsequently etched in 10% hydrogen fluoride (HF) acid for 2 min. A Field-Emission Gun Scanning Electron Microscope (FEG-SEM ZEISS SUPRA 55 VP) was then used for imaging and for analyzing the crystals orientations (EBSD) in the cross section of the lines. This equipment allows examining uncoated insulating or dielectric specimens using low accelerating voltage (typ. in the range of 1 kV) and very low current (a few pA).

## 3 RESULTS

The SEM and EBSD images of laser irradiated traces at the cross-section are presented in figures 1. The photo-induced crystallization happens after laser irradiating with pulse energy 1.5 μJ as the Kikuchi diffraction patterns (figure 1c) was observed in the drop-like trace of laser (figure 1a) in the sample. From EBSD image (figure 1b), the orientation of crystals was observed in the trace.

Increasing the applied pulse energy regularly, the images of size and orientation dependence on pulse energy is obtained by EBSD method as shown in figure 2. We can see that the size of induced-crystals by 0.6  $\mu\text{J}$  is smaller than 1  $\mu\text{m}$ . Then, as the pulse energy is increased to 1.0  $\mu\text{J}$ , larger size of crystals appeared. For small and large energies preferential orientation is clearly demonstrated. Fig. 2 is the map of the axis perpendicular to the plan of the figure. For small energy, it is the b axis (green color) for the large one it is the polar c-axis (red color) of LiNbO<sub>3</sub>. It is noticeable that for 1.6  $\mu\text{J}$ , a large part of pink color in the trace indicated that most of crystals at the center have c axis in the direction of writing with a small dispersion.

Figure1: SEM (a), EBSD image (b) and Kikuchi diffraction pattern (c) of written line with pulse energy 1.5  $\mu\text{J}$

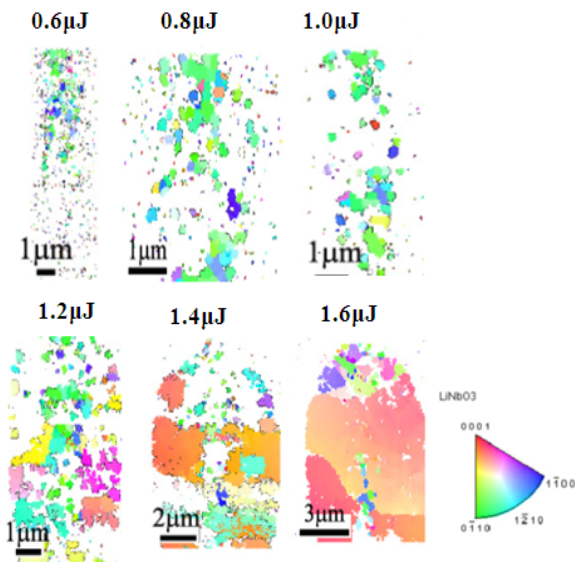


Figure 2: EBSD images of written line at pulse energy from 0.6 to 1.6  $\mu\text{J}$  with a step 0.2  $\mu\text{J}$

#### 4 CONCLUSIONS

Size and orientation of crystallization is shown to be controllable in a traditionnal glass 32.5Li<sub>2</sub>O-27.5Nb<sub>2</sub>O<sub>5</sub>-40SiO<sub>2</sub>. Pulse energy seems to be the main parameters in the problem. This result can be applied for fabricating e.g. doubling or routing waveguides. The discussion in terms of the mechanisms of controllable crystallization and orientation will be presented at the conference to show that it is possible to micro-machine glass structure by femtosecond laser in microscopic *via* manipulating laser irradiation parameters.

#### REFERENCES

- [1] B. Yu, B. Chen, X. Yang, J. Qiu, X. Jiang, C. Zhu, and K. Hirao, J. Opt. Soc. Am. B 21, 83, (2004).
- [2] B. Zhu, Y. Dai, H. Ma, S. Zhang, G. Lin, and J. Qiu, Opt. Express 15 (10), 6069, (2007).
- [3] Y. Yonesaki, K. Miura, R. Araki, K. Fujita, K. Hirao, J. Non-Cryst. Solids 351 (10-11), 885, (2005).
- [4] Y. Dai, B. Zhu, J. Qiu, H. Ma, B. Lu, S. Cao, and B. Yu, Appl. Phys. Lett. 90, 181109, (2007).
- [5] Y. Dai, H. Ma, B. Lu, B. Yu, B. Zhu and J. Qiu, Opt. Express 16, 3912 (2008).
- [6] Y. Dai, B. Zhu, J. Qiu, H. Ma, B. Lu, and B. Yu, Chem. Phys. Lett. 443, 253, (2007).
- [7] A. Stone, M. Sakakura, Y. Shimotsuma, G. Stone, P. Gupta, K. Miura, K. Hirao, V. Dierolf, H. Jain, Opt. Express 17, 23284, (2009).
- [8] A. Stone, M. Sakakura, Y. Shimotsuma, G. Stone, P. Gupta, K. Miura, K. Hirao, V. Dierolf, H. Jain, J. Non-Cryst. Solids 356, 3059, (2010)
- [9] R. S. Weis, T. K. Gaylord, Appl. Phys. A 37, 191, (1985)
- [10] C. Fan, B. Poumellec, H. Zeng, M. Lancry, W. Yang, B. Bourguignon, G. Chen, J. Laser Micro/Nanoen. 6, 158, (2011)

# Effects induced by UV laser radiation on the blue luminescence of silica nanoparticles

L. Spallino\*, L. Vaccaro\*, S. Agnello\*, M. Cannas\*

\*Dipartimento di Fisica, Università di Palermo  
Via Archirafi 36, I-90123 Palermo, Italy

## ABSTRACT

The effects induced by 3.50 eV and 4.66 eV laser photons on the blue luminescence, characteristic of silica nanoparticles, were investigated by monitoring its intensity during and after exposure. The luminescence trend is found to be dependent on the UV photon energy thus evidencing the conversion of luminescent defects towards stable and metastable states.

**Keywords:** silica nanoparticles, laser irradiation, defect transformation, time-resolved photoluminescence.

## 1 INTRODUCTION

The high photon emissivity in a wide spectral range, from IR to visible, is one of the most relevant phenomena emerging from the reduction of silica down to nanoscale; hence it is promising for the development of optical nanotechnologies (down converter, probes, display) [1]. It is well accepted that the origin of this luminescence is related to the high specific surface of silica nanoparticles ( $\sim 100 \text{ m}^2/\text{g}$ ), however the role of specific optically active centers remains poorly understood. An obstacle in the interpretation of data is due to the huge variety of defects arising from the reactions of molecular and atomic species of surrounding atmosphere at the surface sites. Nevertheless, under UV excitation a bright blue photoluminescence (PL) centered around 2.8 eV is usually observed in silica nanoparticles. The blue emission is stable in the ambient atmosphere, it exhibits two excitation peaks around 3.5 eV and 5.0 eV and a short lifetime in the ns timescale [2,3]. The monotonic increase of its intensity with the specific surface indicates that it originates from defects localized in the nanoparticle surface shell [4]. The origin of this PL band remains an open question, only a computational work has assigned it to a metastable defect pair consisting of a dioxasilirane ( $=\text{Si}(\text{O}_2)$ ) and a silylene

( $=\text{Si}^{\bullet\bullet}$ ) [2]. Recently, it has been demonstrated that this

band decreases and red-shifts by addition of  $\text{H}_2\text{O}_2$  or mineral acids ( $\text{HCl}$  or  $\text{H}_2\text{SO}_4$ ); whatever the model, those results suggest that the luminescent center acts as a surface

trap [5,6]. In order to gain information on the structure of blue luminescent defects, the present work concerns with their stability under UV radiation; to this aim we have monitored the blue band both during and after Nd:YAG laser irradiation.

## 2 EXPERIMENTAL METHODS

We investigated samples obtained by two typologies of commercial fumed silica nanoparticles differing for the specific surface (S) and for the average diameter (d): one, named AE300, with  $S=300 \pm 30 \text{ m}^2/\text{g}$  and  $d=7 \pm 1 \text{ nm}$ ; the other, named AE150, has  $S=150 \pm 20 \text{ m}^2/\text{g}$  and  $d=14 \pm 2 \text{ nm}$ . UV irradiations were performed at room temperature using the III (3.50 eV) and the IV (4.66 eV) harmonics of a pulsed Quanta System SYL 201 Nd:YAG laser (pulse width  $\sim 5 \text{ ns}$ ). The radiation exposure was done by maintaining constant the Fluence/s. Visible luminescent centers were monitored by ex-situ time-resolved PL spectra; pulsed excitation light at energy  $E_{\text{exc}}=4.96 \text{ eV}$  (pulse energy  $\sim 0.2 \text{ mJ}$ , pulse width  $\sim 5 \text{ ns}$ , repetition rate 10Hz) was provided by a VIBRANT OPOTEK optical parametric oscillator laser system, pumped by the III harmonic of a Nd:YAG laser. The emitted light was spectrally resolved by a monochromator (SpectraPro 2300i, PI/Acton) using a grating (150 grooves/mm, 300 nm blaze) and acquired by an intensified charge coupled device camera driven by a delay generator (PI-MAX Instruments) that sets the time acquisition parameters, gate width  $\Delta T$  and time delay  $T_D$  since the laser excitation.

## 3 RESULTS AND DISCUSSION

In Figure 1a we report representative PL spectra of the blue band observed in the AE150 sample as a function of the number of III harmonic laser pulses. The exposure was performed with pulse energy density  $E_p=37.5 \text{ mJ/cm}^2$  and repetition rate  $\Gamma=2\text{Hz}$ , up to deposit a total Fluence of  $750 \text{ mJ/cm}^2$ . PL was acquired with  $\Delta T=200 \text{ ns}$  and  $T_D=10 \text{ ns}$ . As indicated by the arrow, the blue PL intensity decreases on increasing the number of pulses deposited on the sample. The post irradiation PL trend, monitored for about 5 hours after the end of the last irradiation, is reported in Figure 1b: the intensity backs and almost recovers its value before irradiation. We note that the spectral features (peak position and width) do not change over all

experimental stages. Moreover, we have performed these experiments on varying the pulse energy density and the repetition rate so as to maintain constant the Fluence/s: the bleaching effectiveness increases on increasing  $E_p$  thus demonstrating that this process is non-linear.

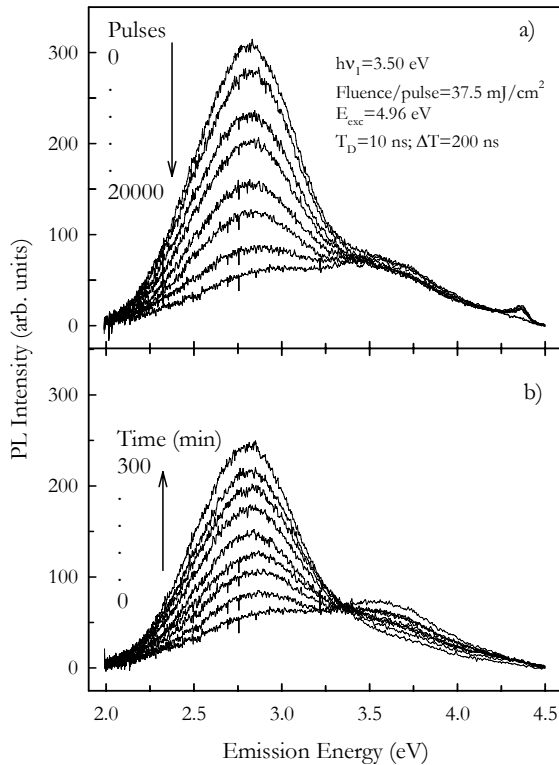


Figure 1: Evolution of PL spectra measured ex-situ on the AE150 sample during (a) and after (b) 3.50 eV laser irradiation. The arrows indicate the trend of the visible blue band.

To better evidence the comparison between the effects induced by  $h\nu_1=3.50\text{ eV}$  and  $h\nu_2=4.66\text{ eV}$  photons on the blue band, in Figure 2 we plot its PL intensity as a function of the Fluence and of the time elapsed since the end of irradiation. During the laser exposure, we observe that the bleaching effectiveness is higher under IV harmonic: after a Fluence $\sim 200\text{ J/cm}^2$  the blue PL is totally removed by  $h\nu_2$  radiation, whereas it is partially reduced ( $\sim 75\%$ ) by  $h\nu_1$  radiation. The destructive effect of  $h\nu_2$  photons is stable in the post irradiation stage, whereas after exposure to  $h\nu_1$  radiation the PL intensity recovers  $\sim 75\%$  of its original value within 5 hours. We note that these results characterize also the blue PL in the AE300 sample.

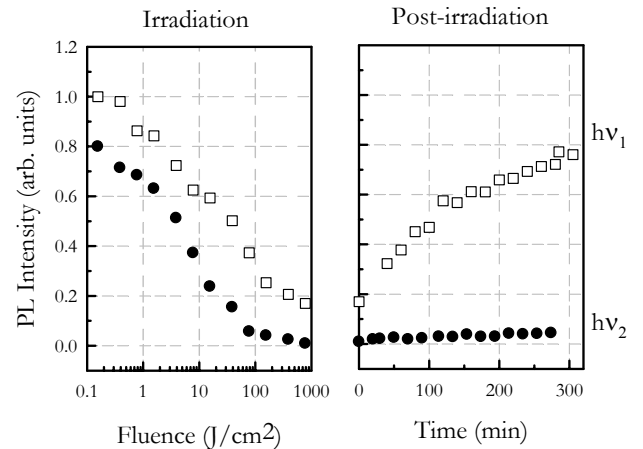


Figure 2: PL Intensity monitored at  $E_{em}=2.60\text{ eV}$  in the AE150 sample as a function of the radiation Fluence (a) and of the elapsed time since the last irradiation (b);  $t=0$  corresponds to the end of the irradiation session; squares refer to  $h\nu_1=3.50\text{ eV}$  and circles to  $h\nu_2=4.66\text{ eV}$ . The intensity is normalized to that measured in the as-grown sample; its uncertainty is  $\sim 10\%$ .

In conclusion, the reported results point out that, under 3.50 eV and 4.66 eV laser radiation, the blue luminescent defects are selectively converted into non optically active states. The one, induced by lower energy photons, is metastable; the other, induced by higher energy photons, is stable.

## REFERENCES

- [1] G. L. Davies, J. E. McCarthy, A. Rakovich, Y. K. Gun'ko, J. Mater. Chem., 22, 7358, 2012.
- [2] T. Uchino, N. Kurumoto, N. Sagawa, Phys. Rev. B, 73, 233203, 2006.
- [3] L. Vaccaro, G. Vaccaro, S. Agnello, G. Buscarino, M. Cannas, Solid State Commun. 150, 2278, 2010.
- [4] G. Vaccaro, S. Agnello, G. Buscarino, M. Cannas, L. Vaccaro, J. Non Cryst. Solids, 351, 1941, 2011.
- [5] S. Banerjee, S. Honkote, A. Datta, J. Phys. Chem. C, 115, 1576, 2011.
- [6] S. Banerjee, S. Maity, A. Datta, J. Phys. Chem. C, 115, 22804, 2011.

# Time resolved measurements of gratings photo- induced by femtosecond pulses in a lead doped glass

S. Chouli, E. Freysz

Université de Bordeaux, LOMA UMR-CNRS 5798  
351 Cours de la Libération 33405 Talence Cedex - France

## ABSTRACT

We report on the formation of grating photo-induced by femtosecond pulses in SF59 glass. Depending on the laser repetition rate and the pulse energy, transient or permanent gratings are photo-induced. We demonstrate that the grating formation is not instantaneous and result from laser induced defects. This results in a change of the real and imaginary part of the index of refraction. A simple set-up that records the temporal evolution of both parameters under laser excitation is also presented. It makes it possible to evaluate the weight of both contributions to the grating diffraction efficiency

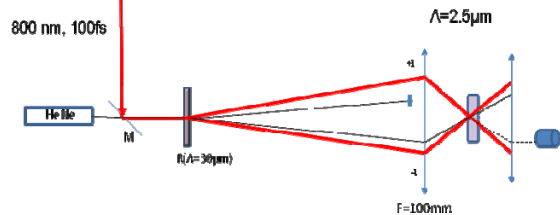
**PACS Keywords:** photo-induced grating, fs pulses, non linear refractive index.

Nowadays femtosecond laser pulses are largely used to induce permanent index modulation inside bulk glass [1]. This method relies on the use of multiphoton absorption for the ultra-short release of the laser energy into a transparent material. This makes it possible to photo-write isotropic or non isotropic three dimensional structures inside bulk glass [2]. Different studies have shown that such femtosecond irradiation induces a structural change of the glass that could locally modify the index of refraction [3]. Aside from structural changes, the induced refractive index may also be due to laser induced color center and/or lattice defects [4]. Hereafter, we have studied the impact of laser induced defects in a lead glass sample during the formation of photo-induced gratings. We demonstrate that the formation is not instantaneous, occurs on the microsecond time scale and results from laser induced defects. The contribution of the modification of both the real and the imaginary part of the index of refraction to the diffraction efficiency is evaluated.

## 1 SET UP

To study the temporal evolution of gratings photo-induced by fs pulses in glass, we used the experimental set up sketched in Fig 1 [5]. A femtosecond pump beam was delivered by a generative amplifier (1 mJ, 50fs, 1 kHz, 800nm). It is overlapped with a continuous wave (CW) He-Ne laser beam used as a probe beam. Both beams are impinging a master phase grating (spatial step, 30 $\mu$ m) that diffracted ~70% of the intensity at 800 nm along +1 and -1 diffraction orders. These two latter diffraction orders are

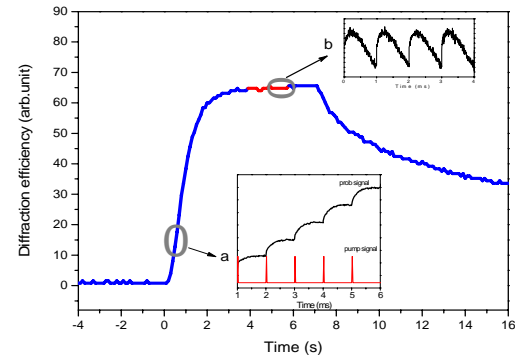
focused on a beam spot (BS) of ~180 $\mu$ m by a 100 mm focal-length lens on a 2 mm thick SF59 glass plate. Notice that only the +1 diffraction order of the He-Ne beam was focused on the sample. The intensity of He-Ne diffracted by the photo-induced grating is focused on a fast photodiode that is connected to a numerical oscilloscope. The latter has a 1 GHz bandwidth.



**Figure 1:** The +1 and -1 diffraction order of the femtosecond laser beam are focused in the studied sample. The He-Ne beam diffracted by the photo-induced grating is recorded by a fast photodiode.

## 2 RESULT

### 2.1 Grating formation



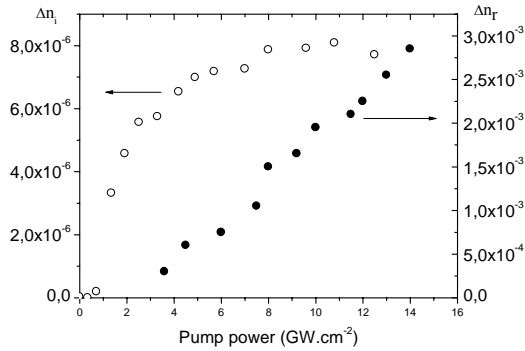
**Figure 2:** Formation and relaxation of grating induced in SF59 by 35 $\mu$ J/pulse. The insets present the evolution of the diffraction efficiency during (a) the formation and (b) saturation of grating. The pulsed femtosecond excitation is

Fig. 2 presents the evolution of the intensity diffracted during the formation and relaxation of the photo-induced grating. When the femtosecond pulses are impinging the sample, we readily record an increase of the intensity of the He-Ne diffracted beam. The latter saturates and reaches a steady state after few seconds. After 7 s when the femtosecond beam is blocked, it relaxes. The insets in Fig. 2 present the evolution of the diffracted intensity on the

millisecond time scale. One should notice that the increase of the reflectivity is not instantaneous indicating the grating evolves slowly on this time scale. During  $\sim 1$  s upon each femtosecond laser excitation, the diffracted intensity increases steadily. Over few seconds and on the millisecond time scale, upon each femtosecond laser excitation the diffracted intensity first increases and then rapidly decreases. This accounts for the saturation of the intensity of the diffracted beam on the long time scale.

## 2.2 Variation of the dielectric constant

While the previous measurements indicate that femtosecond lasers pulses photo-induce a transient or permanent gratings in lead doped glass, it does not indicate the origin nor the amplitude of the modulations of the refractive index. With this goal in mind and using a very simple set-up, we have recorded the evolution of the real and the imaginary parts of refractive index (respectively,  $\Delta n_{\text{re}}$ ,  $\Delta n_{\text{im}}$ ) at the He-Ne laser wavelength (i.e.  $\lambda=632.8$  nm) [5]. The experiment was performed removing the master grating (see Fig. 1). The femtosecond beam was focused at normal incidence on a BS) of  $\sim 180\mu\text{m}$ . The He-Ne beam was parallel but spatially shifted with respect to the femtosecond beam. After the focusing lens and on the sample, it was more tightly focused (BS $\sim 140\mu\text{m}$ ) and slightly off normal incidence angle. The intensity of the transmitted He-Ne beam was detected by photodiode. The latter intensity is given by  $I(e) = I_0 \exp(-4\pi e \Delta n / \lambda_{\text{He-Ne}})$  where  $I_0$  is the transmitted intensity prior to femtosecond irradiation and  $e$  the sample thickness. It makes it possible to measure  $\Delta n_i$ . The He-Ne beams reflected by the front and the back sides of the sample induced an interference pattern in the far field. By counting the fringe shift, we deduced the variation of the real part of refractive index  $\Delta n_r$  induced by the femtosecond pulses. The relation between  $\Delta n_r$  and induced a p-fringe shift is  $\Delta n_r = p\lambda_{\text{He-Ne}}/(2e)$ . To record  $\Delta n_r(t)$ , the small area of the photodiode is placed on maximum intensity of one of the bright fringe when the pump beam is off.



**Figure 3:** Changes of the real ( $\Delta n_r$ ) and imaginary ( $\Delta n_i$ ) parts of the index of refraction in SF59 glass according to the pump power.

Fig. 3 presents the evolution of real and imaginary part of refractive index recorded at steady state versus the pump peak power density.

## 2.3 Evolution of the dielectric constant

The same set-up makes it also possible to record the evolution the real and imaginary part of the index of refraction on the microsecond time scale. These evolutions are presented on Fig 4. When the pump beam is on, the absorption and the index of refraction of the sample increase. They relax when the put beam is off. In agreement with Fig. 3,  $\Delta n_i(t)$  saturates more rapidly than  $\Delta n_r(t)$ . Let-us recall that these latter coefficient are related by a Kramers-Kronig transformation.

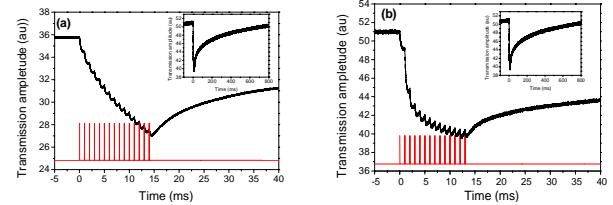


**Fig 4:** Evolution of (a) real and (b) imaginary part of index of refraction when the  $38\mu\text{J}$  pump beam is on and off. The insets show the relaxation recorded on a longer time scale. The red curve shows the femtosecond pulses exciting the sample.

We could easily calibrate the amplitude of  $|\Delta n_r|$ . The sign of  $\Delta n_r$  was inferred from the thermal index variation. In the latter case, we recorded the direction in which the fringe were shifted upon a temperature increase of the sample and compared it to the direction in which the fringes are shifted upon femtosecond laser excitation. They were moving in the same direction. Knowing  $d\eta/dT \sim 5 \cdot 10^{-7} \text{ K}^{-1}$  for SF59, we concluded  $\Delta n_r$  was negative.

This ensemble of measurements makes it possible to evaluate the contributions of both the real and imaginary part to the grating diffraction efficiency. We will show that the contribution of the imaginary part of the index of refraction to the grating diffraction efficiency is negligible. Finally and in agreement with previous works [4], we will show that the femtosecond excitation induces a broad absorption over the whole visible spectral range. It is the latter that accounts for the different evolution recorded for  $\Delta n_r(t)$  and  $\Delta n_i(t)$ .

## REFERENCES

- [1] H. Zhang, S. Eaton, M. Shane; P. Herman, Optics Letters 32, 1 (2007)
- [2] W.Yang, P.G.Kazansky, Y.P.Svirko, Nature Photonics 2, 99 (2008)
- [3] M.Lancry, B.Poumellec, A.Chahid-Erraji, M.Beresna, P.G.Kazansky, Optical Materials Express, 4,711 (2011)
- [4] J.B. Lonzaga, S.M. Avanesyan, S.C. Langford, J.T. Dickinson, Appl. Phys. Letters 94, 4332 (2003)
- [5] Hugues Guillet de Chatelus, E. Freysz, Opt. Letters 27, 1165 (2002).

# Session 4

## Radiation effects



# Prompt Radiation-induced Conductivity in SiO<sub>2</sub> Dielectrics at High Dose Rates

Michael McLain<sup>1</sup>, Fred Hartman<sup>1</sup>, Tom Zarick<sup>1</sup>, Tim Sheridan<sup>1</sup>

<sup>1</sup>Sandia National Laboratories  
P.O. Box 5800, MS 1167, Albuquerque, NM, 87185-1167

## ABSTRACT

It has been shown that the presence of radiation-induced conductivity (RIC) in dielectric films can adversely impact electrical systems intended for use in certain harsh environments. In this summary, the prompt RIC response of silicon dioxide dielectrics at high dose rates is investigated using 20 MeV electron beam exposures produced by a linear accelerator (LINAC). The data indicate that the radiation-induced conductivity in silicon dioxide is linearly dependent on the applied bias and varies as a power of the dose rate.

**Keywords:** radiation-induced conductivity (RIC), dose rate, linear accelerator (LINAC), silicon dioxide (SiO<sub>2</sub>)

## 1 INTRODUCTION

When dielectrics are exposed to ionizing radiation, electron-hole pairs are created via interactions between incident particles/photons and the insulating material[1-5]. The free electrons and holes (i.e., excited electrons in the conduction band and holes in the valence band) generated during a radiation exposure lead to a time-dependent increase in the electrical conductivity known as radiation-induced conductivity or RIC. The RIC is characterized by an initial or prompt component ( $\sigma_p$ ) that occurs during the radiation pulse and a slow decay following the pulse referred to as the delayed component ( $\sigma_d$ ) that exists until all of the free carriers generated during the radiation pulse have recombined. The total current ( $I$ ) and electric field are related to the induced conductivity through

$$I = A \cdot (\sigma_0 + \sigma_p + \sigma_d) \cdot \frac{V_a}{d} + I_{dd} \quad (1)$$

where  $\sigma_0$  is the dark conductivity,  $A$  is the exposure area,  $V_a$  is the applied bias,  $d$  is the sample thickness, and  $I_{dd}$  is the direct drive current produced by the radiation source when the applied bias is zero (i.e., background signal).

In this summary, the RIC response characteristics of silicon dioxide (SiO<sub>2</sub>) dielectrics are investigated as a function of dose rate, pulse width, and applied bias.

## 2 EXPERIMENTAL RESULTS

The 10 mil (254 μm) silicon dioxide films studied in this summary were fabricated by Valley Design Corp. Shown in Figure 1 is a schematic cross-section of the upper (URC)

and lower (LRC) RIC cells within the test fixture apparatus. Each cell consists of an aluminum center electrode ~2.5 cm in diameter, an aluminum guard ring to minimize the electric field distortion at the edges of the center electrode, two dielectric layers, and aluminum ground planes on the outer surface of each dielectric. This design was chosen because it limits the direct drive component during irradiation. The samples were mounted in a custom chamber that provides vacuum levels between ~3 x 10<sup>-4</sup> to 1 x 10<sup>-5</sup> torr. A vacuum chamber is necessary to reduce air ionization effects.

Figure 1: Schematic cross-section of the RIC cells within the test fixture apparatus.

The Little Mountain linear accelerator (LINAC) test facility was used to expose the SiO<sub>2</sub> samples to 20 MeV electron beam exposures at dose rates of 10<sup>8</sup> rad(SiO<sub>2</sub>)/s, 10<sup>9</sup> rad(SiO<sub>2</sub>)/s, and 10<sup>10</sup> rad(SiO<sub>2</sub>)/s. At each dose rate, data were obtained for varying pulse widths (50 ns, 100 ns, 200 ns, and 500 ns) and applied biases (0 V, ± 50 V, ± 100 V, ± 200 V, and ± 500 V) on the center electrode and the guard ring of each cell. The applied bias on the lower and upper RIC cells was equal in magnitude but opposite in polarity. All radiation exposures and electrical measurements were performed at room temperature. A more complete description of the experimental setup, experimental details, and dosimetry will be provided in the final paper and presentation.

Shown in Figure 2 are representative SiO<sub>2</sub> URC RIC signals versus time as a function of applied bias and dose rate. The LINAC was set to a pulse width of 100 ns in these experiments. As expected, the signals are positive for negatively applied biases and the RIC signals monotonically increase when either the applied bias or the dose rate is increased. The observed rise-time characteristics and the post-pulse RC decay are typical features of all biased shots at this pulse width. However, for longer pulse widths (e.g., 500 ns) there is an “early-time” peak and then an approximately linear decrease in the signal until the end of the radiation pulse. When the dielectrics are subjected to longer pulse width radiation exposures, the RIC signals most likely reach a saturated or an equilibrium state whereas for short pulse widths the RIC signal is still increasing when the radiation pulse ends. This is a very interesting result and will be explored further in the final paper. Measurements at the other dose rates and shorter pulse widths exhibited similar dependencies as the

data shown here. The measured values for  $I_{dd}$  and the dark conductivity were insignificant in comparison to the actual RIC signals (refer to (1)). It should be noted that five shots were taken for every experimental condition to ensure that there was minimal shot-to-shot variation. In the final paper, more data showing the pulse width, dose rate, and bias dependencies will be provided.

Figure 2: Measured RIC signal versus time as function of applied bias (-50 V, -100 V, -200 V, -500 V) and dose rate ( $10^9$  rad/s and  $10^{10}$  rad/s). The pulse width was 100 ns.

### 3 DISCUSSION

Shown in Figure 3(a) is a plot of the peak measured RIC signals ( $V_M$ ) versus applied bias for a dose rate of  $10^{10}$  rad(SiO<sub>2</sub>)/s and a pulse width of 50 ns. Plotted in Figure 3(b) is the prompt RIC versus dose rate for pulse widths of 50 ns and 100 ns. The conductivity values are calculated using the slope method[6] which is defined as

$$\sigma_p = \frac{d}{AR_s} \frac{m}{m-1} \quad (2)$$

where  $m$  is the slope of  $V_M$  vs.  $V_a$ ,  $R_s$  is the scope resistance (50 Ω), and  $A$  is the exposure area. The data in Figure 3 indicate that the RIC response is linearly dependent on the applied bias and has a power-law relationship with dose rate ( $D$ ) of the form

$$\sigma_p(D) = k_c D^\Delta \quad (3)$$

In (3) $k_c$  is the RIC coefficient and  $\Delta$  is an experimentally determined parameter. The slope of the conductivity versus dose rate plot is sub-linear on a log-log scale ( $m \approx 0.63$ ).

Figure 3: Plots of the (a) peak RIC signal versus applied bias and (b) prompt RIC versus dose rate.

### 4 CONCLUSION

In this summary, the RIC response characteristics of SiO<sub>2</sub> dielectrics at dose rates of  $10^8$ ,  $10^9$ , and  $10^{10}$  rad(SiO<sub>2</sub>)/s were investigated. The RIC data indicate that the induced conductivity is linearly dependent on the applied bias and varies as a power of the dose rate with a sub-linear slope of  $\sim 0.63$ . These results will ultimately impact the fidelity of advanced models for RIC and aid in the understanding of the deleterious effects that occur in electrical systems used in harsh environments.

### REFERENCES

- [1] T. J. Ahrens and F. Wooten, IEEE Trans. Nuclear Science, vol. NS-23, no. 3, pp. 1268-1272, 1976.
- [2] J. F. Fowler, Proc. Roy. Soc. London. Series A, Mathematical and Physical Sciences, vol. 236, no. 1207, pp. 464-480, Sept. 1956.
- [3] A. Rose, New York: Interscience Publishers, 1963.
- [4] D. K. Nichols and V. A. J. van Lint, IEEE Trans. Nuclear Science, vol. 13, pp. 119-126, 1966.
- [5] D. L. Shaeffer and J. M. Siegel, IEEE Trans. Nuclear Science, vol. NS-29, no. 6, pp. 1745-1753, 1982.
- [6] S. H. Face, *et al.*, IEEE Trans. Nuclear Science, vol. NS-30, no. 6, pp. 4450-4456, 1983.

# Influence of fluorine on the fiber performance studied through the NBOHC-related 1.9 eV microluminescence

L. Vaccaro\*, S. Girard\*\*, A. Alessi\*,\*\*\*, M. Cannas\*, A. Boukenter\*\*\*, Y. Ouerdane\*\*\*, R. Boscaino\*

\*Dipartimento di Fisica - Università di Palermo Via Archirafi 36, I-90123 Palermo, Italy

\*\*CEA-DAM-DIF, Arpajon F-91297, France

\*\*\*Laboratoire H. Curien, UMR CNRS 5516, Université St-Etienne, St-Etienne F-42000, France

## ABSTRACT

The distribution of Non Bridging Oxygen Hole Centers (NBOHC) in Fluorine doped optical fibers was investigated by confocal microluminescence spectroscopy monitoring the characteristic 1.9 eV luminescence band. The results show that these defects are generated by the fiber drawing and their concentration further increases after  $\gamma$  irradiation. The NBOHC profile along the fiber is anticorrelated to the fluorine content. This finding agrees with the role of fluorine in the fiber toughness and is discussed from the microscopic point of view on the basis of previous works.

**Keywords:** optical fiber, silica, F-doping, non bridging oxygen hole center, confocal microluminescence

## 1 INTRODUCTION

The performances of high-purity silica-based optical fibers are strongly conditioned by the generation of point defects [1]. In the visible and ultraviolet (UV) domain the fiber transmission is negatively influenced by two intrinsic silica defects, the dangling oxygen (also named NBOHC), whose structure is  $\equiv\text{Si}-\text{O}\bullet$ , and the dangling silicon (also named E' center), whose structure is  $\equiv\text{Si}\bullet$  [2-4]. The E' center is characterized by an optical absorption (OA) band at 5.8 eV, the NBOHC by several OA bands centered around 2.0 eV, 4.8 eV and 6.5 eV, each of them exciting a peculiar photoluminescence (PL) band at 1.9 eV. Their generation results from different mechanisms: drawing, UV transmission along the fiber core and irradiation in harsh environments. These processes occur in precursor sites: Si-OH bonds or strained Si-O bonds which can be distinguished on the basis of the irradiation dose dependence curves.

To improve the fiber toughness some extrinsic elements are introduced *ad hoc*. One method is the doping with halogen elements such as F that stabilize functional groups (Si-F) so as to reduce the strained bonds [5]. Moreover, since F reduces the refractive index, the fiber doping profile, both multistep- or graded-index, is designed to minimize the dispersion losses.

In this work we report the comparison among three F-doped fibers differing for their doping profile. By the confocal microluminescence technique we study in detail

the NBOHC concentration along the fiber diameter detecting its 1.9 eV PL band. Our purpose is to clarify the role of F in inhibiting the NBOHC generation both by drawing and by  $\gamma$  irradiation.

## 2 EXPERIMENTAL METHOD

We investigate three types of F-doped fibers differing for the F-profile and the doping content. The F and F2-D2 fibers have been provided by iXFiber S.A.S and are four and two step-index fibers, respectively, with an outer undoped high purity silica layer (external cladding) and internal cylindrical layers of highly pure synthetic silica doped with different F amounts. F doping profile grows from  $\sim 0.2$  wt.% in the center (core) to  $\sim 1.6$  wt.% in the outer part (internal cladding). The internal F-doped part of the fibers is made with modified chemical vapor deposition (MCVD) process. The third fiber is a graded-index fiber made up of an outer undoped high purity silica layer (external cladding) and an internal part of highly pure synthetic silica doped with an F amount growing continuously from  $\sim 0.2$  wt.% in the center (core) to  $\sim 5$  wt.% in the outer part (internal cladding). The F-doped part is made with plasma-activated chemical vapor deposition (PCVD) process. Hereafter, it will be named PCVD fiber.

Our fibers have a diameter of 125  $\mu\text{m}$  and have been irradiated at room temperature by using the  $^{60}\text{Co}$  source (1.2 MeV) at the Brigitte facility of SCK-CEN (Belgium); the accumulated dose ranges from  $1.1 \times 10^6$  Gy to  $10^7$  Gy.

NBOHCs along the core of the fibers were detected by the confocal microscopy luminescence (CML) measurements performed with a LabRam Aramis (Jobin-Yvon) spectrometer; it is based on a He-Cd ion laser excitation line (photon energy 3.8 eV, power  $\sim 72$   $\mu\text{W}$ ) and supplied with a CCD camera and microtranslation stages. The excitation beam penetrates of a few micrometers in the sample; the measurement geometry is the back-reflected one. We used a  $40 \times$  objective and a diaphragm diameter of 75  $\mu\text{m}$ ; these experimental conditions lead to a spatial resolution of  $\sim 5$   $\mu\text{m}$ . NBOHCs were detected monitoring the emission photoluminescence (PL) band around 1.9 eV; their concentration has been calculated comparing the amplitude of this PL band with that measured in a reference

neutron irradiated synthetic silica sample (neutron fluence of  $1.6 \times 10^{17} \text{ n/cm}^2$ ) whose NBOHC concentration is known by the intensity of the 2.0 eV optical absorption band.

### 3 RESULTS AND DISCUSSION

Figure 1 shows typical PL spectra measured in the center of the as-grown and 7.8 MGy  $\gamma$  irradiated *F* fiber; they are characterized by a band around 1.9 eV. On the basis of the comparison with the PL spectrum of a neutron irradiated bulk sample, this emission is unambiguously related to NBOHC. This defect is already present in the fiber as the drawing effect; its concentration increases of more than one order of magnitude after  $\gamma$  irradiation.

Figure 2 reports the NBOHC concentration measured along the fiber diameter; data refer to the graded index fiber, *PCVD*, before and after  $\gamma$  irradiation at the dose of 10 MGy. The drawing induce NBOHCs, their concentration is maximum ( $8 \times 10^{16} \text{ cm}^{-3}$ ) at the core center and decreases down to few  $10^{15} \text{ cm}^{-3}$  at 25  $\mu\text{m}$  far from the center. Irradiation induces additional NBOHCs with a similar profile; the maximum concentration ( $1.2 \times 10^{18} \text{ cm}^{-3}$ ) is in the core center. We note that the defect concentration is anticorrelated with the F content as shown in the figure.

These results are common to all typologies of investigated fibers and point out that the F improves the toughness of fibers as concerns the NBOHC generation. From a microscopic point of view, we suggest that Si-F groups reduce the concentration of strained bonds that are precursors of NBOHC defects.

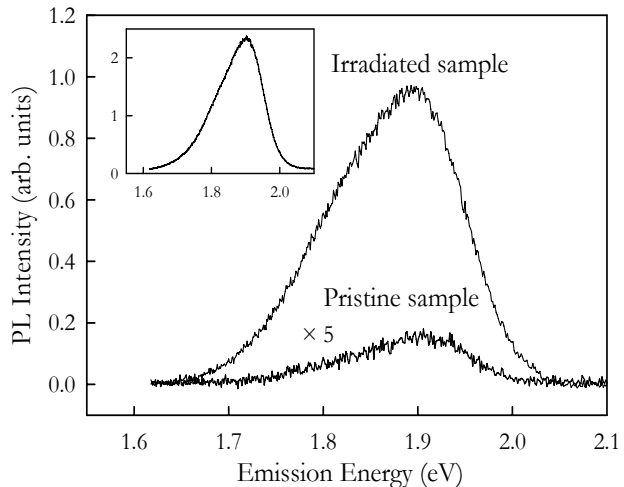


Figure 1: PL spectra measured in the fiber *F* before and after  $\gamma$  irradiation at the dose of 7.8 MGy. The inset shows the PL spectrum of the bulk neutron irradiated sample taken as reference.

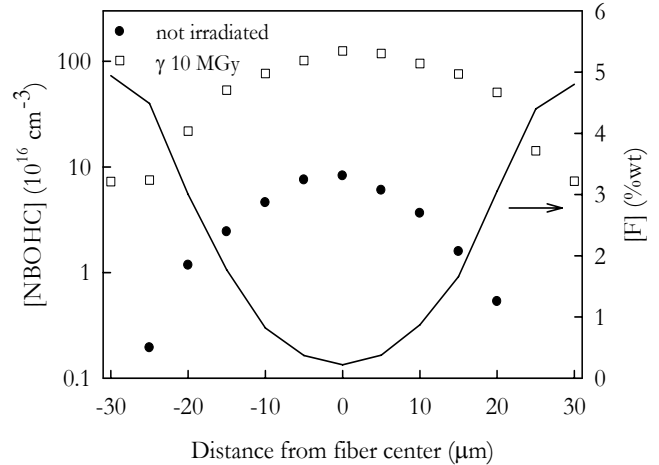


Figure 2: NBOHC concentration profiles along the diameter of the graded-index *PCVD* fiber before (full symbols) and after (empty symbols) 10 MGy  $\gamma$  irradiation.

The F concentration is also reported in the figure in the right y scale.

### REFERENCES

- [1] S. Girard, Y. Ouerdane, G. Origlio, C. Marcandela, A. Boukenter, N. Richard, J. Baggio, P. Paillet, M. Cannas, J. Bisutti, J.-P. Meunier, R. Boscaino, IEEE Trans. Nucl. Sci., **55**, 3473, 2008.
- [2] H. Hosono, K. Kajihara, T. Suzuki, Y. Ikuta, L. Skuja, M. Hirano, Solid State Commun., **122**, 117, 2002.
- [3] S. Girard, J.-P. Meunier, Y. Ouerdane, A. Boukenter, B. Vincent, A. Boudrioua, Appl. Phys. Lett. **84**, 4215, 2004.
- [4] L. Vaccaro, M. Cannas, B. Boizot, A. Parlato, J. Non-Cryst. Solids **353**, 586, 2007.
- [5] G. Origlio, A. Boukenter, S. Girard, N. Richard, M. Cannas, R. Boscaino, Y. Ouerdane, Nucl. Instrum. Methods Phys. Res. B **266**, 2918, 2008.

# Thermal bleaching of gamma-induced-defects in optical fibers

A. Morana\*, A. Boukenter\*, Y. Ouerdane\*, S. Girard\*\*, M. Cannas\*\*\*, J. Périsse\*\*\*\*, J.-R. Mace\*\*\*\*\*

\* Laboratoire Hubert Curien, UMR CNRS 5516, Université St-Etienne, F-42000 St-Etienne, France

\*\* CEA, DAM, DIF, F-91297 Arpajon, France

\*\*\* Dipartimento di Fisica, Università di Palermo, I-90123 Palermo, Italy

\*\*\*\* Areva, F-69456 Lyon Cedex 06, France

\*\*\*\*\* Areva, Tour Areva, F-92084 Paris La défense Cedex, France

## ABSTRACT

Ge-doped and F-doped gamma-irradiated fibers with a maximum accumulated dose of 10 MGy were subjected to isochronal annealing treatments up to 750°C. The thermal treatment influence on the point defect generation and transformation were investigated through Radiation Induced Attenuation (RIA) changes in the visible and IR spectral domains. The thermal bleaching of gamma-induced-defects depends on both temperature and composition of optical fibers.

**PACS Keywords:** silica, fiber, radiation, thermal treatment, optical measurement

## 1 INTRODUCTION

Nowadays the nuclear industry is showing an important interest in the fiber optic technology for both remote handling and sensing applications. However the optical components employed in the nuclear power plants are exposed to a very harsh environment characterized by high neutron fluence and/or high level of ionizing radiation. These cause the formation of point defects in silica and affect the transmission properties of optical fibers. For some of the considered applications, the fiber-based system will also have to operate at high temperature up to 550°C. As the temperature is known to strongly affect the point defect generation and transformation and then the fiber response, we study in this paper the thermal annealing effects on gamma-irradiated optical fibers designed with different compositions.

To this purpose, optical measurements in the visible and IR regions (400-1700nm) were carried out on high-dose-gamma-irradiated fibers subjected to isochronal annealing treatments, to monitor the optical fiber transmission according to the annealing temperature.

## 2 EXPERIMENTAL DETAILS

For all the transmission spectra, we used two white light sources, a spectrometer QE65000 from Ocean Optics for the visible range, between 400 and 700 nm, and an OSA from Yokogawa for the IR range, between 750 and 1700 nm.

Two types of fibers, both singlemode (SMF) and multimode (MMF), were tested: the first, named SM-Ge and MM-Ge, is characterized by a Ge-doped core and the second one, named SM-F and MM-F, is characterized by an F-doping. Both fiber types have a 125 $\mu$ m diameter cladding and a diameter core of 9 $\mu$ m for SMF and 50 $\mu$ m for MMF. The coating is realized in acrylate.

20 meters of each fiber were gamma-irradiated with the Brigitte  $^{60}\text{Co}$  facility at SCK-CEN. The accumulated doses were between 5 and 10 MGy. Spectral attenuation measurements at room temperature were performed some months after the irradiation, by the “cut-back” method.

Depending on the loss level, different lengths of the irradiated samples were heated in air up to 300°C, 550°C and 750°C. Heating rate was fixed at 10°C/min and at each step the temperature was held constant for 15 min, before cooling down to measure the transmission spectra. The fibers were coiled to diameters of around 10 cm and put inside quartz cylinders to avoid contact with the inner surface of the furnace. The acrylate coating can not indeed stand temperatures higher than 100°C. It is totally removed by heat treatment, with no additional effect on the transmitted signal. In fact, this work is focused on the temperature effect on the silica core and cladding properties. Depending on the targeted application, the best fiber type will have to be elaborated with an adapted metallic coating (Cu or Au) compatible with the high temperatures considered.

The recorded optical transmission signal was used to monitor the thermal treatment influence through the changes in the Radiation Induced Attenuation (RIA).

## 3 RESULTS

Figures 1 and 2 display the spectral variations of the RIA in a MM-F fiber irradiated at the highest dose. Fig. 1a and 2a show the RIA measurements recorded with the cut-back technique. Fig. 1b and 2b display the as-measured isochronal anneal difference spectra,  $L(\lambda, T_{\text{ann}}) - L(\lambda, T_{\text{NHT}})$ , where  $L$  indicates the transmitted signal,  $T_{\text{ann}}$  is the annealing temperature and NHT means that no heat treatment was performed. Both  $L(\lambda, T_{\text{ann}})$  and  $L(\lambda, T_{\text{NHT}})$  were recorded at room temperature (RT). Fig. 1c and 2c report the cumulative influence of both irradiation and thermal treatments.

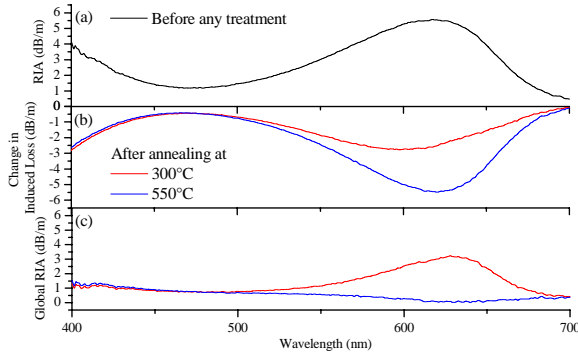


Figure 1: Spectra in the visible range for a gamma-irradiated MM-F fiber at the total dose of 10 MGy: (a) RIA measured at RT after the irradiation; (b) Changes in the gamma-induced loss recorded at RT, as a consequence of the thermal treatment; (c) Residual RIA of the irradiated and thermally treated sample.

As the last treatment at 750°C does not improve the fiber transmission further, the curves are not shown.

In the visible range the RIA (Fig. 1a) is mainly due to two contributions: an UV tail that increases with decreasing wavelength and a band peaked around 625nm. This band, according to photo-luminescence measurements, can be assigned to the Non-Bridging Oxygen Hole Centers (NBOHC) [1]. This defect is completely bleached after the thermal treatment at 550°C, while a residual attenuation in the UV region is still present after the three treatments (Fig. 1c). Moreover, by analysing the NBOHC band shape, the bleaching of 1.94eV (640nm) component starts at 300°C in the F-doped fibers and not in the Ge-doped ones (this will be detailed at the conference).

In the IR range the RIA (Fig. 2a) results from two contributions: a tail that increases with decreasing wavelength, probably linked to the UV-visible tail, and an IR contribution that increases with increasing wavelength. The thermal treatment has almost completely reduced the induced optical loss in this spectral domain and a residual attenuation lower than 0.05dB/m is observed over the entire IR range (Fig. 2c).

## 4 DISCUSSION AND CONCLUSIONS

In this work, we present the temperature dependence of the RIA in the visible and IR range for Ge-doped and F-doped fibers. The treatment at 550°C improves the fiber transmission, above all for the MM-F and SM-F, in fact for the MM-Ge and SM-Ge, whose spectra are not shown here, the attenuation in the visible range remains to an important value after the treatments for some RIA components.

As a consequence of the annealing, the UV component of the RIA is not completely reduced, while the band due to the NBOHC decreases with increasing temperature until 550°C [1]. The IR component of the RIA disappears almost completely with the first two treatments, but the effect of

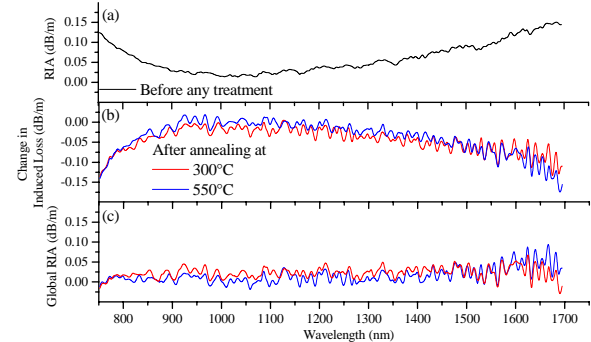


Figure 2: Spectra in the IR range for a gamma-irradiated MM-F fiber at the total dose of 9 MGy: (a) RIA measured at RT after the irradiation; (b) Changes in the gamma-induced loss recorded at RT, as a consequence of the thermal treatment; (c) Residual RIA of the irradiated and thermally treated sample.

the first annealing depends on the fiber type. For the MM-F, as shown in Fig 2, the change in the IR transmission loss is caused principally by the first treatment and not by the second one, while for other fibers, the higher temperature treatment causes the larger bleaching.

Regarding this IR band, a very few studies were published. Regnier et al. [2] observed the same band in gamma-irradiated fibers at the total dose of 100 Gy and they suggest assigning it to STHs. According to the authors, these defects are present in low concentration at room temperature and it was observed thanks to the great fiber length used in their experiments. In our case, the used length is very small and, despite the high gamma-dose employed in our experiments, we can not attribute, due to the annealing temperature, the fiber response to the STH presence. In fact, not only we don't observe the other bands at 660nm and 760nm associated by Griscom to the STHs [3], but, as illustrated by Girard et al. [4], these defects are supposed to be greatly unstable at room temperature and disappear rapidly after the irradiation.

Further investigations are in progress to clarify these evolutions and determinate the origin of this band. More information will be given at the conference.

## REFERENCES

- [1] M. Léon, P. Martin, D. Bravo, F.J. López, A. Ibarra, A. Rascón, F. Mota, Journal of Nuclear Materials, 374, 386-389, 2008.
- [2] E. Regnier, I. Flammer, S. Girard, F. Gooijer, F. Achten, G. Kuyt, IEEE Transactions on Nuclear Science, 54, 4, 1115-1119, 2007.
- [3] D.L. Griscom, Journal of Non-Crystalline Solids, 349, 139-147, 2004.
- [4] S. Girard, D.L. Griscom, J. Baggio, B. Brichard, F. Berghmans, Journal of Non-Crystalline Solids, 352, 2637-2642, 2006.

# Assessment of Ge-doped optical fibres as a TSL-mode detector

M. Benabdesselam\*, F. Mady\*, S. Girard\*\*

\*Université de Nice-Sophia Antipolis, LPMC UMR CNRS 7336

Parc Valrose, 06108 Nice Cedex 2, France

\*\*CEA, DAM, DIF

91297, Arpajon Cedex

## ABSTRACT

This study analyses the thermally stimulated luminescence (TSL) or thermoluminescence glow curve between 300 and 773 K of germanium-doped silica optical fibre. A main glow peak at around 500 K with a characteristic spectral emission centred at 400 nm is found. Both features are particularly suitable for dosimetry.

Thus, an investigation by the TSL technique of some first clinically relevant features of a TSL sensor like the dose- and dose rate-responses is obtained. The presented studies show that germanium doped silica fibres have potential dosimetric properties and should be excellent TSL-mode detectors in instances of radiotherapy (clinical dosimetry) and *in-vivo* radiation dosimetry as well in the field of nuclear facilities.

**PACS** **Keywords:** dosimetry, radiation, silica, thermoluminescence, optical fibres

## 1 INTRODUCTION

In view of their high TSL sensitivity, storage stability and reliability, the outstanding advantages presented by Ge-doped optical fibres are interesting for application in ionising radiation dosimetry and have to be explored.

With the achievement of the modified chemical vapour deposition (MCVD) process, reproducible and large-scale production, high quality optical fibres are now available at moderate cost [1]. In addition, optical fibres are chemically inert, physically robust and biocompatible and their re-use and sterilisation are obtained by simple heating.

Classical dosimeters (TLD) use the property of thermoluminescence signal relative, for practical reasons; to deep trap levels, which the population increases with the radiation-absorbed dose. In this technique, the deep level acts as “a memory cell” of the ionising radiation dose. The trapping properties of the deep level in the TSL process and its concentration are among the critical parameters that control the behaviour of the dosimeter.

The control of the deep level within the silica band gap, by Ge impurities, might lead to a new kind of adequate TSL-mode detectors with probably some better properties than the two commercially available TLDs which have

some detrimental effects like a fastidious use protocol (TLD100) or the sensitivity to ambient light (TLD500).

## 2 EXPERIMENTAL SETUP

The studied fibre presented here is produced by iXFiber SAS from a preform made by MCVD process. The drawing conditions of the 125  $\mu\text{m}$  diameter obtained fibre are described elsewhere [2]. Germanium doping levels are designed to follow a two-step distribution.

Because of heating, the TSL analysis requires the polymer coating removal on a fibre length. The obtained silica material is cleaned, cut in stalks of some millimetres in length and then put on a 10 mm diameter aluminium cupel.

Irradiations were achieved at room temperature (RT) by means of an X-ray tube (Cu target, 45 kV) at different dose rates. One minute after the end of irradiation, thermoluminescence readout was carried out from RT up to 750 K with a linear heating rate of 1 K/s and the signal was recorded by means of a S13 response photomultiplier (250 – 600 nm).

An optical multichannel analyser (OMA) was used to detect the spectral distribution of the TSL peak. The analyser consists of an optical fibre (fused silica) and a Chromex 250 IS spectrograph equipped with a CCD matrix (Princeton Instruments), the spectral response of the system is within the range 200-1100 nm.

## 3 RESULTS AND DISCUSSION

### 3.1 Trapping and luminescence parameters

Among various studied optical fibres, Ge-doped one and named GeD2 is by far, the most sensitive by comparison to the undoped fibre or to those containing other impurities (Al, F, P, RE.). Besides one shoulder at around 373 K, a main glow component peaking at 500 K composes the typical TSL curve of GeD2. The shoulder at 373 K, always observed by TL in all tested silica fibres, is probably due to a common intrinsic defect in silica, acting as a shallow trap level within the band gap of the material. One focuses our study on the deeper trap level characterized by this main TSL peak at 500 K and which suits dosimetric criteria. Trapping parameters associated to this peak are a mean

activation energy  $E \approx 1.46$  eV and a frequency factor of  $1.3 \times 10^{12} \text{ s}^{-1}$ .

Fig. 1 shows the spectral distribution of the main peak at 500 K. It consists of a blue-violet broadband luminescence ( $\text{FWHM}=0.4$  eV) centred at 400 nm (3.1 eV). This well known emission is ascribed to the luminescence of the two-fold Ge centre (=Ge:) [3,4]. D. Griscom has already identified this centre as a trapped-electron one [5]. Indeed, the luminescence of this main peak might be described as a result of recombination on GeODC centres of holes, released at 500 K during TSL process.

Furthermore, whatever the temperature is (strip on the figure), one can see on Fig. 1 that there is only the emission at 400 nm. This implies that the shoulder at 373 K can also be ascribed to a detrapping of holes.

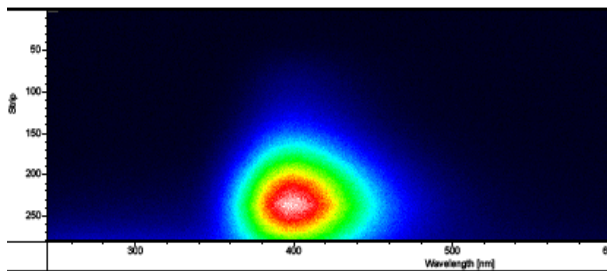


**Fig. 1.** Image of the dosimetric peak emission observed on GeD2 optical fibre after X-ray irradiation at RT.

### 3.2 Dosimetric characteristics of GeD2 fibre

GeD2 fibre shows high TSL response sensitivity of the main peak, which is ideally located in temperature, so avoiding the disturbance of the black body radiation. The luminescence emission of this peak is centred at 400 nm, that is to say in the middle of the spectral band width of all UV-Vis PM tubes used in TSL dosimetry. TSL sensitivity, peak position and spectral response constitute the first main properties of the TSL-mode detector for which GeD2 optical fibre seems to be a potential candidate for some basic dosimetry tests.

The first test was that of TSL response repeatability after five successive readout cycles on a same fibre. The estimated repeatability is within the experimental error.

The second set of tests concerns the TSL response as a function of both the dose and the dose rate of radiation. Results for two different dose rates (60 and 490 rad/s) are shown on Fig. 2. One can note that for both dose rates, the TSL response shows a quite linear behaviour ( $R^2=0.998$ ) within a wide dose range. One can also note that no obvious effect of the dose rate on the TSL response of GeD2 is observed particularly at low doses, where clinical application is concerned. However, although different, these rates remain of the same magnitude.

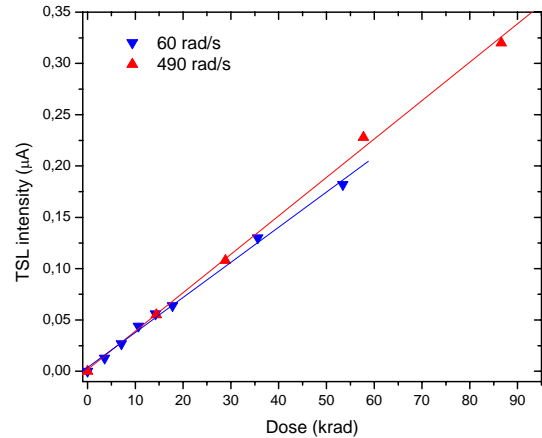


**Fig. 2.** TSL response of the dosimetric peak as a function of the X-ray dose.

Other dosimetric features of GeD2 optical fibre as well as a comparative study with a widely used commercial TLD are in progress.

### 4 CONCLUSION

These preliminary results show that GeD2 optical fibre appears to meet the various required criteria for TSL dosimetry.

The combination of a high sensitivity, a good linearity of response over a wide range of doses (up to 90 krad), an independence of the dose rate and are-use without any tedious treatment, make GeD2 optical fibre, a potential cheap, easy-to-use TSL-mode detector.

It should also be emphasised that the small size of Ge doped silica fibres together with their biocompatibility, physical robustness and chemical inertness, make these fibres well suitable for patient dosimetry.

### REFERENCES

- [1] K.T.V. Grattan, B.T. Meggit, Optical Fiber Sensor Technology. Advanced applications, Bragg gratings and Distributed sensors. Kluwer Academic Publishers. The Netherlands, 2 pp, 2000.
- [2] A. Alessi, Journal of Non-Crystalline Solids 357 (1966-1970), 2011.
- [3] L. Skuja, "Optical Properties of Silica" in Defects in SiO<sub>2</sub> and Relaed Dielectrics: Science and Technology, p108 Edited by G. Pacchioni, L. Skuja and D. L. Griscom, 2000.
- [4] A.N. Trukhin, J. Troks, D. L. Griscom, Journal of Non-Crystalline Solids 353 (1560-1566), 2007.
- [5] D.L. Griscom, Journal of Non-Crystalline Solids 357 (1945-1962), 2011.

# Session 5

## SiO<sub>2</sub> Atomic Structure



# Impact of the fictive temperature on the silica glass anomaly compressibility : in-situ Raman spectroscopy at high pressure

V. Martinez\*, C. Martinet\*, D. de Ligny\*, B. Champagnon\*  
S. Sen\*\*

\* LPCML, Université Lyon 1, Université de Lyon, 12 rue Ada Byron, 69622 Villeurbanne, France.

\*\* Glass Research Division, Corning Incorporated, Corning, New York 14831, USA

The density of common glass decreases as the fictive temperature ( $T_f$ ) increases. This thermodynamic parameter,  $T_f$ , is an indicator of the thermal history of amorphous systems and is correlated to structural relaxation. A glass cooled quickly has a  $T_f$  higher than a glass cooled slowly. Pure silica glass density has an anomalous behavior (from 950 to 1500°C) in regards to  $T_f$ . A maximum in density is shown around 1500°C and more recently Sen [1] demonstrated the existence of a minimum at 950°C (Figure 1).

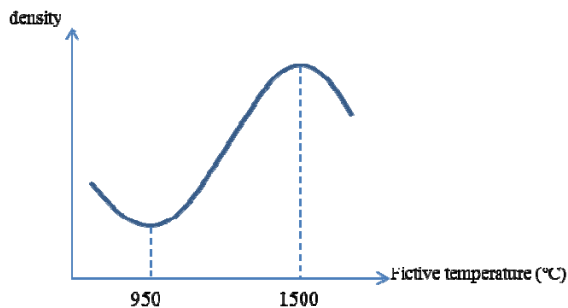


Figure 1. Anomalous evolution of pure silica glass density from Bruckner and Sen

This anomaly could be a proof to a possible transformation between a low density amorphous state (LDA) and a high density amorphous state (HDA). This mixture of LDA and HDA can be thought as a universal characteristic of glasses [2].

Density variations on glass can also be obtained after an applied pressure. Diamond Anvil Cell experiments are very suitable to study the evolution of glass structure under high pressure.

Such experiments performed by Brillouin scattering showed that elastic moduli present a non-monotonous evolution with pressure [3]. Indeed, a decrease of the elastic moduli is observed at the beginning of the compression at around 2,5 GPa for pure silica glass.

Moreover, previous studies present in-situ Raman experiments and correlate the anomaly at 2.5 GPa and the signature positions [4]. The interpretation of this anomaly will be discussed in terms on Si-O-Si bond angles

variations and on  $\alpha$ -to- $\beta$  cristobalite similar transformation in cohesive domains.

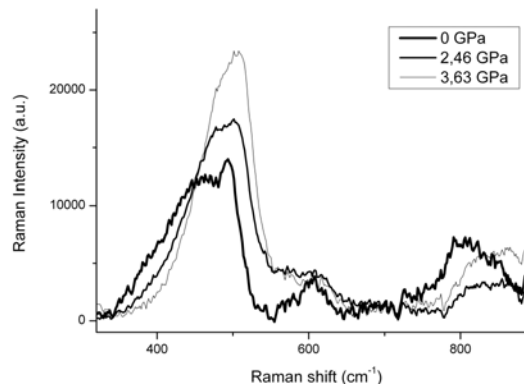


Figure 2 : In-situ Raman spectra at 0, 2,46 and 3,63 GPa

In-situ pure silica Raman spectra at different pressures are shown in figure 2. At ambient pressure, the silica glass Raman spectrum is composed of a broad band at  $440\text{ cm}^{-1}$  assigned to Si-O-Si symmetric stretching mode, two narrow bands at  $491\text{ cm}^{-1}$  and  $606\text{ cm}^{-1}$  attributed to four and three membered rings vibrations respectively, a doublet band at  $800\text{ cm}^{-1}$ . In this paper, three samples having different fictive temperature were studied by Raman spectroscopy. Two of them have the same density but are on both sides of the density minimum (figure 1) and the  $T_f$  of the last one is higher. The influence of thermal history on the compressibility anomaly and on the structure will be discussed. In particular, does the thermal history influence the mechanical behavior on the glass under high pressures ?

[1] S. Sen, R. L. Andrus, D. E. Baker, M.T. Murtagh, Physical Review Letters, 93, 12, 125902, 2004.

[2] V. V. Brazhkin, R. N. S. V. Popova, A. G. Lyapin, New kinds of phase transitions transformations in disordered substances, 81, 239, 2002.

[3] M. Grimsditch, Physical Review B 34, 4372, 1986.

[4] T. Deschamps, C. Martinet, D. de Ligny, B. Champagnon, Journal of Non-Crystalline Solids, 355, 1095, 2009.

Keywords : Raman scattering, pressure effects, fictive temperature

# Impact of fictive temperature on glass density and structure of Ge-doped silica glasses

M. Heili<sup>1,2</sup>, M. Lancry<sup>1</sup>, E. Burov<sup>2</sup> and B. Poumellec<sup>1</sup>, D.R. Neuville<sup>3</sup>, C. Le Losq<sup>3</sup>

<sup>1</sup>Institut de Chimie Moléculaire et des Matériaux d'Orsay, Laboratoire de Physico-chimie de l'Etat Solide, UMR CNRS-UPS 8182, Université Paris Sud 11, Bâtiment 410, 91 405 Orsay Cedex, France

<sup>2</sup>Draka Comteq France SAS, Data Center 4, Bâtiment D0, Route de Nozay, 91460 Marcoussis, France

<sup>3</sup>Géochimie et Cosmochimie, CNRS-IPGP, Sorbonne Paris Cité, 1 rue Jussieu, 75252 Paris, France

## ABSTRACT

Contrary to the other oxide glasses, silica glass exhibits an anomalous behavior: its density increases with increasing fictive temperature. Addition of dopants in the glass, such as germanium, is able to make this special trend disappearing. This doping is also interesting in order to follow the structural changes in the material aiming to understand the origin of this anomaly. Germanium atoms are placed in substitution of the Si atoms.

The density of pure and germanium-doped silica glasses was measured as a function of fictive temperature. Raman spectroscopy was used to observe the evolution of structural signatures. These measurements revealed that the intensities of D<sub>1</sub> and D<sub>2</sub> bands increase with increasing fictive temperature either in pure or in doped glass. They are thus not connected to density.

**Keywords:** Ge-doped silica glass, fictive temperature, structure, density, Raman spectroscopy.

## 1 INTRODUCTION

For many applications, silica glass is the preferred material because of its properties: high transparency from IR to UV, low thermal expansion, high chemical and mechanical resistance and a long longevity. For all these reasons, silica glass constitutes an unquestionable choice for the use in optic field and particularly in optical fibers technology.

Silica glass is an amorphous material, whose structural disorder can be described by the fictive temperature as reviewed recently in [1]. It is well known that the fictive temperature determines various glass properties such as density [2, 3] and Rayleigh scattering [1, 4]. Silica glass is unique and exhibits a special trend unlike the others oxide glasses: the faster the cooling, the higher the fictive temperature, the smaller the specific volume. The density of silica glass increase then with increasing fictive temperature [2, 5]. This behavior is known as the “anomaly of silica”.

Currently, most co-dopants used in optical telecommunications are germanium and phosphorus to increase the refractive index and fluorine to lower it. By

doping silica glass with fluorine, the anomaly of silica disappears for a 3,5mol% concentration [6]. On the other hand, germanium is now widely used as a dopant in silica-based glasses for various reasons. It is usually found in concentrations ranging from 1 to 30wt%. GeO<sub>2</sub> remains also to obtain highly photosensitive silica glass to UV light, allowing thus to write optical components such as fiber Bragg gratings [7].

The purpose of this paper is to study the relation between density and fictive temperature for highly Ge-doped silica glasses. Then Raman spectroscopy is carried out on these samples in order to study the structural according to the glass fictive temperature.

## 2 EXPERIMENTAL PROCEDURES

Two kinds of glasses produced by Plasma Chemical Vapor Deposition (PCVD) process were studied in this work: pure silica glass and a 20wt% germanium-doped silica glass.

In order to alter their fictive temperature, thermal treatments with temperatures ranging from 950°C up to 1400°C were performed during times exceeding their structural relaxation times [1]. The samples were then quenched in water at room temperature to impose the fictive temperature at about the heat treatment temperature.

Infrared reflection spectra were measured using FTIR spectroscopy in order to estimate the fictive temperature of the heat-treated samples [8].

Densities of different samples were estimated with the sink-float method based on the comparison of the weights in air and in toluene. These measurements were made on 10 samples for each fictive temperature with weights varying from 10 to 1000 mg, resulting in a density precision of about 10<sup>-3</sup> (g.cm<sup>-3</sup>).

Raman measurements were carried out with a T64000 Jobin-Yvon-Horiba spectrometer at room temperature equipped with a microscope attachment. The 514 nm Argon laser line is used. All spectra were measured in the same conditions. The normalization was done after have established that the variation of refractive index is

negligible. The obtained values are in agreement with those from Ref. [9].

### 3 RESULTS

The fictive temperature of each heat-treated sample was determined using peak position of the Si-O-Si asymmetric stretching vibration band at  $1120\text{ cm}^{-1}$ , measured by FTIR absorption spectroscopy as described in Ref [1, 8]. At low temperatures ( $T < 1200^\circ\text{C}$ ), heat treatment temperature can be considered as being equal to the fictive temperature of the treated samples. These measurements are used to estimate the fictive temperature of the other samples.

The density as a function of fictive temperature for silica glass and 20wt% Ge-doped silica glass are presented in Figs 1 and 2 respectively. The plotted lines are a guide for eyes. As shown in Fig.1, the density of silica samples increases with increasing fictive temperature, meaning that the anomalous behavior of silica is observed as expected [1, 2, 5]. The slope of the fit straight line is equal to  $9.4 \pm 0.2 \cdot 10^{-6}$ , that is close to the value obtained previously in Ref [10].

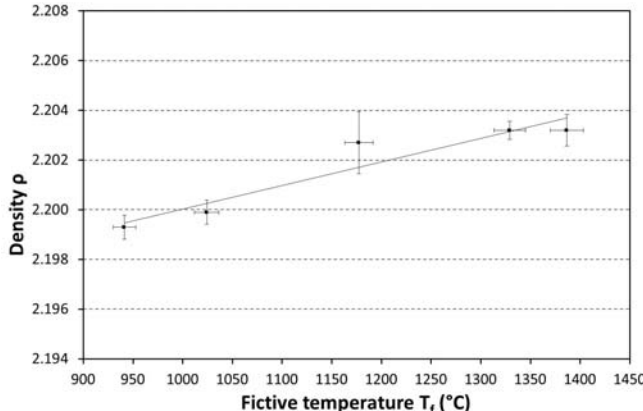


Figure 1: Densities of heat treated PCVD silica glass as a function of fictive temperature

As it can be seen in Fig.2, the opposite trend is noted in 20wt% Ge-doped glass: the higher the density, the lower the fictive temperature. The high germanium doping of 20wt% makes the anomaly of silica disappearing. Kakiuchida *et al.* [10] found that a linear trend is observed by plotting  $d\rho/dT_f$  as a function of F and Cl doping concentrations. We can think it is also the case for germanium doping. The results obtained here for pure and doped silica glasses allow predicting that  $\rho$  would be independent of  $T_f$  for a concentration of approximately 6,7wt% Ge.

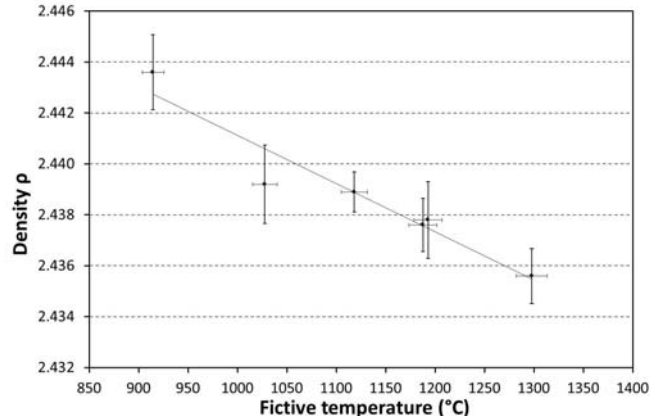


Figure 2: Densities of heat treated PCVD 20wt% Ge-doped silica glass as a function of fictive temperature

Raman spectra were performed on the two types of glass samples from 200 to  $1200\text{ cm}^{-1}$ . For comparison, pure  $\text{SiO}_2$  glass samples were also measured and used as reference samples. The figures 3 and 4 show Raman spectra of pure silica and Ge-doped glasses with three different fictive temperatures, respectively.

The broad band at  $430\text{ cm}^{-1}$  in the spectra of  $\text{SiO}_2$  glass corresponds to the Si-O-Si stretching vibration mode and its width is usually attributed to the dispersion of the Si-O-Si angle.

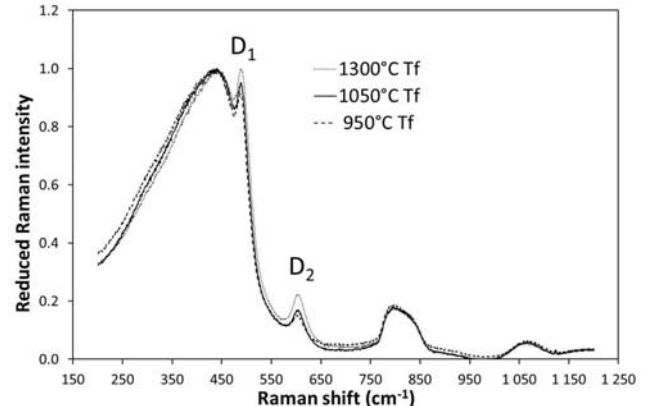


Figure 3: Raman spectra in PCVD pure silica glass samples with the fictive temperature of 1300, 1050 and 950°C.

As it is well known, germanium doping leads to a narrowing of the main band, indicating a reduction of the intertetrahedra T-O-T angles (T=Ge or Si). Ge doping induces also a decrease of the two bands at  $495$  and  $600\text{ cm}^{-1}$  that are the “defects” bands (called  $D_1$  and  $D_2$  respectively) ascribed to the vibration of the three and four-membered rings. A new band is observed at  $680\text{ cm}^{-1}$  on the Ge-doped silica glass spectra, due to the vibrational mode associated with Ge-O-Si bonds [11].

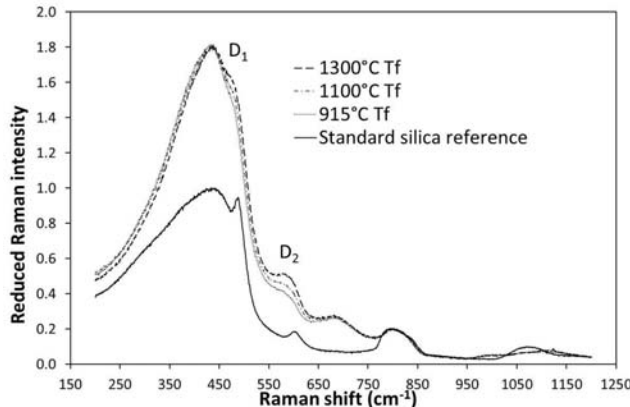


Figure 4: Raman spectra in PCVD 20wt% Ge-doped silica glass samples with the fictive temperature of 1300, 1100 and 915°C.

The main band at  $430\text{ cm}^{-1}$  shifts to the lower wavenumbers when increasing the fictive temperature for the 20wt% Ge-doped silica glass as already reported for low Ge-doping [12]. The linear fit equation is  $\sigma(\text{cm}^{-1}) = 0,0199 T_f + 412,85$ . This is associated with a T-O-T bond angle decrease. A similar conclusion can be deduced from the decrease of the  $1120\text{ cm}^{-1}$  band position that shift from 1111,2 to 1108,4  $\text{cm}^{-1}$  with increasing fictive temperature.

In addition, as it can be seen in Fig.3 and 4, the intensity of the  $D_1$  and  $D_2$  bands increases with increasing the fictive temperature for pure silica and Ge-doped glasses. This means that the number of rings composed of four and three tetrahedra increases and is correlated with a denser network structure [12].

#### 4 CONCLUSION

The variation of the density with fictive temperature for pure and a PCVD 20wt% Ge-doped silica glass has been measured in this work. It has been found that such high Ge doping content makes the anomalous behavior of silica disappearing (density decreases when fictive temperature increases). An interpolation concerning the graph representing  $d\rho/dT_f$  as a function of Ge concentration indicates that for a concentration of about 6,7wt%,  $\rho$  would be independent of  $T_f$ . This concentration is a standard value for the optical fibers applications and maybe explain weak scattering for such a composition.

Raman spectroscopy measurements revealed a decrease of the T-O-T angles for the Ge-doped glass, linked to a shift of the main band position because of fictive temperature. For the two types of glasses, the  $D_1$  and  $D_2$  bands intensities increase with increasing fictive temperature, meaning an increase of the number of 3 and 4-membered rings. Those observations suggest, from previous studies [12], a denser network structure. However this contrast with the macroscopic measurements indicating that Ge-doped glass density decreases with increasing fictive temperature. The evolution of the  $D_1$  and  $D_2$  bands may not be correlated

with density of the glass. Another band of the Raman spectra, such as the band at  $800\text{ cm}^{-1}$  corresponding to the Si-O-Si bending vibration modes, seems rather more connected to density changes.

#### REFERENCES

- [1] Lancry M., et al., "Fictive temperature in silica-based glasses and its application to optical fiber manufacturing," *Progress in Materials Science*, 2011.
- [2] Bruckner R., "Properties and structure of vitreous silica. I," *Journal of non-crystalline solids*, vol. 5, pp. 123-175, 1970.
- [3] Agarwal A. and Tomozawa M., "Correlation of silica glass properties with the infrared spectra," *Journal of non-crystalline solids*, vol. 209, pp. 166-174, 1997.
- [4] Tsujikawa K., et al., "Rayleigh scattering reduction method for silica-based optical fiber," *Journal of lightwave technology*, vol. 18, 2000.
- [5] Shelby J.E., "Density of vitreous silica," *Journal of non-crystalline solids*, vol. 349, pp. 331-336, 2004.
- [6] Shelby J.E., "Fictive temperature and density of doped vitreous silica," *Physics and Chemistry of Glasses-European Journal of Glass Science and Technology Part B*, vol. 50, pp. 7-14, 2009.
- [7] Lancry M. and Poumellec B., "UV laser processing and multiphoton absorption processes in optical telecommunication fibers materials," *Accepted for publication in Physics Reports*, 2012.
- [8] Agarwal A., et al., "A simple IR spectroscopic method for determining fictive temperature of silica glasses," *Journal of non-crystalline solids*, vol. 185, pp. 191-198, 1995.
- [9] Bromage J., et al., "A method to predict the Raman gain spectra of germanosilicate fibers with arbitrary index profiles," *Photonics Technology Letters, IEEE*, vol. 14, pp. 24-26, 2002.
- [10] Kakiuchida H. and Sekiya E., "Refractive index and density changes in silica glass by halogen doping," *Journal of non-crystalline solids*, vol. 353, pp. 568-572, 2007.
- [11] Henderson G.S., et al., "The structure of GeO<sub>2</sub>-SiO<sub>2</sub> glasses and melts: A Raman spectroscopy study," *Journal of non-crystalline solids*, vol. 355, pp. 468-474, 2009.
- [12] Martinez V., et al., "Structural studies of germanium doped silica glasses: the role of the fictive temperature," *Optical Materials*, vol. 24, pp. 59-62, 2003.

# Raman investigation of silica nanoparticles structure

A.Alessi\*, S.Agnello\*, G. Buscarino\*, F.M. Gelardi\*

\* Dipartimento di Fisica Università degli Studi di Palermo  
Via Archirafi 36, I-90123 Palermo, Italy

## ABSTRACT

We investigated the Raman spectra of silica nanoparticles as a function of their size from 7 up to 40 nm diameter. Within the shell-like model, our data confirm and extend some simulative and experimental results and in particular suggest that the structure of the core-shell is only slightly different from that of bulk silica for all the investigated nanoparticles. These data have a relevant role for the understanding of the nanoparticles structure.

**PACS Keywords:** silica, nanoparticles, Raman spectroscopy

## 1 INTRODUCTION

In the last years fumed silica has attracted an increasing attention [1-3]. It consists in amorphous silicon dioxide ( $\alpha$ - $\text{SiO}_2$ ) nano-particles, which can be produced by reacting silicon tetrachloride in an  $\text{O}_2/\text{H}_2$  flame [4]. These nanoparticles found several applications also thanks to the today's miniaturization tendency [1-3]. For this reason many theoretical [5,6] and experimental investigations [1-3,7] have been performed.

The Raman studies [1] highlighted that the spectra of the nano-particles, compared with the ones of the bulk systems, differ for the peak position of the main silica Raman band (R-band), attributed to oxygen vibration in Si-O-Si linkages [8], and for the intensities of the  $D_1$  and  $D_2$  bands, attributed to breathing vibration mode of four-member and three member rings, respectively [8]. These data were attributed to a different distribution of the Si-O-Si angle and to a different ring statistics of the fumed silica with respect to the bulk materials.

It is also important to remind that both experimental [2,3,7] and theoretical [5,6] studies have proposed a shell-like model to explain the structure of the fumed silica. In this model, taking the bulk network as reference, the nanoparticle is considered to be constituted by a surface-shell with a strong modified network and by a core-shell with a more bulk-like matrix. Furthermore, it was proposed that the thickness and the density of the surface-shell, as well as the density of the core are not dependent on the nanoparticles sizes [5,6].

In spite of the many studies focused on the nanoparticles properties, few investigations were performed as a function of the size, as the attention was given to the thermal or the irradiation modifications. For this reason we carried out a detailed study of the Raman spectra of silica

nanoparticles with diameter from 7 to 40 nm performing a comparison with the spectrum of bulk silica.

## 2 EXPERIMENTAL

For our investigation we used commercial Aerosil fumed silica samples produced by Evonik Industries. They were synthesized by  $\text{SiCl}_4$  oxidation in an  $\text{O}_2/\text{H}_2$  flame at 1100-1400 °C. The starting powders of nano-particles were pressed in an uniaxial mechanical press at about 0.3GPa to obtain tablets. In Table I we report the name of the samples, their specific surface and the mean diameter of the primary particles.

Raman spectra were acquired at room temperature by using a Bruker RAMII Fourier Transform Raman spectrometer supplied with a 500 mW Nd:YAG laser at 1064 nm. The applied experimental conditions lead to a spectral resolution of 5  $\text{cm}^{-1}$ .

Name	Specific surface $\text{m}^2/\text{g}$	Particle diameter nm
AEOX50	50	40
AE90	90	20
AE150	150	14
AE200	200	12
AE300	300	7
AE380	380	7

TABLE I: Nanoparticles samples

## 3 RESULTS

In Figure 1, we report some representative Raman spectra acquired for the samples named AEOX50, AE150 and AE380. All the spectra were normalized to the Raman amplitude at 430  $\text{cm}^{-1}$  (this choice was made for illustration reasons only). To compare the spectra of fumed silica with that of bulk material we recorded also the spectrum of a synthetic Suprasil 300 (S300) commercial material by Heareus. We note that the R band (at about 430  $\text{cm}^{-1}$ ) shifts towards larger energies on increasing the specific surface. This information is qualitatively tested by the larger overlap with the  $D_1$  band at about 490  $\text{cm}^{-1}$ . We also note an increase of the relative amplitude of the  $D_1$  and  $D_2$  bands as a function of the specific surface.

Examining the spectra we roughly estimated that the peak position of the R band is at about 436, 444 and 451  $\text{cm}^{-1}$  in bulk silica (S300), AEOX50 and AE150, respectively. A fit procedure is required to better estimate the spectral features especially in the smaller nanoparticles because of the strong overlap with the  $D_1$  band. These changes of the spectral features have been systematically found on varying the nanoparticles size.

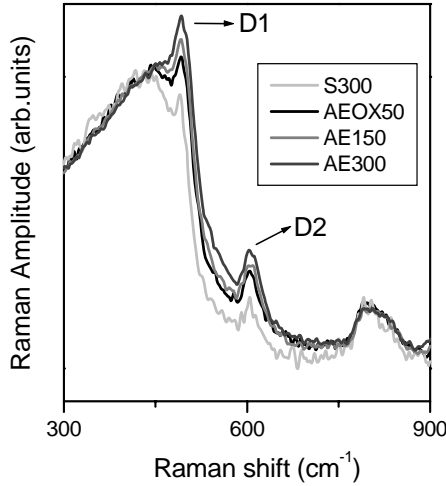


Figure 1: Raman spectra of S300 (—) AEOX50 (—), AE150 (—), AE300 (—).

## 4 DISCUSSION

Using the relation between the peak position of the R band, the Si-O-Si angle and the density [8], we can suggest that the nano-particles have average density higher than bulk materials and that it increases on decreasing the size (increasing of the specific surface). Since the shell-like model predicts the presence of two different regions one can write the following equation:

$$I_R^P = \frac{m_C}{m_p} I_R^C + \frac{m_S}{m_p} I_R^S \quad (1)$$

where  $I_R^P$  and  $m_p$  are the Raman spectrum and mass of the particle,  $I_R^C$  and  $m_c$  are those of the core-shell, whereas  $I_R^S$  and  $m_s$  are the Raman spectrum and the mass of the surface-shell.

Equation (1) indicates that, assuming similar Raman efficiencies, the Raman spectrum tends to be essentially the one of the core when the size increases since the  $m_s/m_p$  ratio decreases. As a consequence, by taking into account the dimension of the AEOX50 sample, one can consider the Raman spectrum of these nanoparticles as the one of the core, so that we can approximately calculate the density of the core (neglecting the surface-shell contribution). In this scheme we found a core density of  $2.26 \text{ g/cm}^3$ , which

means that the core is about 2 % denser than bulk silica. This value, although slightly lower than the ones reported in [3], appears to be sufficiently in agreement with the suggestion made by the authors of the simulative investigation reported in [5]. Similarly, the relative amplitudes of  $D_1$  and  $D_2$  give information on the ring statistics of the core. Our analysis suggests that the ring statistics of the core is slightly different from that of the S300 in support of the hypothesis of a slightly larger density.

Finally, the spectra of the smallest nano-particles (AE300), having a greater surface-shell contribution, indicate that the ring statistic of the surface-shell is shifted towards low member rings, since  $D_1$  and  $D_2$  have more intense amplitudes, and moreover we can guess that its density could be higher than that of the core since the R band shifts to higher energies. All this data agree with the simulation reported in [5,6].

## 5 CONCLUSION

We studied the Raman activities of silica nanoparticles with different sizes. By the spectra analysis and using the shell-like model we estimated that the core of the nanoparticles has a ring statistic similar to the bulk system, even though it is about 2% denser. At variance, the surface-shell is found to undergo more significant structural modifications.

## REFERENCES

- [1] T. Uchino, A. Aboshi, S. Kohara, Y. Ohishi, M. Sakashita, K. Aoki Phys. Rev. B 69, 155409 (2004).
- [2] A. Stesmans, K. Clémer, and V. V. Afanas'ev, Phys. Rev. B 72, 155335 (2005).
- [3] A. Stesmans, K. Clémer, and V. V. Afanas'ev, Phys. Rev. B 77, 094130 (2008).
- [4] Evonik industries online catalog, 2010.
- [5] A. Roder, W. Kob, K. Binder, J. Chem. Phys. 114, 7602 (2001).
- [6] I. V. Schweigert, K. E. J. Lehtinen, , M. J. Carrier, Zachariah, Phys. Rev. B 65, 235410 (2002).
- [7] G. Vaccaro, G. Buscarino, S. Agnello, S. Sporea, C. Oproiu, D.G. Sporea, F.M. Gelardi, J. Phys. Chem C 116, 144, 2012.
- [8] Hehlen, B. J. Phys.: Condens. Matter 22, 025401 (2010).

# Structural and Non-Linear Optical Analyses of Various Thermally Poled Silicate Glasses

T. Crémoux\*, M. Dussauze\*, V. Rodriguez\*, E. Fargin\*\*, T. Cardinal\*\*

\*ISM, UMR 5803 CNRS, Université Bordeaux,  
351 cours de la libération, Talence, F- 33405, France

\*\*ICMBC, CNRS, Université de Bordeaux,  
87 av. Dr. A. Schweitzer, Pessac F-33608, France

## ABSTRACT

Polarized glasses are of great interest for various applications such as photonic or biomaterials.

Thermal polarization treatments permit to entrap a strong and stable electric field right below the anodic surface of a glass slice. This internal electric field is a consequence of a space charge layer induced within a cationic depletion layer. The main parameter influencing the poling mechanisms is the glass composition notably the ionic entities concentrations. According to the glass nature, the space charge thickness and the second harmonic generation (SHG) response can differ. In this context, we have investigated the polarization of different kind of silicate glasses such as bio-glass, soda lime glass, borosilicate glass and SiO<sub>2</sub> glasses.

By coupling vibrational spectroscopy and Second Harmonic Generation techniques, we have characterized the poling effects on silicate networks and linked these structural rearrangements to the non-linear optical (NLO) response. These results contribute to a better understanding of the poling mechanisms and their influences on the NLO properties regarding glass compositions which is necessary to progress towards possible applications.

In this two-page papers for the 2012 SiO<sub>2</sub> Symposium the example of a soda lime glass polarized during 30 minutes will be developed.

**PACS Keywords:** thermal poling, soda lime, borosilicate, SiO<sub>2</sub>, glass, SHG, Raman, IR

## 1 EXPERIMENTAL DETAILS

**Thermal polarization treatments** consisted to heat a commercial soda lime sample at a poling temperature of 216°C and then to apply a voltage of 1 kV during 30 minutes in air. Unpolished doped silicon wafers were used as electrodes. [1] [2]

**Infrared transmission and reflexion** analysis were done using a commercial Thermo Scientific spectrometer (Nicolet 6700 FT-IR).

**Micro-Raman spectroscopy** coupled at **micro-SHG measurements** have been performed along the glass cross section with a modified micro-Raman HR800

(Horiba/JobinYvon). The instrument have been equipped with two different laser sources: a Nd:YAG pico-laser at 1064nm for SHG measurements and a CW laser at 532nm for Raman analyses. Polarized samples have been cut in two parts and the glass cross section was analyzed. Raman spectra from 200 to 4000 cm<sup>-1</sup> were recorded every 0.5 μm from the anode surface toward the inside of glass at regular intervals to form a Raman mapping of the poled zone. The same area was analyzed by micro-SHG spectroscopy to localize the implemented induced electric field. Other details on this setup are available elsewhere. [3]

## 2 RESULTS AND DISCUSSION

### 2.1 Infrared Analysis

**Infrared transmission and Reflexion** spectra are presented in the following figure:

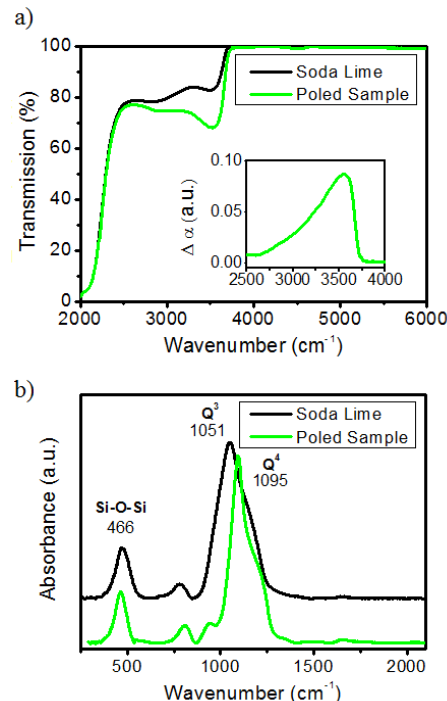


Figure 1: Infrared transmission a) and reflexion b) spectra of initial and poled soda lime glass.

Infrared transmission spectra (Fig1 a) show a difference between soda lime glass before and after thermal poling treatment, with an increase of absorption around  $3500\text{ cm}^{-1}$  attributed to OH groups.

These data denote the injection of hydroxyl groups in the glass induced by the poling treatment. [1]

Infrared reflexion spectra (Fig1 b) present some spectral variations. Before poling the maximum band is around  $1050\text{ cm}^{-1}$  and characteristic of  $\text{Q}^3$  entities.  $\text{Q}^n$  entities give information about the polymerization of silicate network where  $n$  is the number of oxygen bridge ( $\text{Si}-\text{O}-\text{Si}$ ). After poling this band decreases (poled spectrum in green on fig 1 b). The poled sample spectrum presents a peak maximum at  $1095\text{ cm}^{-1}$  characteristic of  $\text{Q}^4$  entities.

The large decrease of  $\text{Q}^3$  entities band after poling treatment to favor the apparition of  $\text{Q}^4$  entities peak shows a densification of the silicate network at the anode surface. [1] [4]

## 2.2 Micro-Raman and Micro-SHG coupling analysis

**Micro-Raman spectroscopy** coupled at **micro-SHG measurements** have been performed along the glass cross section and results are presented on the following figure:

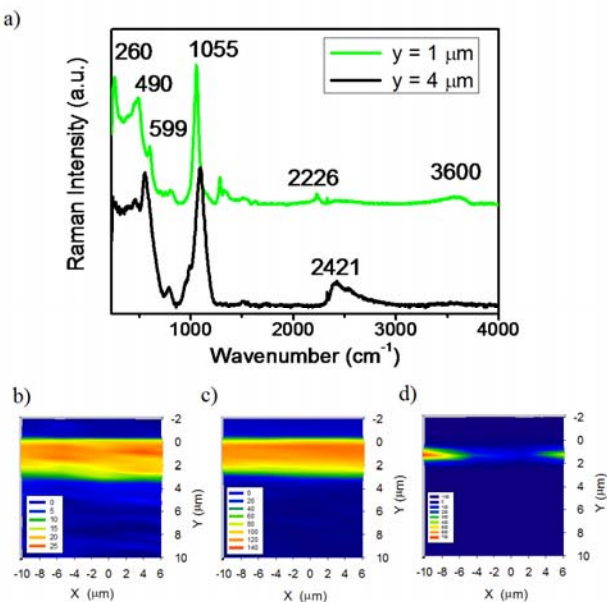


Figure 2: (a) Micro-Raman spectra of soda lime poled cross section. (b) Raman mapping of OH groups. (c) Raman mapping Si-O-Si vibrations. (d) SHG map. ( $y = 0$  correspond to anode glass surface and positive values of  $y$  go toward cathode side)

Micro-Raman analyses of polarized glass cross-section show 2 different kinds of spectra (Fig2 a). The spectrum at  $4\text{ }\mu\text{m}$  under anode surface corresponds to Raman spectrum of un-poled soda lime glass. Changes due to poling

treatment are visible on the first 3 microns under the anode surface. Let's focus on 2 specific changes on the spectrum at  $1\text{ }\mu\text{m}$ : the growth of a new band around  $3600\text{cm}^{-1}$  attributed to hydroxyl groups (OH) and the variation of the band around  $490\text{cm}^{-1}$  due to mixed bending and stretching vibration modes of Si-O-Si bridges. Raman map have been realized for each band (Fig2 b and c). Both OH and Si-O-Si bridges Raman modes have been localized on the same 3 microns thick layer. [1]

Moreover, the localization of the SHG signal shows a spatial correlation between the non-linear optical activity and the structural modifications of glass on the first 3 microns (Fig2 b, c and d). [1] [2] [4]

## CONCLUSION

A clear spatial correlation between SHG activity and structural rearrangements has been measured. The spectral variations observed in both IR and Raman permitted to point out two mechanisms which compensate the depletion of cations:

- (i) The injection of hydroxyl entities (OH) from air toward glass.
- (ii) The condensation of silicate network.

## REFERENCES

- [1] M. Dussauze, V. Rodriguez and al., "How Does Thermal Poling Affect the Structure of Soda-Lime Glass?", Journal of Physical Chemistry C, 114, 12754-12759, 2010.
- [2] H. An and S. Felming, "Second-order optical nonlinearity and accompanying near-surface structural modifications in thermally poled soda-lime silicate glasses", Journal of the Optical Society of America B, 23, 2303-2309, 2006.
- [3] Rodriguez, "Hyper-Raman macro- and micro-spectroscopy in materials: Towards high quality signals and good spatial resolution", Chemical Physics Letters 431, 190-194, 2006.
- [4] D. Möncke, M. Dussauze and al, "Thermal poling induced structural changes in sodium borosilicate glasses"; Physics and Chemistry of Glasses: European Journal of Glass Science and Technology Part B, 50, 229-235, 2009.

# Session 6

Radiation effects - Rare earth



# Gamma rays radiation effects on SiO<sub>2</sub>-Al<sub>2</sub>O<sub>3</sub>-P<sub>2</sub>O<sub>5</sub> doped Yb<sup>3+</sup> optical fiber preforms: effect of the Al/P dopants

T. Deschamps<sup>1</sup>, N. Ollier<sup>1</sup>, C. Gonnet<sup>2</sup>

<sup>1</sup>Laboratoire des Solides Irradiés, UMR 7642 CEA-CNRS-Ecole Polytechnique, 91128 Palaiseau, France

<sup>2</sup>Draka Comteq France, site data 4, route de Nozay, 91460 Marcoussis, France

## ABSTRACT

In this study, the optical properties of ytterbium doped silica glass fiber preforms codoped with aluminum and phosphorous are characterized by photoluminescence and absorption spectroscopy. We show that these properties are directly linked to the Al/P ratio in agreement with our previous structural study in [1]. The behaviour of these fibers after gamma rays radiation is also addressed. The influence of the ratio Al/P is still predominant. The absorption spectra reveal that when phosphorous is introduced in excess compared to aluminum, the creation of colored centers under  $\gamma$ -irradiation is largely reduced. Electronic paramagnetic resonance spectroscopy at low temperature shows that no reduction processes of Yb<sup>3+</sup> species into Yb<sup>2+</sup> species appears after  $\gamma$ -irradiation.

**PACS Keywords:** optical fibers, radiation effects, gamma rays, absorption spectroscopy, photoluminescence.

## 1 INTRODUCTION

High power laser fibers doped with ytterbium ions operating at wavelengths around 1 micron have important interest for many technological applications like material processing, optical telecommunication, amplification or biomedical applications. Such fibers are also particularly adapted for inter-satellite communication, but space environment is radiative. Ionizing radiations induce point defects responsible for an increase of the absorption in a large wavelengths range from UV to IR, which degrade the fibers performance [2]. In this study, we characterize the gamma radiation-induced changes in a set of fiber preforms with different Al, P and Yb<sup>3+</sup> contents using optical absorption, photoluminescence and continuous wave electronic paramagnetic resonance (cw-EPR) spectroscopy.

## 2 EXPERIMENTAL

### 2.1 Samples preparation and composition

Fiber preforms have been synthesised by Draka Comteq Company, using the MCVD (Modified Chemical Vapor Deposition) standard technique. A gas mixture of dioxygen, silicon tetrachloride and phosphorous

trichloride is passed through a rotating pure silica glass tube which is simultaneously heated with a flame. High porosity soot is formed in the inner surface of the glass tube. Rare-earth ions are then incorporated in an aluminium liquid solution and impregnate the porous phase. A series of seven samples with different Al and P contents have been synthesised. The average composition of the core of the fiber preforms has been determined by quantitative chemical analyses using Castaing's microprobe spectroscopy. Each core composition is displayed in the table 1.

preforms	Al	P	Yb	Al/P
A	2.46	0.90	0.08	2.7
B	2.44	1.21	0.09	2.0
C	2.58	1.85	0.07	1.4
D	2.42	1.97	0.07	1.2
E	2.25	2.27	0.08	1.0
F	1.60	2.88	0.07	0.6
G	0.72	2.71	0.09	0.3

Table 1: Molar contents of Al, P and Yb in the core of the different fiber preforms.

### 2.2 Gamma rays radiation experiment and spectroscopic techniques

All the samples have been exposed to <sup>60</sup>Co  $\gamma$ -radiation using an armored cell at CEA Saclay (DSM, SIS2M). The irradiation was performed at a dose-rate of 6.0 Gy.min<sup>-1</sup> during 5 hours, implying a cumulated dose of 1800 Gy, which corresponds to the typical accumulated dose for a 10 years mission in a space environment.

The samples used for the optical spectroscopic characterization are double-face polished (up to an optical grade) thin disks of preform of roughly 2.5 mm diameter and 1 mm thickness. Photoluminescence has been performed using a Jobin Yvon Horiba spectrofluorimeter.

The cw-EPR spectra have been recorded before and after  $\gamma$ -irradiations at 20 K using an X-band EPR-Brüker spectrometer operating at 9.493 GHz, at magnetic field from 0 to 450 mT. The samples used for this experiment were cylinders of 2.5 mm diameter and 3.8 mm height.

### 3 RESULTS

#### 3.1 Optical properties

The table 2 recapitulates the different optical properties (absorption, emission and lifetime) of the  $\text{Yb}^{3+}$  ions in the different samples.

	A	B	C	D	E	F	G
max absorption (nm)	977.5	977.6	977.6	977.6	975.7	975.8	975.8
max emission (nm)	977.5	977.8	--	977.2	--	975.5	975.0
lifetime (ms)	0.90	0.90	0.90	0.97	--	1.31	1.50

Table 2: Optical properties of the seven fiber preforms.

The optical properties of  $\text{Yb}^{3+}$  depends on the excess of phosphorous or aluminum in the glass matrix. These results well confirm our previous pulse EPR study [1] showing two different local environments of  $\text{Yb}^{3+}$  depending on the Al/P ratio.

#### 3.2 $\gamma$ -irradiation effects

The figure 1 displays the A, D and G fiber preforms before and after the gamma irradiation experiment.

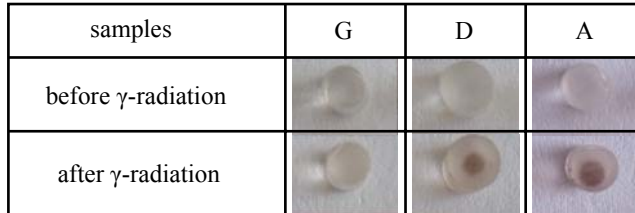


Figure 1: Picture of 3 preforms before and after  $\gamma$ -radiation.

The preform G, with  $P > Al$ , show almost no coloration. The preform D, with  $Al/P \approx 1.2$ , displays a slight coloration. The preform A in which Al is largely introduced in excess compared to P, present an important coloration of its core after irradiation.

This phenomenon is well confirmed by optical absorption measurements. The figure 2 displays the increase of absorption bands in the visible and IR wavelength range with the increase of the Al/P ratio for the  $\gamma$ -irradiated samples.

Using quantitative EPR measurements, we have also shown that the  $\text{Yb}^{3+}$  paramagnetic signal have the same shape and intensity before and after irradiation. This means that the local environment of the rare-earth ions is not modified by  $\gamma$ -irradiation and no reduction processes take place.

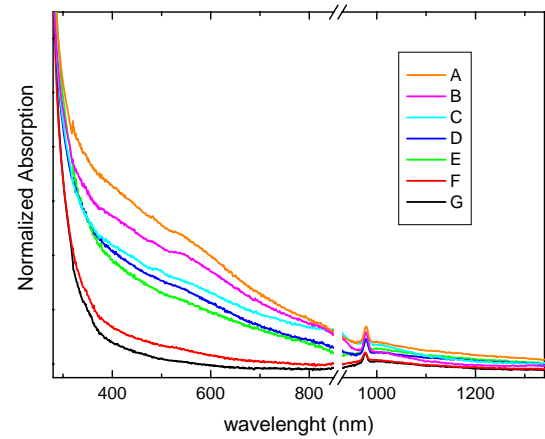


Figure 2: Absorption spectra of the seven samples from 280 to 1340 nm. The break between 850 nm and 930 nm is due to the change of the lamp which deforms the signal.

### 4 DISCUSSION

Many previous experiments using optical absorption, EPR, radiation induced absorption (RIA) or micro-photoluminescence has been performed in order to investigate the effects of different types of irradiation on rare-earth doped fibers [2-4]. However, to our knowledge, we demonstrate for the first time that the Al/P ratio is the parameter which determines the level of radio-darkening in post-irradiated fibers. The colored centers created by gamma rays seem to be the same as the ones created by IR intense irradiation (photodarkening) [4]. This point will be discussed in terms of  $\text{Yb}^{3+}$  clusters and cooperative processes. The nature of the point defects responsible of the coloration will be also addressed.

### REFERENCES

- [1] T. Deschamps, N. Ollier, H. Vezin and C. Gonnet, "Clusters dissolution of  $\text{Yb}^{3+}$  in codoped  $\text{SiO}_2\text{-Al}_2\text{O}_3\text{-P}_2\text{O}_5$  glass fibers and its relevance to photodarkening," *J. Chem. Phys.*, 136, 014503, 2012.
- [2] B. Tortech *et al.*, *J. Non-Cryst. Solids*, 355, 1085, 2009.
- [3] S. Girard *et al.*, *IEEE Trans. Nucl. Sci.*, 54, 2426, 2007.
- [4] I. Manek-Hönninger *et al.*, *Opt. Express*, 15, 1606, 2007.

# Optimum design of radiation-hardened and high power Er<sup>3+</sup>-Yb<sup>3+</sup>-codoped fiber amplifiers by means of particle swarm approach

L. Mescia\*, S. Girard\*\*, G. Fornarelli\*, A. Giaquinto\*, F. Prudenzano\*, M. De Sario\*, A. Boukenter\*\*\*,  
Y. Ouerdane\*\*\*

\*Dipartimento di Elettrotecnica ed Elettronica, Politecnico di Bari

Via E. Orabona 4, 70125 Bari, Italy

\*\* CEA, DAM, DIF

F91297 Arpajon France

\*\*\* Laboratoire Hubert Curien, University of Saint-Etienne

UMR CNRS 5516, F42000 Saint-Etienne, France.

## ABSTRACT

In this paper, the design of a rare earth-doped cladding-pumped fiber amplifiers is carried out by means of a home-made computer code based on particle swarm optimization (PSO) and rate equation model. In particular, taking into account experimental results, a full investigation of radiation-hardened double-cladding Er<sup>3+</sup>-Yb<sup>3+</sup>-doped fiber amplifiers (EYDFAs) has been performed. A detailed rate equation model including the first and secondary energy transfer between Yb<sup>3+</sup> and Er<sup>3+</sup>, the presence of Er<sup>3+</sup> and Yb<sup>3+</sup> clusters, the amplified spontaneous emission (ASE) and the most relevant Er<sup>3+</sup> upconversion and cross relaxation mechanism is considered. The obtained results highlight that the developed PSO algorithm is an efficient and reliable tool for performing the optimum design of radiation-hardened and high-power EYDFAs.

**PACS Keywords:** particle swarm optimization, radiation effects, optical fiber amplifier, cladding-pumped, rare earth.

## 1 INTRODUCTION

Rare earth-doped fiber amplifiers and lasers are key elements in applications requiring compact, high beam quality, and rugged optical sources, consistent with the optical components used in communication systems. Thanks to the progress of booster amplifiers for long haul repeaterless optical links, great effort has been devoted to the development of high-power fiber amplifiers. In particular, during the last years, many research activities have been dedicated to the development of high-power Er<sup>3+</sup>-doped fiber amplifiers (EDFAs) in space applications [1-3]. In general, such devices suffer of gain-saturation problems and, as a consequence, the co-doping with ytterbium Yb<sup>3+</sup> ions is an efficient way to overcome this drawback. Moreover, the evaluation of their vulnerability to the harsh environment is a crucial point to consider in order to estimate the impact of an ionizing radiation on the amplifier performance. To this aim, accurate theoretical and

numerical models for design and analysis purposes are very useful tools to choose the pumping scheme, the geometric and physical parameters of the optical fiber, the rare earth concentration, the operative parameters allowing a control of the radiation effects on the fiber amplifiers. Generally, the knowledge of several spectroscopic and fiber parameters is required to perform an accurate analysis. As a consequence, tremendous efforts have to be made to obtain the most efficient design because all parameters affecting the fiber amplifier performance must be optimized. For this reason, the use of a particular global optimization method is welcomed to find the global best solution. In recent years, well performing and effective approaches using a genetic algorithm (GA) and a neural network have been proposed to solve optimization and characterization problems of rare earth-doped fiber amplifiers [4-6]. However, by taking into account the advantages offered by particle swarm optimizer (PSO), a more robust and reliable optimization algorithm can be developed. Starting from these considerations, in this paper, we present a comprehensive numerical model based on PSO and rate equations analysis allowing a detailed investigation of radiation-hardened double-cladding EYDFAs. In order to test the capability of the developed numerical code, the maximization of the power conversion efficiency (PCE) has been carried out in a large variety of EYDFAs configurations before, during and after the irradiation.

## 2 THEORY AND NUMERICAL RESULTS

The software written for the fiber amplifier simulation is based on the resolution of the nonlinear differential equation system constituted by Er<sup>3+</sup>/Yb<sup>3+</sup> multilevel rate equations, the propagation equations of the pump, signal and both forward and backward ASE powers along the propagation direction of the optical fiber.

In the conventional approach, the solution of the rate and power propagation equations is carried out via shooting and relaxation methods, but the nonlinearity of the differential equations makes these algorithms time

consuming, especially if the optimal values of many parameters have to be evaluated. Global optimization methods can be used to face this problem and, in particular, PSO algorithm has been employed. In fact, by using the social behavior of a swarm of bees during their food-searching activities, PSO can be successfully used to perform the optimum design of EYDFAs.

The design procedure has been articulated in four steps. In the first one, the electromagnetic analysis is performed in order to calculate the electromagnetic field profiles. To this aim, the wave equation of electric field was solved by means of a full-vector finite element method (FEM). The calculated transverse electric field profile has been used to evaluate its overlapping with the doped core at the signal wavelength. In the second step, the spectroscopic analysis has been performed. More precisely, by considering the measured spectral attenuation around the pump and signal wavelength and for different radiation doses, the erbium and ytterbium absorption cross sections have been calculated according to the McCumber theory. In the third step, the developed PSO algorithm has been applied to solve the characterization problem, in which the lifetime of the ytterbium metastable level and the erbium excited pump level, the first and secondary ytterbium to erbium energy transfer coefficients, and the upconversion coefficients of the erbium metastable level have been recovered to fit the experimentally measured signal output power for different input pump current. In the fourth step, the PSO has been employed in the optimization of the design to obtain values of parameters maximizing special amplifier characteristics. A figure of merit for power amplifiers is the power conversion efficiency (PCE). It quantifies the ability of the amplifier in converting pump photons into amplified signal photons. So we considered the function describing the PCE as the fitness function; the fiber length, the input pump and signal power, the pumping scheme as the parameters to be optimized.

The considered fiber is a prototype developed by Ixfiber [7]. It consists of octagonal double-cladding fiber having an Er<sup>3+</sup>/Yb<sup>3+</sup> doped phosphosilicate core. The PSO numerical code has been evaluated by 20 independent runnings and the obtained best solution is reported in the Figure 1 by varying the fiber radius and pumping configuration. For all the pumping configurations, an improvement of about 40% in the optimum PCE is obtained by changing the fiber length from 1.5 to 3.5 m. By numerical investigation, it can be observed that the backward and bidirectional pumping schemes are more efficient than the forward one.

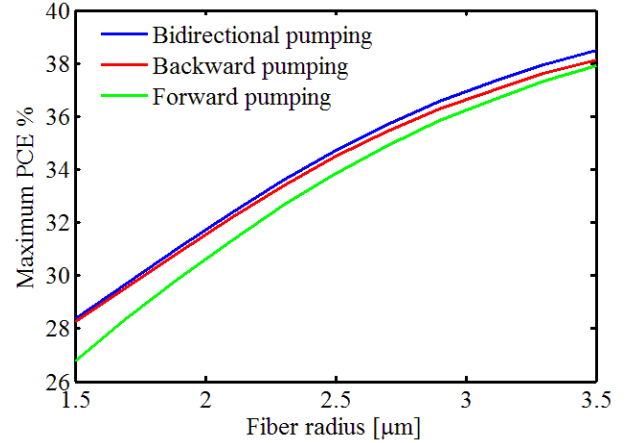


Figure 1: Maximum PCE versus the fiber radius for forward, backward and bidirectional pumping scheme.

## REFERENCES

- [1] E. Rochat, R. Dändliker, K. Haroud, R. H. Czichy, U. Roth, D. Costantini, R. Holzner, "Fiber amplifiers for coherent space communication," IEEE J. Sel. Top. Quantum Electron., 7, 64–81, 2001.
- [2] M. W. Wright, G. C. Valley, "Yb-doped fiber amplifier for deep-space optical communications," J. Lightwave Technol., 23, 1369–1374, 2005.
- [3] V.W.S. Chan, "Optical space communications," IEEE J. Sel. Top. Quantum Electron., 6, 959-975, 2000.
- [4] G. Fornarelli, L. Mescia, F. Prudenzano, M. De Sario, F. Vacca, "A neural network model of erbium-doped photonic crystal fibre amplifiers," J. Optics & Laser Technol., 41, 580-585, 2009.
- [5] L. Mescia, G. Fornarelli, D. Magarielli, F. Prudenzano, M. De Sario, F. Vacca, "Refinement and design of rare earth doped photonic crystal fibre amplifier using an ANN approach," J. Optics & Laser Technol., 43, 1096-1103, 2011.
- [6] F. Prudenzano, L. Mescia, A. D'Orazio, M. De Sario, V. Petruzzelli, A. Chiasera, M. Ferrari, "Optimization and characterization of rare earth doped photonic crystal fiber amplifier using genetic algorithm," J. Lightwave Technol., 25, 2135-2142, 2007.
- [7] S. Girard, M. Vivona, A. Laurent, B. Cadier, C. Marcandella, T. Robin, E. Pinsard, A. Boukenter, Y. Ouerdane, "Radiation hardening techniques for Er/Yb doped optical fibers and amplifiers for space application," Opt. Express, 20, 8457-8465, 2012.

# Radiation responses of Yb/Er-doped phosphosilicate optical fibers: hardening mechanisms related to Ce-codoping

M. Vivona <sup>\*, \*\*, \*\*\*</sup>, S. Girard <sup>\*\*\*\*</sup>, C. Marcandella <sup>\*\*\*\*</sup>, E. Pinsard <sup>\*\*</sup>, A. Laurent <sup>\*\*</sup>, T. Robin <sup>\*\*</sup>, B. Cadier <sup>\*\*</sup>, M. Cannas <sup>\*\*\*</sup>, A. Boukenter <sup>\*</sup>, Y. Ouerdane <sup>\*</sup>

<sup>\*</sup> Laboratoire Hubert Curien, UMR CNRS 5516, Université St-Etienne, F-42000 St-Etienne, France

marilena.vivona@univ-st-etienne.fr

<sup>\*\*</sup>iXFiber, Rue Paul Sabatier, F-22300 Lannion, France

<sup>\*\*\*</sup>Dipartimento di Fisica, I-90123 Università di Palermo, Italy

<sup>\*\*\*\*</sup>CEA DIF Bruyères-le-Châtel, F-91297 Arpajon Cedex, France

## ABSTRACT

In this paper, we investigated the origins of the Ce positive influence on the radiation response of Yb/Er-doped phosphosilicate optical fibers. To this purpose, we carried out during  $\gamma$ -irradiations an online characterization on active optical fiber prototypes, made with different Ce concentrations and integrated in optical amplifiers. The hardening effect of Ce-codoping is highlighted, as well as some aspects related to the radiation response of the phosphosilicate host glass of the active optical fibers.

*PACS Keywords:* Rare-Earth Elements, Optical Amplifiers, Radiation Effects.

## 1 INTRODUCTION

Nowadays, Rare-Earth (RE)-doped optical glasses and fibers are used in many technological applications, as active medium of fiber lasers and optical amplifiers. The RE-doping guarantees high laser performance for these “active” devices, but their use in harsh environments is still a stake. As matter of fact, the RE-doped optical fiber was identified as the most sensitive component to radiations of fiber gyroscopes, lasers, amplifiers. The laser performance and the amplifier gain are decreased as the result of radiation induced modifications in the RE-ions properties and/or in the point defect concentrations within the glass matrix of the RE-doped fiber. In order to limit its vulnerability to radiations, several studies have been devoted to harden the fiber itself. On the basis of phenomenological studies, most authors propose chemical composition modifications (such as Ce-codoping) [1] or post-manufacturing treatments (such as H<sub>2</sub>-loading) [2]. So far, it is not attained a thorough understanding of the origin of the output signal degradation and the action of the hardening process.

This work focuses on active optical fibers with a phosphosilicate core matrix co-doped with Yb/Er and differing in their Ce concentrations. These optical fibers

have been used to design prototype amplifiers (operating at 1.5  $\mu\text{m}$ - Er<sup>3+</sup>-emission). A real-time analysis of these samples, to predict the tolerance/sensitivity at the time of employment, consists in the characterization under  $\gamma$ -ray radiation of the amplifier (with pumping at 915 nm of RE-ions during the test). In addition, we performed a study on passive fibers (without pumped RE-ions) to characterize the radiation induced attenuation (RIA) spectral dependence and evaluate the contribution of the glass matrix to the fiber or amplifier degradation. In the final paper, additional spectroscopic techniques (micro-Raman and photoluminescence measurements) will be carried out to complete our study.

## 2 EXPERIMENTAL PROCEDURES

The investigated optical fibers have been manufactured by a modified chemical vapor deposition process and have been provided by iXFiber SAS. Three optical fibers, named I(PYbEr), J(PYbErCeHigh) and M(PYbErCeLow), with the same double-clad (DC) octagonal geometry, have been elaborated *ad hoc* to take out the role of the Ce. The fiber cores have been doped with P (~12 wt. %) and RE-elements (Yb, Ce and Er) by a solution technique. These samples only differ in the amount of Ce in their cores: Ce is absent in the fiber I(PYbEr) (standard active fiber), whereas its concentration is 0.1wt. % in fiber M(PYbErCeLow) and 0.6 wt. % in fiber J(PYbErCeHigh). Two DC-optical fibers, L(PCeHigh) and N(P), have also been analyzed to assess the glass matrix behavior, without presence of active Yb and Er ions. Chemical core compositions are reported in Tab. 1.

Sample	P (wt. %)	Yb (wt. %)	Er (wt. %)	Ce (wt. %)
I	12.2	1.4	0.07	-
J	12.1	1.5	0.07	0.6
M	11.5	1.5	0.07	0.1
L	10.4	-	-	0.6
N	8	-	-	-

Table 1: Core chemical compositions of the tested fibers.

For the active testing with the amplifier configuration (in counter-pumping scheme), the RE-doped optical fibers I(PYbEr), M(PYbErCeLow) and J(PYbErCeHigh) of 12 m-length are integrated in optical amplifiers (A#1, A#2 and A#3, respectively) and exposed to  $\gamma$ -ray radiation (low dose rate of  $\sim$ 3mGy /s, up to a total dose of  $\sim$ 650 Gy for fiber J(PYbErCeHigh)). The signal- and pump-wavelengths (1550 and 915 nm) are supplied by laser diode sources and propagate in the core and in the inner cladding of the fiber, respectively. The transmitted and amplified signal is acquired by a power-meter (PWM). Two types of RIA measurements are carried out on the L and N optical fibers. In the near infrared (NIR) spectral range (from 1000 to 1650 nm), induced losses measurements are realized with a halogen light source and a CCD spectrometer, while for the pump-wavelength at 915 nm, we employed the same laser diode source and PWM used in the active test. The complementary spectroscopic measurements, highlighting the optical modifications occurred in the samples, will be presented at the conference.

### 3 RESULTS AND DISCUSSION

In Figure 1, we show the laser output power at 1550 nm for the three tested amplifiers as function of the dose. The performance of amplifiers monotonically follows the Ce-content: comparing the curves at 400 Gy, the output power decreases of 75% in the standard amplifier A#1 made with the Ce-free fiber I(PYbEr), 60% in A#2, whereas the hardening effect of Ce-codoping is exploited in the amplifier A#3 based on fiber J(PYbErCeHigh), with a degradation of 15% up to the investigated dose of 650 Gy.

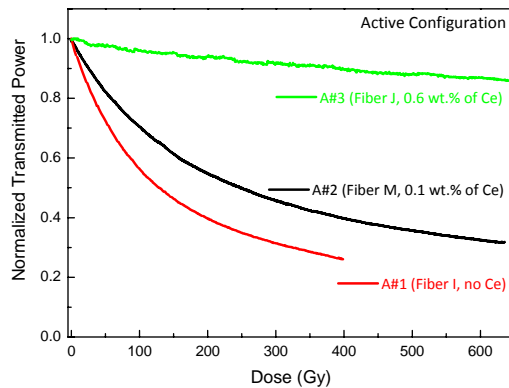


Figure 1: Evolution of the amplifier output power as a function of the  $\gamma$ -irradiation dose for the tested amplifiers.

To improve our knowledge of the matrix degradation processes, we have studied the RIA for the two structurally equivalent fibers, L(PCeHigh) and N(P). The RIA curves, detected by the PWM and related to pump-wavelength at 915 nm, are reported in Fig. 2, while Fig. 3 illustrates the RIA in the spectral range from 1000 to 1650 nm, detected by the CCD spectrometer.

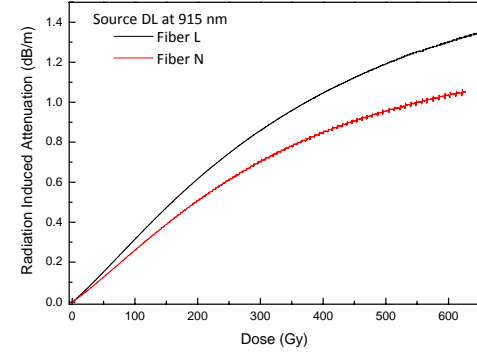


Figure 2: RIA at the 915nm pump power transmission for the fibers L(PCeHigh) and N(P).

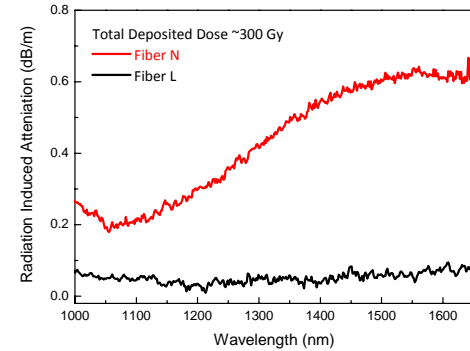


Figure 3: RIA for fibers the N(P) and L(PCeHigh) in the NIR range. Fiber N(P) shows the typical P<sub>1</sub>-defect absorption profile.

We underline that the RIA related to the pump-transmission (Fig.2) consists at least in two contributions: since the pump-signal propagates mainly in the double cladd, but also it interacts with the core glass, both these fiber-sections can be involved in the degradation mechanisms. The attenuation is strong for the N(P) and L(PCeHigh) fibers, with a slight difference of behavior probably depending on the P-content (higher in Fiber L).

Differently, for the radiation induced absorption in the NIR region, the used experimental setup assures that the source signal propagates in the fiber core, similarly with the active testing. It is known that the presence of P entails the P<sub>1</sub>-formation defects under radiation, characterized by an absorbing band around 1.6  $\mu$ m. [3]. Therefore, Ce interacts with P<sub>1</sub> sites and/or its precursors, leading to the performance improvement of the Ce-doped optical fibers.

### REFERENCES

- [1] M. Engholm *et al.*, Opt. Letters, 34, 1285-1287, 2009.
- [2] K. V. Zotov *et al.*, Quantum Electron., 37, 946-949, 2007.
- [3] E. Regnier, *et al.*, IEEE T. Nucl. Sci, 54, 1115-1119, 2007.

# Growth of rare-earth doped oxyde nanoparticles in silica fibers

Valérie Mauroy\*, Wilfried Blanc\*, Michèle Ude\*, Stanislaw Trzesien\*, Bernard Dussardier\*

\*Université Nice-Sophia Antipolis, LPMC CNRS UMR7336 Parc Valrose, 06180 Nice Cedex 2

## ABSTRACT

Rare earth (RE) doped silica-based optical fibers with transparent glass ceramic (TGC) core was fabricated through the well-known modified chemical vapor deposition (MCVD) process without going through the commonly used stage of post-ceramming. The main characteristics of the RE-doped oxyde nanoparticles, their density and mean diameter in the fibers are dictated by various parameters discussed during this presentation. Low scattering losses induced by nano-scale particles and alteration of the spectroscopic properties of the erbium ions were observed. These initial studies should be useful in incorporating new doped materials in order to realize active optical fibers for constructing lasers and amplifiers.

**PACS Keywords:** silica, nanoparticles, erbium, alkaline earth.

## 1 INTRODUCTION

Developing of new rare-earth (RE)-doped optical fibers for power amplifiers and lasers requires continuous improvements in the fiber's spectroscopic properties (like gain and efficiency characteristics, resistance to spectral hole burning and photodarkening,...) besides reduction in device size and economical efficiency. Silica glass as a host material for fibers has proved to be very attractive. However some potential applications of RE-doped fibers suffer from limitations in terms of spectroscopic properties resulting from clustering or inappropriate local environment when doped into silica.

The route of interest here consists of using silica as a mechanical host and support of the fiber optical waveguide, and of embedding RE-ions within oxide nanoparticles of composition and structure different from those of silica, and small enough to induce acceptable scattering loss. We have proposed a straightforward technique allowing to embed RE ions within *in-situ* grown oxide nanoparticles in silica-based preforms [1]. The implemented principle is the spontaneous phase separation process. Two key advantages of this process are that (i) nanoparticles are grown *in-situ* during the course of the fabrication process and (ii) there is no need (and associated risks) of nanoparticles manipulation by an operator. Further, the process takes advantage of the high compositional control and purity typical of the MCVD technique.

In the present paper, we report on the growth of erbium-doped MO-silicate nanoparticles, that are stable after the fiber drawing stage using the MCVD and solution doping techniques. This demonstrates the potentiality of this fabrication technique for applications such as fiber amplifiers.

## 2 EXPERIMENTAL DETAILS

Preforms were fabricated by the conventional MVCD technique. In this process, gaseous chlorides ( $\text{SiCl}_4$ ,  $\text{GeCl}_4$ ,  $\text{POCl}_3$ ) are passed through a rotating silica tube, heated by an external burner in translation along the tube. Due to the high temperature, chlorides oxidize, forming particles which deposit on the inner wall. This porous layer turns into a glassy layer when the burner passes over it (the tube external temperature is around 1500 °C). In the final stage, the tube is collapsed into a rod at a temperature higher than 1800°C. fibers were obtained by stretching preforms in a drawing tower at temperatures higher than 2000 °C under otherwise normal conditions. Opto-geometric properties of the perform (or fiber) are determined by adjusting the composition and number of layers. In our samples, phosphorous and germanium concentrations are ~0.5 mol% and 1 mol%, respectively.

Erbium and alkaline-earth ions were incorporated through the solution doping technique. An alcoholic solution (of desired strength of  $\text{ErCl}_3 \cdot 6\text{H}_2\text{O}$  or  $\text{MCl}_2 \cdot 6\text{H}_2\text{O}$ ) is soaked for two hours in the unsintered core layer. After removing the solution, the layer is dried and sintered. Erbium concentration is estimated through absorption spectra to be around 300 ppm. It is comparable with the concentration in standard Erbium-Doped Fiber Amplifier. Two alkaline-earth concentrations in the solution were prepared: 0.1 and 1 mol/l. The core diameter in the preforms was measured with a preform analyzer (York Technology P 101) to be 1 mm. It is about 8 μm in fibers.

## 3 NANOPARTICLES CHARACTERIZATIONS

Nanoparticles were characterized through scanning electron microscopy (SEM) in the backscattered electrons mode. Typical SEM picture from the exposed core section of cleaved fibers is shown on Fig. 1 (Mg concentration in the solution is 0.1 mol/l).

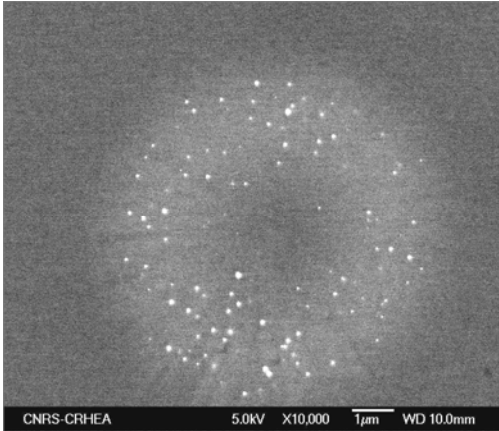


Figure 1: SEM picture of a Mg-doped fiber

The gray disk corresponds to the fiber core. Nanoparticles, visible as bright spots, are only observed when alkaline-earth ions (Mg, Ca or Sr) are added. They show an important compositional contrast compared to the silica background. The dark central part of the core is caused by the evaporation of germanium element; this is a common artifact of the MCVD technique that can be corrected through process optimization.

The statistical histograms of the size distribution of the NP for 0.1 mol/l Mg-doped preform and fiber are presented in Fig. 2. The mean particle size is 50 nm in the preform and 40 nm in the fiber. Those histograms show that the NP are preserved during the drawing step, in spite of the high temperature of this stage ( $\sim 2000$  °C). Moreover, the size distribution is slightly affected by this step : the mean size decreases from 50 nm down to 40 nm, in the preform and the fiber, respectively, while the core diameter is divided by 100.

When the Mg solution concentration increases from 0.1 to 1 mol/l, the mean particle diameter almost doubles to reach 80 nm. In this fiber, NPs up to 160 nm were observed. Ca and Sr incorporations lead also to particle with a mean diameter of 100 nm, even for a concentration in the solution of 0.1 mol/l.

Regarding light attenuation, fibers prepared with 0.1 mol/l of Mg are compatible with applications as losses as low as 0.4 dB/m were measured [2]. Other fibers, with 100-nm NP, lead to high attenuation level, above 100 dB/m.

Erbium spectroscopy is modified by the presence of the NP. Two behaviors are observed : in the case of low Mg concentration, Erbium spectroscopy is related to silica-based sample, while for high Mg concentration, Er spectroscopy is clearly related to phosphate environment [2].

During the presentation, we will discuss the influence of the MCVD parameters (alkaline-earth concentrations, deposit temperature, sintering temperature, collapsing stage) on the growth of NP in order to control their sizes. Relation with erbium spectroscopy will also be reported.

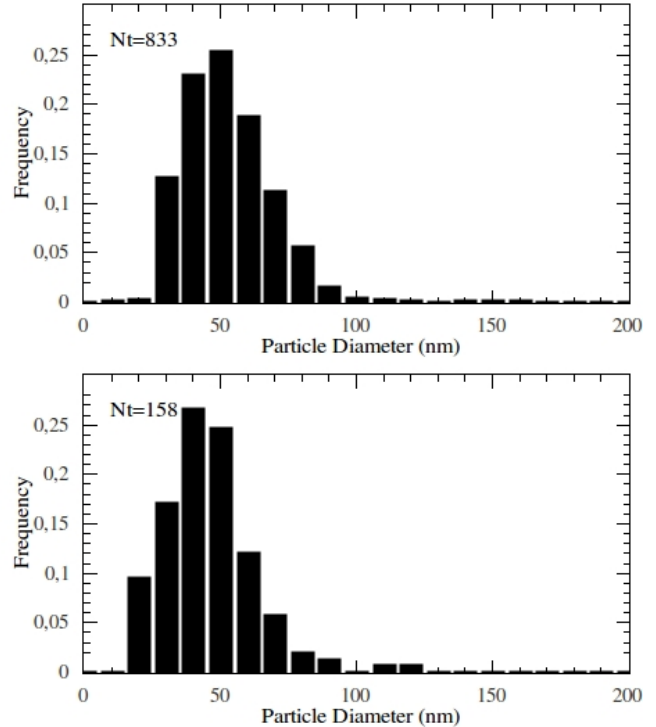


Figure 2: Histograms of the particle size in Mg-doped preform (top) and optical fiber (bottom).

## 4 CONCLUSION

A method to fabricate nanostructured  $\text{Er}^{3+}$ -doped fibers entirely through the MCVD process is demonstrated. By adding magnesium to the silica-based composition, nanoparticles of 40 nm in diameter are obtained through *in situ* growth without requiring a separate process to realize nanoparticles (such as post-process ceramming). Such fibers have low-loss. Moreover, a broadening of the emission spectrum by as much as almost 50% is observed with attractive features to realize gain flattened fiber amplifiers. More generally, this concept has great potentials as possible solutions to nowadays issues in amplifying fibers, including (but not limited to) amplifiers intrinsic gain flattening and/or spectral hole burning, amplifiers irradiation strengthening, photodarkening in fiber lasers, etc.

## REFERENCES

- [1] W. Blanc *et al.*, European Journal of Glass Science and Technology Part A, 50, 79-81, 2009.
- [2] W. Blanc *et al.*, Journal of the American Ceramic Society, 94, 2315-2318, 2011.

# Session 7

## Modeling



# First-principles study of electronic and optical properties of intrinsic defects in a-SiO<sub>2</sub>

Layla MARTIN-SAMOS<sup>\*,\*\*</sup>, Nicolas RICHARD<sup>\*\*\*</sup>, Sylvain GIRARD<sup>\*\*\*</sup>, Aziz BOUKENTER<sup>\*\*\*\*</sup>, Youcef OUERDANE<sup>\*\*\*\*</sup>, Jean-Pierre MEUNIER<sup>\*\*\*\*</sup>

<sup>\*</sup>CNR/IOM Democritos,  
c/o SISSA - via Bonomea, 265  
34136 - Trieste, Italy

<sup>\*\*</sup>University of Nova Gorica, Materials Research Laboratory,  
Vipavska 11C, 5270 Ajdovscina, Slovenia

<sup>\*\*\*</sup>CEA, DAM, DIF,  
F91297 Arpajon, France

<sup>\*\*\*\*</sup>Laboratoire Hubert Curien, Université Jean Monnet UMR CNRS 5516,  
Bâtiment F 18 Rue du Professeur Benoît Lauras  
F42000 Saint-Etienne, France

## ABSTRACT

We calculated the electronic and optical properties of intrinsic point defects in pure and doped amorphous silica by using the Many Body Perturbation Theory to the Density Functional Theory. These calculations allow us to analyze the chemical nature of the transition responsible for the defect optical absorption bands.

**PACS Keywords:** density functional theory, many body perturbation theory, silica, point defects, optical properties

## 1 INTRODUCTION

Amorphous silica is used in numerous applications. In Optical Fibers (OFs), it constitutes the core transmitting the light. In the near future, OFs will be installed massively in harsh environment of installations as ITER, the LMJ or the NIF. In silica, radiations produce point defects or activate pre-existing point defects, which could affect the transmission of the signal by generating new absorption and photo-luminescence bands. In this study, we propose to address the problem of the attribution of absorption bands to a defect structure by using the cutting-edge *ab initio* method. The methodology beyond our approach is presented in two papers [1,2]. In the following, we will expose our computational methodology in a first part, in a second part we will present the results obtained on the electronic structure and the optical properties. Finally, the last part will conclude our study and show in brief the subject that will be presented at the conference.

## 2 COMPUTATIONAL METHOD

Starting from a 108 atoms amorphous silica cell, i.e. 36 silicon atoms and 72 oxygen atoms (see [3] for details on the generation and the analysis of the properties of this amorphous cell), our study consists firstly in calculations in the framework of Density Functional Theory (DFT) in the Local Density Approximation (LDA) to obtain the structural and energy properties and their associated wavefunctions. For this part, we used here the Quantum ESPRESSO package [4]. For all configurations, atoms and cells have been relaxed. With this method, we generate one pure SiO<sub>2</sub> cell and pure and doped cells containing defects (see [5] for details). In every case, a statistical study on all the possible sites has been done, due to the non-equivalence of the atom site in an amorphous material [5]. The Self-Interaction (SI) of each calculated configurations will be evaluated at the DFT stage in order to get a qualitative measurement of the localization of each calculated bands in each configurations. The higher is the value of SI, the higher is the localization. For SI=1, the band is delocalized. In some cases, results are compared to equivalent cases in a 108 atoms  $\alpha$ -quartz SiO<sub>2</sub> cell to observe and understand the effect of disorder.

Starting from the DFT-LDA configurations (structures and wavefunctions), we performed Many Body Perturbation Theory (MBPT) calculations to the DFT with the SaX package [6]. We first introduce the GW approximation to correct the discrepancies on the evaluation of the band gap due to the DFT. Finally calculations solving the Bethe Salpether Equation (BSE) allow to get the optical properties of the configuration.

### 3 RESULTS

Here we will present only examples of results obtained on a pure silica cell containing the SiODC configuration with the lowest formation energy.

#### 3.1 Electronic properties

Using DFT-LDA, we get the structural and energy properties of the configurations. In Figure 1, the Density of States (DOS) and the corresponding SI are shown.

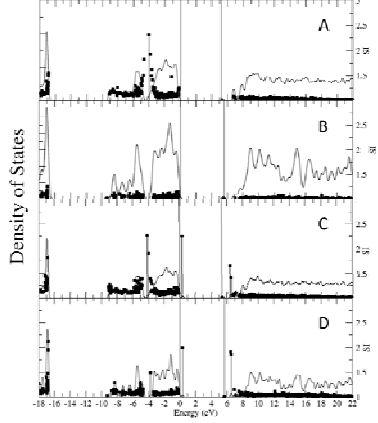


Figure 1: left scale: Density of states (—) in arbitrary units as a function of the energy (eV) obtained in DFT; right scale: Self Interaction (SI) ■ for each calculated band for (A) amorphous silica, (B)  $\alpha$ -quartz, (C) amorphous silica containing one SiODC(I), (D)  $\alpha$ -quartz containing one oxygen vacancy.

First, as it is well known, we observe in Figure 1 that DFT-LDA gives an underestimated value of the band gap: ~5.5 eV compared to ~9 eV experimentally (see for example [7]). Figure 1A and 1B show that disorder introduces the localization of some bands in the valence band. In Figure 1C and 1D, the presence of an oxygen vacancy induces three strongly localized levels in the DOS: one occupied level located in the band gap just above the top valence band and two quasi-degenerate unoccupied levels in the conduction band. The positions of levels are quite equivalent in a-SiO<sub>2</sub> and  $\alpha$ -quartz but the localization is stronger in the amorphous case.

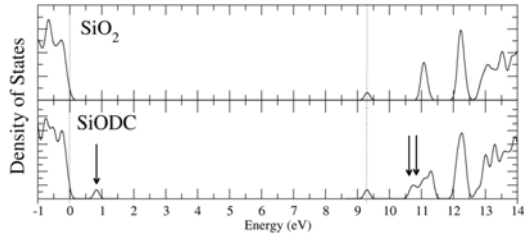


Figure 2: Density of states for (from top to bottom) a-SiO<sub>2</sub> and a-SiO<sub>2</sub> containing one SiODC. Arrows indicate the band due to the defect.

In Figure 2, the DOS calculated using the GW approximation is shown. The calculated value of the band gap is around 9.3 eV in excellent agreement with the experimental value. Positions of levels due to the ODC can then be analyzed with a good confidence.

#### 3.2 Optical Properties

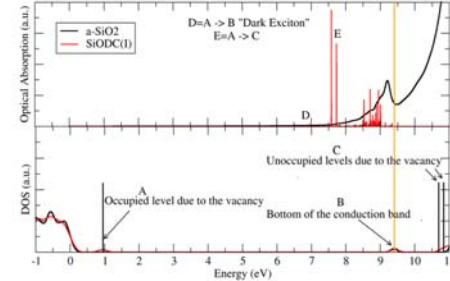


Figure 3: DOS and optical absorption, both in arbitrary units (a.u.) as a function of the energy (eV) for amorphous silica in black and amorphous silica containing one SiODC(I) (in red).

The solution of the BSE gives the optical absorption spectra of amorphous silica and amorphous silica containing one SiODC(I). The presence of a SiODC(I) induces the introduction of a two strong absorption band around 7.6 eV due to the transition between the occupied level due to the vacancy (A in Figure 3) and the two quasi-degenerate levels (C). This value is in good agreement with the experimental value [8]. A dark level with weak oscillator strength is also observed.

### 4 CONCLUSION AND PERSPECTIVES

We estimate the electronic properties and optical properties of silica and the SiODC(I). The use of MBPT allows reproducing correctly the experimental values. In the final paper, the effect of the disorder and the introduction of a defect will be analyzed deeply for the two cases presented here, but also in the cases of other defects and doped amorphous cells.

### REFERENCES

- [1] S. Girard *et al.*, IEEE TNS, 55, 3473, 2008.
- [2] S. Girard *et al.*, IEEE TNS, 55, 3508, 2008.
- [3] L. Martin-Samos *et al.*, Phys. Rev. B, 71, 0114116, 2005.
- [4] P. Giannozzi *et al.*, J. Phys. Condens. Matter, 21, 395502, 2009.
- [5] N. Richard *et al.*, JNCS, 357, 1994, 2011.
- [6] L. Martin-Samos *et al.*, <http://www.sax-project.org>
- [7] S. T. Pantelides *et al.*, Phys. Rev. B, 13, 2667, 1976.
- [8] “Defects in SiO<sub>2</sub> and Related Dielectrics: Science and Technology”, edited by G. Pacchioni, L. Skuja, and D.L. Griscom (Kluwer Academic Publishers, Dordrecht), 2, 73, 2000.

# Electron trapping defects in bulk silica

Al-Moatasem El-Sayed, Alexander Shluger, Matthew Watkins

Department of Physics and Astronomy and London centre for Nanotechnology, University College London, Gower Street, London WC1E 6BT, UK

corresponding author e-mail: al-moatasem.el-sayed.10@ucl.ac.uk

## ABSTRACT

The use of SiGe alloy materials in advanced electronic devices has allowed the discovery of new devices and the improved performance of existing silicon devices [1]. The structure of a SiGe device is formed by implantation of germanium into silicon followed by oxidation. The native oxide formed is mainly  $\text{SiO}_2$  due to the highly negative free energy of formation of  $\text{SiO}_2$  which rejects the germanium forming a sharp germanium rich layer at the interface[2]. Nevertheless, several studies have investigated the concentration of Ge in the native oxide under various processing conditions [3,4,5]. It is found that Ge persists in the oxide, and that the Ge present in the oxide exists as  $\text{GeO}_2$  and not as elemental Ge clusters, which was originally thought to exist due to the processing conditions [6]. The existence of Ge in the oxide has mainly been discussed in the context of processing techniques. Germanium is known to interact with charge carriers in more than one way leading to the Ge(1), Ge(2) and Ge(3) centres in silica [7]. The structures associated with these centres remain ambiguous.

In this contribution the microscopic structure and electronic structure of the  $\text{GeO}_2$  unit (ascribed to the Ge(1) centre) in silica have been studied at the density functional theory level under periodic boundary conditions. For a more accurate description of the electron density, the HSE hybrid functional was used as implemented in the CP2K code. The electron trapping properties of the germanium impurity have been studied in both alpha quartz and amorphous silica in cells of various sizes containing up to 648 atoms. The neutral Ge impurity induces a local distortion of the structure, inducing the longer Ge-O bonds ( $1.72\text{\AA}$ ) with respect to the Si-O bonds ( $1.61\text{\AA}$ ). The neutral Ge impurity introduces an unoccupied state below the conduction band minimum into which an electron was placed and the atomic coordinates were optimised revealing a strong localisation of the electron on Ge (see Fig. 1). This localisation causes two of the neighbouring oxygen atoms to relax away from the Ge atom, extending the Ge-O bonds to  $1.90\text{\AA}$  and opening the O-Ge-O angle from  $109^\circ$  to  $150.1^\circ$ . The calculated spin density plotted in Figure 1 demonstrates the strong localisation of the electron on the Ge atom. The occupied electronic state associated with the Ge impurity relaxes to  $4.2\text{ eV}$  below the conduction band, acting as a deep electron trap. These results generally agree with the previous results by Pacchioni et al. employing a

cluster model [8]. However, the structural relaxation obtained in our periodic calculations is much stronger resulting in longer Ge-O bonds and wider O-Ge-O angle, which allows for a greater portion of the spin density to localise on the surrounding oxygen atoms, as can be seen in Figure 1. The induced lattice distortion is analysed in unit cells of various sizes and the defect's distortion field is found to be long-ranged, extending to more than  $15\text{\AA}$ , with the structure of the defect converging in cells containing at least 243 atoms. The calculated hyperfine constant,  $-30.5\text{ mT}$ , is in excellent agreement with the experiment,  $\sim -28.0$  [7,9]. We obtained the distribution of incorporation energies and defect parameters in the amorphous  $\text{SiO}_2$  structure.

This work made use of the facilities of HECToR, the UK's national high-performance computing service, which is provided by UoE HPCx Ltd at the University of Edinburgh, Cray Inc and NAG Ltd. The authors would also like to thank UCL for the use of the *Legion* High Performance Computing Facility, and associated support services, in the completion of this work

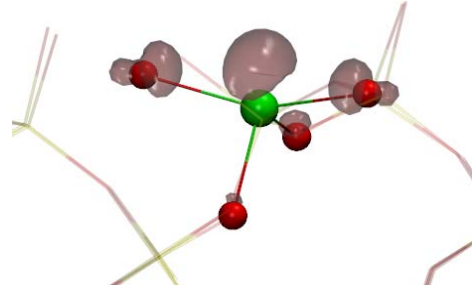


Fig.1. Spin density of germanium electron trap in alpha-quartz. The unpaired electron localizes on the Ge atom and surrounding oxygen atoms causing the O-Ge-O angle to extend.

## References

- [1] Kasper E.: *J. Cryst. Growth* 150 (1995) 921
- [2] Jang, J. H., Wantae, L., Phen, M. S., Siebein, K., Pearson, S. J., Craciun V.: *Appl. Phys. Lett.* 94 (2009) 202104
- [3] Lee, I. M., Takoudis, C. G.: *J. Vac. Sci. Technol. A* 15 (1997) 3154
- [4] Long, E., Azarov, A., Klow, F., Galeckas, A., Kuznetsov A. G., Diplas, S.: *J. Appl. Phys.* 111 (2012) 024308
- [5] Kilpatrick, S. J., Jaccodine, R. J. Thompson, P. E.: *J. Appl. Phys.* 93 (2003) 4896
- [6] Paine, D. C., Caragianis, C., Schwartzman, A. F.: *J. Appl. Phys.* 70 (1991) 5076

- [7] Isoya J., Weil J. A., Claridge, R. F. C.; *J. Chem. Phys.* **69** (1978) 4876
- [8] Pacchioni, G., Mazzeo, C.: *Phys. Rev. B* **62** (2000) 5452
- [9] D. L. Griscom, in *Glass—Science and Technology*, (1991) 151

# **Posters Session**



## Hydrogen reaction kinetics of the Ge P<sub>b1</sub> defect at the (100)Si<sub>1-x</sub>Ge<sub>x</sub>/SiO<sub>2</sub> interface

A. Stesmans, N. H. Thoan, A. P. D. Nguyen, K. Keunen, and V. V. Afanas'ev

*Department of Physics and Astronomy, University of Leuven, 3001 Leuven, Belgium*

The Si dangling bond (DB) type interface defects in the Si/SiO<sub>2</sub> entity, P<sub>b</sub>-type centers as identified by the electron spin resonance (ESR) technique, have been exposed as an archetypal dominant source of interface traps.<sup>1</sup> Fortunately, to the success of Si-based device technology, these can be efficiently passivated by hydrogen to device grade (sub-10<sup>9</sup> cm<sup>-2</sup>eV<sup>-1</sup>) level. One might then expect a close similarity for seemingly isomorphic semiconductor/insulator interfaces, such as the Ge/Ge-oxide system. Yet, the latter interface generally exhibits a high density of (various) differently behaving interface traps.<sup>2</sup> At least for some part, the presence of Ge DB type interface defects at Ge/oxide interface has been demonstrated by ESR<sup>3,4</sup>. So, one may wonder whether the Si DB hydrogen passivation scheme would similarly apply for these interfacial Ge DBs; Here doubts have been raised.<sup>5</sup>

Yet, the recent uncovering in large densities of Ge DBs, typified as GeP<sub>b1</sub> centers, at interfaces of Ge<sub>x</sub>Si<sub>1-x</sub> (0.43<x<0.87) with SiO<sub>2</sub> in condensation grown SiGe-on-insulator structures (SGOI) has created the possibility to carry out such study. The defects can be equally monitored by ESR and the CV technique (see Ref. 6), showing close agreement, also quantitatively, on inferred defect/charge densities. Using this possibility, we here report on a first exploration of the interaction kinetics with H<sub>2</sub> of the GeP<sub>b1</sub> interface defect –a first such study for an interfacial Ge DB. It is carried out on SiO<sub>2</sub>(155 nm)/(100)Ge<sub>0.75</sub>Si<sub>0.25</sub>(16nm)/SiO<sub>2</sub>/(100)Si entities.

The variation in the density of electrically active (unpassivated) GP<sub>b1</sub> defects was determined through monitoring the induced shift ( $\Delta V_T$ ) in “threshold” voltage,  $V_T=Q/C_{TOX}$ , where Q is the inferred (negative) charge and C<sub>TOX</sub> the capacitance of the top SiO<sub>2</sub> layer. In parallel, at some ‘checkpoints’, the density of paramagnetic GP<sub>b1</sub> centers was also measured by conventional first harmonic X band ESR (4.2 K). Routinely, CV monitoring is used rather than ESR, eponymous for the GP<sub>b1</sub>, because of sensitivity/versatility reasons.

Thermal cycles, both isochronically and isothermally, were carried out along the lines described elsewhere.<sup>8</sup> An isochronal passivation cycle consisted of subjecting a set of sample slices (fresh slice for each step) for a fixed time (35±1 min) to passivation in H<sub>2</sub> (99.9999%; 1.05 atm) at selected temperatures (T<sub>an</sub>) in the range 95–450 °C. For the study of defect-H dissociation in vacuum ( $\leq 2 \times 10^{-6}$  torr), a set of slices was initially (exhaustively) passivated in H<sub>2</sub> at 409 °C (41 min) resulting in an interface trap density  $N_{it} \approx [GP_{b1}] \approx 4 \times 10^{12} \text{ cm}^{-2}$  (sample area). Prior to the thermal passivation/activation cycling, as a test, as-received slices were subjected to vacuum treatments up to 425 °C (see Fig. 3); no change was observed in N<sub>it</sub> compared to the initial value  $N_{it,in} = (9.7 \pm 0.5) \times 10^{12} \text{ cm}^{-2}$ , providing a solid basis for the further study.

Figure 2 shows an overview of the results of isochronal passivation in H<sub>2</sub> (full squares) and dissociation in vacuum (34±1 min; open squares) as a plot vs T<sub>an</sub> of  $\Delta V_T(T) / \Delta V_{T,in}$  ( $= N_{it}(T) / N_{it,in}$ ), that is the change in N<sub>it</sub> relative to the initial value N<sub>it,in</sub>, for the range  $25 < T_{an} \leq 450$  °C. Noteworthy aspects include: (a) GP<sub>b1</sub> defect passivation already initiates from T<sub>an</sub>≈120 °C onward, a fairly low temperature; (b) With increasing T<sub>an</sub> of passivation, N<sub>it</sub>(T) decreases monotonically to reach a minimum at T≈375 °C, above which the passivation efficiency appears to degrade; (c) even for the optimum T<sub>an</sub>, the passivation efficiency is disappointingly partial –only ~60% of the defects can be inactivated. A separate check indicated that this situation does not alter for T<sub>an</sub>=600 °C; (d) dissociation initiates from ~325 °C onward, to monotonically increase up to 425 °C, where  $\sim N_{it,in}$  is reached again.

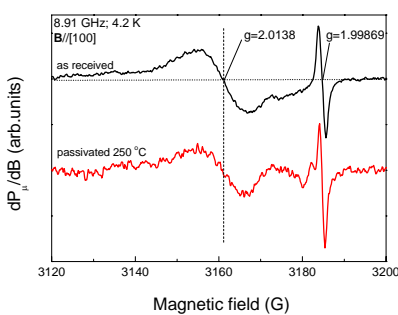


**Fig. 1** X-band ESR spectra of as-prepared (top trace) SiO<sub>2</sub>/Si<sub>0.25</sub>Ge<sub>0.75</sub>/SiO<sub>2</sub>/(100)Si and after passivation in H<sub>2</sub> at 250 °C. (applied magnetic field  $\mathbf{B}/[100]$  interface normal). The narrow signal stems from a Si:P marker.

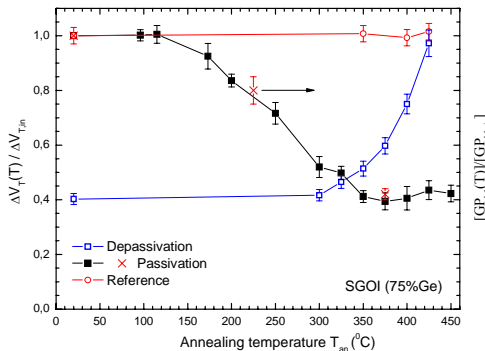


**Fig. 2** Relative shift of threshold voltage  $\Delta V_T(T)/\Delta V_{T,in} = N_{it}(T)/N_{it,in}$  and areal GeP<sub>b1</sub> density (crosses) vs  $T_{an}$  of heating in H<sub>2</sub> (solid squares, crosses) and vacuum (open symbols)

Analysing this way, self consistent fitting of the isothermal passivation data together with those from 3 independently measured isothermal cycles, gives the results  $E_f=1.44 \pm 0.04$  eV,  $\sigma E_f=0.2 \pm 0.02$  eV, for  $k_{f0}=8(+5/-7) \times 10^{-8}$  cm<sup>-3</sup>s<sup>-1</sup>; Fig. 3 illustrates a successful fitting (solid curve). First analysis of the dissociation data gives  $\sigma E_d=0.15 \pm 0.01$  eV for  $k_{d0}=2(+5/-1.5) \times 10^{14}$  s<sup>-1</sup>.

As a prime result, this reveals the presence of considerable spreads in activation energies, ~2.5 times larger than for P<sub>b</sub> in standard<sup>8</sup> Si/SiO<sub>2</sub>. Then, inserting the obtained parameters in the total equation<sup>8</sup> for simultaneous action of passivation and dissociation indicates that only ~80% of the defects taking part in the passivation/dissociation cycling can be passivated, maximally occurring at ~375 °C, as observed indeed. With average activation energies comparable to those of the Si P<sub>b</sub>, the poor degree of passivation is a direct result of the enhanced spreads  $\sigma E_f$ ,  $\sigma E_d$  in the activation energies as encountered before<sup>9</sup>. The latter results from site-to-site variations in defect configuration related to non uniform interfacial strain –the SiO<sub>2</sub>/100)Ge<sub>x</sub>Si<sub>1-x</sub> interface exhibits enhanced randomness compared to the standard Si/SiO<sub>2</sub> one.

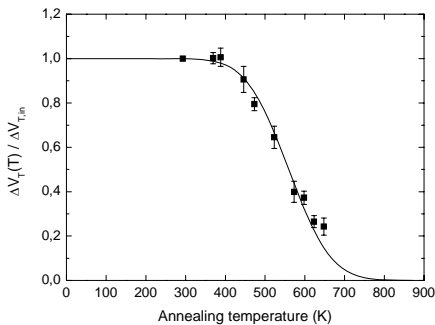


**Fig. 3** Relative threshold voltage shift  $\Delta V_T(T)/\Delta V_{T,in} = N_{it}(T)/N_{it,in}$  under isochronal heating in H<sub>2</sub>. The solid curve represents an optimal fit of the GST model.

The reaction kinetics scheme of P<sub>b</sub> passivation in H<sub>2</sub> and P<sub>b</sub>-H dissociation is consistently described by the general simple thermal (GST) model<sup>8</sup> based on the basic chemical reactions P<sub>b</sub>+H<sub>2</sub>→P<sub>b</sub>H + H and P<sub>b</sub>H→P<sub>b</sub>+H for passivation of P<sub>b</sub> in molecular H<sub>2</sub> and P<sub>b</sub>H dissociation in vacuum, respectively, providing consistent values on the reaction parameters. As to P<sub>b</sub> in Si/SiO<sub>2</sub> the parameters involved are for the forward passivation reaction the activation energy  $E_f=1.51$  eV, its spread  $\sigma E_f=0.06$  eV, and the rate constant pre-factor  $k_{f0}=9.8 \times 10^{-8}$  cm<sup>-3</sup>s<sup>-1</sup>, and analogously  $E_d=2.83$  eV,  $\sigma E_d=0.08$  eV,  $k_{d0}=1.6 \times 10^{13}$  s<sup>-1</sup> for the dissociation reaction. Given the similar situation, we analyzed the current results with the Si P<sub>b</sub> GST defect model. And indeed, the GP<sub>b1</sub> data are found to be well described by the GST model provided the enclosure that there is an amount of ~20% of charge traps not taking part in the passivation/dissociation cycling.

In summary, a first study of the H-passivation/dissociation kinetics of the GeP<sub>b1</sub> defect at the SiO<sub>2</sub>/100)Ge<sub>x</sub>Si<sub>1-x</sub> shows that the behavior can be well described by the Si P<sub>b</sub> GST model based on direct H<sub>2</sub>-defect interaction. As to technology, the interface cannot be passivated in molecular H<sub>2</sub> to device-grade level for thermal budgets up to 600 °C; only ~60 % can be inactivated. With the continuously competing passivation/dissociation reactions, this is a direct consequence of the excessive spreads in activation energies, the current example coming as a manifest demonstration of their spoiling ‘action’.

<sup>1</sup>E. H. Poindexter, G. J. Gerardi, M.-E. Reuckel, P. J. Caplan, N. Johnson, and D. K. Biegelsen, *J. Appl. Phys.* **56**, 2844 (1984)

<sup>2</sup>V. V. Afanas'ev *et al.*, *Appl. Phys. Lett.* **87**, 032107 (2005); D. Bruno *et al.*, *J. Electrochem. Soc.* **155**, H552 (2008)

<sup>3</sup>S. Baldovino, A. Molle, and M. Fanciulli, *Appl. Phys. Lett.* **95**, 242105 (2008)

<sup>4</sup>A. Stesmans, P. Somers, and V. V. Afanas'ev, *J. Phys.: Cond. Matter* **21**, 122201 (2008); *Phys. Rev. B* **79**, 195301 (2009)

<sup>5</sup>L. Tsetseridis and S. T. Pantelides, *Appl. Phys. Lett.* **95**, 262107 (2009); K. Xiong, L. Lin, J. Robertson, and K. Cho, *Appl. Phys. Lett.* **99**, 032902 (2011); H. Matsubara, T. Sasada, M. Takenaka, and S. Takagi, *Appl. Phys. Lett.* **93**, 032104 (2008)

<sup>6</sup>V. V. Afanas'ev, M. Houssa, A. Stesmans, L. Souriau, R. Loo, and M. Meuris, *Appl. Phys. Lett.* **95**, 222106 (2009)

<sup>7</sup>L. Souriau, V. Terzieva, F. Loosen, F. Clemente, B. Brijs, A. Moussa, M. Caymax, M. Meuris, *Thin Solid Films* **517**, 23 (2008)

<sup>8</sup>A. Stesmans, *J. Appl. Phys.* **88**, 489 (2000)

<sup>9</sup>A. Stesmans, *J. Appl. Phys.* **92**, 1317 (2002)

# ACTIVE AREA DEFINITION FOR 80 nm EMBEDDED DEVICES WITH PHASE CHANGE MEMORY AND LOGIC

Authors: Mario Francesco Pistoni, Patrizia Bernardinello, Stefano Colombo

STMicroelectronics

Competence Centre – Technology R&D Agrate Brianza (MB) - Italy

## ABSTRACT

According to Moore's law, memories technology road map mandatory requires continuous lithography scaling with strong investments in term of equipment and technology supports. In the last few years a large effort from industry has been focused on Phase Change Memory (PCM) as the most promising candidate to replace standard floating gate memories. Intrinsic electrical properties of chalcogenide-based PCM devices, like as fast programmability, good read window, bit alterability, low voltage operation, make them suitable for both stand-alone and embedded applications.

In this paper active area definition by means dry etching techniques of silicon and silicon dioxide are presented for a 90 nm technology node embedded non volatile memories and logic and further shrink to 80 nm for applications like as Smart Cards and industrial microcontrollers.

On embedded devices, active area needs to be defined on both array and periphery with different dimensions and features: CMOS transistor for logic requires to keep active area dimension at 120 nm for both technology nodes with a proper defined silicon shape called "Top Corner Rounding", while array definition is hugely challenging since requires to shrink active area dimension form 260 nm to 120 nm keeping same spacing between two neighbor active areas, in case of technology node shrink from 90 nm to 80 nm and consequently cell size reducing from 0.29 mm<sup>2</sup> to 0.15 mm<sup>2</sup>.

193 nm Photoresist as well oxide and nitride hard mask are mandatory allowing dry etching to obtain right dimension and shape; CF chemistries are studied to find the right etch rate and selectivity for hard mask, while dimension is controlled by a dedicated step called "trimming step". It's a CH<sub>2</sub>F<sub>2</sub> chemistry-based step able to guarantee a controlled polymerization along the time and so the desired shrinking from dimension after litho to final expected dimension.

A full study was dedicated to the balancing between CH<sub>2</sub>F<sub>2</sub> (polymerizing gas) and O<sub>2</sub> (de-polymerizing gas) obtaining a function which predicts the final CD dimension according to gas flow applied: it's a linear relationship allowing to properly shrink dimension on different CH<sub>2</sub>F<sub>2</sub> amount.

Similar study on HBr and CHF<sub>3</sub> (both polymerizing gases) brought to develop a controlled process able to guarantee a rounded silicon shape of the active area in periphery (Top Corner Rounded), which is mandatory for the following oxidation on Low and High Voltage transistors.

Shrinking dimension in array requires an innovative filling technique of isolation regions: preliminary un-doped oxide needs to be partially replaced by high density plasma dielectric, so a controlled oxide etch back has been developed with particular care on remaining shape oxide both in array and periphery, preserving nitride erosion as much as possible. Different selectivity between oxide and nitride have been tested with the aim to obtain a controlled oxide etch back, balancing the consumption in array and in periphery even of nitride and silicon, according to the defined targets. Active Area module definition was the first step to build an innovative device, guaranteeing a new breakthrough of PCM and logic.



# Geant4 Physics Processes for Microdosimetry Simulation: Very Low Energy Electromagnetic Models for Electrons in Silicon Dioxide

Mélanie Raine\*, Marc Gaillardin\*, Philippe Paillet\*

\*CEA, DAM, DIF  
F-91297 ARPAJON  
FRANCE

## ABSTRACT

The first steps towards the Geant4 implementation of very low energy electromagnetic models for electrons in silicon dioxide are presented. The experimental Optical Energy-Loss Function (OELF) is fitted with a sum of Drude-type functions. It is the basic quantity for the calculation of inelastic cross sections.

**PACS Keywords:** Electrons, low energy, silicon dioxide, Geant4-DNA.

## 1 INTRODUCTION

The simulation of radiation effects in electronic systems is a critical concern in various domains, such as spacecraft missions. With the decrease of size following the technological roadmap [1], accurate prediction of the sensitivity of electronic devices requires more and more detailed descriptions of ionization profiles. The Monte Carlo simulation toolkit Geant4 [2, 3] is a suitable tool to address this issue and model the microscopic pattern of energy deposition related to an ionizing particle track structure, involving a detailed modeling of the trajectory of all secondary particles. It has already been used successfully, in combination with TCAD simulations [4] or in SEE (Single-Event Effects) prediction tools [5], to study the sensitivity of advanced electronic devices, down to the 45 nm node. However, inherent limits in Geant4 ionization models prevent its use at smaller scales: the recommended production threshold energy of 250 eV for secondary electrons in the low energy electromagnetic package [6] indeed limits the accuracy of the heavy ion track below 10 nm [4]. In order to study the effect of ionizing particles in future highly scaled integrated circuits by means of simulation, new ionization models are thus needed, lowering as much as possible this production threshold energy of secondary electrons.

This project has been initiated with the development of such models in silicon [7-9] for incident electrons, protons and heavy ions. These models have been developed relying on the software design and existing classes of the Geant4-DNA project, originally developed in liquid water for biological applications [10-13]. The calculations of inelastic cross sections in silicon were performed using the approach exposed by Akkerman *et al.* for the generation and

transport of electrons in silicon down to 1.5 eV [14-17]. This approach is actually based on the same initial theory as the Geant4-DNA package, allowing to use it as a basis for implementation. The next step is then to extend these models to other materials used in microelectronics. In the following, the first steps for the calculation of these inelastic cross sections in silicon dioxide are presented. It may be noted that Akkerman's team also developed models for silicon dioxide [18-21], using the same theoretical frame as for silicon. Similar developments were also performed by other teams [22-24].

## 2 MODELING OF THE ENERGY LOSS FUNCTION

All the following developments are based on the theory of Lindhard [25] and Ritchie [26], known as the complex dielectric function theory (CDFT) for the excitation of the free-electron gas systems in solids. In the CDFT, the basic quantity for the calculation of inelastic interactions cross-sections for incident electrons is the Energy-Loss Function (ELF) [27, 28], expressed as:

$$\text{ELF}(\hbar\omega, \vec{q}) = \text{Im} \left[ \frac{-1}{\varepsilon(\omega, \vec{q})} \right] \quad (1)$$

This function is based on the complex dielectric function  $\varepsilon(\omega, \vec{q})$ , with  $\hbar\omega$  and  $\vec{q}$  respectively the energy and momentum transfer from the incident electron to an electron of the target material.

While the ELF is not easily measured, the Optical Energy-Loss Function (OELF), which is the particular case at  $\vec{q} = \vec{0}$ , can be deduced from experimental optical data [29, 30]. The OELF is indeed related to the refraction index  $n$  and the extinction coefficient  $k$ , which are measurable quantities, through equation (2):

$$\text{OELF}(\hbar\omega, \vec{0}) = \text{Im} \left[ \frac{-1}{\varepsilon(\omega, \vec{0})} \right] = \frac{2nk}{(n^2 + k^2)^2} \quad (2)$$

Most materials (including silicon) have a single solid-state phase.  $\text{SiO}_2$  has several polymorphous forms with different densities, different values of the band gap energy,

and different plasmon energies [31, 32], and thus different sets of experimental data exist for  $n$  and  $k$ , corresponding to different phases of  $\text{SiO}_2$ . Nevertheless, Murat *et al.* [19] show that the corresponding OELFs are very similar. The OELF we use here is calculated from the experimental data for glass of Philipp [29], for energies up to 100 eV. For larger energies, one can use Fano's expression [33], which relates the OELF to the photo-ionization cross-sections  $\sigma_{\text{phot}}$  by:

$$\text{OELF}(\hbar\omega, \vec{0}) = \text{Im} \left[ \frac{-1}{\varepsilon(\omega, \vec{0})} \right] = \frac{n_m c \sigma_{\text{phot}}}{\omega} \quad (3)$$

with  $n_m$  the volume density of the inner-shell electrons. Accurate fits to a large set of  $\sigma_{\text{phot}}$  data are provided in published tables [30] for the 50 eV – 10 keV energy range. Both sets of data are shown in Fig. 1, respectively as black squares [29] and empty circles [30]. They are in satisfying agreement on their common energy range 50 eV – 100 eV.

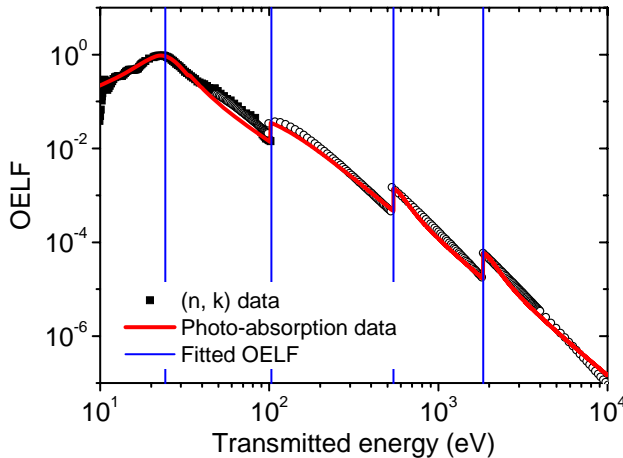


Fig. 1: Fitted OELF in red compared to the experimental OELF in black squares for  $(n, k)$  data [29] and empty circles for photo-absorption data [30]. The vertical blue lines show the positions of the peaks.

The OELF function exhibits a main peak and several discontinuities. The main peak is located at the plasmon energy  $E_p = 24.3$  eV and is attributed to a prominent collective excitation of valence electrons. The discontinuities correspond to shell effects and are related to ionization energies of the target material electrons.

This function is modeled using an extended-Drude expression [34] similar to the one used for silicon by Akkerman *et al.* [14–17], and by other groups over the years for various materials, e.g. [35–37]:

$$\text{Im} \left[ \frac{-1}{\varepsilon(\hbar\omega, \vec{0})} \right] = \sum_j D_j(\hbar\omega) \quad (4)$$

With

$$D_j(\hbar\omega) = \frac{E_p^2 A_j w_j \hbar\omega}{(\hbar^2 \omega^2 - E_j^2)^2 + (w_j \hbar\omega)^2} \quad (5)$$

Except for the first peak related to plasmon excitation, a Heaviside function  $\Theta(\hbar\omega - E_j)$  is introduced in each element of the sum to model the experimentally observed effect of the electronic shells. The parameters  $A_j$ ,  $w_j$  and  $E_j$  are respectively the height, width and position of the peaks.

### 3 PERSPECTIVES

In the final paper, additional information will be provided on the significance of the different peaks chosen to fit the experimental OELF. Various parameters will be examined to check the reliability and internal consistency of this function. In particular, the various sum rules that the OELF needs to satisfy will be calculated.

### REFERENCES

- [1] The 2006 ITRS [Online]. Available: <http://www.itrs.net/Links/2006update/2006UpdateFinal>
- [2] S. Agostinelli, *et al.*, *NIM A*, vol. 506, pp. 250, 2003.
- [3] J. Allison, *et al.*, *IEEE TNS*, vol. 53, pp. 270, 2006.
- [4] M. Raine, *et al.*, *IEEE TNS*, vol. 57, pp. 1892, 2010.
- [5] M. Raine, *et al.*, *IEEE TNS*, vol. 58, pp. 840, 2011.
- [6] G. A. P. Cirrone, *et al.*, *NIM A*, vol. 618, pp. 315, 2010.
- [7] A. Valentin, *et al.*, presented at NSS, USA, 2010.
- [8] A. Valentin, *et al.*, *IEEE TNS*, vol., Under review, 2011.
- [9] A. Valentin, *et al.*, *NIM B*, vol., pp. Under review, 2012.
- [10] Z. Francis, *et al.*, *App. Rad. Isotopes*, vol. 69, pp. 220, 2011.
- [11] S. Incerti, *et al.*, *Medical Physics*, vol. 37, pp. 4692, 2010.
- [12] S. Incerti, *et al.*, *International Journal of Modeling, Simulation, and Scientific Computing*, vol. 1, pp. 157, 2010.
- [13] Geant4-DNA [Online]. Available: <http://geant4-dna.org>
- [14] A. Akkerman *et al.*, *IEEE TNS*, vol. 49, pp. 3022, 2002.
- [15] A. Akkerman, *et al.*, *NIM B*, vol. 227, pp. 319, 2005.
- [16] A. Akkerman, *et al.*, *JAP*, vol. 106, pp. 113703, 2009.
- [17] D. Emfietzoglou, *et al.*, *IEEE TNS*, vol. 51, pp. 2872, 2004.
- [18] A. Akkerman, *et al.*, *Phys. Stat. Sol. (b)*, vol. 198, pp. 769, 1996.
- [19] M. Murat, *et al.*, *IEEE TNS*, vol. 51, pp. 3211, 2004.
- [20] M. Murat, *et al.*, *IEEE TNS*, vol. 53, pp. 1973, 2006.
- [21] M. Murat, *et al.*, *IEEE TNS*, vol. 55, pp. 2113, 2008.
- [22] J. C. Ashley *et al.*, *IEEE TNS*, vol. 28, pp. 4132, 1981.
- [23] S. Tanuma, *et al.*, *SIA*, vol. 17, pp. 927, 1991.
- [24] C. M. Kwei, *et al.*, *Surface Science*, vol. 293, pp. 202, 1993.
- [25] J. Lindhard, *Kong. Dan. Vid. Sels.*, vol. 28, pp., 1954.
- [26] R. H. Ritchie, *Physical Review*, vol. 114, pp. 644, 1959.
- [27] D. Emfietzoglou, *et al.*, *Physics in Medicine and Biology*, vol. 48, pp. 2355, 2003.
- [28] D. Emfietzoglou *et al.*, *NIM B*, vol. 193, pp. 71, 2002.
- [29] H. R. Philipp, *Handbook of optical constants of solids*, 1985.
- [30] F. Biggs and R. Lighthill, Report SAND87-0070, 1988.
- [31] D. W. McComb *et al.*, *NIM B*, vol. 96, pp. 569, 1995.
- [32] L. A. J. Garvie, *et al.*, *Sol. St. Com.*, vol. 106, pp. 303, 1998.
- [33] U. Fano *et al.*, *Rev. of Mod. Phys.*, vol. 40, pp. 441, 1968.
- [34] R. H. Ritchie *et al.*, *Philos. Mag.*, vol. 36, pp. 463, 1977.
- [35] J. C. Ashley, *et al.*, *Thin Solid Films*, vol. 60, pp. 361, 1979.
- [36] C. J. Tung *et al.*, *Phys. Rev. B*, vol. 16, pp. 4302, 1977.
- [37] S. Tougaard *et al.*, *Surface Science*, vol. 143, pp. 482, 1984.

# Optical characterization of Polysilazane based SOD thin films as a function of the growth parameters.

Pier Carlo Ricci<sup>1</sup>, Gianluca Gulleri<sup>2</sup>, Francesco Fumagalli<sup>2</sup>, Carlo Maria Carbonaro<sup>1</sup>, Riccardo Corpino<sup>1</sup>

<sup>1</sup> Dipartimento di Fisica, Università di Cagliari, s.p. n 8 Km 0.700, 09042 Monserrato, Cagliari, Ital

<sup>2</sup>Micron Technologies, Inc.

## ABSTRACT

In this work Polysilazane based SOD thin films growth on different ultra-thin barriers (UTB) and with different thicknesses were studied. The UTB (silicon nitride, silicon dioxide) are studied in terms of their impact on SOD induced conversion percent. The degree of conversion to  $\text{SiO}_2$  was analyzed and the oxide local structure was studied in terms of Si–O–Si bridges by FTIR and Raman spectroscopy. Steady state and time resolved luminescence were applied to further characterize the oxide structure, the presence of defects and the interfaces.

**PACS Keywords:** 71.55.-I, 71.55.Jv, 68.60.-p, 68.65.-k.

## 1 INTRODUCTION

In the fabrication of integrated circuits, semiconductor elements are integrated and laid out within a small area on a chip requiring the devices to be placed in close proximity to each other. With the continuing decrease in the dimensions and spacing of devices on integrated circuits (ICs), insulative materials (typically  $\text{SiO}_2$ ) are deposited to electrically isolate the active components (transistors, resistors, capacitors). For example, interlayer dielectric (ILD) or intermetal dielectric (IMD) layers isolate structures from metal interconnected layers, which may require filling narrow gaps with high aspect ratios (ratio of depth to width). Insulative structures such as shallow trench isolation (STI) regions are also formed in trenches within the substrate between components. Such trenches can have a width as narrow as 10 to 50 nm or smaller, and filling such features can be challenging. In addition, the dielectric material must be able to withstand subsequent processing steps such as etch and cleaning steps.

In this context, International Technology Roadmap for Semiconductors 2010 points its attention on two different ways to scale devices dimensions: geometrical scaling (i.e. Moore's law) and equivalent scaling. Latter regards another way to improve device performances in terms of innovative designs, software solutions and new materials.

High-density requirements are imposing a solution that need of both contributes. Different technologies are scaling down technology node under 40nm. Focusing on insulating oxides materials in all their different applications (shallow trench, inter and pre metal etc..), all techniques utilized until now are not able to respond devices shrinking requests.

SOD represents a valid alternative to High Density plasma and the other techniques from chemical vapor deposition (SACVD, PECVD etc..) regarding gap-filling demand with aspect ratio greater than 5:1 [1]. Flowable materials with high gap filling properties such as SOD and spin-on polymers like silicates, siloxanes, silazanes or silsesquioxanes, have been recently developed [2],[3].

With SOD materials key point is chemical physical quality: furnace conversion degree has to guarantee a reliable oxide in terms of density, robustness and resistivity to breakdown. Wet Etch Rate Ratio between SOD and oxide fields represent first bottleneck. Increasing furnace annealing temperature of furnace give results on flat wafers, but inside trench seems to have no the same effects. Conversion percent decrease increasing trench deep and wet etch rate go over unsustainable values (>7:1) and this represent a real blocking point. We focus our attention on the ultrathin barrier (UTB) deposited between the active areas and the insulating dielectrics.

Here we present interface FTIR analysis between SOD and the relative UTB: silicon nitride and different oxides from furnace. Finally we focus on different bonding Si-O-Si angles to analyze different conversion percent in terms of SOD bulk properties.

## 2 EXPERIMENTAL

Polysilazane based SOD thin films were grown on large high purity silicon mono-crystal substrates in different chamber atmosphere:  $\text{N}_2 + \text{O}_2$ ,  $\text{NH}_3 + \text{SiH}_2\text{Cl}_2$  and  $\text{N}_2\text{O} + \text{SiH}_4$  and with different thin barrier: Oxide - Nitrogen free, Oxide with Nitrogen and Silicon Nitride Thin Barrier. Samples with different SOD thickness were grown. Finally, Furnace oxide was utilized as sample reference to evaluate conversion percent of SOD-based oxide in the different samples. The list of samples and the growth parameters are reported in Table 1.

Raman spectra were collected in back scattering geometry with the 514.5 nm line of an Argon-ion laser. Measurements were performed in air at room temperature with a triple spectrometer Jobin-Yvon Dilor integrated system with a spectral resolution of about  $1 \text{ cm}^{-1}$ .

Photoluminescence (PL) measurements were performed with excitation provided by an optical parametric oscillator with a frequency doubler device (Spectra Physics MOPO), excited by the third harmonic of a pulsed Nd-YAG laser

(Spectra Physics QuantaRay PRO-270), with pulse width at half maximum of 10 ns and 10 Hz of repetition rate.

FTIR measurements were performed in the 1500-400 cm<sup>-1</sup> spectral range.

Samples	SOD Thickness (nm)	Chamber Atmosphere
1A	290	N <sub>2</sub> + O <sub>2</sub>
1B	580	N <sub>2</sub> + O <sub>2</sub>
1C	750	N <sub>2</sub> + O <sub>2</sub>
2A	290	N <sub>2</sub> O + SiH <sub>4</sub>
2B	580	N <sub>2</sub> O + SiH <sub>4</sub>
2C	750	N <sub>2</sub> O + SiH <sub>4</sub>
3A	290	NH <sub>3</sub> + SiH <sub>2</sub> Cl <sub>2</sub>
3B	580	NH <sub>3</sub> + SiH <sub>2</sub> Cl <sub>2</sub>

Table 1: Samples analyzed.

### 3 RESULTS

Figure 1 reports the FTIR spectrum of the samples as spun, showing typical peaks of silicon nitride: after curing step Si-N, and Si-H bonds are mainly substituted by Si-O bonds giving a silicon oxide with standard parameters of silica (figure 2). Absorption peaks of Si–O bonds occur at about 1080 cm<sup>-1</sup> (stretching mode), at 456 cm<sup>-1</sup> (rocking mode) and at 810 cm<sup>-1</sup> (bending mode). No absorptions at 610 cm<sup>-1</sup> due to unsaturated Si-Si bonds were detected, confirming the absence of significant structural imperfections at the interface. However, some differences in the FTIR spectra of the oxides grown in different samples can be detected mainly in the region of the Si-O stretching mode.

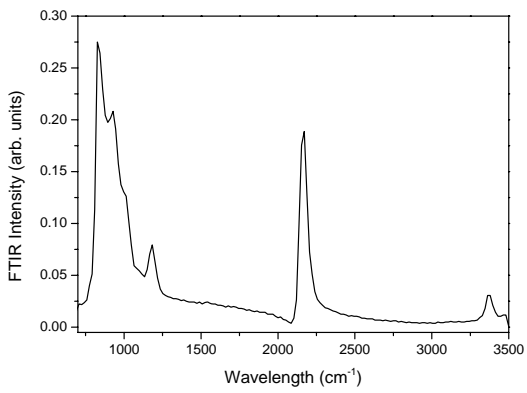


Figure 1: FTIR spectrum "as spun"

Actually, the main oxide absorption band is strongly asymmetric and it is generated by different contribution from the Si-O<sub>x</sub> vibration. We applied random-bonding model (RBM) on polysilazane SOD-based film describing

the effective conversion to stoichiometric SiO<sub>2</sub>. A fitting procedure was applied in order to study the Si-O angles and to deep understand the contribution of the structural units Si-O<sub>2</sub>-Si<sub>2</sub>, Si-O<sub>3</sub>-Si, Si-O<sub>4</sub> and from the presence of defects at interface with silicon or inclusions [5],[6]. In particular, interface effects were isolated (Si-O-N) and a direct correlation between the SOD conversion will be shown.

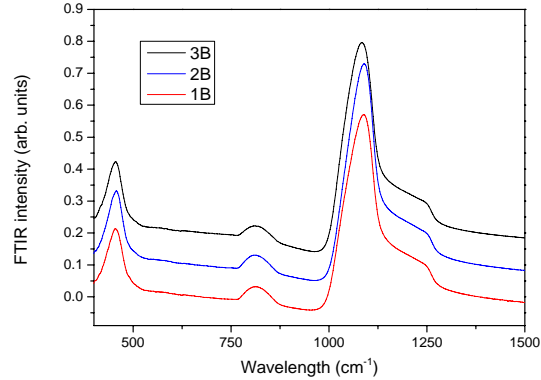


Figure 2: FTIR spectra of SOD based oxide

Finally, Raman and photoluminescence measurements will be performed in order to analyze the effective level of conversion and the properties at the interfaces Si-SiO<sub>2</sub> and inclusions.

The optical characterization will be carried out by investigating the emission properties in the near UV-visible range. The attention will be mainly focused on the emissions at 310, 335 and 420 nm which were related, to the presence of silanol groups. These centers have excitation channels in the UV - VUV range (190-360 nm) and time decay of few ns. The different treatment undergone by the samples and the different synthesis procedure are expected to modify the spectroscopic features of these centers.

### REFERENCES

- [1] B. Lee, Y.-H Park, Y.-T. Hwang, ,Weontae, O.H Yoon, M.,Ree, Nature Materials 4, 147-151, (2005).
- [2] Holzwarth, C.W., Barwickz, T.,Smith, H.I. J. Vac. Sci. Technol. B 25, 2658 (2007).
- [3] Lee, W.-G. Thin Solid Films 520, 3003-3008 (2012)
- [4] H.R. Philipp, J. Non-Cryst. Solids 8–10 627 (1972)
- [5] V.Em. Vamvakas, M. Theodoropoulou, S.N. Georgia, C.A. Krontiras, M.N. Pisanias Microelectronics Reliability 47 (2007) 834–837
- [6] G.Perez, J.M.Sanz Thin Solid Films 416 24–30 (2002)
- [7] C.M. Carbonaro, D. Chiriu, R. Corpino, P.C. Ricci, A. Anedda J. Non-Crystal. Solids 353 550–554 (2007)
- [8] C. M. Carbonaro, P. C. Ricci, A. Anedda Phys. Rev B. 76, 125431 (2007)

## **CONTACT MODULE DEFINITION FOR 110 nm TECHNOLOGY NODE ON BCD PLATFORMS**

Authors: Mario Francesco Pistoni, Sara Paolillo, Ivan Venegoni

STMicroelectronics

Competence Centre – Technology R&D Agrate Brianza (MB) - Italy

### **ABSTRACT**

Since the beginning, BCD (Bipolar – CMOS – DMOS) devices have ever founded their success on the three key factors:

- wide range of final applications: from automotive to industrial field, from home entrainment to consumers and computers;
- low cost of manufacturability
- high power and high voltage applied in spite of non shrinking lithography

Latest factor gives BCD devices a huge field of applications following both laws of semiconductor: Law called “More than Moore”, for which innovative structure as well 3D integration give strong capability and Moore’s Law, in which dimensions are shrunken to reach more aggressive performances and lower cost.

In this paper shrinking dimension of BCD platform from 160 nm technology node to 110 technology node with the introduction of full copper metal lines is considered in term of BEOL (Back end of Line) definition and in particular in term of contacts definition by means dry etching technique.

BCD 110 nm (here called BCD9s) involves shrinking dimension of contacts, metal lines and interconnections, while transistors and gates keep based on 160 nm technology node to allow right power and voltage.

Contact definition was integrated on different photoresist to keep etching compatible with 248 nm lithography, evaluating the opportunity to use a nitride based hard mask according to different thickness of photoresist. Hard mask evaluation was merged with the following process steps (barrier and tungsten deposition and W planarization) in order to provide a complete and reliable full flow.

Several evaluations were carried on both doped and undoped dielectric layers (Boron-Phosphorus silicon glass and TEOS) obtaining different etch rates as well different contact profile.

A study of polymerization degree in term of CF/O<sub>2</sub> gas ratio shows how to define 150 nm contact on different doped dielectric layers, avoid etch stop conditions and matching right final dimension on top and bottom; CF/O<sub>2</sub> gas ratio was also studied to obtain a low etch rate step able to provide controlled polymerization and to limit as much as possible photoresist consumption.

A study of CF/O<sub>2</sub>/N<sub>2</sub> chemistries was also completed demonstrating that contact dimension could also be tuned by BARC etch step according to gas ration and gas amount of CF, O<sub>2</sub> and N<sub>2</sub>.

Borderless Nitride layer and thermal oxide on beneath was also etched and properly time tuned avoiding overetch on misaligned contact or on contact landing top poly gate.

Dry Etching recipe, developed on Lam Alliance Exelan HPT, was also studied depending of different contact mask transmittance factors in order to obtain a dry etching strongly robust to allow future industrialization on wide different products.

Evaluation of different chemicals for following cleanings was also successfully concluded to complete contact module definition.

# Establishing the Link between Densification Mechanisms and Interface Nanostructure in High- $\kappa$ Deposition on Silicon Oxide: A Multi-Scale Modelling Study

C. Mastail<sup>1,2,3</sup>, A. Estève<sup>1,2</sup>, N. Richard<sup>3</sup>, M. Djafari Rouhani<sup>1,4</sup> G. Landa<sup>1,2</sup> and A. Hemeryck<sup>1,2</sup>

<sup>1</sup> CNRS, LAAS, 7 avenue du Colonel Roche, F-31400 Toulouse, France

<sup>2</sup> Univ de Toulouse, UPS, LAAS, F-31400 Toulouse, France

<sup>3</sup> CEA, DAM, DIF, F-91680 Arpajon, France

<sup>4</sup> Univ de Toulouse, LAAS, F-31400 Toulouse, France

## ABSTRACT

Experimentally, the growth of high- $\kappa$  materials on silicon requires a control of the structural properties at the atomic scale. Here, we describe new findings about the growth of HfO<sub>2</sub> on hydroxylated silicon surface through a multiscale modeling strategy, by associating Density Functional Theory calculations and kinetic Monte Carlo methodology. We detail a new atomic mechanism, so-called densification that appears as a key step during the HfO<sub>2</sub> growth. These mechanisms have been characterized in terms of structures and energies thanks to DFT calculations and their influence on the high- $\kappa$  growth is described through kinetic Monte Carlo simulation results.

## 1 INTRODUCTION

The miniaturization trend requires radical changes in the development of future micro-electronic devices. The miniaturization has resulted in dielectric gates of MOS devices as thin as to be permeable to leakage currents. In this framework, hafnium oxide is one of the promising high- $\kappa$  substitutes for SiO<sub>2</sub> as a gate oxide layer in the next generations of MOS transistors. But, at the required thicknesses, the structural and electronic properties of the gate oxide layer strongly depend on the fabrication process, which must be controlled at the atomic scale.

In this study, we present a multi-scale modelling, coupling DFT calculations and a kinetic Monte Carlo Algorithm, to gain a better understanding

of the physic-chemical mechanisms occurring during HfO<sub>2</sub> vapour-deposition processes, such as Atomic Layer Deposition [1]. This methodology brings both fundamental insights and advanced tools for the CAD of high- $\kappa$  oxide layer growth.

## 2 RESULTS

Using DFT calculations, we identified, in addition to more conventional mechanisms, various so-called densification mechanisms, which allow the evolution towards a bulk oxide structure, starting from molecular precursors [2]. Densification mechanisms increase the density of oxygen atoms around the metallic atoms by increasing their coordination numbers. These densification mechanisms have been implemented in a software package, called “HIKAD”, based on a kinetic Monte Carlo methodology. The “HIKAD” simulations allow establishing the link between the atomic scale structure of the growing oxide layer and the real experimental conditions: partial pressures, temperature, various durations... used during the deposition process.

## 3 PERSPECTIVES

In the final paper, we highlight that densification mechanisms are crucial in the high- $\kappa$  layer growth. The evolution of structural characteristics of the layers: coverage, roughness and porosity (as shown in Fig. 1), and the composition of the deposited films: stoichiometry, chlorine contamination will be discussed and compared

with experimental observations. The sensitivity of the results with respect to experimental growth conditions will be also examined.

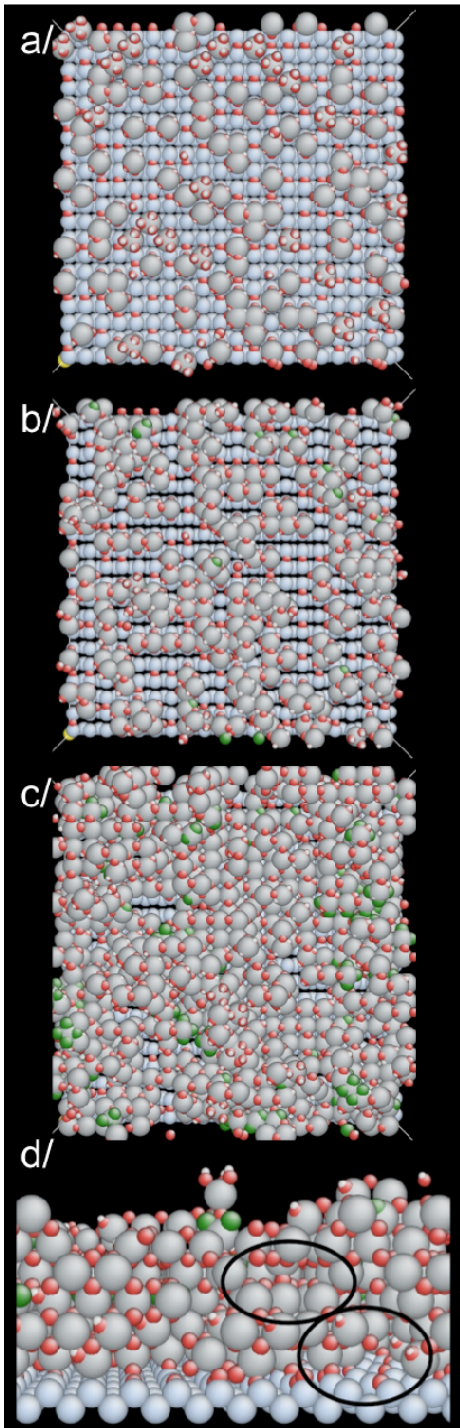


Figure 1: Top view snapshots of the grown layer caught during the deposition process after the (a) the first, b) the second and c) the tenth cycles. (d) A side view cross-section of the deposited layer after ten cycles highlighting void spaces and non-occupied Silicon atoms of the host substrate.

Light blue, red, grey, white and green spheres represent silicon, oxygen, hafnium, hydrogen and chlorine atoms respectively.

## REFERENCES

- [1] C. Mastail, et al., Thin Solid Films (2011), doi:10.1016/j.tsf.2011.10.125.
- [2] A. Esteve *et al.*, Les Techniques de l'Ingénieur. 123, 12 (2009).

# Development of an Empirical Model for Fast prediction of Non Volatile Memory Reliability

H. Aziza\*, J.M. Portal\*, J. Plantier\*\*, C. Reliaud\*\*, A. Regnier\*\*, J.L. Ogier\*\*

\*M2NP, Institut Materiaux Microelectronique Nanosciences de Provence, UMR 6242 CNRS, Aix-Marseille Université, Marseille, France.

\*\* ST-Microelectronics, ZI de Rousset BP 2, F-13106 Rousset CEDEX, France

## ABSTRACT

In this work, the developpement of a NVM reliability model is proposed. This model evaluates accurately the impact of electrical stress, temperature and cycling on the extrinsic  $V_T$  population of a memory array (marginal cell population). The extrinsic  $V_T$  population is related to leakage currents throw the tunnel oxide ( $\text{SiO}_2$  film) under stress. A 700Kbits test chip is used to extract the main reliability parameters of the model.

**Keywords:** Non Volatile Memory (NVM), reliability model,  $V_T$  distributions.

## 1 PRESENTATION

Reliability of Flash EEPROM memory has grown with the understanding of memory cell failure mechanisms [1]. It has been currently observed that Fowler-Nordheim tunneling injection layers (5-10 nm) induces leakage currents called stress-induced leakage currents (SILC). It is now generally accepted that this SILC is caused by inelastic Trap-Assisted Tunnel (TAT) transitions and that these traps are created by the electric high-field stress during the writing and erasing process [2].

Stress induced leakage current (SILC) is now the limiting factor for downscaling the  $\text{SiO}_2$  tunnel oxide thickness. It is very important to have the SILC under control in order to limit the NVM  $V_T$  shift, especially after an extensive number of write/erase cycles or an electrical stress. Indeed, the extrinsec population (i.e. cells providing a  $V_T$  out of specifications) is the main concern in terms of reliability as it can lead to an overlap between write and erase distributions. In this context, a reliability model is developed to predict long term memory failures.

## 2 PROBLEM FORMULATION

In the NVM memory field, reliability is associated with the number of cells present in the extrinsic population. This number, expressed in ppm (parts per million), is a parametric function. This function is given by Equation 1.

$$\text{Def} = A_0 \cdot (t_{ret})^b \cdot \exp\left(-\frac{E_A \cdot q}{kT}\right) \cdot (N_{cycles})^n \cdot (V_{CG})^a \quad (1)$$

With  $\text{Def}$  the defect rate in ppm,  $A_0$  the model adjustment coefficient (unit less),  $E_A$  the traps activation energy (eV),  $k$

the Boltzmann constant, and  $q$  the elementary charge of the electron (Coulombs).

Equation 1 depends of the following parameters:

- The cell control gate read voltage ( $V_{CG}$ ),
- The number of write/erase cycles ( $N_{cycles}$ ),
- The retention temperature ( $T$ ),
- The retention time ( $t_{ret}$ ).

Each of this parameter affects the memory reliability during the normal memory operation. Based on this equation, the model implementation requires the calculation of the following values:  $a$ ,  $b$ ,  $n$ ,  $E_A$ , and  $A_0$ .

## 3 PROBLEM SOLUTION

The extraction of each unknown value is done by considering the evolution of the defect rate independently for each parameter. Fig.1 presents the evolution of the defect rate versus the number of cycles, for different retention time and two different  $V_{CG}$  values.  $n$  is given by the average value of Fig1.a and Fig1.b slopes ( $n \approx 0.8$ ). For confidentiality reasons, the Y-axis has been normalized. The evolution of the defect rate versus the retention time, for different cycle numbers and two different  $V_{CG}$  values is also extracted after measurements to determine the value of  $b$  ( $b \approx 0.9$ ). A same approach is used to determine the value of  $a$  ( $a \approx 5.41$ ). Concerning  $A_0$ , its extraction is performed by comparing the defect rate curves obtained from measurements and defect rate curves calculated by the model without  $A_0$ .  $A_0$  corresponds to the offset between the two set of curves presented in Fig.2 ( $A_0 \approx 2.28 \cdot 10^{-4}$ ). Finally,  $E_A$  is extracted from Arrhenius law ( $E_A \approx 0.25$  eV). The model validation is proposed in Fig.3. The model is in agreement with silicon data for two different wafer lots. Besides, the defect rate can be predicted to 10 years.

## 4 CONCLUSION

In this work, a reliability model is developed predict the long-term reliability of NVM. The model is in agreement with silicon data.

## REFERENCES

- [1] G. Verma, N. Mielke, Reliability performance of ETOX based flash memories, Proc. Of 26th Reliability Physics Symposium, pp. 158-166, 1988.
- [2] A. Modelli, "Reliability of thin dielectric for nonvolatile applications", Microelectron. Eng., vol.48, pp.403-410, 1999.

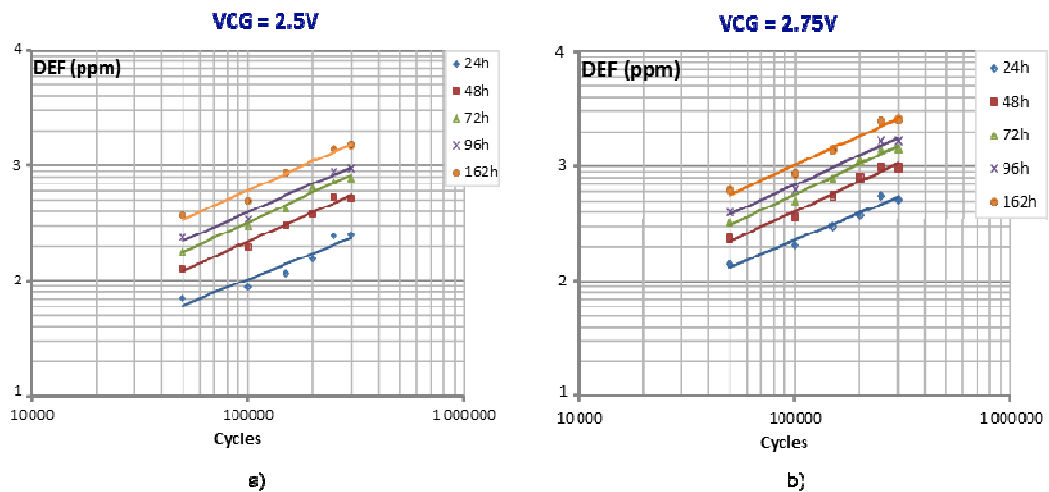


Figure 1: Defect rate versus cycling for (a)  $V_{CG} = 2.5V$  and (b)  $V_{CG} = 2.75V$

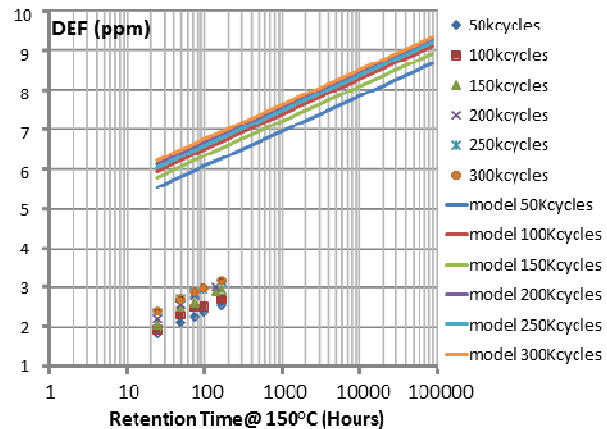


Figure 2:  $A_0$  parameter extraction

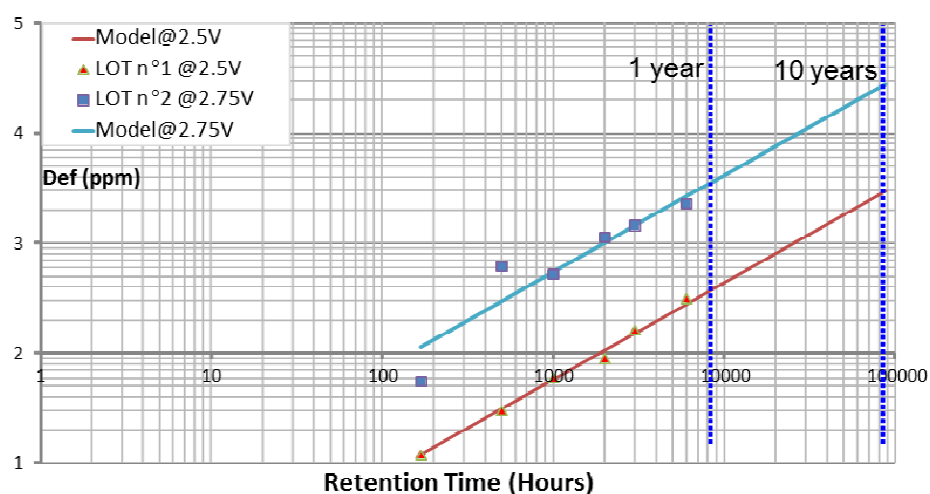


Figure 3: Reliability model application example: Defect rate extrapolation to 10 years.

# Investigation of charge losses through dielectrics in a NVM array using data retention gate stress

J. Postel-Pellerin<sup>\*</sup>, G. Micolau<sup>\*</sup>, P. Chiquet<sup>\*</sup>, J. Melkonian<sup>\*</sup>, R. Laffont<sup>\*</sup>, F. Lalande<sup>\*</sup>, J.L. Ogier<sup>\*\*</sup>

<sup>\*</sup>Aix-Marseille Université, IM2NP-CNRS, UMR 7334  
IMT Technopôle de Château-Gombert, 13451 Marseille, France

<sup>\*\*</sup>STMicroelectronics  
ZI Rousset, 13100 Rousset, France

## ABSTRACT

In this paper we propose a study of leakage paths for electrons during data retention in EEPROM memory cells, based on an original method we have previously published. This method, consisting in biasing the cells during the retention phase, allows investigating the main leakage paths, through SiO<sub>2</sub> tunnel oxide as well as through the tri-layer stack oxide “Oxide/Nitride/Oxide” (ONO). An electrical simulation and a preliminary study have also been previously performed on the choice of the needed biases. Data retention measurements on memory arrays highlight the fact that the mechanism(s) for intrinsic and extrinsic cells are not or lightly activated by electric fields, coherent with a trap-assisted leakage.

**PACS Keywords:** NVM, reliability, data retention, extrinsic cells, gate stress

## 1 INTRODUCTION

As non-volatile memory (NVM) technology gains maturity, new application fields emerge, often implying new product requirements, especially at high temperature. The study of the electrical behavior of memory cells with temperature, and particularly their reliability has become a major issue. The cell retention, which is the capacity of a memory cell to conserve information, is a key criterion for good reliability cells. When considering an NVM cell with its floating gate negatively biased by stored electrons [1], the threshold voltage V<sub>T</sub> is shifted according to (1):

$$V_T = V_{T0} - \frac{Q_{FG}}{C_{PP}} \quad (1)$$

where V<sub>T0</sub> is the natural threshold voltage of the cell, Q<sub>FG</sub> the charge amount in the floating gate and C<sub>PP</sub> the interpoly capacitor.

These electrons classically leak from the floating gate, decreasing the total number of stored electrons and so inducing a progressive data loss. Many previous studies have already dealt with this subject but some of them seem to show a leakage through SiO<sub>2</sub> tunnel oxide [2] while others seem to show other leakage paths through the tri-

layer stack oxide “Oxide/Nitride/Oxide” (ONO) [3] or even through lateral spacers. Nevertheless, better identification of these leakage paths is still a crucial issue in floating gate non-volatile memories. In a previous preliminary study, we have proposed a new experimental study and shown its feasibility [4]. The main idea consists in cancelling electric field in the different dielectrics surrounding the floating gate, during the retention test. Indeed, the floating gate bias V<sub>FG</sub> is linearly linked [5] to the control gate bias V<sub>CG</sub> by the classical relation (2):

$$V_{FG} = \alpha \cdot V_{CG} + \frac{Q_{FG}}{C_{TOT}} \quad (2)$$

where C<sub>TOT</sub> is the sum of all the capacitances in the structure and α is the ratio between C<sub>PP</sub> and C<sub>TOT</sub>.

The EEPROM type NVM has been chosen due to its robustness, which makes it a good candidate for automotive applications. This paper is divided in two major parts describing the work. The first one is devoted to the structures used, experimental details and the feasibility of the method. The second part describes our data retention measurements at 85°C and their discussion.

## 2 DETAILS ON THE METHOD AND CHOICE OF THE BIASES

Due to the low ratio of defectivity in such memory devices, our biased data retention experiments were performed on a specific statistical tool previously developed by STMicroelectronics to qualify data retention of NVM [6], consisting in 1M EEPROM cells parallelly placed, called “CAST” (Cell Array Structure Test). The I<sub>DS</sub>(V<sub>CG</sub>) characteristic of the CAST is the sum of drain currents of all the cells connected in parallel. In a single measurement we observe a cumulative characteristic of a great number of cells. The majority of the cells has identical behavior and threshold voltage, denoted V<sub>T</sub><sup>i</sup> (intrinsic population). Few cells (extrinsic population) can have a threshold voltage lower than the average one, denoted V<sub>T</sub><sup>e</sup>, raising the low values of the CAST current and creating a hump on the characteristic, as shown in Fig.1.

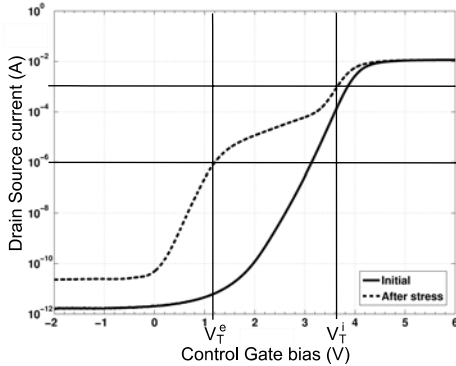


Figure 1: Instance of an  $I_{DS}$  vs.  $V_{CG}$  characteristic of a CAST before and after stress.

In previous studies [4][7], we have demonstrated the interest and the feasibility of our method, leading to first significant results on leakage paths involved for intrinsic and extrinsic populations. Moreover it has allowed us to choose a precise range of control gate biases during retention ( $V_{CG}^{ret}$ ) on which we have to focus. Classical retention test are performed without any external bias applied (all the contacts are floating). We have already demonstrated that it is equivalent to ground all the contact, thus our witness CAST will be grounded. We have also demonstrated that a positive  $V_{CG}^{ret}$  (ie increase the electric field across ONO) has no impact on the data retention [7]. So, we will only investigate a decrease of ONO electric field (and thus an increase of electric field across SiO<sub>2</sub> tunnel oxide) by using negative values of  $V_{CG}^{ret}$ , but not lower than -2.5V, which cancels the electric field across ONO but activates a soft-programming of the cells [7]. Thus, we have chosen to investigate the biases from -2.5V to 0V by 0.5V, as detailed in Table 1.

CAST	1	2	3	4	5	6
Control Gate Bias	0V	-0.5V	-1V	-1.5V	-2V	-2.5V

Table 1: Summary of the investigated retention biases.

### 3 EXPERIMENTAL RESULTS

To accelerate the charge loss, the six CASTs are deposited in a thermal bake at  $T_{ret}=85^\circ\text{C}$ , recommended by [8]. The evolution of the shifts  $\Delta V_T(t)=V_T(t)-V_T(t=0)$  after 700h, for both intrinsic and extrinsic cells, versus control gate bias is presented in Fig. 2 for the six devices. From Fig. 2, we can first notice that extrinsic cells have larger variations than intrinsic cells, due to a higher sensitivity to charge loss. We can also see that for both intrinsic and extrinsic cells the control gate bias  $V_{CG}^{ret}$  has a very limited impact on the threshold voltage variation, excepted for extrinsic cells at  $V_{CG}^{ret} = -2.5\text{V}$  for which we know that we activate the soft-programming effect. This very low dependence on electric field is characteristic of a trap-assisted leakage mechanism.

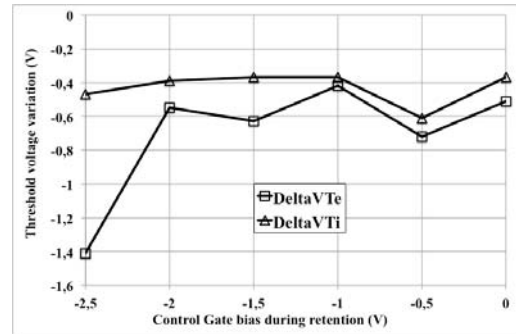


Figure 2: Threshold voltage variation after 700h for intrinsic and extrinsic cells versus  $V_{CG}^{ret}$ .

### 4 CONCLUSION

In this paper, we have developed an original study of gate stress data retention, investigating several bias conditions from  $V_{CG}^{ret} = -2.5\text{V}$ , confirming the soft-programming effect, to the classical data retention condition at  $V_{CG}^{ret} = 0\text{V}$ . We have demonstrated a very low dependence on both electric field across ONO and SiO<sub>2</sub> tunnel oxide, showing a trap-assisted mechanism for the leakage of charges from the floating gate. As a perspective, we can reproduce this study at different temperatures to propose a modeling of the involved mechanism. This method can also be used to characterize emergent or prototypal NVM such as ReRAM, OxRAM or PCM. Indeed, for this kind of devices, we know that the duration of the erasing/programming electric biases is a key point of their requirements.

### REFERENCES

- [1] W. Brown, J. Brewer, IEEE Press, 1998.
- [2] J. Postel-Pellerin, F. Lalande, P. Canet, R. Bouchakour, F. Jeuland, L. Moranco, Microelectronic Reliability, 49 (9-11), 1060-1063, 2009.
- [3] C. Le Roux, Ph.D. Thesis, Aix-Marseille University, Marseille, France, 2008.
- [4] J. Postel-Pellerin, R. Laffont, G. Micolau, F. Lalande, B. Bouteille, Microelectronic Reliability, 50 (9-11), 1474-1478, 2010.
- [5] L.-C. Hu, A.-C. Kang, E. Chen, J. Shih, Y.-F. Lin, K. Wu, Y.-C. King, Microelectronics Reliability, 45, 1331-1336, 2005.
- [6] F. Pio, E. Gomerio, Solid-State Electronics, 45, 1279-1291, 2001.
- [7] R. Djénadi, G. Micolau, J. Postel-Pellerin, R. Laffont, J.-L. Ogier, F. Lalande, J. Melkonian, Proceedings of IEEE ISDRS, College Park (MD), USA, 2011.
- [8] JEDEC Solid State Technology Association, JEDEC Standard JESD22-A103D - High Temperature Storage Life, December 2010.

# Comparison of electronic and optical properties of mixed SiO<sub>2</sub>-GeO<sub>2</sub> amorphous system by first-principles

Nicolas RICHARD\*, Layla MARTIN-SAMOS \*\*, Sylvain GIRARD\*, Aziz BOUKENTER\*\*\*\*,  
Yousef OUERDANE\*\*\*\*, Jean-Pierre MEUNIER\*\*\*\*

\*CEA, DAM, DIF, F91297 Arpajon, France

\*\*CNR/IOM Democritos, c/o SISSA - via Bonomea, 265/a  
34136 - Trieste, Italy

\*\*\*University of Nova Gorica, Materials Research Laboratory,  
Vipavska 11C, 5270 Ajdovscina, Slovenia

\*\*\*\*Laboratoire Hubert Curien, Université Jean Monnet UMR CNRS 5516,  
Bâtiment F 18 Rue du Professeur Benoît Lauras, F42000 Saint-Etienne, France

## ABSTRACT

We have applied first principles method to study the differences in the properties of amorphous silica cells doped with different amounts of germanium. Computations using Density Functional Theory (DFT) and Many Body Perturbation Theory (MBPT) to the DFT as the GW approximation and the resolution of the Bethe Salpeter Equation have been done to evaluate the structural, electronic and optical properties of these germanosilicate systems. Influence of the Ge-content on the properties of neutral oxygen vacancy, also called oxygen deficient center, is also investigated.

**PACS Keywords:** silica, germanium, density functional theory, many body perturbation theory

## 1 INTRODUCTION

Doping amorphous silicon dioxide (a-SiO<sub>2</sub>) with germanium is a fundamental process in fiber optics technology in order to control the refractive-index profile along the fiber diameter and then its guiding properties (attenuation, dispersion). The optical properties of the doped silica layers deposited to design the fiber core and cladding are linked to the structural and electronic properties of these different glasses at the atomic scale, through the presence of absorbing point defects, due to fabrication process. First principles calculations can then help understanding and then controlling these properties by giving new insights about the phenomena happening at this scale and their dependences on the Ge contents. In this study, we focus on the modifications of physical and chemical properties of silica with increasing amounts of germanium using *ab initio* method. In the following, we will first expose our computational methodology. In a second part, we will present the first results obtained on the structural and electronic properties. And finally, we will

conclude our study and briefly show the subject that will be presented at the conference.

## 2 COMPUTATIONAL METHOD

Our study is performed in a 108 atoms amorphous silica cell containing 36 Si and 72 O atoms (see [1] for details on the generation and the analysis of the properties of this amorphous cell). We relax the atomic positions and the periodic cell in the framework of Density Functional Theory (DFT) in the Local Density Approximation (LDA) with the Quantum ESPRESSO package [2] to obtain the structural and energy properties. With this method, we generate one pure SiO<sub>2</sub> cell. We then dope in the cell by incorporating a germanium atom in substitutional position of a silicon atom. To increase the germanium concentration in the cell, we raise the number of replacements of Si by Ge atoms from 1 to 5. In every case, a statistical study on all the possible silicon sites is done to consider the non-equivalence of the atom site in this amorphous material (see discussion in [3]) and in order to select the lowest energy configuration as the more probable to occur during the glass fabrication.

Starting from the DFT-LDA configurations (structures and wavefunctions), we perform Many Body Perturbation Theory (MBPT) calculations to the DFT with the SaX package [4]. We first introduce the GW approximation to correct the discrepancies on the evaluation of the band gap due to the DFT. Finally calculations solving the Bethe Salpether Equation (BSE) allow to get the optical properties of the investigated configurations.

## 3 RESULTS

Images of the lowest cell structure configurations for different concentrations of germanium are shown in Figure 1. We can first notice that germanium atoms have the tendency to pack in small clusters of germania and not to be

homogeneously distributed inside the glass. Such result agrees with experimental work. In the final paper, this particular result will be discussed in details comparing different configurations as well as its implications concerning the generation of point defects in such systems.

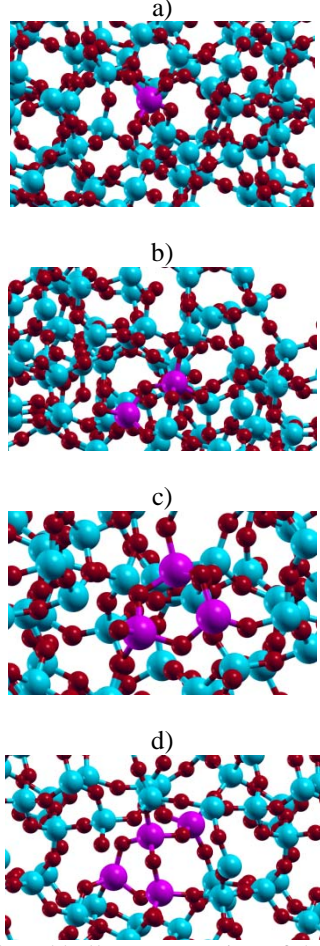


Figure 1: Stick and ball representation of the silica cells with various concentration of Ge : a) 2.8%, b) 5.5%, c) 8.3%, and d) 11.1%.

In Figure 2 are shown the first results obtained in GW concerning the variation of the band gap of silica cells diversely doped with germanium. The values of the band gap (around 9 eV [5]) are in very good agreement with experimental values, thanks to the use of the GW approximation. The band gap decreases smoothly with the increase of the germanium content.

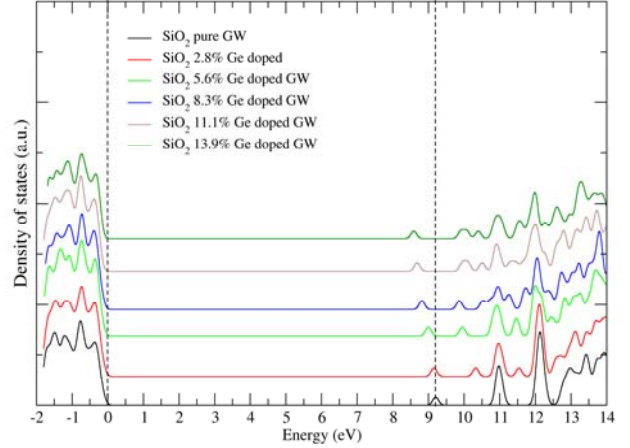


Figure 2: Density of states (in arbitrary units) vs. the energy (in eV) in function of the concentration of germanium.

#### 4 CONCLUSION AND PERSPECTIVES

We estimate the electronic and optical properties of pure and germanium doped silica. MBPT allows to correctly reproduce the experimental values available in literature. In the final paper, results will be presented for dopant concentrations from pure  $\text{SiO}_2$  to total replacement of Si atoms by Ge atoms, i.e.  $\text{GeO}_2$ . The properties of the  $\text{GeO}_2$  glass will be analyzed. Variations of the properties of neutral oxygen vacancy in function of concentration and repartition of germanium in the amorphous silica cell will also be presented. This analysis will help to improve our knowledge on photosensitivity and radiation-induced sensitivities of germanosilicate glasses. The optical absorption properties of these point defects will be discussed in these different glasses

#### REFERENCES

- [1] L. Martin-Samos *et al.*, Phys. Rev. B, 71, 0114116, 2005.
- [2] P. Giannozzi *et al.*, J. Phys. Condens. Matter, 21, 395502, 2009.
- [3] N. Richard *et al.*, JNCS, 357, 1994, 2011.
- [4] L. Martin-Samos *et al.*, <http://www.sax-project.org>
- [5] S. T. Pantelides *et al.*, Phys. Rev. B, 13, 2667, 1976.

# Vibrations of Oxygen Interstitials in $\alpha$ -Quartz

A.N. Kislov, A.F. Zatsepin, I.A. Aleksashina

Institute of Physics and Technology, Ural Federal University,  
620002, Mira Street, 19, Ekaterinburg, Russia  
e-mail address: a.f.zatsepin@ustu.ru

## ABSTRACT

Local configurations and vibration states of oxygen interstitials in different charge states in  $\alpha$ -quartz  $\text{SiO}_2$  are investigated by computer calculations. First-principles potential of the Buckingham type has been used in numerical modeling. A lattice relaxation around interstitials was calculated in the harmonic approximation. The study of the lattice dynamics in defective crystal is performed using the phonon local density of states. Frequencies of localized vibrations induced by oxygen interstitials are determined.

**Keywords:**  $\alpha$ -quartz; oxygen interstitials; defect structure; localized vibrations

## 1 INTRODUCTION

The variety of physical properties of  $\text{SiO}_2$ , such as electrical, mechanical, piezoelectric and optical properties depend crucially on point defects and their concentration. The important class of defects in silicon dioxide is oxygen interstitials presented in several charged states [1]. The computer simulation results of oxygen interstitials would enable the interpretation of experimental data. We reported earlier [2] the results of model calculations of the local configurations and the local lattice dynamics of a low-temperature modification ( $\alpha$ -quartz) of silicon dioxide containing oxygen vacancies in different charge states. The present study is devoted to the numerical calculations of the structure and the vibrational properties of  $\alpha$ -quartz  $\text{SiO}_2$  with oxygen interstitials in different charge states ( $\text{O}^{-2}$ ,  $\text{O}^{-1}$ ,  $\text{O}^0$  and  $\text{O}^{+1}$ ).

## 2 COMPUTER SIMULATION

The lattice relaxation around the oxygen impurities and frequencies of localized vibrations induced by these defects were calculated using first-principles potential of the Buckingham type [3] and the cluster method. In this technique, the crystal with a defect is divided into two spherical regions: an inner region and an outer region. The inner region is treated atomistically. The outer region is treated in the approximation of continuum. Atom displacements were determined by the minimization of the static lattice energy.

The effect of oxygen impurities on the vibration spectrum of  $\alpha$ -quartz was studied by calculating the phonon local densities of states in perfect and defective crystals. The local density of states  $G_\alpha^i(\omega)$  at the site of a  $i$ -th atom in the  $\alpha$ -th Cartesian direction is calculated using the expression [4]

$$G_\alpha^i(\omega) = -\frac{2\omega}{\pi} \operatorname{Im} g_\alpha(i, \omega), \quad (1)$$

where  $g_\alpha(i, \omega)$  are diagonal elements of the Fourier transform of the retarded Green function, which are determined by the relationship [5]

$$g_\alpha(i, \omega) = \langle i\alpha | \frac{I}{I(\omega^2 + i0) - D} | i\alpha \rangle. \quad (2)$$

Here  $I$  is the unit matrix,  $D$  is the dynamic matrix of the atom cluster and the vector  $|i\alpha\rangle$  has the dimensionality  $3N$  ( $N$  being the number of atoms in the cluster).

The calculation of the densities of states is facilitated with Lanczos recursion. The Lanczos algorithm is a technique to transform a dynamic matrix  $D$  into an equivalent tridiagonal form.

Investigations on static and dynamic behaviors of atoms require that a large atomic cluster was used. The cluster technique allows to get accurate description of long-range electrostatic interactions. We have found that a cluster with inner region containing 2000 atoms in which the Lanczos technique is used to 10 – 12 levels of recursion is sufficient to reproduce the local densities of states.

## 3 RESULTS AND DISCUSSION

Using the ab initio pair interatomic potentials [3] for  $\alpha\text{-SiO}_2$  we have modeled the equilibrium structures of the perfect and the defective crystals. For example, the local configuration for the oxygen interstitial  $\text{O}^{-2}$  is shown in Fig. 1. The calculations predict a displacement of the Si(1) and Si(2) atoms to one another. The oxygen atom O(1) is placed away from the oxygen interstitial. The calculations allowed to perform a comprehensive analysis of the lattice relaxation around oxygen interstitials in different charge

states and to show that these defects induce very strong and anisotropic lattice distortions. The values of the bond lengths between oxygen interstitials and some nearest atoms in relaxed configurations are given in Table 1.

Ion	Charge states of interstitial			
	-2	-1	0	+1
O(1)	2.328	2.602	2.565	2.530
Si(1)	1.806	2.565	2.725	2.821
Si(2)	2.165	2.938	3.037	3.101

Table 1: Distance (Å) between oxygen interstitials and nearest atoms.

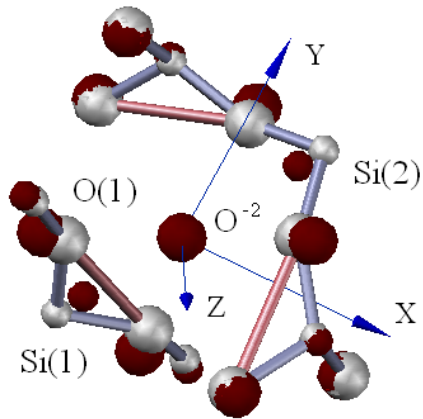


Figure 1: The structure fragment of  $\alpha$ -SiO<sub>2</sub> near the oxygen interstitial O<sup>-2</sup>. The lattice atoms before the relaxation are marked by grey color, brown - after the relaxation.

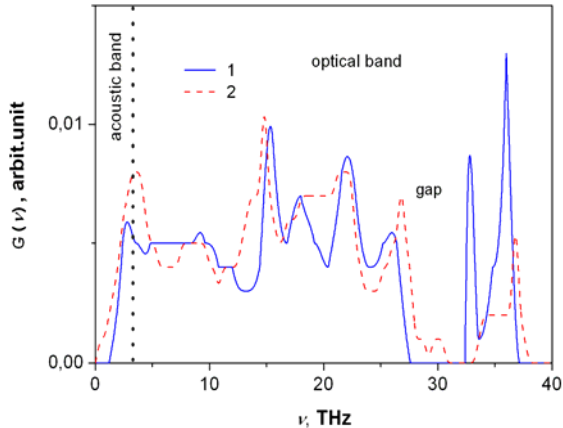


Figure 2: Phonon densities of states for a perfect  $\alpha$ -SiO<sub>2</sub> crystal (curve 1) and  $\alpha$ -SiO<sub>2</sub> containing interstitials O<sup>-2</sup> (curve 2).

The calculations of the phonon local densities of states demonstrated that it is redistributed after transition to oxygen interstitials. By way of example, Fig. 2 shows phonon densities of states for a perfect  $\alpha$ -SiO<sub>2</sub> crystal and  $\alpha$ -SiO<sub>2</sub> with interstitials O<sup>-2</sup>. According to the calculations, oxygen interstitials O<sup>-2</sup> induce the localized vibrations such as resonant, gap and local vibrations. The frequency of local vibration is close to the upper-frequency boundary of the optical band. There are also the two gap vibrations. One of them is connected to movement of silicon atom Si(2) and has frequency near the low-frequency border of the forbidden band. Other gap vibration with frequency situated in the middle part of the forbidden band is caused by movement of oxygen atom O(1). As against gap and local vibrations there are three resonant vibrations which have frequencies in a low-energy optical band of spectrum.

In general, the results of modeling of vibrational spectrum of quartz crystals with oxygen defects allow to conclude that the quantity of the localized vibrations induced by oxygen interstitials and the values of frequencies depend on their charge state.

## REFERENCES

- [1] G. Roma and Y. Limoge, "Density functional theory investigation of native defects in SiO<sub>2</sub>: Self-doping and contribution to ionic conductivity", Phys. Rev. B 70, 174101-1, 2004.
- [2] A.N. Kislov, M.O. Toropov, A.F. Zatsepin, "Configurations and local vibrations of differently charged oxygen vacancies in quartz crystal", J. Non-Cryst. Solids. 357, 1912-1915, 2011.
- [3] B. W. H. van Beest, G. J. Kramer, R. A. van Santen, "Force fields for silicas aluminophosphates based on ab initio calculations", Phys. Rev. Lett. 64, 1955-1958, 1990.
- [4] R. Yamamoto, K. Haga, T. Mihara, M. Doyama, "The vibrational states in a realistic model of amorphous iron", J. Phys. F: Metal Phys. 10, 1389-1399, 1980.
- [5] P.E. Meek, "Vibrational spectra and topological structure of tetrahedrally bonded amorphous semiconductors", Phil. Mag. 33, 897-908, 1976.

# Early Silicon interstitial generation Silicon Oxide Amorphisation via Ring Pattern Nuclei

C. Mastail<sup>1,2,3</sup>, A. Hemeryck<sup>1,2</sup>, A. Estève<sup>1,2</sup>, N. Richard<sup>3</sup>, M. Djafari Rouhani<sup>1,4</sup> and G. Landa<sup>1,2</sup>

<sup>1</sup> CNRS, LAAS, 7 avenue du Colonel Roche, F-31400 Toulouse, France

<sup>2</sup> Univ de Toulouse, UPS, LAAS, F-31400 Toulouse, France

<sup>3</sup> CEA, DAM, DIF, F-91680 Arpajon, France

<sup>4</sup> Univ de Toulouse, LAAS, F-31400 Toulouse, France

## ABSTRACT

Nowadays an atomic scale understanding of the silicon oxidation process is urgently needed with the size reduction of microelectronic devices. In this context, we propose an *ab initio* investigation of the earliest stages of the growth of the silicon oxide interface. We detail the incorporation mechanisms of the first four oxygen molecules. We show how the resulting ring pattern nucleus induces an amorphisation of the silicon surface with the spontaneous generation silicon interstitials.

## 1. Introduction

Due to its importance for electronic devices the Si-SiO<sub>2</sub> interface has been extensively investigated on both experimental and theoretical points of view. It is certainly among the most studied solid-to-solid interfaces. However, despite this impressive knowledge, a detailed understanding of the growing chemical mechanisms of the Si-SiO<sub>2</sub> interface during the oxidation process remains elusive. Today, this understanding is crucial to reach the atomic scale control required for the future generation of devices.

In this context, our previous work was dedicated to the understanding of the early stages of silicon oxidation [1,2]. We showed that a semi-hexagonal oxide nucleus pattern results from the incorporation and the migration of two oxygen molecules on two adjacent dimer units of the topmost layer of the Si(100)-*p*(2x1) surface (see

Fig. 1). This semi-hexagonal network offers a reasonable transition between the silicon cubic network and an amorphous oxide.

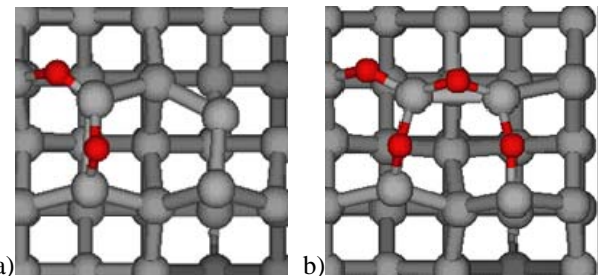


Figure 1: a) The silanone and b) the semi-hexagonal oxide nuclei pattern, which result respectively from the first and second oxygen molecule incorporation. Grey and red balls are respectively silicon and oxygen atoms.

Here we propose an *ab initio* investigation of the following steps of silicon oxidation process. We will present results concerning extension of the semi-hexagonal pattern consecutively to the spontaneous adsorption, dissociation and further incorporation of the third and fourth oxygen molecules into the silicon surface.

## 2. Results

Calculations lead to a spontaneous formation of an oxide nucleus, which forms a ring composed of four oxygen atoms inserted in two dimer units after the adsorption of the third oxygen molecule (see Fig. 2).

This ring oxide nucleus seems to be an unavoidable pattern allowing a layer-by-layer propagation of an amorphous oxide during the oxidation process.

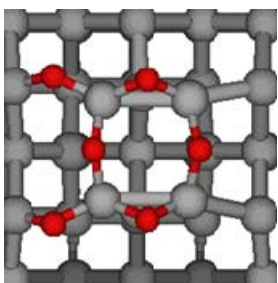


Figure 2: Ring pattern resulting from the incorporation of the third oxygen molecule. Grey and red balls are respectively silicon and oxygen atoms.

Indeed, due to the oxygen concentration in this pattern, a repulsive area is created reducing the oxygen molecule adsorption site around the ring nuclei. The lateral silicon surface oxidation seems to be possible thanks to growth and the coalescence of rings pattern.

Finally, using this ring structure, we will discuss oxidation of the second silicon layer and the spontaneous formation of interstitial silicon defect associated with the silicon oxidation process.

## References

- [1] A. Hemeryck *et al.*, J. Chem. Phys. 126, 114707 (2007).
- [2] A. Hemeryck *et al.*, Phys. Rev. B 79, 035317 (2009).

# A new fast gate current measurement protocol for the study of transient regimes in metal-oxide-semiconductor structures

Philippe Chiquet\*, Pascal Masson\*\*, Gilles Micolau\*, Romain Laffont\*, J. Postel-Pellerin\*, Frédéric Lalande\*, Bernard Bouteille\*, Arnaud Regnier\*\*\*

\* IM2NP, UMR 7334 CNRS, Université d'Aix-Marseille, 38 Avenue Joliot-Curie, 13451 Marseille Cedex 20 France

\*\* Université Nice-Sophia Antipolis, IM2NP UMR CNRS 7334, Polytech' Nice Sophia, 1645 route des Lucioles, 06410 Biot, France

\*\*\* ST MICROELECTRONICS, ZI Rousset, 13100 Rousset, France

## ABSTRACT

A new experimental protocol involving fast tunneling current measurements has been set up to highlight various physical properties of the floating gate / tunnel oxide / drain capacitor of Non-Volatile Memory (NVM) devices. Transient gate currents obtained on  $n^{++}/SiO_2/n^+$  MOS capacitors representative of the real device for negative gate signals are interpreted and successfully modeled.

**PACS Keywords:** MOS, band-to-band tunneling, impact ionization, dynamic current measurement, non-volatile memory.

## 1 INTRODUCTION

In floating gate NVM devices, “written” and “erased” states are obtained by modulating the value of the electric charge contained in the floating gate of the transistor, which is realized by making electrons transit through the tunnel oxide thanks to Fowler-Nordheim (FN) conduction [1]. As shown in [2], a standard FN law is not adequate to explain the voltage dependence of this injection current and parasitic phenomena such as deep depletion in the drain should be taken into account [3,4].

To understand the origin and consequences of such phenomena on the functioning of NVM devices, an experimental protocol, involving dynamic tunneling current measurements on test capacitors, has been set up to highlight some transient and stationary properties of the floating gate / tunnel oxide / drain zone of NVM cells. The transient evolution of the gate current is then explained and modeled taking into account several mechanisms such as band-to-band tunneling, FN current and impact ionization.

## 2 EXPERIMENTAL PROTOCOL

Current measurements are performed using an Agilent B1500A and its fast I-V module (WGFMU – B1530A) [5] on large area ( $A_{eff} \sim 100000 \mu m^2$ ), 7.5 nm thick oxide  $n^{++}/SiO_2/n^+$  capacitors (Fig.1), which are representative of

the floating gate / tunnel oxide / drain injection zone of NVM cells. The general shape of the electric signals applied to the gates of the test capacitors during this kind of measurement is represented in figure 2. In this case, both the tunneling and displacement currents can be acquired.

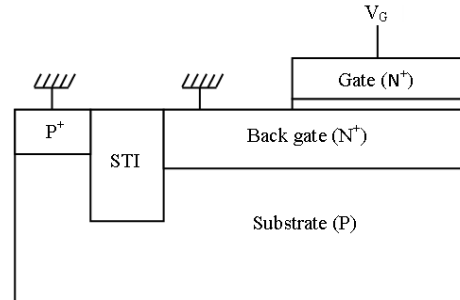


Figure 1: Simplified representation of the tested n-type capacitors. The signal is applied to the gate and current measurements are realized while the two other terminals are grounded.

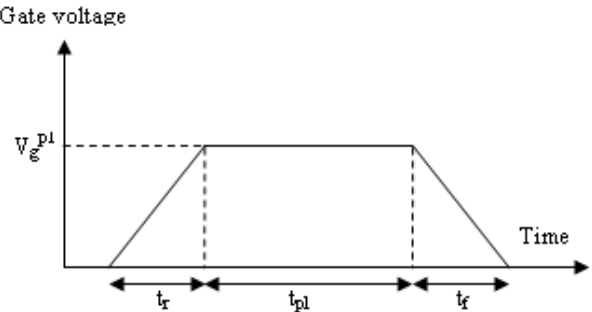


Figure 2: Gate signal versus time for dynamic current measurement. The shape of the pulse is determined by its rise time  $t_r$ , plateau time  $t_{pl}$ , fall time  $t_f$  and plateau voltage  $V_g^{pl}$ .

## 3 RESULTS

A typical example of dynamic current measurement carried out when a negative electrical signal is applied on the capacitor's gate is shown in figure 3. The measured gate and back gate currents can be divided into several zones of

interest. The back gate is first driven into deep depletion as the minority carriers cannot be created fast enough (zone 1) by thermal generation. The surface potential in the back gate becomes greater than the silicon bandgap value and band-to-band tunneling of electrons from the valence band to the conduction band occurs. The induced holes create the inversion layer at the oxide/back gate interface (zone 2). When the electric field in the oxide becomes high enough, band-to-band tunneling vanishes because of the increased inversion charge and is replaced by Fowler-Nordheim tunneling (zone 3). Further hole creation is generated through impact ionization and the permanent regime is finally reached (zone 4). Leakage of holes towards the substrate occurs when the minority carrier charge in the back gate reaches a threshold value, explaining the difference between both currents.

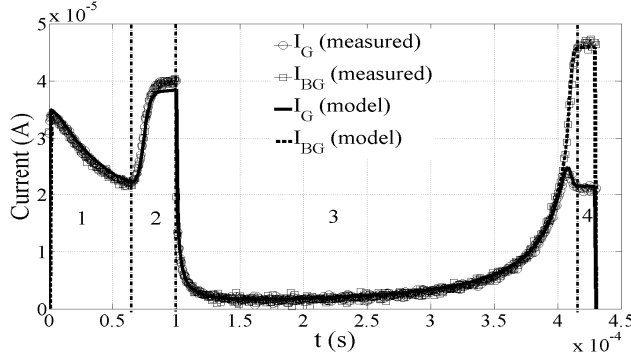


Figure 3: Comparison of measured gate and back gate currents with simulation obtained from our model ( $t_r = 100 \mu\text{s}$ ,  $V_g^{\text{pl}} = -8.4\text{V}$ ).

To account for the non-equilibrium situation in the back gate, a Fermi quasi-level  $E_{\text{FP}}$  is introduced for minority carriers (holes). This energy level, which depends on the hole concentration, lies above the electron Fermi level for zones 1 and 2 and below it for zones 3 and 4. The total charge in the back gate  $Q_{\text{BG}}$  can be decomposed as:

$$Q_{\text{BG}}(t) = Q_{\text{D}}(t) + Q_{\text{P}}(t) \quad (1)$$

where  $Q_{\text{D}}$  is the charge due to majority carriers (electrons) and ionized doping impurities, and  $Q_{\text{P}}$  is the charge due to minority carriers. The total gate and back gate currents result from several contributions as follows:

$$I_{\text{G}}(t) = I_{\text{TUN}}(t) + dQ_{\text{G}}(t)/dt \quad (2)$$

$$I_{\text{BG}}(t) = I_{\text{TUN}}(t) (1 + \alpha_{ii}) + I_{\text{BBT}}(t) + I_{\text{SLC}}(t) \quad (3)$$

where  $I_{\text{TUN}}(t)$  is the current tunneling through the oxide,  $Q_{\text{G}}(t)$  the gate charge,  $\alpha_{ii}$  the number of electron/hole pairs generated per electron tunneling through the oxide,  $I_{\text{BBT}}(t)$  the band-to-band tunneling current in the back gate modeled with a QFT approach (charge  $\times$  impact frequency  $\times$  tunnel transparency).  $I_{\text{SLC}}(t)$  is the current resulting from

the space charge length modulation, defined as the derivative of  $Q_{\text{D}}$  with respect to time:

$$I_{\text{SLC}}(t) = dQ_{\text{D}}(t)/dt \quad (4)$$

According to the analysis above,  $Q_{\text{P}}$  can be written at a given time as:

$$Q_{\text{P}}(t) = Q_{\text{P}}(t - \Delta t) + [\alpha_{ii} \cdot I_{\text{TUN}}(t - \Delta t) + I_{\text{BBT}}(t - \Delta t) - I_{\text{LEAK}}(t - \Delta t)] \cdot \Delta t \quad (5)$$

At each time step, the new position of  $E_{\text{FP}}$  is deduced from  $Q_{\text{P}}(t)$ . Typical simulated gate and back gate currents with some of their components are shown in figures 3 and 4. The agreement with experimental data is very good.

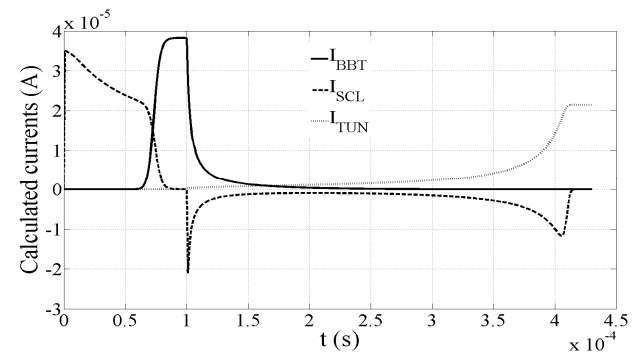


Figure 4: Temporal evolution of  $I_{\text{BBT}}$ ,  $I_{\text{TUN}}$ ,  $I_{\text{SCL}}$  ( $t_r = 100 \mu\text{s}$ ,  $V_g^{\text{pl}} = -8.4\text{V}$ ).

## 4 CONCLUSION

A new experimental protocol involving dynamic current measurements to study the physical properties of MOS capacitors has been presented. It has been shown that the transient gate and back gate currents are successively due to: 1) deep depletion in the back gate, 2) band-to-band tunneling (modeled with a QFT approach) in the back gate which creates the inversion charge layer, 3) an increase in oxide electric field, 4) impact ionization in the back gate enhancing the inversion charge above its equilibrium value.

## REFERENCES

- [1] S.M. Sze, Physics of Semiconductor devices, 2<sup>nd</sup> edition, Wiley-Interscience, pp. 496-498, 1981.
- [2] N. Baboux, C. Busseret, C. Plossu, P. Boivin, Microelectron. Reliab., vol. 45, pp. 911–914, 2005.
- [3] J. Sune, M. Lanzoni, R. Bez, P. Olivo, B. Ricco, IEDM Tech. Dig. 1991, pp. 905-908.
- [4] A. Kolodny, S. Nieh, B. Eitan, J. Shappir, IEEE Trans. Electron Devices, vol. 33, pp.835-844, 1986.
- [5] B1530 manual, Agilent Technologies.

# Porous Silica as host for PEG-supported coumarin molecules.

C.M. Carbonaro\*, M.F. Casula\*\*, P.C. Ricci\*, M. Cubeddu\*\*, G. Tocco\*\*\*

\*Department of Physics, University of Cagliari  
Campus of Monserrato, s.p. n° 8 Km 0.700, 09042 Monserrato (Italy)  
\*\*Department of Chemical and Geological Sciences, University of Cagliari  
Campus of Monserrato, s.p. n° 8 Km 0.700, 09042 Monserrato (Italy)  
\*\*\*Department of Life Sciences and Environment, University of Cagliari  
Palazzo delle Scienze, Via Ospedale, 72, 09124 Cagliari (Italy)

## ABSTRACT

The chemical and physical properties of organic-inorganic systems made of PEG-supported coumarin and porous silica are presented. The hybrid system is based on a sol-gel silica support and infrared spectroscopy and thermogravimetric analysis indicates the embedding of the PEG – supported coumarin within the silica host. The optical properties of the systems are evaluated by means of UV-VIS optical absorption, steady-state and time resolved photoluminescence.

**PACS Keywords:** porous silica, coumarin, optical spectroscopy

## 1 INTRODUCTION

Since its discovery and isolation in the late 1820, the coumarin family, belonging to the flavonoid class of plant secondary metabolites, grew up to more than 1000 derivatives. The coumarin unit (5,6-benzo-2-pyrone, Fig. 1a) can be found in many natural and synthetic drug molecules with applications ranging from the biological and pharmacological fields, for their antioxidant, anticoagulant, antibacterial and anti-HIV properties, to the photophysical and photonic fields, because of their fluorescence characteristics, typically in the blue-green visible range [1]. Indeed coumarin derivatives find applications as laser dyes, solar energy collectors, fluorescent labels and probes in biology and medicine, or as base-compounds for fragrances, agrochemicals, and insecticides [1]. Among the others, 7-hydroxycoumarin (Fig. 1b), also known as umbelliferone or coumarin 4 (C4), is often regarded as the parent molecule of more complex coumarin derivatives and its photochemical and photophysical properties are largely investigated as the archetypal characteristics of the coumarin family. In particular, since C4 displays amphoteric features, depending on the solvent properties, such as pH and viscosity, proton transfer from the hydroxyl group to the carbonyl oxygen acceptor can occur and UV excited light emission from different species can be recorded [2]. In this respect, one of the main drawbacks of coumarins which poses severe restrictions to further

developments and applications is the poor solubility in water. In a previous paper we have shown that a successful strategy to circumvent this problem is the immobilization of coumarin derivatives on modified poly(ethyleneglycol) (PEG) supports [3]. Indeed, the PEG-supported hydroxyl coumarins do preserve their emission properties and the presence of the polymeric support, as expected, do confer to the compound the requested water solubility. In addition the PEG support is non-toxic and could allow the slow release of the supported molecules in view of possible pharmacological applications.

In the last decades, the research on dye molecules was dedicated to the realization of hybrid systems based upon organic dyes, such as rhodamines and coumarins, hosted within transparent inorganic matrices, such as amorphous silica glasses prepared by the sol-gel method. These attempts aimed to improve the chemical and physical properties of the dye, as compared to the solution systems, in particular concerning the mechanical and thermal properties, the photostability and the optical properties of these dyes. The fabrication of organic-inorganic hybrids can find applications both in the photophysics and photonics fields, in order to realize, for example, solid-state gain media, or in biomedicine to obtain new drug delivery systems [4].

In this work we present the characterization of the chemical and physical properties of PEG-supported 7-hydroxy-4-methyl coumarin embedded within porous silica synthesized by means of sol-gel method. The aim of the paper is to investigate the efficiency of the impregnation procedure for the investigated systems, the preservation of the optical properties of the dye molecules when embedded in the silica matrix and the possibility to release the supported molecules in biocompatible solvents such as water.

## 2 METHODS

PEG-supported 7-hydroxy-4-methyl-coumarin (Fig. 1b, in the following indicated as PEG-7H4MC) were synthesized by using the soluble support approach applied to the von Pechmann reaction as reported in a previous paper [3].

Porous xerogel silica matrices were synthesized by means of a two-step acid-base-catalyzed sol-gel procedure that uses tetraethoxysilicate (TEOS, Aldrich, 98%) as silica precursor, ethanol (EtOH, Carlo Erba, 95%) as solvent and urea,  $\text{CO}(\text{NH}_2)_2$ , as basic catalyst which promotes fast and controlled gelation. After reflux for 2 hours at  $85^\circ\text{C}$ , a very viscous sol was obtained and allowed to gel at  $40^\circ\text{C}$  in a sealed container. Finally, the  $\text{SiO}_2$  xerogel was obtained by calcination at  $200^\circ\text{C}$  in static air.

The Coumarin-Silica hybrid systems were realized by wet impregnation of  $\text{SiO}_2$  powders (420 mg) from an ethanolic suspension containing the PEG-supported dye (100 mg of PEG-7H4MC in 100 ml of Et-OH) under stirring. The rinsing procedure was performed by immersion of the hybrid system (450 mg of PEG-7H4MC / $\text{SiO}_2$ ) into distilled water (100 ml) under stirring. In both the cases, the solid phase was extracted by centrifugation and thermally treated at  $40^\circ\text{C}$  ( $100^\circ\text{C}$ ) to remove the residual Et-OH (water) solvent.

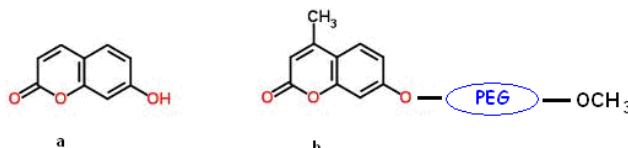


Figure 1: Scheme of C4 (a) and PEG-7H4MC (b).

Fourier Transform Mid-IR spectroscopy and thermogravimetric and differential thermal analysis (TGA-SDTA) were used for a qualitative and quantitative assessment of the dye loading into the silica xerogel. The coumarin uptake by the silica porous support was also monitored by UV-Vis absorption and photoluminescence spectroscopy. FTIR absorption measurements were performed by means of FTIR spectrophotometer Vector 22 (Bruker) in the 400-4000  $\text{cm}^{-1}$  with a spectral resolution of 4  $\text{cm}^{-1}$ . The thermogravimetric analysis was performed by means of a Mettler Toledo thermobalance (mod. TGA/SDTA 851) allowing the simultaneous acquisition of both the thermogravimetric (TGA) and differential thermal analysis (DTA) under Ar gas carrier (50 ml/min flux) and  $\text{O}_2$  reactive gas (40 ml/min flux) in the 25 – 1000  $^\circ\text{C}$  range with a 10  $^\circ\text{C}/\text{min}$  rate.

### 3 RESULTS AND DISCUSSION

Figure 2 shows the DTA and TGA diagrams of the hybrid system and, for comparison, of the pure silica powders. It can be seen that the hybrid system is characterized by two processes: the first one endothermic, below  $200^\circ\text{C}$  related to the release of the residual engulfed solvent (weight loss of about 10%); the second one, above  $200^\circ\text{C}$ , is exothermic and related to the burning of organic compounds (weight loss of about 14%). The thermogravimetric analysis displays that the embedding procedure allows to introduce the PEG-supported coumarin molecules within the silica host. This finding is well

confirmed by the FTIR spectra reported in Figure 3: in addition to the features typical of sol-gel silica, the peak at about 2800  $\text{cm}^{-1}$  related to the C-H vibrations is a clear fingerprint of the presence of PEG-supported coumarin within the silica matrix. Preliminary results on the chemical and physical properties of the systems after the rinsing treatment indicate the possibility to efficiently release the embedded compounds, the first step to engineer a porous silica based drug delivery system.

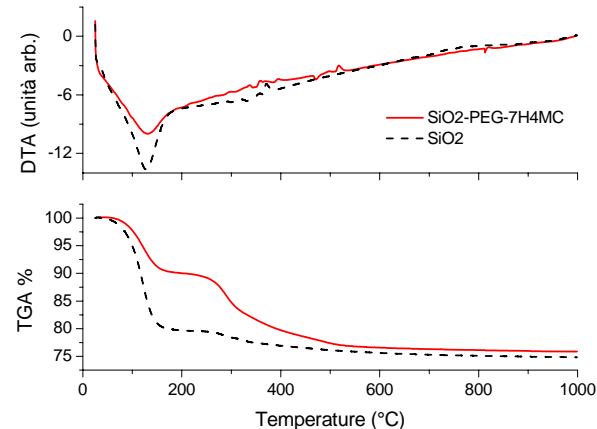


Figure 2: DTA and TGA diagrams of the hybrid system and, for comparison, of the pure silica powders.

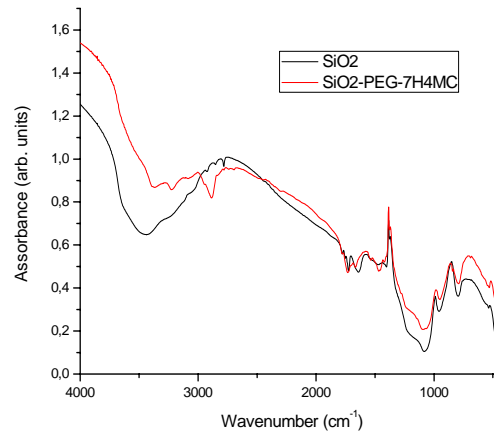


Figure 3: FTIR spectra of the hybrid system and, for comparison, of the pure silica powders.

### REFERENCES

- [1] S.R. Trenor, A.R. Shults, B.J. Love, T.E. Long, Chem Rev 104, 3059, 2004
- [2] I. Georgieva, N. Trendafilova, A. Aquino, H. Lischka, J. Phys. Chem. A 109, 11860, 2005.
- [3] G. Tocco, C.M. Carbonaro, G. Meli, G. Podda, Molecules 14, 210, 2009
- [4] C.M. Carbonaro, P.C. Ricci, S. Grandi, M. Marceddu, R. Corpino, M. Salis, A. Anedda, RSC Advances, 2, 1905, 2012.

# Temperature dependence of O<sub>2</sub> singlet photoluminescence in silica nanoparticles

S. Agnello\*, L. Vaccaro\*, G. Iovino\*, M. Cannas\*, K. Kajihara\*\*

\*Physics Department, University of Palermo, Via Archirafi 36, I-90123 Palermo, Italy.

\*\*Department of Applied Chemistry, Graduate School of Urban Environmental Sciences, Tokyo Metropolitan University, 1-1 Minami-Osawa, Hachioji 192-0397, Japan.

## ABSTRACT

The lifetime of O<sub>2</sub> singlet excited state is determined for the molecules embedded in silica nanoparticles. The photoluminescence band area and its lifetime are determined by measurements under infrared excitation from room temperature down to 10 K. These observations provide insights into the relaxation mechanisms from the excited state. Data are interpreted on the basis of active non-radiative relaxation channels involving high energy vibrational modes of silica.

**Keywords:** O<sub>2</sub> singlet state, silica nanoparticles, time-resolved photoluminescence, near infrared emission.

## 1 INTRODUCTION

Since many years much interest has been shown in the study of oxygen molecules embedded in silica systems [1]. In particular, the oxidative process of silicon in Metal Oxide Semiconductor devices is governed by the diffusion of oxygen through the growing silica layer. On the other side, the presence of oxygen molecules inside silica has relevant effects on the material radiation sensitivity. In this context, it has been observed that the O<sub>2</sub> molecule can be directly detected by its near infrared (NIR) emission and a deep characterization of oxygen spectroscopy has developed in silica also in view of the potentiality that spectroscopic detection has for the study of the above mentioned processes [2].

A point of particular interest is the study of the relaxation mechanisms of the excited states and the role of the interaction with the host matrix. These features indeed affect the overall emission efficiency and the possibility to detect the molecule. It has already been shown that the presence of impurities in the silica matrix and also the same silica vibration affects the O<sub>2</sub> de-excitation [3]. The relaxation, in particular, seems to be affected by high energy vibrational modes that induce an energy release through an electronic to vibration transfer mechanisms. The presence of other non radiative processes of O<sub>2</sub> in silica could be relevant and need to be investigated. In this respect the study of the lifetime and emission features as a function of temperature could be of help in clarifying the overall relaxation mechanisms [4].

Starting from the enhanced emission properties of nanosilica particles loaded with O<sub>2</sub> molecules [5], in this study we report an investigation of the temperature dependence of the singlet emission from room temperature down to 10 K.

## 2 EXPERIMENTAL METHODS

The samples used in this work are obtained by pressing powders of commercial silica nanoparticles with average diameter 40 nm. The obtained tablets were opportunely loaded with O<sub>2</sub> molecules [5].

Both for photoluminescence (PL) and PL lifetime measurements we used the excitation from the fundamental of a Nd:YAG laser at 1064 nm. In the PL measurements, the light from the sample was spectrally resolved by a monochromator (SpectraPro 2300i, PI/Acton) installing a 600 grooves mm<sup>-1</sup> grating and was acquired by a liquid nitrogen cooled InGaAs photodiode. The bandwidth of the spectrometer was ~3 nm.

For lifetime measurements, a mechanical chopper was inserted between the Nd:YAG and the sample, and the signal from the photodiode was recorded by a digital oscilloscope. Measurements as a function of temperature were executed in a liquid helium cryostat.

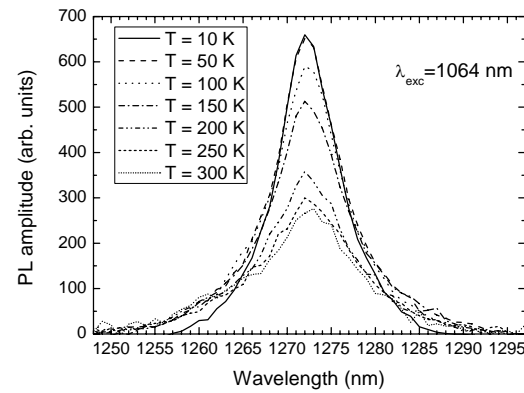


Figure 1: PL spectra of O<sub>2</sub> in nanosilica measured under excitation at 1064 nm at different temperatures.

### 3 RESULTS

As reported in Fig.1, the usual emission band of O<sub>2</sub>, with peak position almost fixed at 1272 nm, was observed at all the investigated temperatures. These bands can be fitted by a Lorentzian lineshape. As shown in Fig.1 and summarized in Table 1, the PL band amplitude and the area decreased on increasing T. The amplitude decreased from 10 K to 300 K by a factor 2.5 whereas the area decreased by about 60%. The full width at half maximum monotonically increased on increasing the temperature. These results were somehow limited by the spectral resolution of our experimental setup but evidence in any case that some temperature related effects are present.

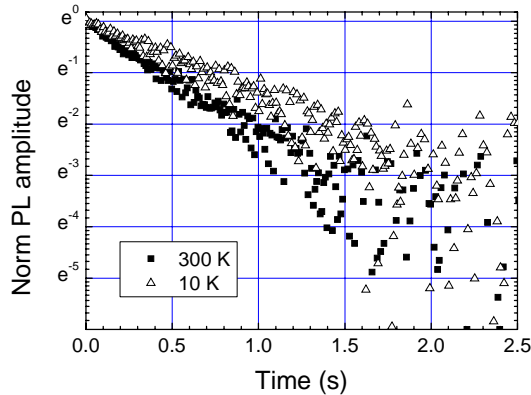


Figure 2: Normalized PL decay curves at 300K and 10 K of the emission at 1272 nm under excitation at 1064 nm.

The PL decay curves are reported in Fig.2 for measurements at 300 K and 10 K.. The decay was enhanced on increasing the temperature. The fit of the data with a single exponential decay function yielded the PL decay constant of  $(0.46 \pm 0.01)$  s at 300 K and  $(0.70 \pm 0.02)$  s at 10 K. These data further support the presence of thermally activated processes that influence the emission features.

TABLE 1: Spectral parameters of the Lorentzian curves best fitting the data reported in Fig.1

T (K)	Emission center (nm)	Emission Width (nm)	Emission Area (arb. Units)	Amplitude (arb.units)
10	1272	8.4	9278	658
50	1272	8.9	9304	645
100	1272	9.6	9085	585
150	1272	10.6	8688	500
200	1272	12.0	6731	339
250	1272	12.6	5953	287
300	1272	12.7	5401	263

The obtained results of the temperature dependence of the PL spectral shape and lifetime suggest that low energy phonons related mechanisms are coupled with the O<sub>2</sub> excited singlet state. The occurrence of a temperature dependence of the lifetime further shows that thermally activated phonons have to be considered in removal of energy from excited state. These aspects could be relevant in evaluating the quantum efficiency of O<sub>2</sub> emission and the improvement of its detection in silica.

### REFERENCES

- [1] G. Pacchioni, L. Skuja, and D. L. Griscom, eds., Defects in SiO<sub>2</sub> and Related Dielectrics: Science and Technology (Kluwer Academic Publishers, Dordrecht, 2000).
- [2] K. Kajihara et al., J. Non Cryst. Solids, 354, 224-232, 2008.
- [3] K. Kajihara et al., Appl. Phys. Expr., 2, 056502 1- 3, 2009
- [4] L. Skuja et al., Phys. Rev.B, 58, 14296-14304, 1998.
- [5] S. Agnello et al., J. Phys. Chem. C, 115, 12831-12835, 2011.

# Properties of methyl radical induced by irradiation in high-purity amorphous SiO<sub>2</sub> and in natural SiO<sub>2</sub>-clathrate Melanophlogite

G. Buscarino, S. Agnello, F.M. Gelardi and R. Boscaino

Dipartimento di Fisica dell'Università di Palermo  
Via Archirafi 36, 90123, Palermo, Italy

## ABSTRACT

We report an experimental investigation by electron paramagnetic resonance (EPR) on methyl radical induced by  $\gamma$ -ray irradiation in high-purity amorphous silicon dioxide ( $a\text{-SiO}_2$ ) and in a polycrystalline sample of Melanophlogite, a rare natural form of SiO<sub>2</sub>-clathrate. From the analysis of the EPR spectra we have estimated the correlation time of the hindered rotational motion of CH<sub>3</sub><sup>•</sup> molecules in the two different materials both for T=300 K and T=77K. This physical quantity gives a quantitative measure of the degrees of freedom of the motion of CH<sub>3</sub><sup>•</sup> molecules trapped in the two solid systems, putting forward relevant information on the properties of the cavities in which the radicals are confined. In particular, our data suggest that in  $a\text{-SiO}_2$  the CH<sub>3</sub><sup>•</sup> molecules are trapped in interstices with diameter significantly lower than 5.7 Å.

**PACS Keywords:** methyl radical, electron paramagnetic resonance, radiation effects, clathrate, silica.

## 1 INTRODUCTION

Methyl radical play a relevant role in many fields of research, as in biochemistry [1,2], in solid state physics [3-5] and in geology [6]. It is usually recognized in EPR spectra by its characteristic multiplet of four hyperfine components with relative intensities 1:3:3:1 and 2.28 mT splitting between adjacent lines. Griscom have identified CH<sub>3</sub><sup>•</sup> radicals in  $a\text{-SiO}_2$  X-ray irradiated at a dose of 4.6x10<sup>7</sup> Gy, and concluded that it is generated by radiodissociation of either CH<sub>4</sub> or CO dissolved in the material during fusion process and subsequent reaction of C with radiolitic H. Methyl radicals were also observed and characterized in clathrate structures (see, for example, ref. 6). In these systems they are usually formed by dissociation of some of the CH<sub>4</sub> molecules which naturally reside into the cages of the material.

Here we report a characterization and a comparative discussion of the properties of the hindered rotations motion of CH<sub>3</sub><sup>•</sup> molecules trapped in high-purity  $a\text{-SiO}_2$  and in the SiO<sub>2</sub>-clathrate Melanoflogite.

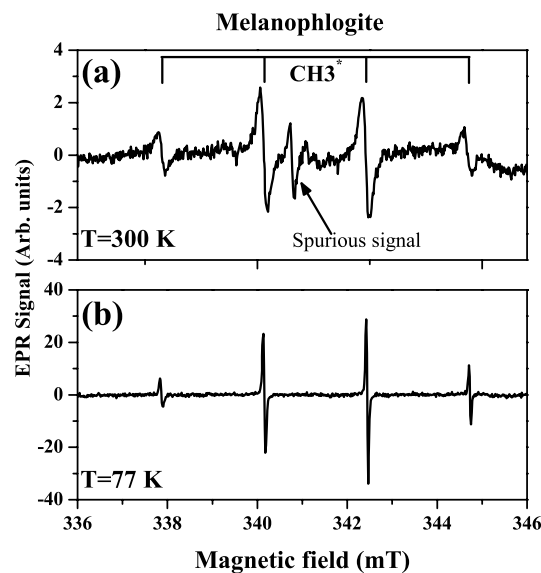


**Fig. 1** EPR spectra obtained for the methyl radical in the sample of Melanophlogite at (a) T=300 K and at (b) T=77K.

## 2 EXPERIMENTAL

The materials considered here consist in a sample of commercial Suprasil 1 produced by Heraeus [7] and a sample of natural Melanophlogite from Fortullino (Italy).

The materials considered were subjected to  $\gamma$ -ray irradiation at the doses of 500 kGy (Suprasil 1) and 100 kGy (Melanophlogite).

EPR measurements were carried out at T=300 K and at T=77 K with a Bruker EMX-micro-Bay spectrometer working at frequency of about 9.8 GHz (X-band) and with magnetic-field modulation frequency of 100 kHz. Low temperature spectra were obtained by putting the sample into a dewar flask filled with liquid nitrogen.

## 3 RESULTS

In Fig. 1(a) we report the EPR spectrum obtained at T=300 K for the Melanophlogite sample. As it is evident,

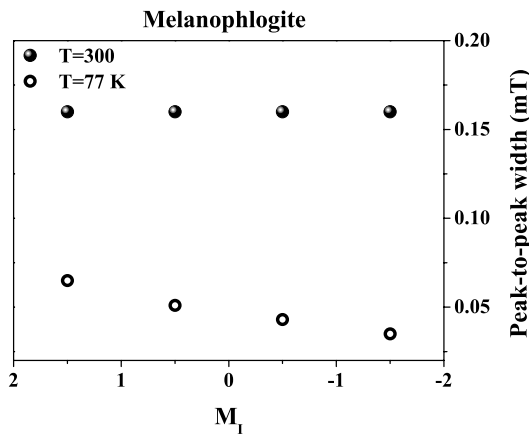


**Fig. 2** Peak-to-peak width of the component lines of the methyl radical hyperfine multiplet corresponding to different values of the quantum number  $M_I$  (Melanophlogite).

the characteristic hyperfine multiplet of methyl radical is readily recognized. For sake of comparison in Fig. 1(b) we report the EPR spectrum acquired for the same sample at  $T = 77\text{ K}$ , where a strong narrowing of all the four hyperfine components is observed. This effect is shown more quantitatively in Fig. 2, in which we report the peak-to-peak width of the component lines of the methyl radical multiplet corresponding to different values of the quantum number  $M_I$ . It can be observed that together to the overall line width narrowing, another effect is also found: at low temperature the line width depends on  $M_I$ . It is well known that this effect is due to the hindered rotational motion of the radical [8]. In particular, it has been shown that by fitting the line width of the components of the multiplet at different values of  $M_I$  by a specific second order polynomial equation, the correlation time of the tumbling motion,  $T_c$ , can be estimated [4, 8]. The values of  $T_c$  obtained with this procedure for methyl radical observed in Melanophlogite are reported in the first row of Table 1. These data give a quantitative estimation of the degrees of freedom of the molecules in Melanophlogite at low and at room temperatures.

**Table 1**

	$T_c$ ( $T=300\text{ K}$ )	$T_c$ ( $T=77\text{ K}$ )
$\text{CH}_3^\bullet$ in Melanophlogite	$<<10^{-8}\text{ s}$	$2 \times 10^{-8}\text{ s}$
$\text{CH}_3^\bullet$ in Suprasil 1	$2 \times 10^{-8}\text{ s}$	$6 \times 10^{-8}\text{ s}$

A study similar to that above described was also applied to the methyl radical induced in Suprasil 1. The line widths of the hyperfine components estimated at  $T=300\text{ K}$  and at

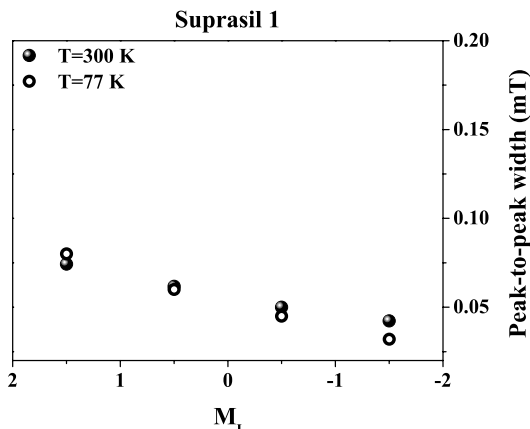


**Fig. 3** Peak-to-peak width of the component lines of the methyl radical hyperfine multiplet corresponding to different values of the quantum number  $M_I$  (Suprasil 1).

$T=77\text{ K}$  are reported in Fig. 3. As shown, in Suprasil 1 going from room to low temperature, a very limited narrowing effect and a somehow different dependence on  $M_I$  have been observed. Furthermore, it is interesting to note that the line widths observed in Suprasil 1 at room temperature are significantly narrower than those observed at the same temperature in Melanophlogite. The values of  $T_c$  obtained for methyl radical observed in Suprasil 1 are reported in the second row of Table 1.

The comparison of the correlation times of the methyl radical measured in Melanophlogite and in Suprasil 1 clearly indicates that  $\text{CH}_3^\bullet$  molecules rotate more easily in the former material than in the latter. As a consequence, it is reasonable to assume that the cavities in which the radical is trapped are larger in the former than in the latter. Finally, since it is well known that Melanophlogite is characterized by cages with diameters larger or equal to  $5.7\text{ \AA}$ , we conclude that the interstitial position in which  $\text{CH}_3^\bullet$  molecules are trapped in  $\alpha\text{-SiO}_2$  are significantly smaller than  $5.7\text{ \AA}$  in diameter.

## REFERENCES

- [1] A. Romieu, S. Bellon, D. Gasparutto, J. Cadet, Org. Lett., 2, 1085, 2000.
- [2] S. Hix, M.B. Kadiis, R.P. Mason, O. Augusto, Chem. Res. Toxicol., 13, 1056, 2000.
- [3] R.A.B. Devine, J.-M. Francou, Chem. Phys. Rev. B, 18, 12882, 1990.
- [4] E.J. Friebele, D.L. Griscom, J. Non-Cryst. Solids, 57, 167, 1983.
- [5] C.L. Gardner, E.J. Casey, Canadian J. Chem., 46, 207, 1968.
- [6] L.O. Anderson, Phys. Chem. Minerals, 35, 505, 2008.
- [7] Heraeus Quartzglas online catalog, 2010.
- [8] J. A. Weil, J. R. Bolton and J. E. Wertz, Electron Paramagnetic Resonance (Wiley, New York, 1994).

# Comparative study of fused silica materials for ArF laser applications

Ch. Mühlig\*, S. Bublitz, H. Bernitzki\*\*

\* Institute of Photonic Technology  
Albert-Einstein-Str. 9, 07745 Jena, Germany  
\*\* JENOPTIK Optical Systems GmbH  
Göschwitzer Str. 25, 07745 Jena, Germany

## ABSTRACT

We report on a comparative study of a variety of fused silica materials for ArF laser applications, which differ regarding their OH content. Laser induced deflection (LID) technique is applied to measure directly and absolutely the absorption coefficient in fused silica materials at 193 nm as a function of the incident laser fluence in the range 1...3 mJ/cm<sup>2</sup> before and after applying 20 million shots at a fluence of 5 mJ/cm<sup>2</sup>. In addition the laser induced refractive index change is detected by interferometer measurements after the prolonged irradiation for all samples.

**PACS Keywords:** Silica glass, absorption coefficients, laser induced degradation, compaction, luminescence

## 1 INTRODUCTION

For DUV laser applications different modifications of fused silica (FS) are on the market to serve for distinct requirements defined by various applications or even within one application. The most prominent example is the ArF laser lithography where particular requirements regarding absorption and refractive index change need to be fulfilled. Most of fused silica's modifications have been connected with the tuning of material parameters like the OH and the H<sub>2</sub> contents.

The aim of the present work is to define and carry out an appropriate evaluation that gives insights in the differences between these fused silica modifications. Furthermore, possible correlations between the obtained optical properties and material parameters have been investigated by measuring the OH and H<sub>2</sub> contents as well as the laser induced fluorescence (LIF).

## 2 EXPERIMENTAL

For investigating the absolute bulk absorption coefficients ArF laser irradiation, the laser induced deflection (LID) technique is applied [1]. In this work, a total of 16 fused silica samples from different vendors have been investigated, 7 of them show a low OH content of less than 80 wt-ppm. Further 7 samples feature a high OH content of larger than 900 wt-ppm. The remaining two samples are of medium OH content in the range 200...650 wt-ppm. The

sample geometry was chosen to be 25x25x20 mm<sup>3</sup> which allows for pure bulk absorption measurements. For 193 nm irradiation an ArF excimer laser (Excistar S Industrial, Coherent GmbH) with a repetition rate f = 1 kHz was applied. The ArF laser beam has been shaped by a diffractive optical element to achieve a homogeneous intensity distribution (top-hat) of 6x6 mm<sup>2</sup> at the sample's position. For the ArF laser pulses an integral-square pulse width  $\tau_{IS} \sim 16$  ns is calculated. For absorption characterization before and after prolonged irradiation, the fluence range 1...3 mJ/cm<sup>2</sup> has been applied according to the application specifications. The prolonged irradiation has been carried out over 20 million pulses at 5 mJ/cm<sup>2</sup>.

The OH and H<sub>2</sub> contents have been determined by infrared spectral photometric measurements. The ArF laser induced refractive index changes (phase difference) have been detected by interferometer measurements at 633 nm ( $\mu$ Phase Plano 2", FISBA OPTIK). Laser induced fluorescence measurements have been carried out according to a previously described manner [2].

## 3 RESULTS

At the initial stage of irradiation, low OH containing fused silica ([OH] < 80 wt-ppm) exhibits both, the lowest absorption coefficient and the lowest absorption increase with fluence (dk/dH) in the range 1...3 mJ/cm<sup>2</sup>. During 20 million laser pulses at 5 mJ/cm<sup>2</sup>, however, the absorption and the dk/dH values show a strong increase for the low OH containing fused silica. In contrast, the absorption of the medium OH containing samples ([OH] = 200...650 wt-ppm) is highest prior to the long term irradiation but is remarkably lowered throughout the 20 million laser pulses. High OH containing fused silica ([OH] > 900 wt-ppm) shows an intermediate absorption level, which only slightly increases or decreases during the irradiation with 20 million laser pulses. Figure 1 displays the summary of the absorption coefficients at 1 mJ/cm<sup>2</sup> prior and after the laser irradiation test. Figure 2 displays the summary of the fluence dependent absorption dk/dH (1...3 mJ/cm<sup>2</sup>) prior and after the laser irradiation test.

The ArF irradiation induced refractive index change is positive (= compaction) for all samples at the fluence 5 mJ/cm<sup>2</sup>. For analysis, a particular material classification is taking into account.

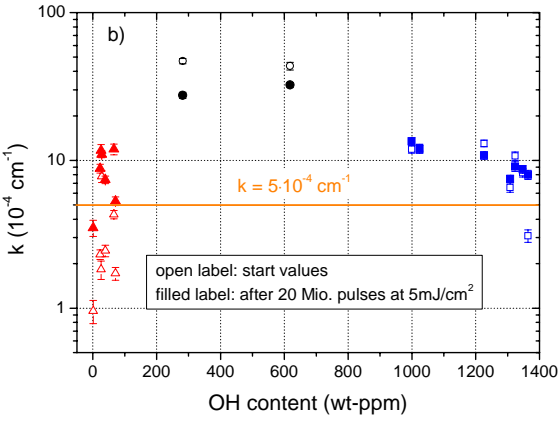


Figure 1: Change of the absorption  $k$  ( $H = 1 \text{ mJ/cm}^2$ ) during prolonged ArF laser irradiation with 20 Mio. pulses at  $5 \text{ mJ/cm}^2$

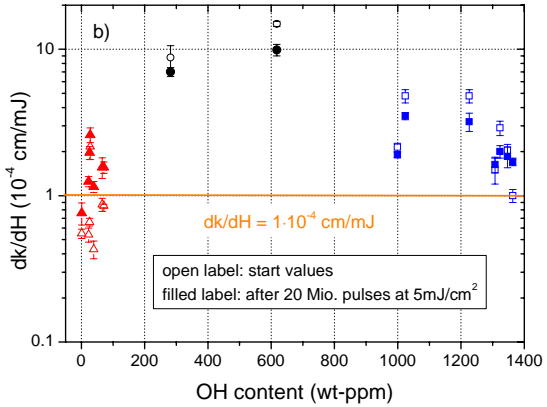


Figure 2: Change of the fluence dependent absorption  $dk/dH$  in the range  $1 \dots 3 \text{ mJ/cm}^2$  during ArF laser irradiation with 20 Mio. pulses at  $5 \text{ mJ/cm}^2$

For low and medium OH containing samples, referred to as compaction-dominated, the compaction factor defined by [3]

$$dn = k^{(1)} \cdot \frac{N \cdot I^2}{\tau} \quad (1)$$

increases with the OH content (Fig. 3).

For high OH containing samples, referred to as rarefaction-dominated, the resulting compaction factor is defined by

$$dn = k^{(2)} \cdot \left( \frac{N \cdot I^2}{\tau} \right)^{0.6} \quad (2)$$

and decreases with increasing  $H_2$  content (Fig. 4).

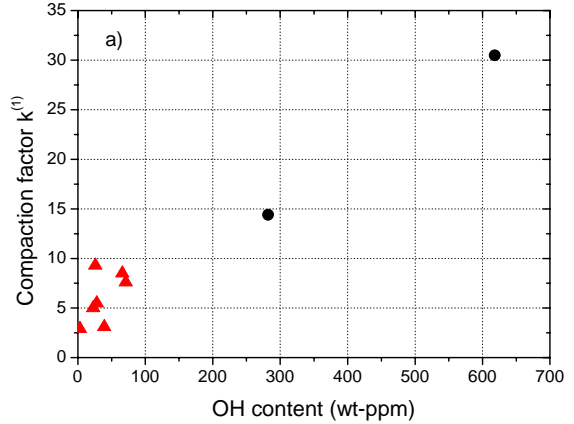


Figure 3: Compaction factor  $k^{(1)}$  (Eq. 1) as a function of the OH content for low to medium OH containing samples

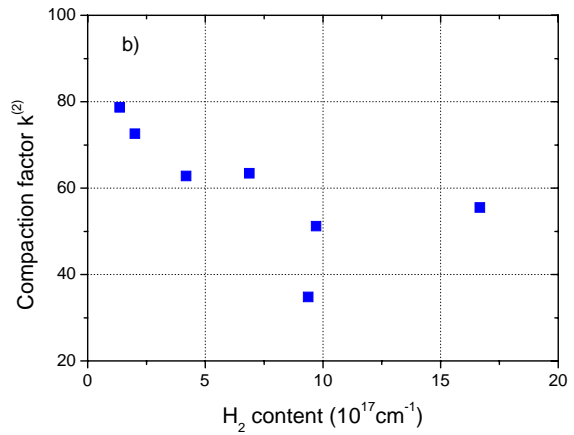


Figure 4: Compaction factor  $k^{(2)}$  (Eq. 2) as a function of the  $H_2$  content for high OH containing samples

## REFERENCES

- [1] Ch. Mühlig, W. Triebel, S. Kufert, S. Bublitz, Appl. Opt., 47, C135-C142, 2008.
- [2] Ch. Mühlig, S. Kufert, W. Triebel, F. Coriand, Proc. SPIE, 4779, 107-116, 2002.
- [3] J.M. Algots, R. Sandstrom, W. Partlo, K.Takahashi, H. Ishii, Y. Hasegawa, Proc. SPIE, 5377, 1815-1827, 2004.
- [4] R.E. Schenker, W.G. Oldham, J. Appl. Phys., 82, 1065-1072, 1997.

# Influence of the Substrate tube Quality on TSL Features of Yb-doped Silica Preforms of Optical Fibres.

M. Benabdesselam\*, F. Mady\*

\* Université de Nice-Sophia Antipolis, LPMC UMR CNRS 7336  
Parc Valrose, 06108 Nice Cedex 2, France

## ABSTRACT

We have demonstrated by spectral analysis of thermally stimulated luminescence that depending on the quality of the substrate-tube used during the MCVD technique, Yb-doping of silica preforms might be responsible for both the formation of the non-bridging hole centres (NBOHC) and their amount within the final preform. If these centres as well as those originating from the substrate tube are still present even after drawing, they will give rise to absorbing defects and thus a detrimental effect – like photo-darkening - on the performance of the ytterbium-doped optical fibres serving as amplifier (YDFA) or in high-power fibre lasers.

To describe the TSL of Yb-doped preforms, we also propose a mechanism based on the oxidation/reduction process involving hole traps and Yb impurities as recombining centres.

**PACS Keywords:** Thermoluminescence, silica, point defects, radiation, ytterbium.

## 1 INTRODUCTION

Among possible applications of active fibres, Yb-doped silica fibres are well appropriate for high-power fibre lasers and amplifiers (YDFA). Nevertheless, such fibres exhibit severe transmission losses in visible with a tail reaching the spectral region around 1  $\mu\text{m}$  where Yb-doped fibre lasers and amplifiers operate. These optical losses during operation of YDFA, known as photodarkening, as well as some possible physical mechanisms responsible of this effect have also been reported [1,2].

In this work, we introduce an original approach based on the thermally stimulated luminescence (TSL) and its spectral analysis. This technique offers the advantage of reflecting both recombination centres (e.g. Yb) and defects that absorb in a wide wavelength range (from UV up to NIR), thus participating probably in photodarkening. In addition to the characteristic emission of Yb, our measurements also reveal the luminescence pattern of NBOHC and that of other centres already present within the substrate tubes used for the MCVD.

## 2 MATERIALS AND EXPERIMENTAL DETAILS

The samples presented here consist of two pieces named TA and TB cut from two different commercially available fused-quartz substrate tubes and two round polished slices (1 mm thick) cut from the preformed rod grown by MCVD. The preforms PA and PB, made with tubes TA and TB respectively are of the same compositions: impurities are introduced by doping solution technique. TSL measurements were performed using a homemade reader. After irradiation by X-rays (45 kV, 30 mA) at room temperature (RT), TSL readout was performed by linear heating rate of 1  $\text{K s}^{-1}$  from RT to 773 K. The signal was recorded by means of a PM tube and an optical multi-channel analyser equipped with a CCD matrix detected the spectral distribution of TSL peaks.

## 3 RESULTS

TSL curves relative to preform PA and substrate tube TA are characterised by the same peaks with intensities of same order of magnitude and are composed of one main peak at 433 K and a small one at around 730 K. The similarity in peak positions indicates that at least two similar defect groups are populated by irradiation in both samples. These broad peaks are the result of the thermal release from closely distributed trap levels spread within the band gap.

TSL curves relative to preform PB and the corresponding tube TB do not show the TSL peak observed around 730 K in PA and TA. One assumes that it exists but because of its low intensity, it cannot be detected and probably hidden within the blackbody radiation. For the same conditions of irradiation and readout, the TSL curve of preform PB is characterised by two peaks located near 390 and 503 K. These two peaks probably exist in the glow curve of PA preform but hidden within the main broad peak at 433 K dominating the TSL signal. Indeed, the maximum TSL intensity of PB is much lower than that of PA. Concerning the substrate tube TB; it is not thermoluminescent at all. In terms of point defects, it means that the substrate tube TB is of much higher quality, compared to the tube TA.

According to TSL glow curves, one may consider that in addition to trap defects probably formed during synthesis of the PB preform and made from highest quality substrate tube, some other defects originating from the substrate tube TA itself still prevail during collapse of the preform PA. Afterwards, in order to know more about the defects acting as recombining centres in the TSL process of the substrate tube TA, spectral analysis of the emission of its 433 K peak is carried out. It shows three bands peaking at around 1.56, 2.4 and  $\sim$ 3.1 eV. The 3.1 eV band might be related to  $B_{2\beta}$  centre already observed in PL in fused silica glass after both  $\gamma$  and X irradiations [3]. The two other components are not relative to any well-known defect reported yet in silica.

Spectral distribution of the main peaks observed at 433 and 503 K on respectively PA and PB glow curves is presented on Fig. 1. For both preforms, the predominant feature in the spectra is the main characteristic emission of the  $^2F_{5/2} \rightarrow ^2F_{7/2}$  transition of Yb<sup>3+</sup> ions that seems to be unique in the spectrum of PB. Thus one can consider that the only recombining centres occurring in preform PB are Yb ions whereas in the case of preform PA, besides the dominant Yb<sup>3+</sup> emission, one can see that the emissions at 1.56 and 3.1 eV, already observed in the corresponding substrate tube TA still occur while the 2.4 eV band is completely quenched. The defect relative to this last band has been probably annealed during the preform synthesis. The new feature is the appearance on the spectrum of a pronounced shoulder at around 650 nm (1.9 eV).

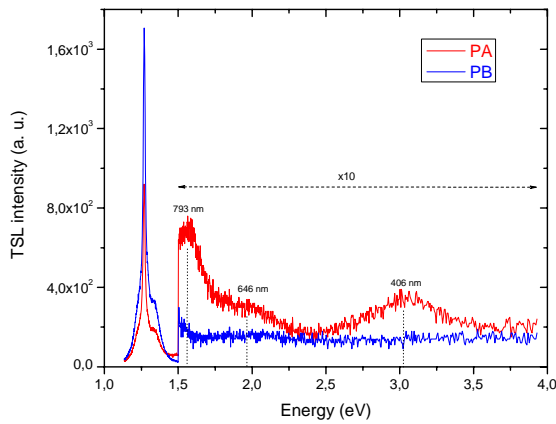


**Fig. 1.** Emission spectra of 433 and 503 K TSL peaks obtained on PA and PB preforms respectively

#### 4 DISCUSSION

It is shown in this study that at least two main trap defects are involved in TSL of each preform. The main emission of these TSL peaks is that of Yb<sup>3+</sup> ions at 1.27 eV. Hence, even if the origin of the trap defects still remains unknown, one can advance the hypothesis that these traps are of the same nature since they give arise mainly to the same luminescence emission. Thus, one probable physical

mechanism describing the observed TSL signal in these Yb-doped preforms might be the classical redox process.

According to this possible mechanism one can refine our previous hypothesis regarding the origin of traps by considering that all the TSL peaks observed on both preform correspond to hole trap defects.

Besides the trivalent Yb emission, the spectral emissions shown on Figure 1 have a shoulder at around 1.9 eV (PA) and a very weak signal at the same energy for PB. This band corresponds to the well-admitted emission usually attributed to the non-bridging oxygen hole centres in amorphous silica [4]. Our hypothesis concerning the TSL mechanism involving hole traps is somewhat comforted by the presence of these NBOHC centres known as a possible “reservoir” for released holes.

Another interesting feature on the data of Fig. 1 concerns the TSL intensity of the characteristic emission of Yb ions that is almost twice higher in the case of PB preform made from substrate tube of higher quality. It suggests that the emission efficiency of Yb is much better when this impurity is seen by the released holes during stimulation as the only possible recombining centre than when occur some competing centres (as for PA preform). The TSL spectral analysis relative to the lower quality substrate-tube (TA) does not show any feature at around 1.9 eV and the substrate-tube TB is not thermoluminescent at all. So, one can consider that NBOHC centres may arise effectively from the presence of Yb doping or during collapse. This is in good agreement with results of Dragic et al. [5], which showed that the introduction of Yb species increases the NBOHC concentration.

#### 5 CONCLUSION

We characterised the TSL properties of two identically Yb doped preforms after X- irradiation. Our data suggest that the TSL mechanism occurring in the preforms may be explained in terms of a redox process involving hole traps. The proposed mechanism is supported by the presence of NBOHC centres whose content seems to depend on the quality of the substrate tube used for the preform growth. Thus, to guard against possible problems of photodarkening in Yb doped fibres; it is shown here that the choice of the substrate-tube upstream might be a criterion that could be important on the quality of the preform.

#### REFERENCES

- [1] L. Van Pietersen, M. Heeroma, E. De Heer, A. Mijerink, J. Luminescence **91**, 177 (2000).
- [2] J.J. Koponen, M.J. Söderlund and J. Hoffman, Optics Express **14**, 24, 11539 (2006).
- [3] Y. Yoshida, T. Tanabe, S. Takahara and H. Yoshida, Nucl. Instrum. Meth. Phys. Res. B **191**, 382 (2002).
- [4] L. Skuja, in: G. Pacchioni et al. (Eds.), Defects in SiO<sub>2</sub> and Related Dielectrics, Kluwer, 73, (2000).
- [5] P.D. Dragic, C.G. Carlson and A. Croteau, Optics Express **16**, 7, 4688 (2008).

# Design of mid-infrared Er<sup>3+</sup>-doped microsphere laser

F. Prudenzano\*, L. Mescia\*, P. Bia\*, M. De Sario\*

\*Dipartimento di Elettrotecnica ed Elettronica, Politecnico di Bari  
Via E. Orabona 4, 70125 Bari, Italy

## ABSTRACT

A mid-infrared lasing system based on a tapered fiber coupled to a Er<sup>3+</sup>-doped microsphere has been modeled and numerically investigated. In order to design and optimize the device performance, a dedicated 3D numerical code exploiting the coupled mode theory and rate equations has been developed. The main energy level transitions, the secondary ion-ion interactions, the amplified spontaneous emission and the fiber-microsphere coupling phenomena have been taken into account. In order to optimize the lasing performance, several parametric simulations have been carried out. The obtained numerical results show that a low laser threshold can be obtained by using small microspheres.

**PACS Keywords:** tapered fiber, erbium, chalcogenide, whispery gallery modes, resonators.

## 1 INTRODUCTION

During the last years, micro- and nanosphere resonators have attracted a lot of interest because their striking properties such as high Q-quality factor ( $>10^8$ ), flexible choice of resonator material for lasing, construction easiness and low cost of fabrication. Such devices are used in many scientific applications like quantum information processing [1], nonlinear optics, cavity quantum electrodynamics (QED), biosensor analysis [2, 3]. Moreover, research efforts in rare earth doped microspheres have opened novel opportunities for enhancing the amplifier and laser performance in the mid-infrared wavelength range [4-6]. The electromagnetic field sustained by a dielectric microsphere, called whispering gallery mode (WGM), exhibits an high quality factor and small modal volume. As a consequence, it allows a good optical energy storage [7]. Chalcogenide glasses are suitable as laser and amplifying materials because of their high refractive index, higher capability to host rare-earth ions like erbium, low phonon energy and infrared transparency. These properties make possible a strong interaction of the electromagnetic field inside the microsphere with rare earth ions, allowing the development of a new generation of mid-infrared lasers. Even if many mathematical models of both passive [8,9] and active microsphere have been developed [4-6][10-11], more accurate models are essential for design and analysis purposes. To this aim, in this paper we propose a detailed 3D mathematical model allowing the performance evaluation of the laser formed of a tapered fiber coupled to

the Er<sup>3+</sup>-doped chalcogenide glass microsphere. The model takes into account, i) the stimulated emission at the signal wavelength, ii) the radiative and nonradiative rates among the Er<sup>3+</sup>-energy levels, at both the pump and the signal wavelengths, iii) the Er<sup>3+</sup>-energy level lifetimes, iv) the amplified spontaneous emission (ASE) noise around the signal wavelength, v) the ion-ion energy transfers. The obtained results show that, by using a pump signal at the wavelength  $\lambda_p=980$  nm, a lasing action in the wavelength range from 2740 nm to 2820 nm can occur.

## 2 MODEL AND NUMERICAL RESULTS

An accurate electromagnetic analysis has been performed. In particular, the modal electromagnetic field distribution and the z-depending propagation constant of the guided modes of the tapered optical fiber have been calculated by using the local modal theory, while the WGM field profiles in the microsphere have been evaluated by solving the scalar Helmholtz equation in spherical coordinates [12]. In the developed numerical code, several WGMs (l,m,n), in the signal wavelength range 2740 nm÷2820 nm, and the fundamental WGM (l=352, m=352, n=1), at the pump wavelength  $\lambda_p=980$ nm, have been considered.

Many parametric simulations have been performed to find the optimal geometrical parameters allowing control of the pump power circulating in the sphere and the lasing power transmitted through the coupled tapered fiber. In particular, the considered parameters are the fiber-microsphere gap g, the microsphere radius R<sub>0</sub>, the fiber waist radius a, the taper angle  $\delta$  and the thickness of the doped region S. By using a pump signal at the wavelength  $\lambda_p=980$  nm, it is possible to generate a population inversion between the Er<sup>3+</sup>-energy levels  $^4I_{11/2}$ ,  $^4I_{13/2}$ . Moreover, because of the high dopant concentration and the comparable lifetime of the  $^4I_{13/2}$ ,  $^4I_{11/2}$ ,  $^4I_{9/2}$  energy levels, a stimulated emission can occur in the wavelength range from 2740 nm to 2820 nm, i.e. where the erbium emission cross section exhibits a peak.

The modeling of the active behavior requires the calculation of the coupling coefficients, describing the fiber-microsphere interaction, the quality factor, depending on the losses in the system, the overlap factor, describing the overlap between the WGMs and the doped region, the transition rates among the Er<sup>3+</sup>-energy levels. To evaluate the device performance, the lasing output power  $P_{l,n}^{out}$  has been calculated by using the equation:

$$P_{out}^{l,n}(t) = \sum_{m=l-N}^l \sqrt{\frac{T_{l,m,n}^c}{\tau_{l,m,n}^{ext}}} P_{l,m,n}(t) \quad (1)$$

where the three integers  $l, m, n$  identify each WGMs propagating inside the microsphere,  $T_{l,m,n}^c$  is the circulating time inside the microsphere (round trip time) and  $\tau_{l,m,n}^{ext}$  is the intrinsic lifetime. In the calculation, the output power is calculated by adding the powers of all the  $N$  degenerate lasing modes, where  $1 - N \leq m \leq l$ .

Figure 1 shows the lasing output power  $P_{out}^{l,n}$  versus the input pump power  $P_{in}$ . It can be observed that for low pump powers, lower than 55 mW, no lasing occurs because the power is not enough to generate the ion population inversion. Moreover, also the effects due to the ion-ion interaction strongly influence the population dynamics. Increasing the input pump power over the threshold one ( $\approx 60$  mW), a lasing action arise for three different WGMs: WGM  $l=118, n=1$  with a power of -15 dBm, WGM  $l=111, n=2$  with a power of -22 dBm, and WGM  $l=88, n=7$  with a power of -25 dBm. All the other WGMs are not shown because their lasing power is lower than -90 dBm.

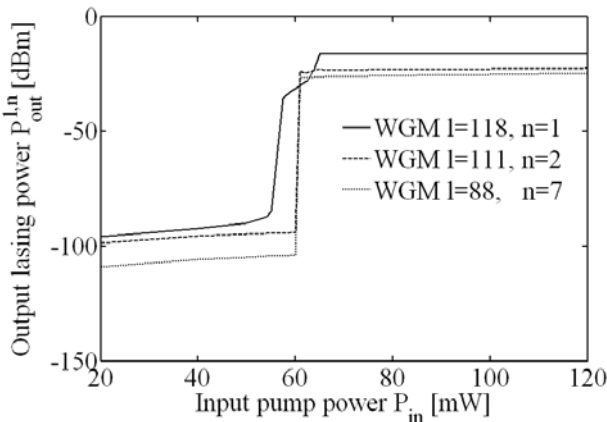


Figure 1: Output lasing power  $P_{out}^{l,n}$  versus the input pump power  $P_{in}$ .

## REFERENCES

- [1] L. Yang and J. Vahala, "Gain functionalization of silica microresonators," Opt. Lett., 28, 592-594, 2003.
- [2] Ren Hai-Cang, F. Vollomer, S. Arnold, and A. Libchaber, "High-q microsphere biosensor-analysis for adsorption of rodlike bacteria," Opt. Express, 15, 17410-17423, 2007.
- [3] F. Vollomer and A. Stephen, "Whispering-gallery-mode biosensing: label-free detection down to single molecules," Nature Meth., 5, 591-596, 2008.
- [4] L. Mescia, P. Bia, M. De Sario, A. Di Tommaso, and F. Prudenzano, "Design of mid-infrared amplifiers based on fiber taper coupling to erbium-

doped microspherical resonator," Opt. Express, 20, 7616-7629, 2012.

- [5] L. Mescia, F. Prudenzano, M. De Sario, T. Palmisano, M. Ferrari, and G.C. Righini, "Design of rare-earth-doped microsphere," IEEE Photon. Technol. Lett., 22, 422-424, 2010.
- [6] G.R. Elliott, G.S. Murugan, J.S. Wilkinson, M.N. Zervas, D.W. Hewak, "Chalcogenide glass microsphere laser," Opt. Express, 18, 26720-26727, 2010.
- [7] L. Xiao, S. Trebaol, Y. Dumeige, Z. Cai, M. Mortier, and P. Féron, "Miniaturized optical microwave source using a dual-wavelength whispering gallery mode laser," IEEE Photon. Technol. Lett., 22, 559-561, 2010.
- [8] M.L. Gorodetsky and V.S. Ilchenko, "Optical microsphere resonators: optimal coupling to high-Q whispering-gallery modes," J. Opt. Soc. Am. B, 16, 147-154, 1999.
- [9] Chan-Ling Zou, Y. Yang, Chun-Hua Dong, Yun-Feng Xiao, Xiao-Wei Wu, Zheng Fu Han, and Guang-Can Guo, "Taper-microsphere coupling with numerical calculation of coupled-mode theory," J. Opt. Soc. Am. B, 25, 1895-1898, 2008.
- [10] T. Kouki and T. Makoto, "Optical microsphere amplification system," Opt. Lett., 32, 3197-3199, 2007.
- [11] Y.G. Boucher and P.Féron, "Generalizad transfer function: A simple model applied to active single-mode microring resonators," Opt. Commun., 282, 3940-3947, 2009.
- [12] B.E. Little, J.P. Laine, and H.A. Haus, "Analytic Theory of Coupling from Tapered Fibers and Half-Blocks into Microsphere Resonators," J. Lightwave Technol., 17, 704-715, 1999.

# Luminescence of fused and unfused Bi-doped amorphous silica fabricated by SPCVD

Anatoly Trukhin\*, Janis Teteris\*, Aleksey Bazakutsa\*\* and Konstantin Golant\*\*

\*Institute of Solid State Physics, University of Latvia,  
LV-1063 Riga, Latvia

\*\*Kotel'nikov Institute of Radio-engineering and Electronics of RAS,  
Mokhovaya 11-7, Moscow, 125009, Russia

## ABSTRACT

Bismuth-doped high purity silica samples synthesized by surface-plasma chemical vapor deposition (SPCVD) are studied to investigate the origin of Bi-associated defects responsible for near infrared (NIR) luminescence. Two types of samples are studied: unfused Bi-doped silica film immediately deposited on the inner surface of a substrate silica tube and the same material after fusion obtained as the result of the tube collapsing to a rod by external heating. Luminescence is excited by pulsed UV (ArF – 193 nm, KrF – 248 nm) and green (532 nm) lasers. Luminescence bands centered at 620-650 nm, 808 nm and 1400 nm wavelengths are observed in both fused and unfused samples. Orange and near-infrared luminescences excited by the green laser have decay time constant of about 3  $\mu$ s for the 650 nm and of about 0.6 ms for the 1400 nm band at room temperature. Intensities of both bands do not depend on temperature in the 12 - 450 K range.

**PACS Keywords:** bismuth doped silica, near-infrared luminescence, surface-plasma chemical deposition technology

## 1 INTRODUCTION

Bismuth-doped silica attracts more and more attention as a new gain media for fiber amplifiers and lasers operating in the 1.1-1.5 microns wavelengths band [1]. Lack of alternative activators for this band distinguishes Bi-doped silica fibers regardless their currently rather poor gain properties as compared to Er- and Yb- doped fibers, which operate in longer and shorter wavelengths bands.

There are two main problems to tackle. The first one is the absence of a more or less reasoned energy diagram for the bismuth defect in a silica network, responsible for quantum transitions yielding lasing. The second problem results from the fact that there is no immediate correlation between the increase of Bi content in silica and the increase of gain. Instead, starting from a rather small concentration, typically not exciding  $10^{19} \text{ cm}^{-3}$ , further increase of Bi content leads to a significant decay of lasing performance of the fiber.

Current presentation summarizes results of our experiments on luminescence in bismuth doped silica fabricated by the SPCVD technology. Distinctive feature of

this technology is the possibility to synthesize high purity and differently doped amorphous silica in an unfused state, when its structure is developed by species' chemical adsorption from the gas phase on a substrate at a relatively low temperature.

Our study is aimed at getting more information regarding luminescence of Bi-associated defects in fused and unfused silica under different high energy optical excitations of materials. Particular attention is paid on temperature dependences of luminescence parameters which have not been documented for the case of Bi-related centers in silica yet. The comparison of as received unfused Bi doped silica film and its fused counterpart reflects possible impact of fiber fabrication process on the NIR.

Pulsed high energy light sources are used in our experiments for the luminescence excitation. ArF -193 nm wavelength excimer laser is able to excite localized states in silica network, a KrF – 248 nm and a diode – 532 nm wavelengths lasers are able to excite only intra-center transitions of an activator located in silica network.

## 2 EXPERIMENTAL

In our experiments Heraeus F300 silica tube 20 mm in outer diameter and 2 mm wall thickness is used as a substrate. In order to trace possible effect of fusion on the luminescence we fabricated the following structure. The structure consists of two deposited one by one layers of about 100 microns in thickness each. Bi-doped silicon dioxide (the first layer) is covered by undoped silica (the second layer) to prevent bismuth escape during subsequent tube high-temperature collapsing. Vapors of anhydrous  $\text{BiCl}_3$  together with other halides mixed with oxygen are used as a starting gas mixture supplied to reaction zone of the scanning plasma column. After deposition the tube is collapsed into a preform only on a half of the deposited length. The other half of the tube with the deposited on its inner surface amorphous material remained un-collapsed, and is used as an unfused sample for luminescence measurements.

Fig. 1 illustrates refractive index profile of the collapsed part of the tube. It is seen that bismuth contributes to an increase of the silica's refractive index. Oscillations in the refractive index profile are associated with variations of  $\text{BiCl}_3$  flow during the deposition.

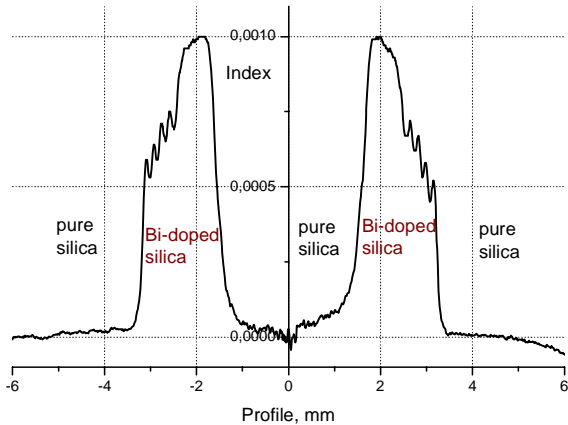


Fig. 1. Refractive index profile of collapsed Bi-doped two-layer silica structure used in luminescence experiments.

The ArF (193 nm) and KrF (248 nm) excimer lasers of Neweks, Estonia (model PSX-100 with pulse energy and duration of  $\sim 5$  mJ and  $\sim 5$  ns respectively) are used for luminescence excitation. The green (532 nm) pulsed diode laser is applied for luminescence excitation as well. Luminescence is recorded by means of MDR-3 grating monochromator equipped by photomultiplying tubes H6780-04 for UV-VIS and H10330A-45 for NIR (900 – 1400 nm) spectral bands as photoreceivers.

### 3 RESULTS

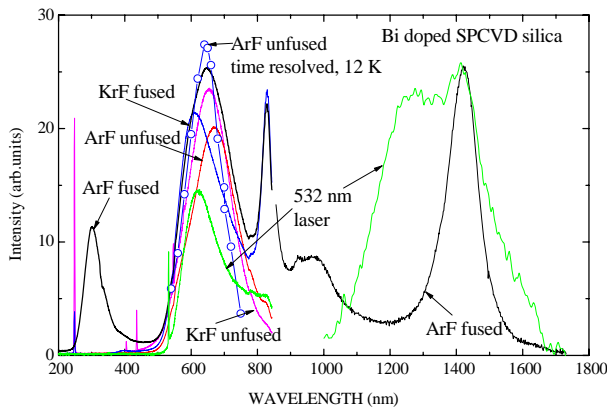


Fig.2. Photoluminescence spectra of Bi doped fused and unfused SPCVD silica measured at 293 K.

Main luminescence bands, which can be excited in the samples under investigation, are presented in Fig.2. Four bands can be stood out: near infrared bands centered at 1400 nm and 820 nm, an orange band at 620 - 650 nm and a UV band at 300 nm. The UV band is observed only under ArF laser excitation in the fused sample, and likely could be attributed to silica matrix rather than to Bi impurity.

Orange luminescence kinetics excited by ArF and/or KrF lasers in addition to the 3  $\mu$ s decay component contains

a slower one. Corresponding time constant of the slow component increases with the decrease of temperature up to 1 ms.

NIR luminescence band centered at 1400 nm exhibits practically exponential decay with time constant of about 650  $\mu$ s. NIR luminescence intensity of the 1400 nm band weakly depends on temperature in a range from 11 K to 700 K.

### 4 DISCUSSION

Whilst visible and NIR luminescence bands likely correspond to centers associated with Bi, the band at 300 nm, which is observed in the collapsed (fused) sample only, is most likely associated with luminescence of oxygen deficient centers in silica and thus is not immediately associated with Bi doping.

Under the excitation by 532 nm laser (an intra-center process) luminescence band intensity at 650 nm as well as decay time constant ( $\sim 3.5$  :s) do not depend on temperature up to 400 K. Since for allowed transitions the decay time constant should be in a range of nanoseconds, one can conclude that the transition observed is partly forbidden demonstrating such a rather slow decay.

The absence of any characteristic features in photoluminescence, which could be attributed to the presence of an  $\text{ns}^2$  mercury-like activator, testifies to the absence of bismuth incorporated into silica network in the form of  $\text{Bi}^{3+}$  ions. Indeed, triplet-to-singlet luminescence kinetics of  ${}^3\text{P}_1\text{-}{}^1\text{S}_0$  transition should strongly depend on temperature without significant variation in luminescence intensity.

The observed decay time constant increase of orange luminescence up to 1 ms with cooling is accompanied by the decrease of luminescence intensity and therefore could not be attributed to  ${}^3\text{P}_1\text{-}{}^1\text{S}_0$  transition with the capture of excited state on  ${}^3\text{P}_0$  level.

### 5 CONCLUSION

Lack of any signature of  $\text{Bi}^{3+}$  ions in both fused and unfused Bi-doped silica samples means that the observed luminescence bands are related to bismuth interstitials weakly bonded to silica network. The later is also confirmed by the absence of thermal quenching, which is characteristic for luminescence of alternative dopants, which are strongly chemically incorporated into silica network.

### REFERENCES

- [1] E.M.Dianov, "Amplification in Extended Transmission Bands," Optical Fiber Communication Conference (OFC) 2012 paper: OW4D.1

# Investigation on the generation process of HO<sub>2</sub><sup>•</sup> radicals induced by $\gamma$ -ray irradiation in O<sub>2</sub>-loaded fumed silica

G. Buscarino\*, S. Agnello\*, A. Parlato\*\*, F. M. Gelardi\*

\* Department of Physics, University of Palermo,  
Via Archirafi 36, 90123, Palermo, Italy

\*\* Dipartimento dell' Energia, Universita' di Palermo  
Viale delle Scienze, Edificio 6, 90128 Palermo, Italy

## ABSTRACT

We report an experimental investigation on the effects of  $\gamma$ -ray irradiation in three types of fumed silica previously loaded with O<sub>2</sub> molecules. Our data indicate that the main effect of irradiation in these systems is to generate a very large concentration of HO<sub>2</sub><sup>•</sup> interstitial radicals (about 10<sup>18</sup> molecules/cm<sup>3</sup>). Furthermore, the number of generated HO<sub>2</sub><sup>•</sup> was found to be larger in the samples with higher O<sub>2</sub> content before irradiation. This correlation suggests that HO<sub>2</sub><sup>•</sup> radicals are induced by reaction of interstitial O<sub>2</sub> molecules with radiolytic H atoms, as previously suggested for O<sub>2</sub>-loaded bulk amorphous silicon dioxide (a-SiO<sub>2</sub>) samples. However, at variance with respect to previous studies, in fumed silica the radiolytic H does not arise from SiOH or SiOOH groups, as no EPR signal due to Non-Bridging Oxygen Hole Centers (NBOHC) or to Peroxy Radicals (POR) is detected in the spectra of irradiated samples. A reasonable alternative we propose here is that radiolytic hydrogen atoms could arise from radiation induced breaking of interstitial H<sub>2</sub>O molecules, indicating that fumed silica in its pristine form could possess a very large concentration of interstitial water molecules.

**PACS Keywords:** HO<sub>2</sub><sup>•</sup>, H<sub>2</sub>O, O<sub>2</sub>, fumed silica, electron paramagnetic resonance spectroscopy, Raman spectroscopy.

## 1 INTRODUCTION

Hydroperoxy radical (HO<sub>2</sub><sup>•</sup>) is one of the most important intermediates in reactions in acidic solutions and its formation is usually controlled by various catalysts [1]. Among them, a-SiO<sub>2</sub> plays a key role, thanks to its interstitial voids which are able to encapsulate small diamagnetic and paramagnetic molecules [2-4]. In particular, HO<sub>2</sub><sup>•</sup> radical has been studied in O<sub>2</sub>-loaded bulk a-SiO<sub>2</sub> irradiated by F<sub>2</sub>-laser at T=77 K [5,6]. In those studies it has been shown that irradiation induces radiolytic hydrogen by breaking O-H bonds in SiOH and SiOOH groups. Once formed, these H atoms promptly react with interstitial O<sub>2</sub> molecules generating the HO<sub>2</sub><sup>•</sup> radicals. It is worth to note that, in this scheme together with the

hydroperoxy radicals, a comparable amount of NBOHC plus POR are also induced, as experimentally observed by Kajihara *et al.* [5,6].

## 2 EXPERIMENTAL

The materials considered here are three different types of fumed silica produced by Evonik [7]. Their commercial names are Aerosil300<sup>®</sup> (nickname AE300), Aerosil150<sup>®</sup> (AE150) and AerosilX50<sup>®</sup> (AOX50), and differ in the average diameters of the constituting nanoparticles, which are 7 nm, 14 nm and 40 nm, respectively. All the pristine materials were preventively loaded with O<sub>2</sub> molecules by treating them at T~473 K in oxygen atmosphere (P=50 bar). Subsequently the materials were subjected to  $\gamma$ -ray irradiation at the dose of 130 kGy in a <sup>60</sup>Co source.

In order to passivate NBOHC and POR in the irradiated samples, they were also exposed to H<sub>2</sub> atmosphere (P=140 bar) for 13 hours at T=300 K.

FT-Raman measurements were carried out by a Bruker RAMII spectrometer equipped with a Nd:YAG laser source at 1064 nm (9398 cm<sup>-1</sup>) that enabled detection of both the intrinsic vibrational Raman modes of a-SiO<sub>2</sub> and the photoluminescence emission from O<sub>2</sub> molecules [8]. This latter optical activity was used to estimate the O<sub>2</sub> content of loaded samples, as described in details elsewhere [8]. EPR measurements were carried out at T=300 K and at T=77 K with a Bruker EMX-micro-Bay spectrometer working at frequency of about 9.8 GHz (X-band) and with magnetic-field modulation frequency of 100 kHz. Low temperature spectra were obtained by putting the sample into a dewar flask filled with liquid nitrogen.

## 3 RESULTS

In the not irradiated samples no EPR signal was detected and the Raman/PL band of O<sub>2</sub> was found, whose amplitude gives an estimate of O<sub>2</sub> content from 2 up to 14 x10<sup>18</sup> molecules/cm<sup>3</sup> on increasing the nanoparticles diameter. At variance, after irradiation a strong EPR signal is observed in all the investigated samples, whose spectroscopic features are compatible with those attributed to HO<sub>2</sub><sup>•</sup> radicals [5,6,9]. The intensity of the detected EPR

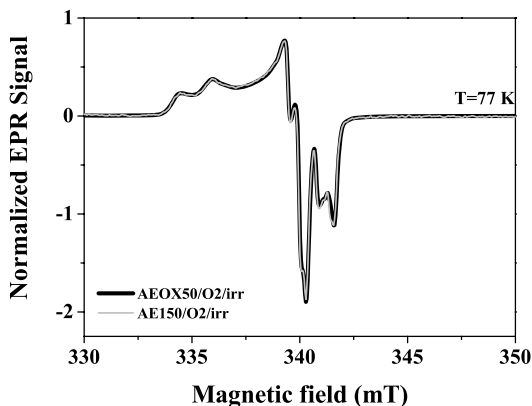


**Fig. 1** Comparison between the normalized EPR spectra obtained for O<sub>2</sub>-loaded and irradiated AEOX50 and AE300 materials.

signal is larger in the samples with higher O<sub>2</sub> content, ranging from 4x10<sup>17</sup> spins/cm<sup>3</sup> to 4x10<sup>18</sup> spins/cm<sup>3</sup> going from the material with the smallest nanoparticles to that with the largest ones. In spite of these differences, the shape of the EPR resonance was found to be virtually indistinguishable in all the investigated materials. This result is shown in Fig. 1, where the normalized EPR spectra obtained for AEOX50 and for AE300 are compared. These results and the strict correspondence between the spectra observed in the present work and those reported for HO<sub>2</sub><sup>·</sup> in D<sub>2</sub>O [9], suggest that the signal reported in Fig. 1 essentially represents the “isolated” HO<sub>2</sub><sup>·</sup> EPR lineshape. This point is relevant because, at variance to previous experimental investigations focused on bulk a-SiO<sub>2</sub>, in the observed spectra no signals ascribable to NBOHC and POR radicals are present, so suggesting that these defects are not induced in fumed silica upon irradiation. To further investigate this point the irradiated samples were subjected to H<sub>2</sub> loading. Since NBOHC and POR radicals are known to be very reactive with H<sub>2</sub> [10,11], this treatment is expected to cancel out the contribution of these centers to the overall EPR spectrum, if any. The results of these experiments are reported in Fig. 2, where the normalized EPR spectra obtained for AEOX50 before and after H<sub>2</sub> loading are compared. As it is evident, the treatment does not affect the resonance lineshape at all, strongly supporting the conclusion that no NBOHC nor POR centers are induced in O<sub>2</sub>-loaded fumed silica upon  $\gamma$ -ray irradiation. Similar results were also obtained for AE150 and AE300 materials.

The absence of NBOHC and POR radicals in the EPR spectra of the irradiated materials indicates that radiolytic H atoms, which interact with O<sub>2</sub> molecules to give HO<sub>2</sub><sup>·</sup> radicals, do not arise from SiOH or SiOOH groups, as in the case of bulk a-SiO<sub>2</sub>. Furthermore, it is also unreasonable that radiolytic hydrogen could arise from H<sub>2</sub> molecules dissolved into the material, as they are expected to escape efficiently from the material by rapid diffusion at room

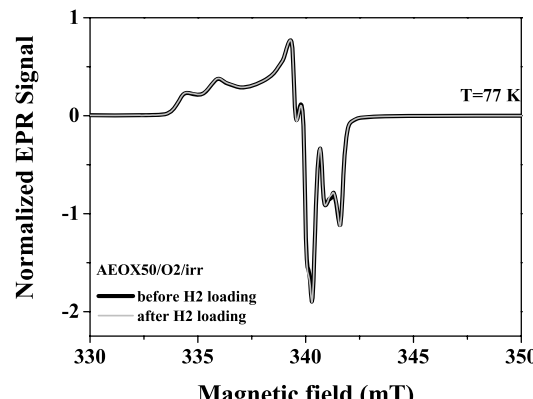


**Fig. 2** Comparison between the normalized EPR spectra obtained for O<sub>2</sub>-loaded and irradiated AEOX50 before and after H<sub>2</sub> loading.

temperature. At variance, a reasonable alternative we propose here is that the radiolytic hydrogen atoms could arise from radiation induced breaking of interstitial H<sub>2</sub>O molecules. In principle, water molecules should also diffuse rapidly in a-SiO<sub>2</sub> at room temperature. However, we assume that, since the outer surface of the particle is completely covered by a water film, due to air humidity, a relevant concentration of H<sub>2</sub>O molecules could reside into the fumed silica network in interstitial position.

This conclusion is interesting and could help in future works to understand to a very higher level the physical and chemical properties of fumed silica and of other similar nanodimensional high-surface materials.

## REFERENCES

Corresponding author: [gianpiero.buscarino@unipa.it](mailto:gianpiero.buscarino@unipa.it)

- [1] R. E. Buhler, J. Staehelin, H. Hoigne', J. Phys. Chem., 88, 2560, 1984.
- [2] C. T. Kresge, M. E. Leonowicz; W. J. Roth; J. C. Vartuli; J. S. Beck, Nature, 359, 710, 1992.
- [3] S. A. Bagshaw, E. Prouzet, T. J. Pinnavaia, Science, 269, 1242, 1995.
- [4] Y. Inaki, H. Yoshida, T. Yoshida, T. Hattori, J. Phys. Chem. B, 106, 9098, 2002.
- [5] K. Kajihara, M. Hirano, L. Skuja, H. Hosono, J. Am. Ceram. Soc., 128, 5371, 2006.
- [6] Kajihara *et al.*, J. Non-Cryst. Solids, 354, 224, 2008.
- [7] Evonik industries online catalog, 2010.
- [8] S. Agnello *et al.*, J. Phys. Chem. C, 115, 12832, 2011.
- [9] D. Mihelcic, A. Volz-Thomas, H. W. Patz, D. Kley, M. Mihelcic, J. Atm. Chem., 11, 271, 1990.
- [10] D. L. Griscom, J. Non-Cryst. Solids, 68, 301, 1984.
- [11] F. Messina, PhD Thesis, University of Palermo, 2007.

# A physico-chemical approach for the modification energy threshold by femtosecond laser irradiation in glasses

A.ERRAJI CHAHID, B. POUANELLEC and M. LANCRY

Institut de Chimie Moléculaire et des Matériaux d'Orsay, UMR CNRS-UPS 8182, Université de Paris Sud, Bât.410, 91405 Orsay Cedex, France  
[abdelouahad.erraji-chahid@u-psud.fr](mailto:abdelouahad.erraji-chahid@u-psud.fr)

## ABSTRACT

We describe a physico-chemical approach for determining the properties involved in the energy threshold for permanent modification when glasses are irradiated with a femtosecond laser. The key of the model is the minimum energy density for maintaining the glass at a temperature during a time larger than the material relaxation time at this temperature.

## I. INTRODUCTION

One important point when we want to process a glass by femtosecond laser irradiation is to know what properties determine the minimum energy to produce a permanent modification. For this aim, all authors start from the beginning of the mechanism i.e. the photo-absorption process and search for its characterization assuming that it is the limiting stage and not the material lattice properties. With this approach, they are not able to explain, for example that the energy threshold is not sensitive to doping in silica glasses [1]. For us, we have taken the problem by the end, from the lattice properties and have obtained results in agreement with some of the observations.

## II. THE ELECTRON EXCITATION AND THE INTERACTION VOLUME

As the laser pulse energy is high enough, multiphoton absorption is the primary cause of energy transfer to the glass. In this case, it is possible to achieve interband transitions in otherwise transparent materials at linear absorption. Specifically in pure silica glass, for the IR laser Ti :Al<sub>2</sub>O<sub>3</sub> emitting at 800nm, it needs 6 photons [2-3] for an electron to transit from valence band to conduction one. In such a case, multiphoton ionization (MPI) leads to electron-hole pairs formation. This is well described in [4]. Once the free electron density in the conduction band has become non-zero, further absorption increases the kinetics energy of the electron plasma i.e. its temperature (typ. up to 30eV in SiO<sub>2</sub> [5] but most of them have less than 10 eV in our conditions). Electron collision between accelerated electrons and valence ones can also increase the plasma density. In the range of intensity considered in this paper, the electron excitation by tunneling seems to be not working [6].

Usually, the experiments are performed by focusing the laser beam a few hundreds microns into the glass by means of a lens. Then, the beam is moved transversally (usually) or longitudinally (more scarcely). Because the shape of the interaction volume changes on laser parameters, the light

intensity distribution in this volume changes influencing the energy threshold [7]. It is a combination of optical and physical processes. It changes with the focusing strength and the interaction region exhibit different shapes.

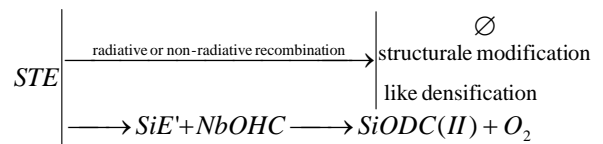
It is therefore, necessary to define the interaction not only by the energy intensity but by also the numerical aperture (NA) of the lens used to focus the beam into the material.

Furthermore, the NA does not alone define the focusing but the power intensity in the beam itself plays also a role in the focusing (index is non-linear:  $n=n_0+n_2I_{loc}$ ,  $n_2=3.2 \cdot 10^{-16} \text{ cm}^2/\text{W}$ ) [8-9]. Increasing the beam energy results therefore in the displacement of the focus to the sample entrance face and the interaction volume become elongated before the geometrical focus (linear focus). Above a critical beam energy ( $P_{CR}=\frac{\lambda}{2\pi n_0 n_2}$ ), a non diverging trace beyond the geometrical

focus appears. This is due to a balance between the non-linear increase of the refractive index and the defocusing effect of the electron plasma [4]. In conclusion, the power intensity is no longer an input parameter of the experiment but the beam power or the beam energy is. We have therefore to classify the experiments according to: laser pulse energy, NA, pulse duration instead of light intensity even if, at a point, intensity is the relevant parameters for material changes.

## III. THE RELAXATION PROCESSES AND THE EFFECT IN THE MATERIAL: THE THRESHOLD DEFINITIONS

Glass modifications are the result of relaxation of photoexcited electron. Electrons relax first into self-trapped excitons (STE) by electron-phonon coupling and then annihilate radiatively (lifetime of nanoseconds at room temperature) or not (coupling with lattice phonons), or transform into point defects (e.g. into SiE' and NBOHC (bond breaking) and then into a silicon oxygen deficient center quoted as SiODC(II)) [10-11] following the reaction scheme sketched below:



The yield for defect production is small [12] compared to the other ways but nevertheless can play a striking role in memory effect [13-14]. The first observation we can report

under irradiation powerful enough is the transmission decrease. It is observed on a large wavelength range from IR to blue [15-16]. This reveals that glass is modified in its extended microstructure. We speculate that such glass modification is the results of electron energy transmitted to the lattice by non-radiative coupling of electron with the lattice. This coupling corresponds to an increase of non-equilibrium temperature of the lattice that can reach several thousands of degrees in the illuminated area limited by thermal conduction. The temperature increase during a time long enough can lead to glass melting and to a change of average disorder i.e. a change of glass fictive temperature. We can define this temperature ( $T_c$ ) by saying that the relaxation time defined by the ratio between the viscosity ( $\eta$ ) and the shear modulus ( $G$ ) should be smaller than the time during which the matter overcome this temperature. This can be written as :

$$\eta(T_c)/G(T_c) = \delta t(T > T_c) \quad (\text{Eq. 1})$$

On the other hand, the time-temperature profile of the irradiated area is mainly defined by the amount of energy density released in the lattice by the STE divided by the specific heat capacity and the thermal diffusivity. Considering that the energy density ( $W$ ) finally transferred to the lattice is expressed as the product of (a), of the forbidden energy gap  $E_g$  of the glass and of the STE concentration at the end of the pulse i.e.  $W = a \cdot E_g \cdot [\text{STE}]$  where  $a$  is an enhancing coefficient taking into account the acceleration energy after interband excitation of the electrons. Considering also that only a fraction  $\alpha$  of the incident energy is absorbed by the matter due to partial reflection by the plasma, in these conditions, for pure silica, the rough estimate of the fictive temperature is obtained at 2490°C. Because STE production is the result of MPI in our case, the STE concentration varies as  $N_o \cdot \sigma I_{T_1}^{-n} \tau$ .  $I_{T_1}$  is the intensity threshold corresponding to energy threshold  $T_1$ ,  $N_o$  the density of states at the top of valence band,  $\sigma$  is the multiphoton absorption cross section,  $\tau$  is the pulse duration. In sum-up, the minimum energy density required for glass modification defined  $W$ , from that we get the intensity threshold  $I_{T_1}$ . Then from non-linear propagation law, we deduce the  $T_1$  energy of the beam. As mentioned above, only a fraction of the incident pulse energy ( $T_1$ ) is absorbed by the matter i.e. a part is reflected by the plasma [3]. Due to focusing and taking into account the absorption length, we have:

$$T_1 = 2.3 \frac{I_{th}}{\alpha} \cdot \tau \cdot S(NA, 2.3 \frac{I_{th}}{\alpha}) \quad \text{where } S(NA, I_{th}) \text{ is the average cross section of the focal volume alike the expression given by Schaffer et al. [4]}$$

$$S(NA, I) = \frac{\lambda^2}{\pi(NA)^2 + I 2\pi n_0 n_2} \quad \text{valid for } NA > 0.1. \quad \alpha, \text{ is a}$$

*priori* unknown but assumed constant

#### IV. CONCLUSION

What is important for a permanent modification of the glass is for it to stay, at a given temperature larger than its starting fictive temperature (its internal order), a time long enough called relaxation time. This one depends on the viscosity and

the shear modulus of the material, the lower the viscosity, the larger the shear modulus, the smaller the relaxation time and globally the larger the  $T$ , the smaller the relaxation time. If it is the case, the glass changes its fictive temperature and refractive index changes (increase for pure silica, decrease for most of the other glasses). This transformation occurs well after the photoexcited electron relaxation and thermodynamics is applicable.

On the other side, the change on time of  $T$  on a point of the matter after light absorption is defined by the thermal capacity, the geometry of the interaction volume, the thermal diffusivity and the energy density absorbed in this volume. Our computation applied to doped silica show that the minimum energy for overcoming the relaxation time does not change significantly on doping as it is experimentally observed. Examination of threshold in other glasses are in progress.

#### REFERENCES

- [1] M. Lancry, B. Poumellec, A. Chahid-Erraji, M. Beresna, and P. G. Kazansky, "Dependence of the femtosecond laser refractive index change thresholds on the chemical composition of doped-silica glasses", Optical Material Express submitted.
- [2] M. Lancry, N. Groothoff, B. Poumellec, S. Guizard, N. Fedorov, and J. Canning, "Time-resolved plasma measurements in Ge-doped silica exposed to IR femtosecond laser," Physics Review B **To be submitted**.
- [3] F. Quéré, S. Guizard, and P. Martin, "Time-resolved study of laser-induced breakdown in dielectrics," EPL (Europhysics Letters) **56**, 138 (2001).
- [4] C. B. Schaffer, A. Brodeur, and E. Mazur "Laser-induced breakdown and damage in bulk transparent materials induced by tightly focused femtosecond laser pulses," Measurement Science Technology **12**, 1784-1794 (2001).
- [5] F. Quéré, S. Guizard, P. Martin, G. Petite, H. Merdji, B. Carré, J. Hergott, and L. Le Déroff, "Hot-electron relaxation in quartz using high-order harmonics," Physical Review B **61**, 9883 (2000).
- [6] B. Rethfeld, "Free-electron generation in laser-irradiated dielectrics," Physical Review B **73**, 035101 (2006).
- [7] S. Skupin and L. Bergé, "Self-guiding of femtosecond light pulses in condensed media: Plasma generation versus chromatic dispersion.,," PHYSICA D **220**, 14-30 (2006).
- [8] T. Kato, Y. Suetsugu, and M. Nishimura, "Estimation of non-linear refractive index in various silica-based glasses for optical fibers.,," Optics Letters **20**, 2279-2281 (1995).
- [9] S. Le Boiteux, P. Segonds, L. Canioni, L. Sarger, T. Cardinal, C. Duchesne, E. Fargin, and G. Le Flem, "Nonlinear optical properties for  $\text{TiO}_2$  containing phosphate, borophosphate, and silicate glasses.,," Journal of Applied Physics **81**, 1481-1487 (1997).
- [10] M. Lancry, N. Groothoff, S. Guizard, W. Yang, B. Poumellec, P. Kazansky, and J. Canning, "Femtosecond laser direct processing in wet and dry silica glass," Journal of Non-Crystalline Solids **355**, 1057-1061 (2009).
- [11] S. Mao, F. Quéré, S. Guizard, X. Mao, R. Russo, G. Petite, and P. Martin, "Dynamics of femtosecond laser interactions with dielectrics," Applied Physics A: Materials Science & Processing **79**, 1695-1709 (2004).
- [12] S. Guizard, P. Martin, G. Petite, P. D'Oliveira, and P. Meynadier, "Time-resolved study of laser-induced colour centres in  $\text{SiO}_2$ ," Journal of Physics: Condensed Matter **8**, 1281 (1996).

- [13] P. Rajeev, M. Gertsvolf, P. Corkum, and D. Rayner, "Field dependent avalanche ionization rates in dielectrics," *Physical Review Letters* **102**, 83001 (2009).
- [14] R. Taylor, C. Hnatovsky, and E. Simova, "Applications of femtosecond laser induced self organized planar nanocracks inside fused silica glass," *Laser & Photonics Reviews* **2**, 26-46 (2008).
- [15] A. Couairon, L. Sudrie, M. Franco, B. Prade, and A. Mysyrowicz, "Filamentation and damage in fused silica induced by tightly focused femtosecond laser pulses," *Physical Review B* **71**, 125435 (2005).
- [16] L. Sudrie, "Propagation non-linéaire des impulsions laser femtosecondes dans la silice," Université de Paris Sud XI Orsay  
[http://wwwy.ensta.fr/ilm/Archives/Theses\\_pdf/L\\_Sudrie\(2002\).pdf](http://wwwy.ensta.fr/ilm/Archives/Theses_pdf/L_Sudrie(2002).pdf).
- [17] M. Lancry, B. Poumellec, A. Chahid-Erraji, M. Beresna, and P. Kazansky, "Dependence of the femtosecond laser refractive index change thresholds on the chemical composition of doped-silica glasses" *Opt. Mat. Express Accepted*
- [18] S. Mao, F. Quéré, S. Guizard, X. Mao, R. Russo, G. Petite, and P. Martin, "Dynamics of femtosecond laser interactions with dielectrics," *Applied Physics A: Materials Science & Processing* **79**, 1695-1709 (2004).

# Spectral UV-losses in 355 nm pulsed laser delivery system at low temperatures

J. C. Heimann<sup>1,4</sup>, C. P. Gonschior<sup>1,2,4</sup>, K.-F. Klein<sup>1,4</sup>, G. Hillrichs<sup>3</sup>, E. Takala<sup>5</sup>

<sup>1</sup>Technische Hochschule Mittelhessen, Competence Center “Optical Technologies and Systems”,  
Wilhelm-Leuschner-Str. 13, 61169 Friedberg, Germany,

e-mail: karl-friedrich.klein@iem.thm.de, phone: +49-6031-604-214/216

<sup>2</sup>City University London, Northampton Square, London EC1V 0HB, United Kingdom

<sup>3</sup>Hochschule Merseburg, Geusaer Str., 06217 Merseburg, Germany

<sup>5</sup>CERN, Department TE-MSC, 1211 - Geneva – 23, Switzerland

## ABSTRACT

Synthetic silica is a material of major interest for transmitting NUV-laser light. However, additional loss is caused by irradiation with commercially available NUV-laser systems. For high-OH polyimide coated all-silica multimode-fibers the photodegradation and annealing was investigated for 355 nm laser light with different pulse intensities at room temperature as well as cryogenic temperatures. An examination of induced loss showed an improved resistance of the fiber material to UV-light at low temperatures featuring enhanced transmission performance at 214 nm and 265 nm. These results were compared to UV-induced loss by irradiation with a deuterium lamp.

**PACS Keywords:** 355 nm pulsed laser, multi-mode fibers, single-mode fibers, UV-defects, low temperatures

## 1 INTRODUCTION

In silica-based light delivery systems, UV-defects are generated during the operation itself. Due to further improvements in manufacturing, the concentration of UV-defects after fiber drawing could be significantly reduced in the fiber core, based on high-OH and low-OH synthetic silica [1].

UV-damage in excimer-laser delivery systems has been studied at room temperature in detail [2]. In addition to these lasers at 193, 248 and 308 nm, lasers based on 3<sup>rd</sup> harmonic of Nd-YAG laser at 355 nm wavelength are of commercial interest, too. Because the photon energy is 3.5 eV, the deep-UV defects [3] at 214 nm (E'-centers) or 265 nm (NBOH-centers) cannot be generated by single-photon absorption. Although two-photon absorption [5] at 355 nm is at least one and a half orders of magnitude lower in comparison to the excimer lasers, the deep-UV defects can be generated. Based on application requirements, the studies including surface damage [6] have mainly been carried out at room temperature. However, due to increasing interest for delivery systems at lower temperatures (liquid nitrogen, liquid helium), such as

studying the stability of superconducting strands [7], first results of spectral transmission losses including deep-UV defects in the undoped silica core and waveguiding properties of the fibers will be shown and discussed.

## 2 EXPERIMENTAL SETUP

The setup consists of two Nd-YAG pulsed laser systems (see Table 1), an imaging system, the fiber under test (FUT) on a high precision multi-axis translation stage and a Dewar flask with liquid nitrogen which sustained the well-defined bended FUT at a total temperature of 77 K. The distal end of the FUT was mounted in front of a thermopile power meter for measuring average power. Pulse energies were evaluated using a pyroelectric detector.

Spectral measurements were performed using a standard deuterium ( $D_2$ ) lamp as broadband light source and an optimized imaging system [7]. The distal end of the FUT was coupled into a fiber-optic spectrometer (FOS).

The FDP-FUT is an all-silica MMF with un-doped high-OH silica core and F-doped silica cladding, surrounded by a Polyimide coating [8]. The core diameter, the length and the numerical aperture of the step-index fiber in these tests were fixed: 100  $\mu m$ , 5.0 m and 0.22, respectively.

The pulse energy of the High Pulse Power (HPP) laser system was attenuated with a dielectric mirror. The attenuated pulse energy of about 20  $\mu J$  according to a peak power of 2 kW resulted in maximum power densities of 26 MW/cm<sup>2</sup> in the fiber core of 100  $\mu m$  diameter and 13 MW/cm<sup>2</sup> for the Low Pulse Power (LPP) laser system respectively.

Table 1: Overview of the laser systems.

	High Pulse Power System (HPP)	Low Pulse Power System (LPP)
Wavelength	355 nm	355 nm
Pulse energy	90 $\mu J$	1 $\mu J$
Pulse duration	10 ns	1 ns
Max. repetition rate	200 Hz	25 kHz

### 3 RESULTS AND DISCUSSION

All samples (each with 5 m length) were irradiated for four hours using HPP and LPP laser system and D<sub>2</sub> lamp. The additional loss at 214 nm was about 3 dB after irradiation with D<sub>2</sub> lamp in contrast to 14 dB using HPP laser system and 10 dB using LPP laser system (see Figure 1). With increased pulse energy the maximal loss at 265 nm was about 7 dB. Induced NBOH defect centers were affected by pulse energy, which can be explained by different mechanisms of bond-breaking.

Comparing laser induced loss by the HPP laser system into the FUT from Figure 2 with laser induced loss while maintaining the sample at a temperature of about 77 K shows a decrease of both absorption bands in the order of 5 dB (265 nm) up to 9 dB (214 nm) (see Figure 2). The induced loss by two-photon absorption seems to depend on ambient temperature.

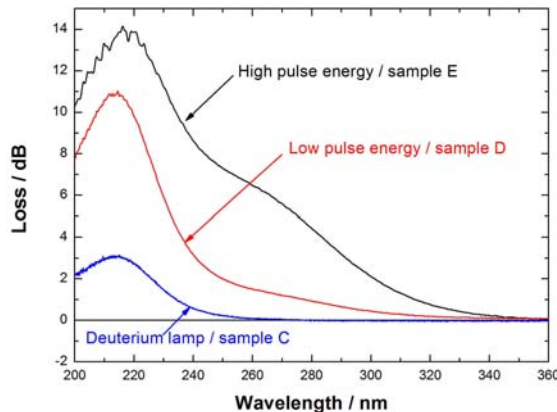


Figure 1: Induced loss by different pulse intensities into the FUT (5 m length) at room temperature.

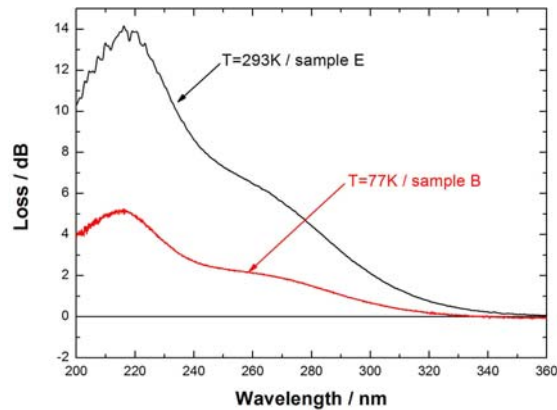


Figure 2: Comparison of induced loss by HPP laser system into the FUT (5 m length) at different temperatures.

The annealing process of laser induced absorption by irradiation with HPP laser system at a total temperature of 77 K was examined during warming the fiber at room temperature again. For the data shown in Figure 2 (sample B) the induced loss, which was measured straight after irradiation, decreases exponentially with a boundary value

of about 50 percent of that starting value. The time constant of that decrease was in the order of 2 min, so that the induced loss was 2.8 dB at 214 nm and 0.7 dB at 265 nm after several minutes.

In contrast to these results a significant lower ratio of transient defect generation was observed with samples irradiated at room temperature, leading to a decrease of the induced loss shown in Figure 2 (sample E) of about 2 dB at 214 nm and 1 dB at 265 nm, which was achieved only in a considerable larger time period of about 2 hours.

### 4 SUMMARY AND OUTLOOK

The tested fiber with a high-OH core has an extremely high UV-resistance due to further improvements in preform und fiber [1]. Reduction of two-photon absorption correlated with the generation of laser induced E' and NBOH defect-centers was observed at lower cryogenic temperatures, which can be related to the temperature dependence of Urbach Edge in silica [9]. However, no induced absorption was observed at the laser wavelength of 355 nm.

So far, the annealing process after irradiation has been studied for specific cases. Detailed studies with D<sub>2</sub>-lamp and NUV-laser systems will be carried out in the near future.

### REFERENCES

- [1] V. Khalikov et.al., "High-OH Fibers with Higher Stability in the UV-Region," SPIE-Proc., 6083, 6083-08, 2006.
- [2] K.-F. Klein et.al., "Possibilities and Limitations Of Optical Fibers for the Transmission Of Excimer Laser Radiation," SPIE-Proc., 2966, 564-573, 1996.
- [3] D. L. Griscom, "Defect Structure of Glasses" Journal of Non-Crystalline Solids, 73, 51-77, 1985.
- [4] R. K. Brimacombe et.al., "Dependence of the Non-linear Transmission Properties of Fused Silica Fibers on Excimer Laser Wavelength," J. Appl. Phys., 68, 3584-3591, 1990.
- [5] G. Hillrichs et.al., "Performance of Low-Mode and Single Mode Optical Fibers for High Peak Power 355 nm Laser Irradiation," SPIE-Proc., 7894, 2011
- [6] E. Takala et.al., "Silica-Silica Polimide Buffered Optical Fiber Irradiation and Strength Experiment at Cryogenic Temperatures for 355 nm Pulsed Lasers," Cryogenics, 52, 77-81, 2011.
- [7] M. Huebner et.al., „Fiber-optic systems in the UV-region“. SPIE-Proc. BiOS‘00, Vol. 3911, pp. 303-312, 2000
- [8] Polymicro Technologies LLC, Phoenix (Az, US), "Data sheets about UV-fibers," ([www.polymicro.com](http://www.polymicro.com))
- [9] F. Kühnlenz, "Vacuum UV Spectroscopy on synthetic silica during pulsed UV laser irradiation-(in German)" Friedrich-Schiller-University Jena, PhD-thesis, 2003.